GKSS FORSCHUNGSZENTRUM in der HELMHOLTZ-GEMEINSCHAFT

Quantitative X-ray Microtomography with Synchrotron Radiation

(Vom Department Physik der Fakultät für Mathematik, Informatik und Naturwissenschaften der Universität Hamburg als Dissertation angenommene Arbeit)

Author:
T. Donath

ISSN 0344-9629

HELMHOLTZ | GEMEINSCHAFT

wissen schafft nutzen

GKSS 2007/17

GKSS 2007/17

Quantitative X-ray Microtomography with Synchrotron Radiation

(Vom Department Physik der Fakultät für Mathematik, Informatik und Naturwissenschaften der Universität Hamburg als Dissertation angenommene Arbeit)

Author:
T. Donath
(Institute of Materials Research)

GKSS-Forschungszentrum Geesthacht GmbH · Geesthacht · 2007

Die Berichte der GKSS werden kostenlos abgegeben.
The delivery of the GKSS reports is free of charge.

Anforderungen/Requests:

GKSS-Forschungszentrum Geesthacht GmbH
Bibliothek/Library
Postfach 11 60
D-21494 Geesthacht
Germany
Fax.: (49) 04152/871717

Als Manuskript vervielfältigt.

ISSN 0344-9629

GKSS-Forschungszentrum Geesthacht GmbH · Telefon (04152)87-0
Max-Planck-Straße 1 · D-21502 Geesthacht / Postfach 11 60 · D-21494 Geesthacht

GKSS 2007/17

Quantitative X-ray Microtomography with Synchrotron Radiation

(Vom Department Physik der Fakultät für Mathematik, Informatik und Naturwissenschaften der Universität Hamburg als Dissertation angenommene Arbeit)

Tilman Donath

209 pages with 58 figures and 15 tables

Abstract

Synchrotron-radiation-based computed microtomography (SRμCT) is an established method for the examination of volume structures. It allows to measure the x-ray attenuation coefficient of a specimen three-dimensionally with a spatial resolution of about one micrometer. In contrast to conventional x-ray sources (x-ray tubes), the unique properties of synchrotron radiation enable quantitative measurements that do not suffer from beam-hardening artifacts. During this work the capabilities for quantitative SRμCT measurements have been further improved by enhancements that were made to the SRμCT apparatus and to the reconstruction chain. For high-resolution SRμCT an x-ray camera consisting of luminescent screen (x-ray phosphor), lens system, and CCD camera was used. A significant suppression of blur that is caused by reflections inside the luminescent screen could be achieved by application of an absorbing optical coating to the screen surface. It is shown that blur and ring artifacts in the tomographic reconstructions are thereby drastically reduced. Furthermore, a robust and objective method for the determination of the center of rotation in projection data (sinograms) is presented that achieves sub-pixel precision. By implementation of this method into the reconstruction chain, complete automation of the reconstruction process has been achieved. Examples of quantitative SRμCT studies conducted at the Hamburger Synchrotronstrahlungslabor HASYLAB at the Deutsches Elektronen-Synchrotron DESY are presented and used for the demonstration of the achieved enhancements.

Keywords: quantitative microtomography, synchrotron radiation, SRμCT, center of rotation, tuning-fork artifact, sinogram, x-ray phosphor, scintillator crystal, luminescent radiation, optical coating, absorbing backing, backing layer, black backing, reconstruction artifacts, ellipse phantom, friction stir welding, hydroxyapatite scaffolds, fiberboard, cortical bone

Quantitative Röntgen-Mikrotomographie mit Synchrotronstrahlung

Zusammenfassung

Die Mikrotomographie unter Verwendung von Synchrotronstrahlung (SRμCT) ist eine etablierte Methode, die die drei-dimensionale Untersuchung des Röntgen-Schwächungskoeffizienten einer Probe mit einer Ortsauflösung von etwa 1 μm ermöglicht. Gegenüber konventionellen Röntgenröhren ermöglicht der Einsatz der Synchrotronstrahlung quantitative Messungen, die nicht durch die Strahlaufhärtung (beam hardening) beeinträchtigt werden. Im Rahmen dieser Arbeit wurden die Möglichkeiten der quantitativen SRμCT-Untersuchung erweitert. Dies konnte durch Verbesserungen am SRμCT-Aufbau und an der Rekonstruktionskette erreicht werden. Für die hoch-auflösende SRμCT wurde eine Röntgenkamera, bestehend aus Leuchtschirm, Linsensystem und CCD-Kamera eingesetzt. Die in diesen Kameras durch Reflektionen im Leuchtschirm verursachte Unschärfe konnte durch das Aufbringen einer absorbierenden optischen Beschichtung auf die Leuchtschirmoberfläche deutlich gemindert werden. Es wird gezeigt, dass hierdurch auch Unschärfe und Ringartefakte in der tomographischen Rekonstruktion drastisch reduziert werden. Desweiteren wird eine Methode vorgestellt, die es ermöglicht, das Drehzentrum in gemessenen Projektionsdaten (Sinogrammen) mit Sub-Pixel-Genauigkeit zu bestimmen. Durch die Implementierung dieser Methode in die Rekonstruktionkette konnte der Rekonstruktionsprozess vollständig automatisiert werden. Beispiele quantitativer SRμCT-Untersuchungen, die am Hamburger Synchrotronstrahlungslabor HASYLAB am Deutschen Elektronen-Synchrotron DESY durchgeführt wurden, werden präsentiert. Anhand dieser Untersuchungen werden die erzielten Verbesserungen demonstriert.

Manuscript received / Manuskripteingang in TKP: 9. August 2007

Table of Contents

List of important symbols and acronyms

$*$, $**$	Convolution operator (one-dimensional, two-dimensional)
a_{10}	Spatial resolution corresponding to 10% contrast transfer
A	Numerical aperture of the lens system
b_t, b_z	Binning factor along the direction perpendicular (t-direction) and parallel to the rotation axis (z-direction)
d, $d(x,y)$	Recorded dark image of the CCD camera
E_0	Photon energy (x-rays)
E_{lum}	Photon energy (luminescence photons)
$f(x,y)$	Representation of a tomographic slice, also $\mu(x,y)$
$f(x_i,y_i)$, f_{ij}	$f(x,y)$ in the discrete case
$F(u,v)$	Fourier transform of $f(x,y)$
H, $H_{discrete}$	Image entropy (or histogram entropy) of continuous and discrete gray value images
$\tilde{f}(x,y)$	Tomographic reconstruction of $f(x,y)$
i, $i(x,y)$	Recorded radiographic image of the sample
j, ι	Imaginary unit such that $j^2 = \iota^2 = -1$, ι is used, where j is used as index variable
k	f-number of the lens system in the x-ray camera
$K(u)$	Box car function, unity for $\|u\| < 1/2$ and zero elsewhere
m	Optical magnification factor of the x-ray camera
m_0	0-th order moment of a tomographic slice $f(x,y)$ or 0-th order moment along t for any projection $p_\theta(t)$
μ	X-ray attenuation coefficient
$\mu(x,y)$	X-ray attenuation coefficient in the tomographical slice, also $f(x,y)$
N_θ	Number of projection angles θ_j
N_t	Number of sampling position t_j in projection space
N, $\overline{N}$, $\langle N \rangle$	Number of charge quanta recorded by the CCD (average $\overline{N}$, expectation value $\langle N \rangle$)
N_0, $\overline{N_0}$, $\langle N_0 \rangle$	Number of incident x-ray photons (average $\overline{N_0}$, expectation value $\langle N_0 \rangle$)
n_{el}	Readout noise of the CCD in units of charge quanta (electrons)
n_{ls}	Refractive index of the luminescent screen
$p_\theta(t)$	Mathematical: projection of $f(x,y)$ under projection angle θ; physical: projection of the attenuation coefficient $\mu(x,y)$
$p_{\theta_i}(t_j)$, p_{ij}	$p_\theta(t)$ in the discrete case
$\hat{p}$	True value of the projected attenuation coefficient, in calculations where p is not mathematically exact
$P_\theta(w)$	One-dimensional Fourier transform of $p_\theta(t)$

Q	Image metrics for the determination of the center of rotation, metrics based on entropy (Q_H), integral of the absolute value (Q_{IA}), and the integral of the negative values (Q_{IN})
$Q(\tilde{f})$, $Q(\tilde{t}_r)$	Image metric value for a reconstruction $\tilde{f}$ performed for center of rotation $\tilde{t}_r$
r, $r(x,y)$	Recorded radiographic reference image
t, t_j	Spatial coordinate in projection space in the continuous and discrete case
t_r, $\tilde{t}_r$	Position of the center of rotation in the projections (true, assumed)
t_c	Position of the center of mass in the projections
τ	Sampling interval, also referred to as effective pixel size (given by the pitch of CCD pixels τ_{CCD} divided by the optical magnification factor m)
θ, θ_i	Projection angle for the continuous and discrete case respectively
$u(\alpha)$	Heaviside step function, unity for $\alpha \geq 0$ and zero elsewhere.
w, w_k	Frequency coordinate for the continuous and discrete case respectively, corresponding to t-coordinate in real space
x, x_m	Spatial coordinate in the reconstructed slice or on the detector, depending on context
y, y_n	Spatial coordinate in the reconstructed slice or on the detector, depending on context
z, z_h	Spatial coordinate, parallel to the rotation axis
ADU	Analog-to-digital converter units (of the CCD)
CCD	Charge coupled device
CNR	Contrast-to-noise ratio
CT	Computed tomography
DQE	Detective quantum efficiency
DR	Dynamic range
ESF	Edge spread function
FW	Full width
LSF	Line spread function
MTF	Modulation transfer function
μCT	Microtomography (also: micro-CT)
PSF	Point spread function
QE	Quantum efficiency
SEM	Scanning electron microscopy
SNR	Signal-to-noise ratio
SR	Synchrotron radiation
SRμCT	Synchrotron-radiation-based computed microtomography

Chapter 1

Introduction

X-ray computed tomography (CT) is an established method for cross-sectional and fully three-dimensional imaging of the internal structure of an object. The first commercial x-ray CT scanner for medical diagnosis was presented by Hounsfield [81] in 1971. Since then the further development of medical CT continued as described in an overview by Natterer and Ritman [109]. Besides its medical application, x-ray CT has found wide-spread use in industry, e.g., for non-destructive testing and reverse engineering as well as in many scientific areas. At the microscopic scale CT is known as microtomography (μCT). The performance of μCT systems, however, is strongly limited by the properties of conventional x-ray tube sources, which always require a trade off between source size (resolution) and intensity (speed). These limitations can be circumvented by the application of synchrotron radiation as an intense x-ray source.

Synchrotron-radiation-based computed microtomography (SRμCT) was first developed and applied by Bonse *et al.* [22], [23] and Flannery *et al.* [61] in the mid 1980s. In recent years it has become available for researchers as a 'user experiment' at the continuously growing number of dedicated synchrotron-radiation laboratories (today about 40 worldwide). SRμCT enables fast, three-dimensional imaging with about 1 μm spatial resolution and has been applied in a wide range of research studies. The investigated specimens include: bone, teeth, implant materials, small blood vessels, wood, paper, micro-fossils, rocks, soil, concrete, and metal or polymer foams, to name only a few examples.

Synchrotron radiation has several fundamental advantages for quantitative CT measurements, when compared to conventional x-ray tube sources. High intensity and strong collimation of the synchrotron-radiation beam allow for short scan times and for the application of simple (parallel-beam) reconstruction techniques. More importantly these characteristics enable the efficient use of monochromators, which are used to select the photon energy. The photon energy can thus be optimized for the examination of each sample, and due to the small bandwidth of the resulting photon spectrum, non-linear effects (beam hardening), that are observed in conventional CT, are not observed in SRμCT.

The determination of quantitative measures from the tomographic reconstructions is known as quantitative computed tomography (QCT). Here morphological parameters such as distances, areas, or volumes are extracted from the data or sometimes, simply a precise value of the attenuation coefficient is determined. With the today available computational power, even more sophisticated morphological characterization of three-dimensional structures has become possible. Software packages for three-dimensional image processing and analysis (e.g., ITK, DIPlib, VIGRA, or MAVI)[1] have become applicable to volumetric data sets of reasonable size and enable, e.g., the calculation of pore size distributions or the calculation of skeleton models. All these quantitative CT measurements commonly rely on distortion-free (artifact-free) tomographic reconstructions.

The application of two-dimensional x-ray detectors in SRμCT enables efficient use of the x-ray flux and allows to reconstruct the three-dimensional volume structure from a single series of two-dimensional projection images. Today the best x-ray cameras available for SRμCT achieve spatial resolution of about one micrometer [102]. They consist of a luminescent crystal (x-ray phosphor) that is lens-coupled to a charge-coupled device (CCD). This type of x-ray camera is usually also applied in other types of synchrotron-radiation tomography such as phase-contrast tomography [10], [36] or nano-tomography, which achieves sub-micrometer resolution by the use of x-ray optical elements such as mirrors, refractive lenses [133], zone plates [156], or Bragg magnifiers [116],[139]. However, light reflections inside the luminescent crystal cause blur of a small fraction of light over large distances. This long-range blur, although almost invisible in the radiographic images, can give rise to blur or even to non-linear effects in the tomographic reconstruction. Furthermore, inhomogeneities on the surface of the luminescent screen can result in systematic artifacts (ring artifacts) in the tomographic reconstruction. In this work suppression of blur in the recorded images is demonstrated physically by application of an optical coating (black backing) to the luminescent screen and mathematically by correction of the recorded images (image deconvolution).

With the constantly increasing speed of SRμCT measurements by the application of fast CCD cameras in combination with high-flux beams (direct wiggler beams [98], direct undulator beams [44], or beams from monochromators with large bandwidth), the need for fast and automated data evaluation has become more and more important, but especially the determination of the center of rotation (position of the sample rotation axis) in the recorded projection data has so far hindered the automation of the reconstruction. The center of rotation, however, is an important input parameter for the tomographic reconstruction and must be determined before the reconstructions can be calculated. The commonly used automated methods were not capable of determining the center of rotation with the required precision. In this work a robust method for the determination of the

[1] Examples of 3D image processing and analysis software: ITK - Insight Segmentation and Registration Toolkit, available online at `http://www.itk.org/`. [83]; DIPlib - The Delft Image Processing library, available online at `http://www.ph.tn.tudelft.nl/DIPlib/`; VIGRA - Vision with Generic Algorithms, available online at `http://kogs-www.informatik.uni-hamburg.de/~koethe/vigra/`; MAVI - Modular Algorithms for Volume Images, copyright 2004, Fraunhofer Institut für Techno- und Wirtschaftsmathematik, information available online at `http://www.itwm.fhg.de/mab/projects/MAVI/` [visited November, 5th 2006].

center of rotation is presented and compared with two other commonly applied methods (center-of-mass method, image registration) for both simulated and measured data.

The main goals of this work were to enhance the capabilities of SRμCT for quantitative measurements and to achieve further automation of SRμCT. The SRμCT apparatus that was worked on is operated by the GKSS-Research Center Geesthacht at the Hamburger Synchrotronstrahlungslabor HASYLAB at the Deutsches Elektronen-Synchrotron DESY. As examples, four selected studies carried out using SRμCT during this work are presented to demonstrate the achieved enhancements.

Publications

The method for the determination of the center of rotation was published in [49]. Numerical calculations on the resolution that can be achieved with the method were recently published in [50].

Several SRμCT studies were performed at HASYLAB during this work in collaboration with internal (GKSS) and external research groups. Only a selection of these studies is presented in this work. A number of articles in refereed journals and proceedings that originated from these studies have been published and are listed below. Publications in HASYLAB annual reports[2] are denoted as reports.

The following studies were performed on **new materials and processes**: Material flow in friction stir welding was investigated (see Section 6.1). Results have been published in [13], [47], [163], [164], [165] and in the reports [48], [161], [162]. The investigation of the 3D structure of fiberboard (see Section 6.4) was published in [152] and in the reports [150], [151]. The morphological characterization of porous NiTi alloy used as implant material was performed [123]. Results from the morphometric analysis of polyurethane scaffolds (polymer foams) intended for the use as biocompatible replacement material were presented in [46] and report [73]. Details on this study can be found in the PhD thesis of Heijkants [74]. The study of Ti-6Al-4V alloy metal foams prepared at the GKSS was presented in [13] and report [45]. Further studies so far presented in reports, included the study of root flaw in friction stir welds [149], the measurement of the corrosion of Mg alloys [59], [60], [159], the study of cobalt/diamond composites [39], the impact effects of space debris on Kapton polymers [147], the morphology of bone replacement materials [141], and the pore structure of Al foam [29].

The following studies were performed on **medical or biological specimens**: The functional morphology of sponges (Tethya species) has been investigated with SRμCT [112], [113] and the x-ray camera was also used for in vivo x-ray microimaging of the sponges [114]. Preliminary results of these studies were presented in reports [110] and [111]. The morphological characterization of biominerals (snails, statoliths, human teeth) was presented in [124] and in report [122]. The gravity

[2] HASYLAB annual reports are available online at: `http://www-hasylab.desy.de/science/annual_reports/main.htm` [visited November, 5th 2006].

sensing organs in jellyfish were visualized and the location of statoliths determined [9]. The bone structure around dental implants was studied and the SRμCT reconstructions were compared with the data of conventional CT measurements in [35] and in reports [33] and [34]. Further studies so far presented in reports included the investigation of the architecture of osteoporotic bone [143], the investigation on neurological structures in a honeybee head [97], and the pore space analysis of soil aggregates [118].

The new stations for SR tomography at the HARWI-II beamline of GKSS at HASYLAB, DESY and the neutron tomography station GENRA-3 at GKSS were presented in [14], [15], [16], and [17].

Chapter 2

Instruments and methods: Microradiography

2.1 Synchrotron radiation source

Under acceleration charged particles emit electromagnetic radiation, which in the case of relativistic charged particles and acceleration by magnetic fields is called synchrotron radiation. The emission of synchrotron radiation is the cause of a significant energy loss in accelerators built for high-energy (particle) physics experiments and limits the achievable particle energies in circular accelerators. At specific synchrotron radiation laboratories, however, the emitted synchrotron radiation can be usefully applied and serves as a photon source with excellent properties.

At synchrotron radiation laboratories electrons (or equivalently positrons) are stored in bunches inside a vacuum ring (storage ring) and forced to travel in a closed loop by strong magnetic fields. This acceleration of the particles perpendicular to their travel direction causes the emission of synchrotron radiation. As an effect of relativity the radiation is emitted into an extremely forward-pointing cone of radiation as schematically shown in Figure 2.1. The half opening angle of the emission cone in the horizontal plane of emission θ_x and in the vertical plane θ_z is approximately given by

$$\theta_x \approx \gamma^{-1} \tag{2.1}$$

$$\theta_z \approx 0.565\,\gamma^{-1}\left(\frac{\lambda}{\lambda_c}\right)^{0.425} \quad \text{for } 0.2 < \frac{\lambda}{\lambda_c} < 100\,, \tag{2.2}$$

with the Lorentz factor $\gamma = \frac{E_e}{m_e c^2}$, where E_e is the energy of the electron and $m_e c^2 = 511\,\text{keV}$ is the rest energy of the electron. The parameter λ_c is the critical wavelength given by

$$\lambda_c[\text{Å}] \approx 5.59 \frac{R[\text{m}]}{E_e[\text{GeV}]} \tag{2.3}$$

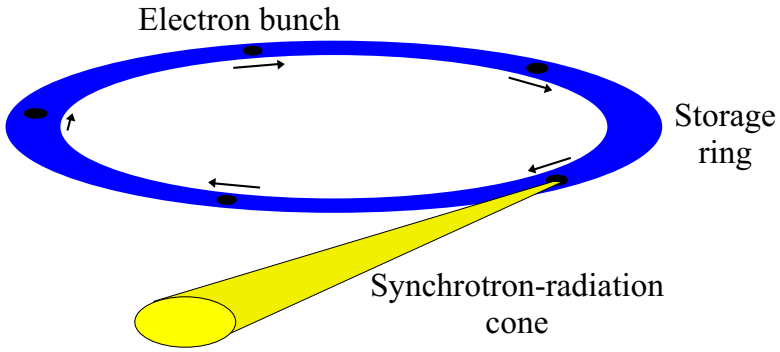

Figure 2.1: Schematic representation of the electron bunches inside the vacuum pipe of the storage ring. The bunches travel with a velocity close to the speed of light. Upon acceleration by ring magnets, the electrons emit synchrotron radiation into a strongly forward-peaked cone.

and separates the photon spectrum into two parts of equal power. Here R is the bending radius of the electron orbit. The very small divergence described by θ_x and θ_z of the photon beam makes synchrotron radiation the brightest known source for x-rays.

Wigglers and undulators are employed for a further amplification of the generated intensity. These so-called 'insertion devices' are periodic magnetic structures that are placed in straight sections of the storage rings and cause an oscillation of the electron beam. The wiggler and undulator parameter is defined as

$$K = \lambda_0 \, B_0 \, \frac{e}{2\pi m_e c} = 0.0934 \, \lambda_0[\mathrm{mm}] \, B_0[\mathrm{T}] \tag{2.4}$$

with λ_0 the field period and B_0 the maximum of the magnetic flux. The maximum angular deviation θ_w of the electron motion from the electron orbit is given by

$$\theta_w = K\gamma^{-1} \, . \tag{2.5}$$

The distinction between wigglers and undulators is made by the K parameter. Devices with $K > 1$ are called wigglers, while devices with $K < 1$ are called undulators.

The bending in undulators is weak, whereby emission from the subsequent wiggler periods occurs coherently and the emitted radiation becomes quasi monochromatic. Radiation from bending magnets and wigglers has a broad intensity spectrum. A small energy band from the radiation is typically selected by single crystals using Bragg reflection. E.g., for the Si(111) reflex of silicon in symmetric Bragg geometry the bandwidth is $\Delta E/E \approx 1.33 \times 10^{-4}$ (taken from Authier [3]). Larger bandwidth can be achieved by the application of tempered crystals, bent crystals, or multilayer devices as monochromator crystals.

More details on the generation of synchrotron radiation by bending magnets, wigglers, and undulators can, e.g., be found in the books by Wille [158] and Jackson [87].

2.1.1 DORIS III of HASYLAB

The measurements presented in this work were carried out at the DORIS storage ring of the Hamburger Synchrotronstrahlungslabor (HASYLAB) at the Deutsches Elektronen-Synchrotron (DESY). DORIS[1] was built between 1969 and 1974 as an electron-positron storage ring for collision experiments at particle energies of 3.5 GeV. HASYLAB was opened in 1980 for the application of synchrotron radiation for research. While in the beginning DORIS was used only one third of the time as a radiation source, from 1993 on the storage-ring solely served that purpose under the name DORIS III.

Today HASYLAB has 42 experimental stations and DORIS III is operated with positrons (e^+) of energy 4.45 GeV that circulate in the ring in usually five packets (bunches) as schematically shown in Figure 2.1. The circumference of the ring is ~300 m, the bunch length at DORIS is ~120 ps and the distance between two bunches in 5-bunch mode is ~193 ns. During operation the storage ring current and thus the beam intensity decays exponentially from typically 140 mA to 90 mA within the run duration of about 8 hours.

2.1.2 Beamlines W2 and BW2

All measurements presented in this work were carried out at HASYLAB beamlines BW2 and W2, which both are wiggler sources. The measurements at beamline W2 that are presented were performed before refurbishment of the beamline and installation of a new wiggler in 2005. The old setup of beamline W2 will be referred to in the text as 'W2 (old HARWI)'.

The technical parameters of **beamline BW2** were described by Drube *et al.* [51].[2] The double-crystal monochromator shown schematically in Figure 2.2(a) is set up in a fixed-exit Bragg geometry and uses the Si(111) reflex. The first monochromator crystal in use at beamline BW2 has to withstand the heat load of the incident white beam. The high-heat-load monochromator design that was described by Schulte-Schrepping *et al.* [134] is used for adaptive compensation of the occurring mechanical crystal bowing. A pair of gold-coated mirrors is available at the BW2 beamline for total reflection of the beam and can be introduced as a low-pass filter. The mirrors were not applied for the measurement presented in this work. Due to the exponentially decaying beam current, the heat load constantly changes over time, which in turn effects the crystal bending and thus the beam profile. Therefore, the beam profile is constantly measured for normalization of the recorded projection images. The monochromator parameters are adjusted during the measurement if necessary.

The technical details of the wiggler at **beamline W2 (old HARWI)** have been described by Graeff *et al.* [67]. At this beamline a double-crystal monochromator in Laue geometry shown in

[1] DORIS – Doppel-Ring-Speicher ('double storage ring')

[2] Data of HASYLAB beamline BW2 is available online at: `http://www-hasylab.desy.de/facility/experimental_stations/BW2/BW2_new.html` [visited June, 10th 2006].

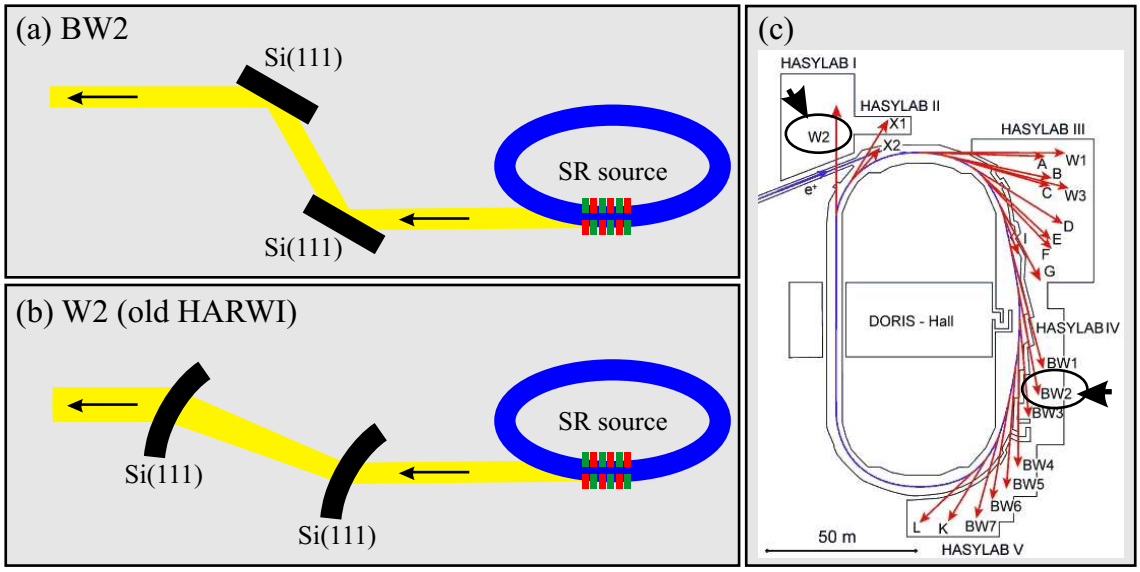

Figure 2.2: Scheme of the monochromator setup at HASYLAB wiggler beamlines BW2 and W2 (old HARWI). (a) Beamline BW2: fixed exit Si(111) double-crystal monochromator in Bragg geometry. (b) Beamline W2 (old HARWI): fixed exit Si(111) double-crystal monochromator in bent-Laue geometry. (c) Overview of stations at DORIS III.

Figure 2.2(b) was used for the tomography measurements. The monochromator comprised of two asymmetrically cut silicon crystals using Bragg reflection at the Si(111)-plane with the reflection plane tilted by 35.26^o with respect to the crystals' surface normals. The crystals were 112×22 mm in total size and their active part was 0.6 mm thick and 11 mm high. The crystals could be bent for vertical focusing and were set to a defocussed position for the tomography measurements, whereby a vertical beam size of about 4 mm was obtained at the sample position. The principle of the bent monochromator crystals was described by Illing *et al.* [85]. Crystal bending relaxes the Bragg condition, whereby the energy bandwidth of the beam is increased as $\delta E/E \propto T/\rho$, where T is the crystal thickness and ρ is the bending radius (compare Illing *et al.* [85, Equation (3)]). Hereby, a significant increase in the photon flux is obtained. The heat-load problem for the first monochromator crystal in Laue geometry is much less eminent than for the Bragg geometry. Efficient cooling becomes at the same time more difficult and was provided from the upper and lower side of the crystal (compare Lohmann *et al.* [99]).

Table 2.1 summarizes the parameters of beamlines BW2 and W2 (old HARWI). Also, the integrated flux from the wiggler and the flux for photon energies of 10, 20, and 40 keV was calculated using XOP[3] and is given. Note that the horizontal and vertical source sizes of the positron beam σ_x and σ_z given in Table 2.1 generally differ from the effective source size that is seen from the sample position. The effective source size depends on the positron beam path and the optical elements of the beamline. A pinhole measurement was carried out at beamline BW2 to

[3]XOP 2.1 - X-ray Oriented Programs. Authors: Manuel Sanchez del Rio and Roger J. Dejus. The software is online available at: `http://www.esrf.fr/computing/scientific/xop/` [visited July, 1st 2006]

Table 2.1: Source characteristics of beamlines BW2 and W2 (old HARWI).

Parameter	Unit	BW2	W2 (old HARWI)
Positron energy E_e	GeV	4.45	
Positron current	mA	140 – 70	
Source size (hor.) σ_x[d]	mm	2.220	1.797
Source size (vert.) σ_z[d]	mm	0.509	0.514
Wiggler period	cm	14.0	24.0
Number of periods		28 (56 poles)	10 (20 poles)
Wiggler gap (variable)	mm	45	30
B_0	T	0.69	1.26
K		9.0	28.2
L	m	~35	~35
E_c [a]	keV	9.1	16.6
Total power[a]	W/mA	23	48
Integrated flux[a,b]	ph/s/mm^2	5.5×10^{15}	2.0×10^{15}
Flux at 10 keV[a,b,c]	ph/s/mm^2/(0.1% BW)	1.7×10^{12}	6.1×10^{11}
Flux at 20 keV[a,b,c]	ph/s/mm^2/(0.1% BW)	1.0×10^{12}	5.9×10^{11}
Flux at 40 keV[a,b,c]	ph/s/mm^2/(0.1% BW)	3.4×10^{10}	1.4×10^{11}
Monochromator (MC)		double-crystal Si(111), Bragg, in vacuum	double-crystal Si(111), bent Laue, in vacuum
MC-to-sample dist.		~10 m	~5 m
Beam size (typ.)	mm	10×3	20×4
Energy range	keV	8 – 24	15 – 60

[a] Calculated with XOP (see text).

[b] Flux at sample position through a central 1×1 mm aperture at 100 mA ring current.

[c] BW is the bandwidth given by the full width of the half maximum of the flux spectrum.

[d] Values from: `http://www-hasylab.desy.de/facility/doris/beamsizes.htm` [visited June, 10th 2006].

estimate the influence of source size and beam divergence on the tomography measurements and showed that this influence is negligible (compare Appendix D.7).

2.2 Microtomography apparatus

The microtomography apparatus that was used for this thesis was originally designed and constructed in the group of Prof. Bonse at the University of Dortmund. Operation and further development of the apparatus continued at HASYLAB/DESY and since 2003 at the GKSS outstation at HASYLAB/DESY. A description of the original setup was presented by Bonse and Busch [23] and in the PhD thesis of Beckmann [11]. The implementation of a fast horizontal sample translation stage was described by Crostack *et al.* [38]. Also during this work, several enhancements to the apparatus have been made, one of which is the implementation of a continuously rotating sample stage (see Section 2.2.1).

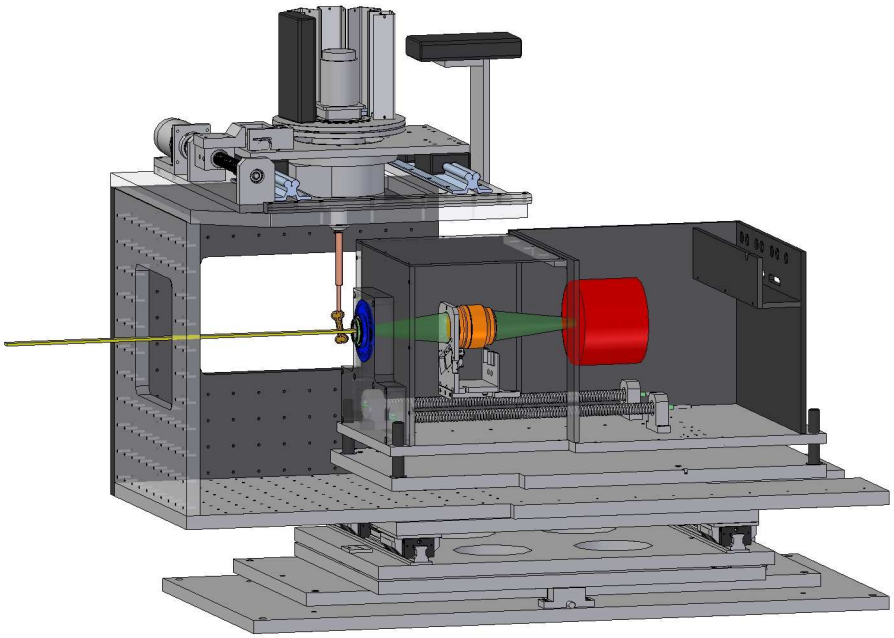

Figure 2.3: CAD 3D model of the tomography apparatus. The front covers have been made transparent to allow for the view onto the apparatus interior: luminescent screen holder (blue), objective (orange), and CCD camera (red). The x-ray beam (yellow) and the luminescence light (green) have been inserted into the drawing. The rotation axis can slide on the rails (light blue) for the measurement of reference images. The two CANbus/bluetooth interfaces (black) have replaced cable connections. Drawing by J. Fischer.

Figure 2.3 shows a CAD 3D model of the microtomography apparatus. The apparatus mainly consists of a two-dimensional x-ray detector (x-ray camera), that is described in detail in Section 2.2.2, and the sample manipulator stage with the sample rotation axis. Furthermore, it contains several translations, rotations, and sensors that enable the alignment of rotation axis, detector, and sample. The sample rotation axis is oriented vertically. Prior to the measurement samples are glued to sample holders, which are then attached to the bottom of the sample stage. This geometry allows to investigate samples in a liquid medium, which is essential for interferometric phase contrast microtomography, for which the apparatus was originally designed (see Beckmann *et al.* [10] and Bonse *et al.* [24]). For attenuation contrast tomography the liquid medium is sometimes used to prevent biological samples from drying.

The apparatus is used for measurements in the photon-energy range from 8 to about 80 keV, which allows for the examination of low-density components as polymers as well as high-density components of higher atomic number. The resolution of the CCD-camera in the horizontal plane (1536 pixels) defines the typical size of the tomographic reconstruction grid of 1536×1536 pixels. The maximum field of view of the x-ray camera and, correspondingly, the maximum sample diameter that can be investigated is ~15 mm (or ~30 mm in '360deg mode', see Appendix D.2). The minimum field of view of the x-ray camera has a width of ~2.3 mm. Smaller samples can be investigated with reduced number of pixels. A detailed description of the alignment and measurement procedure is given in Appendix D.

2.2.1 Mechanical components

While the camera remains locally fixed with respect to the synchrotron radiation beam, the sample manipulator stage provides the sample rotation needed for realization of different projection angles θ as well as the horizontal translation of the sample to an out-of-beam position that is needed for the measurement of reference images. The entire rotation axis is driven by a stepper motor on rails from the in-beam-position to an out-of-beam position. The in-beam position is defined by the contact point of a motor-driven micrometer screw with a metal plate. Adjustment of the micrometer screw is used for positioning of the rotation axis (center of rotation) relative to the detector. Normally, the center of rotation should be in the center of the recorded images (compare Appendix D.2). This allows to make optimal use of the detectors field of view, i.e., examination of samples with a maximum sample diameter.

Sample rotation (rotation axis θ) is provided by a selected goniometer, model 410 by supplier Hans Huber AG[4], that is equipped with an extra translation along the rotation axis. The translation along the rotation axis (z-direction) is used for sample positioning for scanning the sample in stacked scans (see Appendix D.2). The precision of goniometer rotation is typically described by eccentricity and wobble. Eccentricity, also called concentricity, defines the deviation of the center of rotation from its mean position. Wobble is defined as the angular deviation of the axis of rotation over one revolution. The specification of our goniometer is: eccentricity $< 2\,\mu$m, wobble $< 0.002^o = 3.49 \times 10^{-5}$ rad.

An xy-translation stage mounted below the goniometer allows to center the sample with respect to the rotation axis. In order to free the xy-translation from cables that prohibit continuous rotation, a cable-free rotation platform has been designed and implemented recently. The details have been described by Fischer *et al.* [60]. The rotation platform carries the motor controllers for the xy-translation stage and rotates together with the goniometer. The motor controllers are CAN-bus devices[5] that are controlled via a cable-less CAN-Bluetooth/Bluetooth-CAN bridge. Power is provided via sliding contacts to the rotation platform.

A slit system and an x-ray shutter (not shown in Figure 2.3) are installed at the entrance of the x-ray apparatus. The slit system reduces the x-ray beam in size to the field of view of the camera to avoid stray radiation, while the x-ray shutter protects the sample during CCD readout from the incident beam and, thereby, reduces the accumulated dose to the sample.

[4]Online: `http://www.xhuber.com/en/positioning/circle/400/410/410.htm` [visited November, 5th 2006].

[5]CAN-stepcon-1h controllers supplied by ESD Electronics, Hannover, online: `www.esd-electronics.com` [visited November, 5th 2006].

2.2.2 X-ray camera

This section describes the design of the high-resolution, lens-coupled x-ray camera that has been used throughout this work. Its main components are: luminescent screen,[6] lens system, and CCD camera. A summary of the component characteristics in tabular form is given in Appendix G.

We shall limit our discussion to the applied type of x-ray camera. Different detector concepts for x-ray microradiography have been developed and were reviewed by Gruner *et al.* [70]. Martin and Koch [102] summarized recent developments in x-ray imaging with micrometer spatial resolution including a discussion on potential scintillator materials.

The x-ray camera is shown schematically in Figure 2.4. The impinging x-rays are absorbed in the luminescent screen, and a fraction of the absorbed x-ray energy is converted into visible light. This process is called luminescence.[7] The light distribution generated in the luminescent screen is imaged by a lens system onto a charge-coupled device (CCD) camera. The magnification factor m is determined by the screen-to-lens and lens-to-CCD distance and can be calculated from the formulas of lens imaging. A continuous range of optical magnification factors m in the range $m = 0.7 - 6.0$ can be realized by translation of lens and CCD camera along the optical axis of the system. The edge length of a CCD pixel $\tau_{CCD} = 9\,\mu$m thus corresponds to an effective pixel size (sampling distance) of between $1.5\,\mu$m for $m = 6.0$ and $12.8\,\mu$m for $m = 0.7$ on the luminescent screen. This corresponds to a field of view between 2.3×1.5 mm and 19.7×13.2 mm for the x-ray camera.

The x-rays from the synchrotron radiation source can be considered to be parallel, and they enter the luminescent screen under normal incidence. Therefore, the light intensity distribution can be regarded as a two-dimensional image that decays exponentially in intensity in the third dimension with increasing distance from the crystal surface. For a thick crystal, which is much thicker than the attenuation length μ^{-1}, the radiation is almost entirely absorbed, and the average plane of light generation is at a distance below the crystal surface that is equal to the attenuation length.

Luminescent screen, lens system, and CCD camera are mounted in in-line geometry, i.e., the center of all components lies on the same optical axis. Therefore, penetration of high energy x-rays through the system onto the CCD is possible and must be avoided. The direct interaction of x-rays with the CCD would result in an undesired massive local creation of charge carriers (bright pixels) and might harm the CCD. However, at energies of up to 60 keV the attenuation length of $CdWO_4$ is still below 350 μm. The direct x-rays will thus be almost entirely absorbed in the luminescent crystal or in the lens system. When a relevant amount of high energetic radiation entered the

[6] The terms ‘luminescent screen’, ‘phosphor’, or ‘scintillator’ are often used for the x-ray luminescent materials applied in x-ray imaging. Some authors use the term ‘x-ray phosphor’ when the application requires a powder screen, and the term ‘scintillator’ when a single crystal is applied [20, Chapter 8].

[7] Note, the general term ‘luminescence’ and ‘luminescent screen’ is used in this work to avoid wrong use of the terms ‘fluorescence’ or ‘phosphorescence’, which describe specific physical processes. The difference has been pointed out by Blasse [20, Appendix 3].

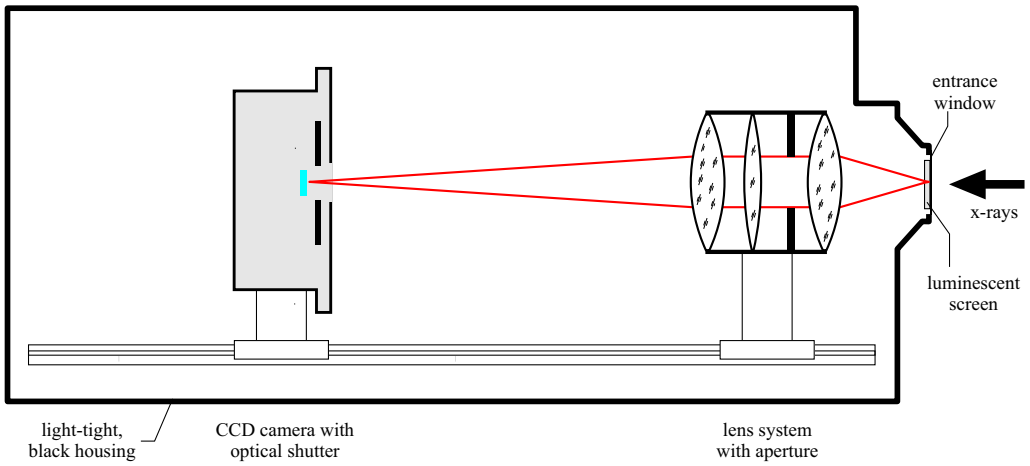

Figure 2.4: Scheme of the x-ray camera: The incident x-ray beam is absorbed by the luminescent screen and partly converted into visible light. The lens system (objective) images the luminescent light onto the CCD camera, where an inverted image is created. Translation of lens and CCD camera along the optical axis allows to set the optical magnification factor *m*.

lens system over a longer period, the development of haze on the objectives was observed, which might influence the point spread function of the system (see Appendix B.1 with Figure B.1). For measurements at photon energies above 60 keV the CCD must be protected from the incident x-ray beam. For this purpose a mirror system and an absorber can be installed in the gap between the luminescent screen and the lens system (see Beckmann *et al.* [12]).

The whole system is assembled in a case with blackened surfaces, in order to protect the system from external light sources and to minimize straylight. The otherwise transparent luminescent screen is protected against light by the layer of black lacquer paint that was introduced in this work (see Chapter 4) and additionally by black Kapton® foil. The so formed x-ray entrance window is largely transparent for x-rays of photon energy above 8 keV.

As **luminescent screen** $CdWO_4$ single crystals of different thickness (0.080 – 1.0 mm) were used during this work. The $CdWO_4$ crystals have polished surfaces and are optically clear. They are mounted in a specially fabricated crystal holder that ensures parallel orientation of the crystal relative to the system's optical axis. The luminescent screens can be exchanged quickly together with the entire crystal holder. It was observed that the crystals develop surface defects upon continuous x-ray exposure over several days. Presumably, these defects are induced by chemical reactions with the surrounding air, but the mechanism of defect creation has not been identified yet. For protection of the crystals a new holder was designed that allows for the application of a scavenging gas. Helium, which is available at the beamlines, is used for this purpose. In this work a light-absorbing coating was introduced that is directly applied to the luminescent crystals for the suppression of internal reflections. The optical properties of the backing layer of black lacquer paint will be discussed in detail in Chapter 4.

As **lens system**, either of two objectives (photographic lenses) from Nikon with focal lengthes of 35 mm and 50 mm, can be mounted in the x-ray camera. The objectives are operated in retro-

focus position, i.e., the side that normally faces the photographic film now faces the luminescent screen. Apertures inside the objectives are used to control light flux and resolution. The aperture opening is described by the f-number (designated by k, while f is the focal length) and adjusted to obtain an optimum trade off between collected light intensity and spatial resolution.

The **CCD camera** (model: KX2, Apogee Instruments) has an active area of 1536×1024 pixels with a pixel size of $9 \times 9\,\mu$m. An optical iris shutter is part of the camera and protects the CCD from exposure during readout. To suppress thermal noise the CCD is operated at -15 ^{o}C. Cooling is provided by a Peltier element inside the camera and an external water cooling circuit. The camera digitizes with 14 bit resolution at a rate of 1.3 MHz and with a true dynamic range of 12.7 bits. The gain factor of the CCD is fixed at $g = 5$. The exposure time of the CCD camera can be as low as 0.03 seconds and is typically chosen in the range between 0.2 and 10.0 seconds. Readout of a full-frame CCD image requires ~1.2 seconds. The CCD camera allows for the selection of sub-frames and enables on-chip binning. With on-chip binning the accumulated charge contained in several CCD wells (pixels) is combined before digitization. Both sub-frame selection and binning reduce the readout time accordingly. The influence of binning on the tomographic reconstruction is discussed in Section 3.3.4. The necessary calibration of the recorded CCD images is discussed in Appendix D.5.

2.3 Statistical characteristics of the x-ray camera

Quantum efficiency (QE), detective quantum efficiency (DQE), and dynamic range (DR) describe the statistical characteristics of imaging systems. These quantities are closely related to the quality of the recorded images, which is typically characterized by noise level and signal-to-noise ratio (SNR) in the images. We shall first define all of these quantities in Section 2.3.1. Thereafter, in Section 2.3.2 we derive the quantum efficiency of our x-ray camera from the efficiencies of the individual components and processes. The derived efficiencies are used to express the DQE in Section 2.3.3 and noise, signal-to-noise ratio (SNR), and dynamic range (DR) in Section 2.3.4.

2.3.1 Definitions

The noise level is used to describe statistical fluctuations of a noisy signal s and is defined as

$$\sigma = \sqrt{\overline{(\Delta s)^2}} = \sqrt{\overline{(s - \overline{s})^2}}\,, \tag{2.6}$$

where $\overline{s}$ is the average of the signal and $\overline{(\Delta s)^2}$ is the signal variance. The relative error in the measurement of signal s is described by the signal-to-noise ratio defined as

$$\mathrm{SNR} = \frac{\overline{s}}{\sigma}\,. \tag{2.7}$$

The quantum efficiency (also: responsive quantum efficiency [40]) of a system is defined as the ratio

$$\mathrm{QE} = \frac{\overline{N_{out}}}{\overline{N_{in}}} , \tag{2.8}$$

where $\overline{N_{out}}$ and $\overline{N_{in}}$ are the average number of events at the output and at the input of the system and N_{out}, N_{in} are quantized signals. For a detector N_{out} has to be understood as the number of counted (detected) quanta. The quantum efficiency links the input with the output numbers in quantity but not in quality.

To describe the change of signal quality the detective quantum efficiency[8] (DQE) of a system is introduced as

$$\mathrm{DQE} = \frac{\mathrm{SNR}_{out}^2}{\mathrm{SNR}_{in}^2} . \tag{2.9}$$

Here SNR_{out} and SNR_{in} are the signal-to-noise ratios of the incoming signal and the outgoing (or detected) signal respectively. The DQE describes the degradation of the signal-to-noise ratio by the system. An ideal detector has DQE = 1, whereas any real detector introduces noise in the measured signal and has DQE $\leq$ 1. The quantum efficiency defined in Equation (2.8) can be much higher than unity at the same time.

For example, an input signal that is Poisson distributed with average $\overline{N}_{in}$ and variance $\overline{(\Delta N_{in})^2} = \overline{N}_{in}$ has a signal-to-noise ratio SNR_{in} given by $\mathrm{SNR}_{in}^2 = \overline{N}_{in}^2/\overline{N}_{in} = \overline{N}_{in}$. For the signal-to-noise ratio of the output signal we know from the definition of the DQE in Equation (2.9) that $\mathrm{SNR}_{out}^2 \leq \overline{N}_{in}$, as if it was due to a Poisson-distributed signal with less quanta than the original signal. For this reason SNR^2 is also referred to as the noise equivalent quanta (NEQ), since for any distribution it gives the equivalent average number of quanta, a Poisson process of the same signal-to-noise ratio would have.

So far, we have described the signal in every pixel of an image individually and neglected possible correlations. However, the DQE for an imaging system can also be introduced more generally as a function of spatial frequency $\mathrm{DQE}(u, v)$. For a system like ours, with amplification and scattering (blur), the $\mathrm{DQE}(u, v)$ was theoretically calculated by Rabbani *et al.* [126, Eqs. (39,41)]. The $\mathrm{DQE}(u, v)$ describes correlations that are introduced into the noise of the output signal, due to the amplification in the system. For our systems, with low amplification [$\gamma \approx 0.01$, see Equation (2.12)], the correlation introduced by the system is negligible. Therefore, we omit the introduction of this quantity and describe the system by the scalar DQE introduced above, which is related to its frequency-dependent counterpart by $\mathrm{DQE} = \mathrm{DQE}(0,0)$.

The capacity of a detector limits the signal quality that can be obtained in a single measurement. The dynamic range (DR) of the detector system can be defined as

$$\mathrm{DR} = \frac{s_{max}}{\overline{s}(\mathrm{SNR}=1)} , \tag{2.10}$$

[8] According to Dainty [40], the concept of DQE was first proposed by Rose in 1946.

Table 2.2: Contributions to the quantum efficiency of the x-ray camera.

Description	Symbol	Value	Definiton
Absorption efficiency for x-rays	ϵ_{abs}	~1.0	Eq. (2.15)
Luminescence photons per absorbed x-ray	ν_{lum}	$(\sim 272)^a$	Eq. (2.16)
Transmission efficiency, luminescent screen	$\epsilon_{t,ls}$	0.84	Eq. (2.20)
Light collection efficiency	ϵ_{coll}	$(\sim 2.33\times10^{-4})^b$	Eq. (2.17)
Transmission efficiency, objective	$\epsilon_{t,obj}$	0.93	App. G
Transmission efficiency, CCD cover glass	$\epsilon_{t,cov}$	0.90	Eq. (2.20)
Spectrally-weighted CCD efficiency	ϵ_{ccd}	0.22	Eq. (2.21)
X-ray camera quantum efficiency		9.80×10^{-3}	Eq. (2.13)

[a] Calculated for x-ray photons of energy $E_0 = 20\,\text{keV}$.

[b] Calculated for $f = 35\,\text{mm}$, $m = 1$, and $k = 3.56$.

and describes the number of resolvable quantization steps of the detector. Here s_{max} is the maximum signal that can be recorded before the detector goes into saturation, and $s(\text{SNR=1})$ is the signal with SNR = 1, i.e., the smallest resolvable signal. For systems with signal-independent noise level σ the dynamic range, thus, simplifies to

$$\text{DR} = \frac{s_{max}}{\sigma}\,, \tag{2.11}$$

which corresponds to the SNR of the maximum signal. The noise of the detector system alone, e.g., the electronic readout noise of a CCD chip, is often signal independent. In this case, the DR is well defined by Equations (2.10) and (2.11). If σ depends on the signal, e.g., when the photon noise is understood as part of the camera system, the DR defined in Equation (2.10) gives an optimistic estimate of the number of resolvable quantization steps. Other definitions of the DR exist that are sometimes used in this case.

The dynamic range can be specified in different forms. It is often given as the ratio in Equation (2.10), the value in Dezibel as $20\log_{10}(\text{DR})$, or in units of bits (exponent of two) as $\log_2(\text{DR}) = \log_{10}(\text{DR})/\log_{10}(2)$. Values are given in Appendix G for the CCD of our x-ray camera.

2.3.2 QE of the x-ray camera and its components

The average number of electronic charge quanta $\overline{N}$ that are detected by the CCD, when the average of $\overline{N}_0$ x-ray photons are impinging, is given by

$$\overline{N} = \underbrace{\epsilon_{ccd}\,\epsilon_{t,cov}\,\epsilon_{t,ls}\,\epsilon_{t,obj}\,\epsilon_{coll}\,\nu_{lum}}_{\gamma}\;\epsilon_{abs}\,\overline{N}_0\,. \tag{2.12}$$

Here the factors ϵ_{ccd}, $\epsilon_{t,cov}$, $\epsilon_{t,ls}$, $\epsilon_{t,obj}$, ϵ_{coll}, ν_{lum}, and ϵ_{abs} are the quantum efficiencies of the individual processes that take place inside the x-ray camera. An overview of all processes that will be described in detail below is given in Table 2.2. The quantity γ that is defined in Equation (2.12)

gives the average number of detected luminescence photons per absorbed x-ray and is a characteristic system parameter. We will be able to express the signal-to-noise ratio and the detective quantum efficiency of our system as a function of the two parameters γ and ϵ_{abs} below.

The quantum efficiency was defined in Equation (2.8) as the ratio of output to input events. From Equation (2.12) we thus obtain for the quantum efficiency of our x-ray camera

$$\mathrm{QE} = \frac{\overline{N}}{\overline{N_0}} = \gamma\,\epsilon_{abs}\ , \tag{2.13}$$

which is simply the product of the quantum efficiencies of the individual processes. A large number of generated luminescence photons ν_{lum} and a high photon collection efficiency ϵ_{abs} can result in a QE above unity. This will, however, not necessarily result in increased signal quality as is further discussed in Section 2.3.4.

Note that the QE in Equation (2.13) is given for the average number of collected charge quanta in the CCD and not for the CCD output signal. The average CCD output signal $\overline{N}_{ADU}$ in units of the analog-to-digital converter units (ADU) is related to the number of charge quanta $\overline{N}$ through

$$\overline{N_{ADU}} = g^{-1}\overline{N}\ , \tag{2.14}$$

where g is the CCD gain factor in units of [e^-/ADU].

The quantum efficiency of the x-ray camera was calculated for a typical camera setting at photon energy $E_{ph} = 20\,\mathrm{keV}$ and with magnification factor $m = 1$. The resulting efficiencies are given in Table 2.2. The quantum efficiency of the x-ray camera for this setting is $\mathrm{QE} \approx 9.80 \times 10^{-3} \approx 1\%$. Together with the CCD gain factor of $g = 5$ this results in an average CCD signal of 0.002 ADU per incident x-ray photon.

We will now derive the quantum efficiency for individual processes of the x-ray camera.

Absorption and conversion efficiency of the luminescent screen: ϵ_{abs} and ν_{lum}

The quantum efficiency of the luminescent screen for x-ray-to-light conversion is characterized by two parameters, the absorption efficiency for x-rays ϵ_{abs} inside the screen and by the average number of light quanta ν_{lum} generated in the luminescent process per absorbed x-ray photon. The quantum efficiency is given by the product of the two parameters.

The absorption efficiency is given by the probability for photoelectric absorption of x-ray photons in the luminescent screen. It is (neglecting other interaction mechanisms as elastic or Compton scattering, compare Appendix A) given by

$$\epsilon_{abs} = 1 - exp(-\mu_{tot} d)\ , \tag{2.15}$$

where μ_{tot} is the total attenuation coefficient of the luminescent screen material and d is the screen

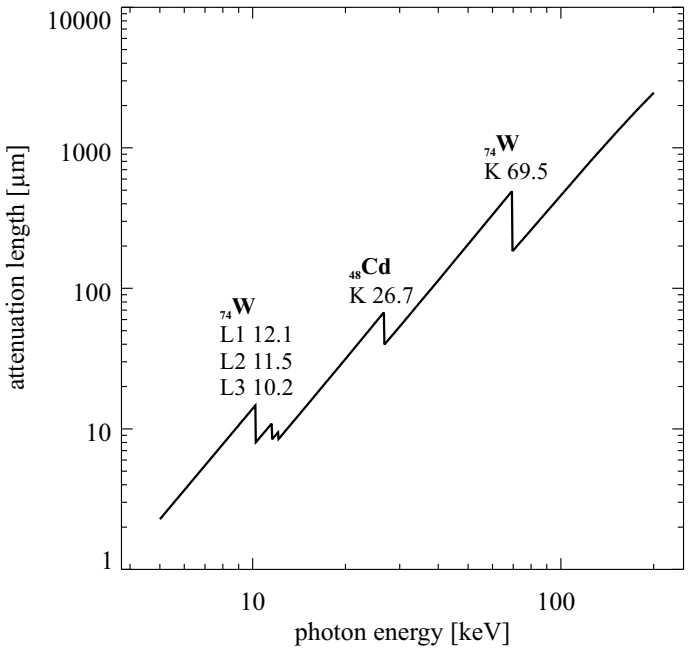

Figure 2.5: Attenuation length μ_{tot}^{-1} in $CdWO_4$ as a function of photon energy, with μ_{tot} the total attenuation coefficient. The absorption edges are labeled with the corresponding electron shells and their binding energies in units of keV. Data calculated from the tables of Plechaty *et al.* [119].

thickness. The absorption efficiency is close to unity, as long as $d > \mu_{tot}^{-1}$, where the inverse of the attenuation coefficient μ_{tot}^{-1} is the attenuation length. The attenuation length is a strong function of the (x-ray) photon energy, which is plotted for $CdWO_4$ in Figure 2.5.

Example: For a photon energy of 40 keV and a screen thickness of $d = 200\,\mu$m the attenuation length becomes $\mu_{tot}^{-1} \approx 100\,\mu$m and the resulting absorption efficiency is $\epsilon_{abs} \approx 1 - e^{-2} \approx 0.86$.

An x-ray photon of energy E_0 generates on the average ν_{lum} luminescence photons (visible light) with an average energy of E_{lum}. The conversion efficiency ϵ_{conv} of the luminescent screen is defined through the equation

$$\nu_{lum} = \epsilon_{conv} \frac{E_0}{E_{lum}} \ . \tag{2.16}$$

Experimentally determined values for the conversion efficiency of $CdWO_4$ have been discussed by Busch [31] and a recent comparison of scintillator materials for medical imaging was presented by van Eijk [146]. Busch used the value ϵ_{conv}=0.034 in his calculations. The crystal supplier Saint-Gobain specifies the light yield for $CdWO_4$ as $\nu_{lum} = x/[\text{keV}]$ with x in the range 12 to 15. For comparison Busch's value ϵ_{conv}=0.034 and assuming 500 nm luminescent radiation, which corresponds to the photon energy $E_{lum} = 2.5$ eV, results in $x = 13.6$, and is thus in the same range. The value cited by van Eijk differs slightly and corresponds to $x = 20.0$. Nagornaya [107] recently reported a similar value of $x = 19.5$ for high-quality $CdWO_4$ single crystals with low absorption. We shall use the value ϵ_{conv}=0.034 given by Busch as an estimate for the following calculations.

The probability distribution of the number of generated photons is discussed by Moses [105]. For simplicity we will assume the variance of a Poisson distributed signal in the calculation of the detective quantum efficiency.

Light collection efficiency: ϵ_{coll}

Only a small fraction of all luminescence photons generated inside the luminescent screen enter the aperture opening of the objective. In addition to the geometrical limit the high refractive index of the luminescent crystal further reduces the collection efficiency. This is due to the increase in the divergence of the luminescent light, as the light leaves the crystal.

The accepted fraction of light was calculated by Busch [31] assuming an isotropic angular distribution of luminescence photons. The gap between luminescent screen and objective was assumed to be filled with air, with refractive index $n \approx 1$. Busch's result is correct except for a missing factor of two. The corrected calculation is presented in Appendix C.1 of this work.

The resulting light collection efficiency [Equation (C.5)] is given by

$$\epsilon_{coll} \approx \left[\frac{1}{4n_{ls}} \frac{m}{k(m+1)} \right]^2 , \tag{2.17}$$

where m is the magnification factor, n_{ls} is the refractive index of the luminescent screen and k is the f-number of the objective given by $k = f/D$, with the focal length f and the pupil diameter D. Equation (2.17) can also be expressed in terms of the numerical aperture A [Equation (C.8)] as

$$\epsilon_{coll} \approx \left(\frac{A}{2n_{ls}} \right)^2 . \tag{2.18}$$

The numerical aperture is defined as $A = n \sin\alpha$, where n is the refractive index in the space between object and lens and α is the half-opening angle of the light cone that is accepted by the aperture. For typical settings of our system the numerical aperture is small and the collection efficiencies in the above equations are valid approximations. The exact forms of both formulas are given as Equations (C.4) and (C.7) in Appendix C.1.

The higher the magnification factor m in Equation (2.17), the higher is the collection efficiency ϵ_{coll}, which may be somewhat counterintuitive. This effect is due to the fact that for increasing magnification the objective comes closer to the luminescent screen, whereby the numerical aperture increases. Note that at the same time the flux (photons/area/time) decreases with the magnification factor m as m^{-2}. Thus, the measured intensity per pixel will decrease as expected.

The measurements presented in this work were mostly carried out with the 35 mm objective and with aperture openings corresponding to either f-number $k = 3.56$ or $k = 4.76$. The collection efficiency for these two settings and for the extremal magnification factors $m = 1$ and $m = 6$ for this objective have been calculated and are given in Table 2.3.

Table 2.3: Calculated light collection efficiencies.

Magnification m	f-number k	Numerical aperture[a] A	Collection efficiency[b] ϵ_{coll}
1.0	3.56	0.070	2.33×10^{-4}
6.0	3.56	0.119	6.85×10^{-4}
1.0	4.76	0.052	1.30×10^{-4}
6.0	4.76	0.089	3.83×10^{-4}

[a] According to Equation (C.6).

[b] According to Equation (2.17) with $n_{ls} = 2.3$ for $CdWO_4$.

Note that the f-number values imprinted on the aperture ring of the objectives are in principle not valid for operation of the objective in retrofocus position. The f-number is specified for the entrance pupil of the objective. Nevertheless, the f-number can be used as a good approximation also for the exit pupil (entrance pupil for retrofocus operation), as long as the numerical aperture A is small.

Optical transmission efficiencies: $\epsilon_{t,ls}$, $\epsilon_{t,obj}$, and $\epsilon_{t,cov}$

Part of the generated luminescent radiation is lost through absorption and reflections, which can be described by the transmission efficiency of the individual optical components. Self-absorption in the thin luminescent crystal and absorption in the optical path are assumed to be small and are neglected in the following. However, reflections at optical surfaces must be taken into account.

The reflectivity at an optical surface between two media with refractive indices n, n' can be calculated from the Fresnel equations. For unpolarized light under normal incidence, which is a good approximation for small aperture settings, the reflectivity ρ is given by [25]

$$\rho = \left(\frac{n' - n}{n' + n}\right)^2 \tag{2.19}$$

and the transmittance is $\epsilon_t = 1 - \rho$. For material-to-air surfaces it is $n' = 1$ and, thus, the transmission efficiency for a single surface is

$$\epsilon_t = 1 - \left(\frac{n - 1}{n + 1}\right)^2 . \tag{2.20}$$

The luminescent light generated inside the luminescent screen traverses several optical surfaces, before it reaches the CCD-camera:

- Part of the light is reflected at the surface of the luminescent screen. From Equation (2.20) and the refractive index of $CdWO_4$ ($n_{ls} \approx 2.3$) we calculate a transmission efficiency of $\epsilon_{t,ls} = 0.84$. Here normally incident radiation was assumed, which serves a good approx-

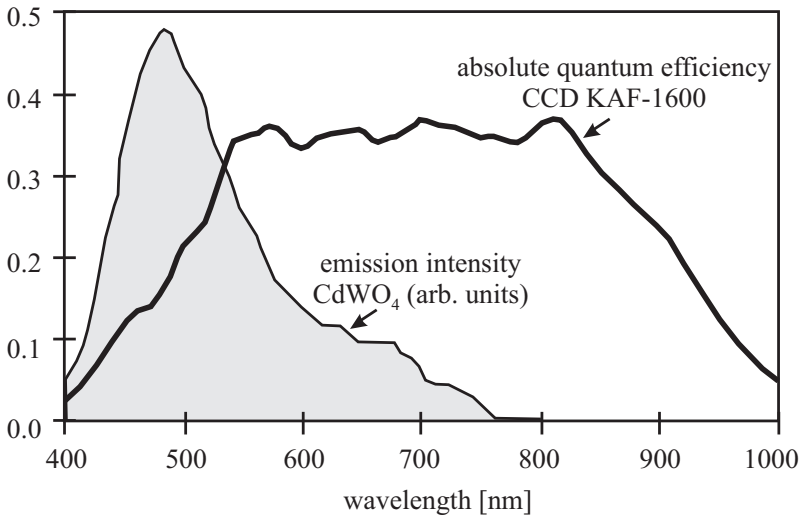

Figure 2.6: The CCD quantum efficiency overlayed to the emission spectrum of $CdWO_4$. The CCD quantum efficiency has been reproduced from 'KAF-1600 performance specifications', Eastman Kodak Company. The emission spectrum has been reproduced from a data sheet by the crystal supplier Saint Gobain (available online at http://www.detectors.saint-gobain.com/).

imation for a large range of angles. [Compare the plot of reflectivity at the crystal-to-air surface as a function of incidence angle in Figure 4.6(a).]

- The lenses in the objective are covered with anti-reflective coatings. The objective transmission efficiency at 500 nm is $\epsilon_{t,obj} = 0.932$ for the 35 mm and $\epsilon_{t,obj} = 0.958$ for the 50 mm objective respectively.

- The CCD camera itself is protected by an entrance window of glass. The corresponding transmission efficiency through both window surfaces is $\epsilon_{t,cov} \approx 0.90$, when for the refractive index $n = 1.55$ is assumed.

Spectrally-weighted CCD efficiency

In the charge-coupled device (CCD) of the CCD camera luminescence photons are converted into charge carriers. By the absorption of photons electrons in the CCD are promoted from the valence band to the conduction band of the semiconductor material. This process can occur for photon energies $h\nu = hc/\lambda > \Delta E$, where ΔE is the bandgap of the semiconductor. For silicon it is $\Delta E \approx 1.1$ eV and accordingly the wavelength must be $\lambda \lesssim 1000$ nm in order to create an electron-hole pair. Thus, for the central part of the $CdWO_4$ luminescence spectrum (400 – 700 nm) either one or no electron-hole pair is created per impinging luminescence photon.

The absolute quantum efficiency (sensitivity) $S(\lambda)$ of the CCD describes the average number of charge carriers created per incident luminescence photon as a function of photon wavelength λ. The function $S(\lambda)$ for our CCD is plotted in Figure 2.6 overlayed to the emission spectrum $W(\lambda)$ of $CdWO_4$. The spectrally-weighted detection efficiency ϵ_{ccd} of the CCD is obtained by convolution

of $S(\lambda)$ with the emission spectrum $W(\lambda)$ of $CdWO_4$ according to

$$\epsilon_{ccd} = \frac{\int_0^\infty S(\lambda)\, W(\lambda)\, d\lambda}{\int_0^\infty W(\lambda)\, d\lambda} \,. \tag{2.21}$$

This spectrally-weighted detection efficiency ϵ_{ccd} is equal to the matching factor used for the description of light-source-photodetector combinations by Giakoumakis [64] except for a constant factor.[9] From the plots in Figure 2.6 we can estimate that for our screen/CCD combination the spectrally-weighted detection efficiency is $\epsilon_{ccd} \approx 0.22$.

2.3.3 DQE

The DQE defined in Equation (2.9) of the x-ray camera can be calculated from the known statistical properties of the involved processes (given by the elements of Table 2.2) using the variance theorem. The calculation is presented in Appendix C.2. The number of luminescence photons generated from a single absorbed x-ray photon is assumed to obey Poisson statistics with the average value ν_{lum}. Moreover, it is assumed that the number of incident quanta N_0 is Poisson distributed with average $\overline{N_0}$ and variance $\overline{(\Delta N_0)^2} = \overline{N_0}$. From the calculation the system's detective quantum efficiency is finally obtained [Equation (C.24)] as

$$\mathrm{DQE} = \frac{\mathrm{SNR}^2}{\mathrm{SNR}_0^2} = \frac{\epsilon_{abs}}{1 + \gamma^{-1}} \,, \tag{2.22}$$

where γ is the average number of detected (not generated) luminescence photons per absorbed x-ray defined in Equation (2.12) and ϵ_{abs} is the luminescent screen's absorption efficiency for x-rays from Equation (2.15). SNR is the signal-to-noise ratio of the charge quanta that are generated in the CCD.

The DQE of the x-ray camera in Equation (2.22) is a function of only two parameters. We shall discuss the dependencies. The DQE is limited by the absorption efficiency of the scintillator ϵ_{abs}, to which it is directly proportional. This limit is independent of the γ value. The dependency on γ in the limits of high and low γ values can be approximated by

$$\mathrm{DQE} \approx \begin{cases} \epsilon_{abs} & \text{for } \gamma \gg 1 \\ \gamma\, \epsilon_{abs} & \text{for } 0 \le \gamma \ll 1 \end{cases} \,. \tag{2.23}$$

For $\gamma > 1$ the DQE converges rapidly against ϵ_{abs}. This means that there is no relevant enhancement of the DQE for $\gamma \gg 1$, i.e., when much more than one luminescence photon is detected from the shower of luminescence photons created by one x-ray.[10] In the limit of small γ the camera DQE

[9] Giakoumakis calculates the matching factor by replacing $S(\lambda)$ in Equation (2.21) with the normalized spectral sensitivity $s(\lambda)$, which has a maximum value of unity.

[10] This is not necessarily true for the frequency-dependent DQE discussed in Section 2.3.1. Limited detector resolution may cause a spatially-correlated detector signal. In this case the DQE at high frequencies increases with γ.

is approximately given by the quantum efficiency QE in Equation (2.13). This approximation can thus be used for our camera with DQE ≈ QE ≈ 1%.

2.3.4 Noise, SNR, and DR

The variance of the number of collected charge quanta N is derived in Equation (C.28) as

$$\overline{(\Delta N)^2} = \overline{N}\,(1+\gamma) + n_{el}^2\,, \tag{2.24}$$

where $\overline{N}$ is the average number of recorded charge quanta, γ is the average number of detected luminescence photons per absorbed x-ray defined in Equation (2.13), and n_{el} is the readout noise in units of electrons. Digitization noise has been neglected here. The noise level is given by the square root of $\overline{(\Delta N)^2}$. From the above equation and the definition of the signal-to-noise ratio in Equation (2.7) directly follows the signal-to-noise ratio of our system [Equation (C.29)]:

$$\mathrm{SNR} = \frac{\overline{N}}{\sqrt{\overline{(\Delta N)^2}}} = \frac{\overline{N}}{\sqrt{\overline{N}\,(1+\gamma) + n_{el}^2}}\,. \tag{2.25}$$

Note that a γ value of around or above one will reduce the SNR in the images significantly. Ideally, it should be $\gamma \approx 1$ to achieve an optimal combination of SNR and QE. For our detector it is $\gamma \ll 1$ and we can set $1+\gamma \approx 1$. Then SNR is determined by the Poisson statistics of the collected charge quanta N for large $\overline{N}$ and by the readout noise for small $\overline{N}$.

In order to calculate the dynamic range of our x-ray camera according to the definition in Equation (2.10) we need to calculate the signal with SNR = 1. From Equation (2.25), with $\gamma \ll 1$ and $n_{el} = 15$ for our x-ray camera, we find that SNR = 1 is reached for an average signal of $\overline{N} \approx n_{el}$. Thus, we obtain

$$\mathrm{DR} \approx \frac{N_{max}}{n_{el}}\,. \tag{2.26}$$

Here N_{max} is the CCD full well capacity in electrons and n_{el} is the readout noise in electrons. The derived DR is signal-independent, as if photon noise would not be understood as part of the system. The same DR is obtained for the CCD alone. For CCD cameras with adjustable gain g and in order to understand the variation of DR as a function of g the dependence of n_{el} on g and the digitization noise must be introduced into Equation (2.26). Note that the dynamic range of the x-ray camera also depends on the homogeneity of the x-ray beam profile. If the imaged beam profile is inhomogeneous, the full dynamic range will only be available at the local maximum of the beam profile. The dynamic range for other pixels is limited by the local beam intensity. Hence, the beam profile in a measurement should be as flat as possible.

Numerical values: For our x-ray camera, we have $\gamma \approx 1\%$, $n_{el} = 15$, and a maximum signal of $N_{max} = 2^{14} \times 5 = 81\,920$. The minimum noise level is obtained for $\overline{N} = 0$ in Equation (2.24) and is given by the electronic readout noise as $\sigma_{min} = n_{el} = 15$. The noise level in the maximum signal

is $\sigma_{max} \approx \sqrt{N_{max}} \approx 286$, which is dominated by photon noise. The corresponding relative errors described by the signal-to-noise ratio are $\mathrm{SNR}_{min} = 0$ and $\mathrm{SNR}_{max} \approx 286$. The dynamic range in Equation (2.26) of the CCD and thus of the x-ray camera is $\mathrm{DR} \approx 81.920/15 \approx 5461$.

2.4 Spatial system response of the x-ray camera

Imaging systems are often described by the concepts of linear systems theory. Assuming that the response of the imaging system to an input signal is linear and shift invariant (LSI), the output can be calculated from the input by convolution. The convolution kernel that describes the spatial system response is the system's point spread function (PSF). Reversely, when the PSF is known, it may be used for correction of blur in the recorded images using deconvolution techniques (compare Section 2.5.3).

Measurement of the PSF or the related MTF (see Section 2.4.1 below) is required for the full characterization of the spatial system response. The PSF describes the system response to a delta-peak shaped input signal, i.e., it describes the image that is recorded for a point-like source. Such a source can be realized only approximately and is not well suited for direct PSF measurements, also because of its limited intensity and the limited dynamic range of the detector. Therefore, the PSF is typically derived indirectly from images of objects with simple, well known structure (e.g.: slits, edges). The measurement of edge profiles with our system and the calculation of the PSF from the measured edge profiles is described in Appendix D.1. The derivation of simple resolution parameters from the measured data is presented in Section 2.4.3.

The spatial resolution of the applied type of x-ray camera is limited by diffraction, depth of field, spherical aberrations, and energy spread in the luminescent screen. Approximative resolution limits for these effects are discussed in Appendix B.

2.4.1 Response function in real and in frequency space (PSF/MTF)

In microtomography, we measure the image $i(x,y)$ that is given by

$$i(x,y) = s(x,y) \ast\ast o(x,y) = \int_{-\infty}^{\infty}\int_{-\infty}^{\infty} s(x-x', y-y')\, o(x',y')\, dx'dy' \;, \tag{2.27}$$

where $s(x,y)$ is the point spread function (PSF), the function $o(x,y)$ describes the object, and the symbol $\ast\ast$ designates two-dimensional convolution. Since we deal with intensities here, all functions in real space are real functions. We define the point spread function such, that it is normalized to unity, i.e.,

$$\int_{-\infty}^{\infty}\int_{-\infty}^{\infty} s(x,y)\, dx\, dy = 1 \;. \tag{2.28}$$

This means that the integral intensity in the images is unchanged by the convolution operation, which describes a system with efficiency of unity. We could introduce the system efficiency as an

additional factor into Equation (2.27). However, this is not necessary for our applications, since we are not interested in absolute quantities in our measurements.

From the convolution theorem we know that convolution of two functions in real space can be expressed as multiplication in Fourier space. Thus Equation (2.27) becomes

$$I(u,v) = S(u,v)\,O(u,v) \tag{2.29}$$

in Fourier space, where we have used the corresponding capital letters for the Fourier transforms. The Fourier transform $S(u,v)$ of the point spread function is called optical transfer function (OTF). This generally complex function can be split into amplitude and phase as

$$S(u,v) = M(u,v)\,e^{i\,\Psi(u,v)}\,, \tag{2.30}$$

where $\Psi(u,v)$ is called the phase transfer function (PTF) and

$$M(u,v) = \frac{|S(u,v)|}{S(0,0)} = |S(u,v)| \tag{2.31}$$

is the modulation transfer function (MTF) of the system. Note that the second equality holds because of the normalization of the PSF in Equation (2.28), which gives $S(0,0) = 1$. It can be shown that the $M(u,v)$ describes the reduction in contrast[11] for a sinusoidal signal with spatial frequency u, v.

The PSF $s(x,y)$ is generally assumed to be radially symmetric and can be described by a one-dimensional representation $s(t)$ that only depends on the radial distance t. In this case the Fourier transform $S(u,v)$ will be radially symmetric too, and can be written as a function $S(w)$ of the radial spatial frequency w. The one-dimensional representation of the object transfer function can again be split into amplitude and phase as

$$S(w) = M(w)\,e^{i\,\Psi(w)}\,, \tag{2.32}$$

where $M(w)$ and $\Psi(w)$ are representations of the radially symmetric MTF and PTF. The functions $s(t)$ and $S(w)$ still are two-dimensional functions (in polar coordinate representation) and are not (!) each others one-dimensional Fourier transforms. Their relation is discussed in the following section.

In the case of a real and radially symmetric point spread function $s(t)$, that is typically assumed, the two-dimensional Fourier transform $S(w)$ is real, too.[12] Thus it is $S(w) = M(w)$, and the MTF fully describes the system response in this case.

[11] Contrast is universally defined as $C = \Delta s/\overline{s}$, where Δs is the signal difference and $\overline{s}$ is the average signal background.

[12] Any real even function has a real even Fourier transform.

2.4.2 Edge spread function and line spread function (ESF/LSF)

The edge spread function (ESF) is the spatial system response to an edge-shaped input signal, while the line spread function (LSF) is the response to a line-shaped input signal. Both, the ESF and the LSF are two-dimensional functions that are constant along the direction parallel to the edge or line. Thus, both ESF and LSF have one-dimensional representations. We will show, that the LSF is the derivative of the ESF and, furthermore, that the LSF is the projection of the PSF.

Without loosing generality we shall define a line object $o_L(x,y)$ and an edge object $o_E(x,y)$ with orientation parallel to the y-axis as

$$o_L(x,y) = \delta(x) \tag{2.33}$$

and

$$o_E(x,y) = o_E(x) = \begin{cases} 0 & \text{for } x < 0 \\ 1 & \text{else} \end{cases} \quad . \tag{2.34}$$

Both functions are independent of y.

The line spread function is defined as the system's spatial response to the line object given by

$$\begin{aligned} \mathrm{LSF}(x) &= s(x,y) \mathbin{**} o_L(x,y) \\ &= \int_{-\infty}^{\infty}\int_{-\infty}^{\infty} s(x-x', y-y')\,\delta(x')\,dx'dy' \\ &= \int_{-\infty}^{\infty} s(x,y')\,dy' \ , \end{aligned} \tag{2.35}$$

where $s(x,y)$ is the point spread function defined in Equation (2.27). The line profile described by $\mathrm{LSF}(x)$ is equal to the projection of the point spread function in y direction, as can be seen from the last line of Equation (2.35).

The spatial system response to the edge function is given by

$$\begin{aligned} \mathrm{ESF}(x) &= s(x,y) \mathbin{**} o_E(x,y) \\ &= \int_{-\infty}^{\infty}\int_{-\infty}^{\infty} s(x-x', y-y')\,o_E(x)\,dx'dy' \\ &= \int_{-\infty}^{\infty} o_E(x') \int_{-\infty}^{\infty} s(x-x', y-y')\,dy'\,dx' \\ &= o_E(x) * \mathrm{LSF}(x) \ , \end{aligned} \tag{2.36}$$

where $*$ designates one-dimensional convolution. For the derivative of the ESF in x-direction (across the edge profile) we find

$$\frac{d}{dx}\mathrm{ESF}(x) = \frac{d}{dx}[o_E(x) * \mathrm{LSF}(x)] = \delta(x) * \mathrm{LSF}(x) = \mathrm{LSF}(x) \ , \tag{2.37}$$

where we have used the fact that the derivative of a convolution product of two functions may be

given by the convolution of either function with the derivative of the other. The application of the derivative to the edge function $o_E(x)$ gave the delta function $\delta(x)$. Hereby, we have shown that the derivative of the ESF in the x-direction for any value of y gives the LSF.

The above derivation can be generalized for arbitrarily oriented edges and lines that run through the coordinate center. We now introduce a rotated st-coordinate system (as used in the next chapter), with the t-direction parallel to the x-axis for rotation angle $\theta = 0$. The t-direction shall be perpendicular to the line or the edge. We will write $s_\theta(t)$ for the point spread function in rotated coordinates and $\mathrm{LSF}_\theta(t)$ for the line spread function for a line that is tilted by angle θ with respect to the y-axis. Equivalently we introduce the expressions $\mathrm{ESF}_\theta(t)$ and $\mathrm{S}_\theta(w)$.

For the line and edge rotated by angle θ and with the new coordinates Equation (2.35) becomes

$$\mathrm{LSF}_\theta(t) = \int_{-\infty}^{\infty} s(x,y)\, ds, \tag{2.38}$$

and Equation (2.37) becomes

$$\frac{d}{dt}\mathrm{ESF}_\theta(t) = \mathrm{LSF}_\theta(t)\ . \tag{2.39}$$

The function $\mathrm{LSF}_\theta(t)$ is the projection of the point spread function $s_\theta(t)$ as a function of t and θ. $\mathrm{LSF}_\theta(t)$ is called the Radon transform of $s_\theta(t)$. The Radon transform and inversion formulas for the Radon transform will be presented in detail in the following chapter on tomographic reconstruction. Using these inversion techniques it is possible to determine the two-dimensional point spread function $s(x,y)$ from a series of edge profile measurements $\mathrm{LSF}_\theta(t)$ recorded under variation of the edge angle θ.

From the Fourier-slice theorem (that will also be introduced in the next chapter) we know that

$$S_\theta(w) = \mathcal{F}^1[\mathrm{LSF}_\theta(t)]\ , \tag{2.40}$$

where $\mathcal{F}^1$ denotes the one-dimensional Fourier transform. $S_\theta(w)$ can be identified with the Fourier transformed projections $P_\theta(w)$ in Equation (3.8). Thus, the PSF can be reconstructed from edge profile measurements using tomographic reconstruction techniques.

For a radially symmetric point spread function the edge spread function is independent of the projection angle θ. In this case the spatial system response can be described by a single edge profile. We shall assume a real and radially symmetric point spread function $s(t)$, for which $S_\theta(w) = S(w)$ is real and independent of angle. Thus, it is $\mathrm{MTF}(w) = S(w)$ independent of angle and we have

$$S(w) = \mathcal{F}^1[\mathrm{LSF}(t)]\ . \tag{2.41}$$

Since $S(w)$ is real, it is equal to the system's MTF, i.e., $M(w) = S(w)$. Thus, the one-dimensional representation of the MTF describes the PSF uniquely.

Equation (2.41) will be used for the determination of the MTF from a single edge profile.

Reconstruction of the PSF from the single edge profile is possible using the filtered backprojection technique that is introduced in the next chapter or using a Hankel transform.[13]

2.4.3 Measures of spatial resolution

The point spread function fully describes the spatial system response of an LSI system. However, sometimes, it is more convenient to describe the system resolution by a single parameter. Reduction of the PSF to a single value requires the assumption of a model. If, e.g., the PSF is assumed to be a two-dimensional Gaussian function, then it can be described by its full width at half maximum uniquely. For the description of our camera, such a model is not well suited. The point spread function of our x-ray camera exhibits a strong intensity drop over a short range and, simultaneously, slowly decreasing intensity in the tails. Such a PSF clearly can not be described by a Gaussian function. The sum of several Gaussian functions would give a better approximation; but the shape of the LSF in Figure 4.4(c) and (d) can not be well described by Gaussian functions, which fall of more rapidly in the logarithmic representation than the determined LSF.

Several resolution parameters are used in this work. The spatial frequency f_{10}, at which the MTF of the system falls below 10% is often used to calculate the characteristic length

$$a_{10} = \frac{1}{2\, f_{10}} \tag{2.42}$$

as a measure of resolution. This resolution measure is rather sensitive to high-frequency components. When the MTF stays above 10% for values up to the Nyquist frequency f_{Nyq}, this measure is no longer well defined. In this case, we would set $f_{10} = f_{Nyq}$, which gives $a_{10} = 1/(2\, f_{Nyq}) = \tau$, with the sampling distance τ. However, this situation was not observed for our system.

Another resolution measure was used by Koch *et al.* [96]. It defines the resolution as the full width that covers 50% or 90% of the integrated (symmetrized) PSF. In particular the 90% integrated PSF value is more appropriate for the characterization of the long tails in the PSF.

2.5 Projection images

The radiographic projection images $i(x, y)$ from the x-ray camera are not projections in the mathematical sense. We have to calculate projection images $p(x, y)$ from the recorded radiographs that are used as input for the tomographic reconstruction.

The fundamental interaction mechanisms of x-rays with matter are presented in Appendix A. For sample diameters of below 1 cm correspondingly low photon energies are applied in the measurement, and we can therefore assume that attenuation is dominated by photoelectric absorption

[13] For a rotationally symmetric function PSF $s(t)$, the functions $s(t)$ and $S(w)$ are related by a Hankel transform, which is equivalent to a two-dimensional Fourier transform with a circular symmetric kernel.

(compare Section A.3). The observed x-ray flux behind the object [Equation (A.4)] is given by

$$\Phi = \Phi_0 \, \exp\left(- \int \mu(s') \, ds' \right) , \tag{2.43}$$

where Φ_0 is the incident x-ray flux and the integral in the exponential function describes the projected attenuation coefficient. The equation has to be understood as a two-dimensional function that describes the projected attenuation at each point in our images. The projected attenuation coefficient is the integral inside the exponential function. We shall define

$$p = \int \mu(s') \, ds' , \tag{2.44}$$

which has to be understood as a three-dimensional function $p_{\theta_i}(t_j, z_h)$ of the position (t_j, z_h) of each camera pixel and the projection angle θ_i. Then we can calculate the projected attenuation as

$$p = - \ln \frac{\Phi}{\Phi_0} . \tag{2.45}$$

The calculation of projection images with our x-ray camera is realized as follows: We record radiographic images of the sample i, reference images of the beam profile r and dark images with no illumination d. The projected attenuation image p is calculated from these as

$$p = - \ln \frac{(i - \overline{d})/t_i}{(r - \overline{d})/t_r} , \tag{2.46}$$

where $\overline{d}$ is an average dark image, and t_i and t_r are the exposure times for recording the images i and r respectively. The calculation of projection images according to Equation (2.46) during a tomographic scan is described in detail in Appendix D.4. The calibration and correction of CCD images is described in Appendix D.5.

2.5.1 PSF for the projection

We have introduced the concept of the detector PSF for the description of the spatial detector response in Section 2.4.1. The PSF describes blur in the recorded images. Can we also apply the detector PSF for the description of blur in the projection images p that are calculated from the recorded images? We shall discuss, in which cases this is possible and, furthermore, in which cases non-linear effects can appear.

The projected attenuation image p is calculated according to Equation (2.46). We shall assume, that the radiographic image i and the reference image r are dark image corrected and recorded with identical exposure times $t_i = t_r$ in the following. Then Equation (2.46) simplifies to

$$p = - \ln \frac{i}{r} . \tag{2.47}$$

Blur in the images r and i is described by the detector's point spread function s. Thus, we can rewrite the measured projection more explicitly as

$$p = -\ln \frac{s ** (r_0\, e^{-\hat{p}})}{s ** r_0} \,, \tag{2.48}$$

where r_0 is the unblurred reference image, $\hat{p}$ is the true attenuated projection, and the radiographic image i was explicitly written as $r_0 \exp(-\hat{p})$. The symbol $**$ designates two-dimensional convolution. We shall assume that the reference image is homogeneous and that all detector pixels have the same sensitivity. In this case the reference image can be treated as a constant factor r_0 and Equation (2.48) simplifies to

$$p = -\ln\left(s ** e^{-\hat{p}}\right) \,. \tag{2.49}$$

If the argument of the logarithm in Equation (2.49) fulfills the condition

$$s ** e^{-\hat{p}} = e^{-s\ **\ \hat{p}} \,, \tag{2.50}$$

then Equation (2.49) simplifies to

$$p = s ** \hat{p} \,. \tag{2.51}$$

Thus, the detector's point spread function s describes the blur in the calculated projection images, when the condition in Equation (2.50) is fulfilled or, equivalently, when the expressions of Equations (2.49) and (2.51) are equal.

The following calculation shall demonstrate, in which cases the expressions in Equations (2.49) and (2.51) are approximatively equal. We introduce

$$\hat{p}(x,y) = \hat{p}(x_0,y_0) + \hat{p}'(x,y) \,, \tag{2.52}$$

where $\hat{p}(x_0,y_0)$ is the projected attenuation for any arbitrary point (x_0,y_0) and $\hat{p}'(x,y)$ describes the deviation from $\hat{p}(x_0,y_0)$, which by definition is zero at the point (x_0,y_0). Starting with substitution of $\hat{p}(x,y)$ into Equation (2.49), we calculate

$$\begin{aligned}
p(x,y) &= -\ln\left[s ** e^{-\hat{p}(x_0,y_0)-\hat{p}'(x,y)}\right] && (2.53)\\
&= \hat{p}(x_0,y_0) - \ln\left[s ** e^{-\hat{p}'(x,y)}\right] && (2.54)\\
&\approx \hat{p}(x_0,y_0) - \ln\left[s ** (1-\hat{p}'(x,y))\right] && (2.55)\\
&= \hat{p}(x_0,y_0) - \ln\left[1 - s ** \hat{p}'(x,y)\right] && (2.56)\\
&\approx \hat{p}(x_0,y_0) + s ** \hat{p}'(x,y) && (2.57)\\
&= s ** \left[\hat{p}(x_0,y_0) + \hat{p}'(x,y)\right] && (2.58)\\
&= s ** \hat{p}(x,y) \,, && (2.59)
\end{aligned}$$

where we obtain the expression of Equation (2.51) in the final Equation (2.59). Here we have made

the only assumption that $x = \hat{p}'(x, y)$ is small with $0 \leq x \ll 1$. In this case the exponential function in Equation (2.54) can be approximated by $e^{-x} \approx 1 - x$. The distributivity of the convolution and $s ** 1 = 1$ is used to obtain Equation (2.56). Using the approximation $\ln(1 - x) \approx -x$ for small x we obtained Equation (2.57).

We have now shown that $s(x, y)$ approximately describes the point spread function for the attenuated projection images at any point (x_0, y_0), when the variation $\hat{p}'$ in the attenuated projection is small (and the reference image is flat). In fact one can further show that the variation $\hat{p}'$ must be small over the range of the PSF only.

In which cases is the variation $\hat{p}'$ small? If the projected attenuation p is small everywhere then as a direct consequence the variation $\hat{p}'$ will be small everywhere. Therefore, in the case of low absorbing objects with $p \ll 1$, the point spread function of the detector can be used as the point spread function of the attenuated projection. But the requirement on p can be further reduced. Only the variation $\hat{p}'$ must be small over the extend of the point spread function at each point (x_0, y_0). This means that the point spread function of the detector can be used as the point spread function for the attenuated projection if the gradient of $\hat{p}$ is sufficiently small. Fortunately the gradient in the projections is usually less strong than in the tomographic slice itself (with the exception of straight edges). Therefore, the detector PSF describes the PSF of the projected attenuation well in most situations.

For non-homogeneous x-ray beams (reference image r not flat), we must think in terms of intensity. Typically, the variation of the intensity in the recorded images is relatively low over distances of only a few pixels. Hence, blur in this range cannot produce non-linear effects in the projection and will not produce artifacts other than blur in the reconstruction. A problem is imposed by long-range contributions (long tails) to the detector PSF. They can spread intensity into regions, where the value of the attenuated projection is high (for strongly absorbing objects) and ideally only little intensity should be recorded. The relative change in the recorded intensity can thus be large. The blur from bright into dark regions of the image will generally result in the underestimation of the integral projected attenuation coefficient (zeroth-order moment). Thus, the spatial extension of the PSF limits the usefully applicable dynamic range of the detector, since low intensity values cannot be recorded correctly in the presence of a relevant amount of blur.

2.5.2 Noise in the projection

Noise in the radiographic images and in the reference images propagates into the projected attenuation images. We are interested in the measurement of the projected attenuation coefficient with optimum signal-to-noise ratio. Furthermore, we would like to know, whether the logarithm operation in the presence of noise can result in a shift of the measured projected attenuation p relative to the true attenuation value. A shift can be expected, since the logarithm function in the calculation of p is a non-linear function. Both questions can be answered by calculation of the measured average projected attenuation $\langle p \rangle$ as a function of the true projected attenuation $\hat{p}$ and

the variance $\langle \Delta p^2 \rangle$, with $\Delta p = p - \langle p \rangle$. The calculation is presented in Appendix C.3. We will summarize the results here.

In the calculation of the variance it is assumed that the measured attenuated intensity is described by the random variable N and that the measured reference intensity is described by the random variable N_0, with $\langle N \rangle = \langle N_0 \rangle \exp(-\hat{p})$. Both N and N_0 shall obey Poisson statistics and can be identified with the number of charge quanta recorded in a CCD pixel. CCD readout noise and noise in the averaged dark image are neglected. The variance of the projected attenuation coefficient is then obtained as [Equation (C.42)]

$$\langle \Delta p^2 \rangle \approx \frac{1}{\langle N_0 \rangle} \left(e^{\hat{p}} + 1 \right) , \tag{2.60}$$

which is a valid approximation in the limit of $\langle N \rangle \gg 1$ and $\langle N_0 \rangle \gg 1$. The noise described by $\langle \Delta p^2 \rangle$ will enter into the tomographic reconstruction. It is further found that p is measured with an optimum signal-to-noise ratio for $p \approx 2.218$, which corresponds to the minimum of the relative variance $R(p) = \langle \Delta p^2 \rangle / \langle p \rangle^2$. When noise in the reference N_0 can be neglected, the optimum signal-to-noise ratio is obtained for $p = 2$.

Therefore, it is common practice in SRμCT measurements to select sample thickness and photon energy such that the simple condition $p \lesssim 2$ is fulfilled for all sampling points (if possible).

Note that in the presence of detector blur this typically assumed optimum condition with $p \lesssim 2$ must be questioned. In combination with long tails of the detectors PSF a lower p value can be a better choice, when non-linear effects (compare Section 2.5.1) can thereby be avoided. This is especially true, when strong gradients are present in the projection images. However, a reduction of p comes at the cost of a reduced signal-to-noise ratio. The plot of the relative noise level in Figure C.46(b) shows the dependence of p on the relative noise level. E.g., a reduction of the projected attenuation coefficient to $p \approx 1$ results in an increase of the relative noise level by about a factor of two, i.e., a reduction of the signal-to-noise ratio to about one-half. However, this may be acceptable for many applications and will reduce the risk for non-linear artifacts drastically.

The difference between the measured average attenuation $\langle p \rangle$ and the real attenuation $\hat{p}$ is found [Equation (C.45)] to be given by

$$\langle p \rangle - \hat{p} \approx \frac{1}{2\langle N_0 \rangle} \left(e^{\hat{p}} - 1 \right) , \tag{2.61}$$

which is again a valid approximation in the limit of $\langle N \rangle \gg 1$ and $\langle N_0 \rangle \gg 1$. The equation describes a shift of the measured projected attenuation towards higher values with decreasing average count numbers. In the example of Appendix C.3 it is shown that for typical values for N_0 and $\hat{p}$ the shift is negligible.

2.5.3 Deconvolution

The goal of deconvolution is restoration of the object image $o(x, y)$ in Equation (2.27) from the recorded image $i(x, y)$ and the known point spread function $s(x, y)$. Deconvolution of the point spread function is an inverse operation that can easily be expressed in frequency space. From Equation (2.29) we find

$$O(u, v) = \frac{I(u, v)}{S(u, v)} \, . \tag{2.62}$$

Here $S(u, v)$ is given by the one-dimensional representation of the MTF in Equation (2.32) when we assume that the PSF is radially symmetric. Fast Fourier Transforms (FFTs) are usally applied for the conversion between real and frequency space to actually perform deconvolution.

The deconvolution approach described by Equation (2.62) is termed Fourier deconvolution or direct deconvolution. Direct deconvolution typically results in a strong amplification of high-frequency noise (compare, e.g., Jähne [88, Chapt. 17.8.3]). But as long as the noise level is low, and $S(u, v)$ does not fall off to zero over the frequency range that is to be recovered, Fourier deconvolution will give a good approximation to the original image. However, more sophisticated deconvolution methods take the noise characteristics of the system into account. E.g., the Wiener filter is the optimal filter in the least squares sense [120] but beyond that, a variety of other deconvolution techniques exist. More details on deconvolution (and image restoration) techniques can be found, e.g., in [90], [120], and in a recent review paper by Puetter *et al.* [125].

Use of deconvolution in SRμCT or similar techniques has been reported only a few times. Direct and iterative deblurring methods were applied to SRμCT data by Cloetens [36]. Graafsma and de Vries [66] used a maximum-entropy algorithm for the deconvolution of the two-dimensional point spread function of phase images.

In this work Fourier deconvolution has been applied to recorded radiographic images in order to suppress long-range blur and to enhance the spatial resolution in the tomographic reconstructions. An example is presented in Section 6.2 for the measurement of cortical bone, where also the details of the implementation of the deconvolution procedure are described. A properly measured detector PSF ($s(x, y)$) is required for the deconvolution operation according to Equation (2.62). The determination of the PSF/MTF from edge profile measurements is described in detail in Appendix D.1. Thus, we can make use of the MTF ($S(u, v)$) that is determined in the resolution measurement also for deconvolution.

Chapter 3

Instruments and methods: Tomographic reconstruction

3.1 Introduction

Computed tomography[1] (CT) allows to generate a three-dimensional image of the internals of an object from a series of x-ray projections (one or two-dimensional) taken in varying directions around a single axis of rotation. At a synchrotron radiation source, the so-called parallel-beam geometry is approximately realized. Using a two-dimensional x-ray detector, the projection data of several slices (cross-sections) of the object are recorded in parallel, and the three-dimensional reconstruction of the object is obtained as a stack of two-dimensional reconstructions.

The mathematical foundation of tomography was laid by Radon in 1917 [127]. The mathematical description of the projection is, therefore, called the Radon transform. Tomographic reconstruction is the inverse problem that deals with the inversion of the Radon transform.

This chapter presents the mathematics and the implementation of two direct reconstruction algorithms used in this work that are based on backprojection. A general introduction to tomographic methods and tomographic reconstruction algorithms can be found in textbooks, e.g., by Kak and Slaney [93] or by Herman [76]. A more mathematical treatment of tomographic reconstruction can be found in a book by Natterer [108]. A list of reconstruction techniques has been presented by Budinger and Gullberg [30].

[1] The word tomography is derived from the greek words for ‘slice’ (‘tomos’) and ‘describing’ (‘graphia’).

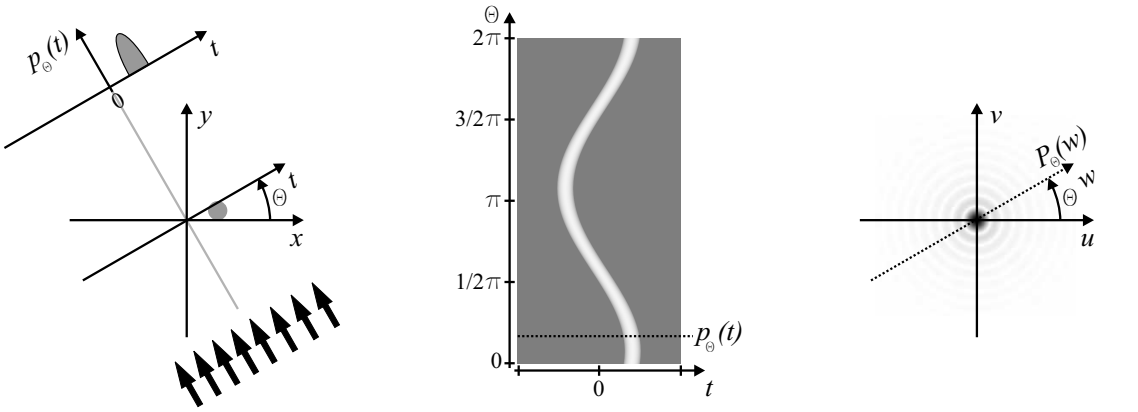

(a) real space: *f(x,y)* (b) projection space: $p_\Theta(t)$ (c) frequency space: *F(u,v)*

Figure 3.1: Representation of a two-dimensional object in (a) real space, (b) projection space (called 'Radon transform' or 'sinogram'), and (c) frequency space. The one-dimensional Fourier transform $P_\theta(w)$ of a projection $p_\theta(t)$ correspond to radials in frequency space as it is described by the Fourier slice theorem. The representation in frequency space is a complex function, of which only the absolute is shown here.

3.1.1 Radon transform and Fourier slice theorem

Let an object be represented by the two-dimensional scalar function $f(x,y)$, which describes some physical property of the object at position (x,y). In our case $f(x,y)$ is the object's attenuation coefficient for x-rays $\mu(x,y)$ that was introduced in Section 2.5. However, the following definition of the Radon transform will be independent of the physical meaning of $f(x,y)$. The nomenclature in the following has been adopted from Kak and Slaney [93], except that functions in real space are designated by small letters, while their corresponding Fourier transforms are designated by capital letters. Note that the *xy*-coordinate system is now used to describe the position in the tomographic slice, which differs from its use in the previous chapter. The position on the x-ray camera is now described by the *tz*-coordinate system. One-dimensional projections of the function $f(x,y)$ can be defined as

$$p_\theta(t) = \int_{\text{line}} f(x,y)\, ds \,, \tag{3.1}$$

where the line integrals are evaluated along lines of constant

$$t = x\cos\theta + y\sin\theta \,, \tag{3.2}$$

with the projection angle θ. The (θ, t) coordinate system is defined according to Figure 3.1. The definition of the Radon integral is sometimes written using a Dirac delta function $\delta(t)$ as

$$p_\theta(t) = \int_{-\infty}^{+\infty}\int_{-\infty}^{+\infty} f(x,y)\,\delta(x\cos\theta + y\sin\theta - t)\, dx\, dy \,. \tag{3.3}$$

The function $p_\theta(t)$ as a function of θ and t is known as the **Radon transform** of $f(x,y)$.[2]

[2]Restrictions to the function $f(x,y)$ shall not be discussed here. See the book by Helgason [75] on the Radon

For tomography data one also refers to $p_\theta(t)$ as the **sinogram**, since by definition of the Radon transform, every point (x_0, y_0) in (x, y) space is projected onto a sinusoidal line in the (θ, t)-space. Figure 3.1(b) shows a sinogram.

The information content of $p_\theta(t)$ can be understood by conversion of $f(x, y)$ and $p_\theta(t)$ into Fourier space. The two-dimensional Fourier transform of the slice $f(x, y)$ is given by

$$F(u, v) = \int_{-\infty}^{+\infty} \int_{-\infty}^{+\infty} f(x, y)\, e^{-\iota\, 2\pi(ux+vy)}\, dx\, dy\ , \tag{3.4}$$

where we introduced the Greek letter iota (ι) for the imaginary unit to avoid confusion with the index i that we will use below. The one-dimensional Fourier transform of the projection with respect to t is given by

$$P_\theta(w) = \int_{-\infty}^{+\infty} p_\theta(t)\, e^{-\iota\, 2\pi wt}\, dt\ . \tag{3.5}$$

The **Fourier slice theorem** relates the projection $p_\theta(t)$ and the function $f(x, y)$ in Fourier space: The Fourier transform $P_\theta(w)$ for angle θ gives the values of $F(u, v)$ along a line through the origin and rotated by angle θ with respect to the x-axis. Or in other words:

$$P_\theta(w) = F(w \cos\theta, w \sin\theta)\ , \tag{3.6}$$

where $F(w \cos\theta, w \sin\theta)$ is the representation of $F(u, v)$ in polar coordinates (θ, w) with $(u, v) = (w \cos\theta, w \sin\theta)$. The Fourier slice theorem is represented by Figure 3.1(c).

The full information for the reconstruction is known, when projections $p_\theta(t)$ are given over a range π of projection angles θ. When the projections are known, their one-dimensional Fourier transforms $P_\theta(w)$ are known too. According to the Fourier slice theorem, these one-dimensional Fourier transforms can be identified with radials in the two-dimensional Fourier transform $F(u, v)$. The radials cover the entire Fourier space. Thus, $f(x, y)$ can be recovered from the given projection data.

3.1.2 Filtered backprojection

The filtered backprojection is usually derived from the Fourier representation of $f(x, y)$ as the starting point. The derivation can be found in the books cited above. Only the main steps are presented here.

Trivially $f(x, y)$ can be recovered by inverse Fourier transform of $F(u, v)$ as

$$f(x, y) = \int_{-\infty}^{+\infty} \int_{-\infty}^{+\infty} F(u, v)\, e^{\iota\, 2\pi(ux+vy)}\, du\, dv\ . \tag{3.7}$$

By introduction of the polar coordinate representation of (u, v), substitution of $t = x \cos\theta + y \sin\theta$,

transform, which also includes a reprint of the original paper by Radon [127], and Natterer [108] for details.

use of the Fourier slice theorem of Equation (3.6), and rearrangement of the integration variables we obtain

$$f(x,y) = \int_0^{\pi}\int_{-\infty}^{+\infty} |w|\, P_\theta(w)\, e^{\imath\, 2\pi w t}\, dw\, d\theta\ . \tag{3.8}$$

Here, the inner integral is referred to as the **filtered projection**. The term 'filtered' refers to the frequency filter $|w|$. The outer integral describes the so called **backprojection**. Inversion algorithms based on this equation are called filtered backprojection algorithms. Note that the backprojection operation requires the knowledge of the position of the rotation axis ($t = 0$) in the recorded projection data. The determination of the position of the center of rotation in the recorded sinogram will be discussed in detail in Chapter 5.

There are a variety of possibilities to derive reconstruction algorithms from Equation (3.8). The main difference between these lies in the way, in which the filtering is implemented and in the selection of different additional filters. A filter function $H(w)$ is generally introduced in the above equation as

$$f(x,y) = \int_0^{\pi} \underbrace{\int_{-\infty}^{+\infty} H(w)\, P_\theta(w)\, e^{\imath\, 2\pi w\, t}\, dw}_{q_\theta(t)}\ d\theta\ , \tag{3.9}$$

with

$$H(w) = B(w)\, |w|\ . \tag{3.10}$$

Here, we have defined the filtered projection including the additional filter as $q_\theta(t)$. The factor $|w|$ in the filter is an essential part of the reconstruction, while the factor $B(w)$ is used to suppress noise at high frequencies at the cost of a decreased resolution. Filter functions are discussed by Huesman *et al.* [82]. The filter operation can be replaced by a convolution operation in real space according to the convolution theorem (e.g., see Jansson [90]) resulting in

$$f(x,y) = \int_0^{\pi} h(t) * p_\theta(t)\, d\theta\ . \tag{3.11}$$

Here, $*$ denotes the one-dimensional convolution operation and $h(t)$ is the inverse Fourier transform of $H(w)$.

Reconstruction algorithms implemented in frequency space according to Equation (3.9) are frequently referred to as filtered backprojection (FBP) algorithms. In contrast to this, algorithms based on the convolution operation in real space according to Equation (3.11) are referred to as convoluted backprojection (CBP) algorithms. This notation is, however, not uniquely applied in literature. Mathematically, convolution in real space and filtering in frequency space are equivalent operations.

The FBP algorithm can be implemented by use of fast Fourier transform methods, which allows to make the filter operation fast. The CBP algorithm can be implemented as fast or even faster as the FBP algorithm by use of specially designed hardware [93]. The bottleneck for both types of algorithms is the backprojection step, as is shown in Section 3.2.4.

3.2 Implemented reconstruction algorithms

Different implementations of the filtered backprojection reconstruction have been applied in this work. For fast standard reconstructions an algorithm from the RECLBL library[3] is implemented. The algorithm has been reimplemented in this work in the IDL[4] programming language. The IDL implementation, although slower than the RECLBL code, allows the fast application of changes to the algorithm and simplifies the call of the reconstruction within other self-written IDL software, as the iterative optimization presented in Chapter 5. It was noted during this work, that reconstructions calculated with the standard reconstruction algorithm showed a slight overall shift (DC-shift) of the attenuation value towards negative values. The reason for this shift was identified during this work and can be avoided by use of a variant of the algorithm as discussed in Section 3.2.2. Both algorithms have been reimplemented in this work in one IDL procedure. By default the IDL procedure performs the reconstruction as described in the following section. Setting the keyword 'DC_CORRECT=1' performs the reconstruction according to Ramachandran described thereafter.

3.2.1 "BKFIL" of the RECLBL library

The "BKFIL" algorithm of the RECLBL library has been used in this work for standard reconstructions in combination with the frequency filter 'BUTER'. The algorithm is based on Budinger and Gullberg [30] and is a discrete version of Equation (3.9). "BKFIL" stands for 'backprojection of filtered projections'.

The "BKFIL" algorithm performs the following sequence of operations: Fourier transform the projection data vector; multiply the complex values by the frequency (i.e. with the ramp filter) or an alternative filter; inverse Fourier transform these modified frequencies; and back-project the modified projection data. The algorithm implements the necessary discrete Fourier transforms (DFTs) by use of the fast Fourier transform (FFT) algorithm and adequate zero padding. Zero padding means the extension of the projection data with zeros. It is incorporated, to avoid effects of the otherwise cyclic behavior of the DFT.[5]

As filter, the Butterworth function defined as

$$B(w) = \left[1 + (w/w_m)^{2n}\right]^{-\frac{1}{2}} \tag{3.12}$$

is used. This frequency filter is named "BUTER" in the RECLBL library. It is used for our standard reconstruction with the filter parameters "ORDERX" = $2n$ = 10.0 and "FREQX" = w_m = 0.5. Figure 3.2 shows the Butterworth filter for this selection of parameters. As can be

[3]The RECLBL library [82] is a package of routines for the reconstruction of projection data written in the programming language FORTRAN. Available online at `http://cfi.lbl.gov/software/` [visited August 7th, 2006].

[4]IDL: Interactive Data Language, supplier: ITT Visual Information Solutions (formerly RSI Research Systems Inc.), `http://www.ittvis.com/` [visited August 7th, 2006].

[5]For the properties of the DFT see, e.g., Bracewell [26] or Jansson [90, p.406].

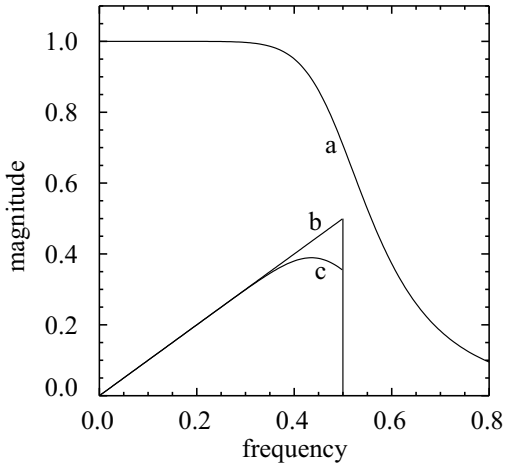

Figure 3.2: Frequency filters used in the tomographic reconstruction. (a) Plot of the Butterworth filter for parameters ORDERX=10.0 and FREQX=0.5, (b) ideal ramp filter, (c) product of (a) and (b). The frequency is plotted in units of the sampling frequency τ^{-1}. In these units, the Nyquist frequency corresponds to 0.5.

seen from the plot, this selection of parameters causes only a mild suppression of high frequency components and maintains high resolution. The routine "BIN" of the RECLBL library is used for backprojection and performs linear interpolation of the inverse fourier transformed data onto the reconstruction grid.

The input for the reconstruction is the projection $p_{\theta_i}(t_j)$ sampled on a regular sampling grid t_j. The calculation is performed in mathematical detail in the following steps:

1.) Zero pad the projection data: Find the smallest integer '*pow*', for which 2^{pow} is larger than the number of given sampling points. Fill up the projections with zeros to a size of $N_t = 2^{pow+1}$ sampling points.

2.) Calculate the discrete Fourier transform (DFT) of the projections using a Fast Fourier transform algorithm as

$$P_{\theta_i}(w_k) = \frac{1}{N_t} \sum_{j=0}^{N_t-1} p_{\theta_i}(t_j)\, e^{-\iota\, 2\pi k j/N_t} \tag{3.13}$$

for the discrete frequencies[6]

$$w_k = \begin{cases} k/N_t & \text{for } k \le N_t/2 \\ 1 - k/N_t & \text{for } k > N_t/2 \end{cases} . \tag{3.14}$$

3.) Calculate the frequency filter

$$H(w_k) = B(w_k)\,|w_k| \,. \tag{3.15}$$

[6]This is the interpretation of the frequencies in tomography, where it is generally assumed that all frequency components in the projections are smaller than the Nyquist frequency, i.e., $|w_k| < 1/2$. The DFT is cyclic: frequencies w_k differing by integer numbers are thus mathematically identical.

4.) Calculate the filtered projections by use of inverse DFT's

$$q_{\theta_i}(t_j) = \sum_{k=0}^{N_t-1} H(w_k)\, P_{\theta_i}(w_k)\, e^{\iota\, 2\pi k j/N_t} \ . \tag{3.16}$$

5.) Backproject the filtered projections

$$\tilde{f}(x_m, y_n) = \frac{\pi}{N_\theta} \sum_{i,j} F_{mn}^{ij}\, q_{\theta_i}(t_j) \ . \tag{3.17}$$

Here we wrote $\tilde{f}(x_m, y_n)$ for the reconstruction of the slice $f(x, y)$ on a discrete reconstruction grid (x_m, y_n). The implementation of the backprojection based on Equation (3.9) requires values of $q_{\theta_i}(t)$ at positions $t(x_m, y_n, \theta_i) = x_m \cos\theta_i + y_n \sin\theta_i$ that generally do not coincide with the sampling points t_j of the (filtered) projections. The routine "BIN" provides linear interpolation of the value at two sampling points with $t_j < t < t_{j+1}$. The interpolation is described by the weighting factors F_{mn}^{ij} in Equation (3.17).

The reconstruction $\tilde{f}(x_m, y_m)$ in Equation (3.17) is given in dimensionless units. The interpretation in tomography is that it describes the measured attenuation coefficient $\tilde{\mu}$ per sampling distance τ in the projections, i.e., $\mu(x_m, y_n) = \tilde{f}(x_m, y_n)/\tau$. In the dimensionless case it is $\tau = 1$.

3.2.2 DC-shifts and the alternative "RALA" implementation

A slight shift in the zero frequency component (DC-shift) of the reconstructions algorithm towards negative values has been recognized during this work for reconstructions calculated with the "BKFIL" algorithm. The shift also varied in magnitude for individual reconstructions. It was found that this shift is generally caused by this type of reconstruction algorithm as has been discussed by Kak and Slaney [93, p. 74]. The shift can be avoided by use of a different reconstruction algorithm based on Ramachandran and Lakshminarayanan [128].

The algorithm of Ramachandran is available in the RECLBL library as "RALA" with the convolution implemented in real space by the subroutine "CONVO". The manual of the RECLBL library [82, p. 36] states that the "RALA"-type algorithm would achieve the same results as the "BKFIL" algorithm described above.[7] This cannot be true, since it contradicts the discussion by Kak and Slaney, who explain the observed DC-shift.

The difference of the two reconstruction algorithms shall be explained here in a unified nomenclature, in order to provide clarity for the future use of the RECLBL library. Therefore, it is necessary to present the reconstruction algorithm proposed by Ramachandran and compare it with

[7] RECLBL library manual [82, p. 36]: "Real space convolution and frequency filtering are equivalent operations. As is shown in examples ..., the RAMP filter used with the algorithm BKFIL achieves the same result as the RALA convolution function used with CONVO."

the "BKFIL" algorithm. The reconstruction algorithm "BKFIL" has already been described by Equations (3.13) through (3.17).

Ramachandran's reconstruction algorithm is a discrete version of Equation (3.11) and hence based on convolution in real space. The discrete convolution function

$$h(j\tau) = \begin{cases} \frac{1}{4\tau^2} & \text{for } j = 0 \\ -\frac{1}{\pi^2 j^2 \tau^2} & \text{for } j = \text{odd} \\ 0 & \text{else} \end{cases} \tag{3.18}$$

is used to calculate the filtered projections by discrete convolution according to

$$q_{\theta_i}(j\tau) = \tau \sum_{k=-\infty}^{\infty} h(j\tau - k\tau)\, p_\theta(k\tau) \; . \tag{3.19}$$

These filtered projections are backprojected as before using Equation (3.17). The convolution function $h(j\tau)$ is the discrete representation of the analytical (i.e., mathematically exact) inverse Fourier transform of the ideal ramp filter $H(w)$ shown in Figure 3.2, with $H(w) = |w|$ for $|w|$ below the Nyquist frequency and $H(w) = 0$ otherwise. As discussed by Kak and Slaney the filtered projections obtained by Equation (3.19) are not identical to those obtained by Equation (3.16). This is because the discrete Fourier transform of the discrete convolution function $h(j\tau)$ is not equivalent to the discrete filter $|w_k|$ in Equation (3.15).[8] While the filter $|w_k|$ becomes zero at $w_k = 0$, the DFT of $h(j\tau)$ is different from zero at this point. This DC-shift is the main difference between the two algorithms. The magnitude of the DC-shift will depend on the given sinogram data and it will be reduced by additional zero padding of the data. The "BKFIL" routine increases the sinogram size (projection width N_t) to a number that is a power of two. Hence, the magnitude of the DC-shift can change drastically, when the projection width of the original sinogram changes from, e.g., 1023 to $1024 = 2^{10}$. The DC shift will be demonstrated in an example in Section 6.3.

3.2.3 Optimum sampling

The optimum sampling rate for the reconstruction is discussed by several authors. Results for both the optimum number of sampling points N_t and the optimum number of projections N_θ are summarized here. The application of the sampling conditions to our setup is discussed.

The optimum sampling frequency is discussed in the book of Kak and Slaney [93, Chapt. 5]. The sampling distance τ_s in the tomographic projections defines the sampling frequency $1/\tau_s$. According to Shannon's sampling theorem, a band-limited signal can be recorded without loss of information, when the sampling frequency is at least twice the band limit of the data. This can be

[8] Discrete convolution can also be performed in frequency space using the product of DFTs. This gives a mathematically identical result, when the data are adequately zero-padded. Any algorithm described by convolution in real space can, thus, be implemented in frequency space and vice versa. The frequency representation of the filter $h(j\tau)$ should thus be identical to the filter $H(w_k)$.

expressed as

$$\frac{1}{2\tau_s} \geq B \tag{3.20}$$

or equivalently as

$$\tau_s \leq \frac{1}{2B}\,, \tag{3.21}$$

where B is the band-limit in the data. Thus, frequencies below the so-called Nyquist frequency $1/(2\tau_s)$ can be recovered from the data.

Generally, tomographic projections are not band-limited and will contain frequency information above the Nyquist frequency. Kak and Slaney discuss the optimum sampling for a signal that is recorded with a rectangular detector sampling function (as the sampling function of our CCD). For a rectangular detector sampling function of width τ (edge length of a CCD detector pixel), the highest recorded frequency component can be estimated by the frequency, at which the Fourier transform of the detector sampling functions [given by Equation (D.3) for an ideal detector] drops to zero for the first time; this occurs at the frequency $B = 1/\tau$. According to the Nyquist theorem in Equation (3.20), the sampling distance must, thus, be $\tau_s \leq (1/2)\tau$, when the signal shall be recovered. For a CCD based detector we can assume that $\tau_s = \tau$, i.e., the sampling distance is given by the edge length of a pixel. The signal is, therefore, undersampled by a factor of two. In praxis this can be compensated by an increase of the number of sampling points. This can be achieved by a second measurement, in which the detector is shifted by the distance $(1/2)\tau$. For tomography, a more elegant way to achieve the two images is given by the possibility to perform a scan over 360^o instead of the required 180^o range of projection angles. When the position of the projected center of rotation is located at 0.25 bin distance from a pixel center, images recorded at θ and $\theta + 180^o$ will give mirror images that are shifted by $(1/2)\tau$ and the sampling density is doubled.[9]

The system response of our system is not simply described by the rectangular sampling function assumed above. The point spread function of our system reduces the band-limit to $B \approx f_{10}$, where f_{10} is the frequency, at which the MTF of our system falls below 10% (see Section 2.4.3). This frequency, in terms of the sampling frequency, is $B = f_{10} = b\,(1/\tau_s)$, where we typically have $b \approx 0.25$. From the Nyquist theorem in Equation (3.20), we then find $\tau_s \leq \tau/(2b) \approx 2\tau$. Thus, our data are generally oversampled because of the suppression of high-frequency components caused by the detector's point spread function.

For the case that N_θ projections are recorded at evenly spaced angular positions $\theta_i = i\,(\pi/N_\theta)$, with $i = 0, ..., N_\theta - 1$, the optimal ratio of N_t and N_θ for standard parallel-beam geometry is given by

$$N_{\theta,opt} = \frac{\pi}{2} N_t \tag{3.22}$$

[9]The interlaced sampling geometry can be more efficient then the standard sampling geometry that is used here. According to Natterer [108, p. 71], sampling in the 'interlaced geometry' provides a reconstruction with the same resolution with only one-half of the data. In the interlaced geometry, only one-half of the sampling positions is required. The position of the sampling positions alternates in successive projections.

as discussed by Natterer [108, p. 84] and Kak and Slaney [93, p. 186]. Equation (3.22) corresponds to the simple geometric requirement that the distance between two points $(t, \theta) = (N_t\tau/2, \theta_i)$ and $(N_t\tau/2, \theta_{i+1})$ corresponds to τ, where τ is the distance between sampling points. According to Natterer, the resolution will not improve, when more than $N_{\theta,opt}$ projections are recorded.

As Budinger and Gullberg [30] pointed out, a tomographic slice $f(x, y)$ is normally not a complete random image. Spatial correlations in $f(x, y)$ exist. The reconstruction from a reduced number of projections will, therefore, generally still result in a good reconstruction. In our case the correlation in the recorded data is additionally increased by the limited detector resolution.

Numerical example: For a typical tomographic reconstruction we record data at $N_t = 1536$ sampling points (corresponding to the CCD width) and at $N_\theta = 720$ projection angles, i.e., in steps of 0.25 degree. According to Equation (3.22), the optimal number of projections would thus be $N_{\theta,opt} \approx 2413$. As discussed, we will generally still obtain a good reconstruction, even when using only $N_\theta = 720$ projections, i.e., with an undersampling of a factor of ~3.

3.2.4 Computational costs

The order of the number of operations [designated by $O()$] required by the filtered backprojection algorithms is given by Natterer [108, p. 111]. The total computational costs are given by the sum of the operations required for the filtering and the backprojection operation as

$$O(\text{reconstruction}) = O(\text{filter}) + O(\text{backprojection}) \; . \tag{3.23}$$

When the filtering operation is implemented as convolution, we have $O(\text{filter}) = O(N_\theta\, N_t^2)$. The filter implemented in Fourier space and application of the fast Fourier transform reduces this number to $O(\text{filter}) = O(N_\theta\, N_t \log N_t)$ operations. Backprojection requires $O(\text{backprojection}) = O(N_\theta\, N_t^2)$ operations. The total computational costs using fast Fourier transforms, thus, are given by

$$\begin{aligned} O(\text{reconstruction}) &= O(N_\theta\, N_t \log N_t) + O(N_\theta\, N_t^2) && (3.24) \\ &= O(N_t^2 \log N_t) + O(N_t^3) \; , && (3.25) \end{aligned}$$

where we have used the relation $N_\theta = (\pi/2)\, N_t$ in Equation (3.25), which is the optimum sampling condition discussed above. The total computational costs are dominated by the backprojection process.

3.3 Reconstruction quality

3.3.1 Spatial resolution

The spatial resolution in the reconstruction $\tilde{f}(x,y)$ can be described by a point spread function $\mathrm{PSF}_{\tilde{f}}$ of the reconstruction as

$$\tilde{f}(x,y) = \mathrm{PSF}_{\tilde{f}}(x,y) ** f(x,y) \,, \tag{3.26}$$

where $f(x,y)$ is the original slice and $**$ designates two-dimensional convolution. The point spread function $\mathrm{PSF}_{\tilde{f}}$ of the reconstruction is obtained by reconstruction of a centered point-like object, whose projections are given by $p_\theta(t) = \delta(t)$. The Fourier transform of the delta function is unity for all frequencies w, and we thus have $P_\theta(w) = 1$ for all projection angles θ. The reconstruction in Equation (3.9) then gives

$$\mathrm{PSF}_{\tilde{f}}(x,y) = \int_0^\pi \int_{-\infty}^{+\infty} H(w)\, e^{\imath\, 2\pi w\, t}\, dw\, d\theta \,, \tag{3.27}$$

where $H(w)$ is the ideal ramp filter multiplied by the optional filter function and $t = x\,\cos\theta + y \sin\theta$. The effect of the ideal ramp filter can be described by setting the integration limits to plus and minus the Nyquist frequency, which is $1/2\tau$ for sampling interval τ. This band-limit has the same effect on $\mathrm{PSF}_{\tilde{f}}$ as a circular aperture has for the PSF of an optical system. Thus, oscillations are caused by the band-limit, which are sometimes referred to as 'ringing'. Figure 3.3(a) shows the $\mathrm{PSF}_{\tilde{f}}$ that was obtained from our standard reconstruction of a point-like oject. The reconstruction grid was defined with a $0.25\,\tau$ spacing here, where τ is the sampling distance in the projection. In the plot through the center in Figure 3.3(b), the oscillation between positive and negative values is visible.

The influence of the detector point spread function can be incorporated into Equation (3.27). By insertion of the radially symmetric modulation transfer function $M(w)$ of the detector that was introduced in Equation (2.32), we obtain:

$$\mathrm{PSF}_{\tilde{f}} = \int_0^\pi \int_{-\infty}^{+\infty} H(w)\, M(w)\, e^{\imath\, 2\pi w\, t}\, dw\, d\theta \,. \tag{3.28}$$

Here, we have used the two-dimensional representation $M(w)$ of the detector MTF for the description of the blur within a one-dimensional projection. This was also done by Busch [31, p. 73 f.], who referred to Glover and Eisner [65]. However, it must be pointed out that Equation (3.28) only gives a correct description of blur, when the two-dimensional recorded projections are independent of the z-direction as for cylindrical samples. Only in this case $M(w)$, which is the one-dimensional Fourier transform of the detector line spread function, describes the blur in the one-dimensional projection correctly.

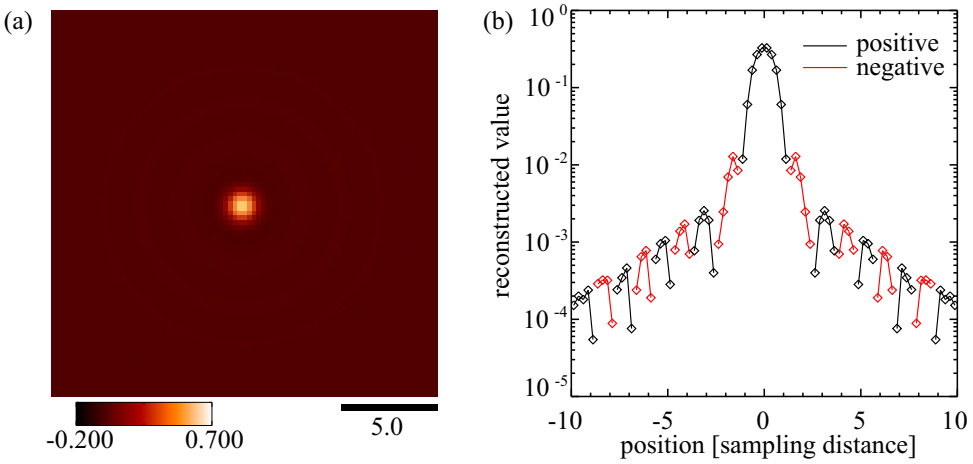

Figure 3.3: Calculation of the PSF $\tilde{f}$ of the standard reconstruction according to Budinger. The combination of ideal ramp filter and Butterworth filter of Figure 3.2(c) was used in the reconstruction. (a) Reconstruction of a sinogram with $N_t = 101$ sampling points, $N_\theta = 200$ projections, and $p_\theta(t_{50}) = 1$ in the central pixel and otherwise zero. The resolution of the reconstruction grid is $0.25\,\tau$, with τ the sampling distance in the projection. (b) Plot of the central intensity profile. For negative values the absolute value is plotted (red).

3.3.2 Noise

This section deals with the propagation of the noise from the projection images p into the reconstructed slices $\tilde{f}$. Noise in the reconstructed slices is sometimes referred to as 'density resolution' and is seen as the broadening of peaks in the histogram of a reconstruction. The standard deviation σ_μ, which is the statistical variation in a point of the reconstructed slice $\tilde{f}$, can be used to estimate the width of the peaks in the histogram.

Noise in the projection images p is dominantly caused by statistical fluctuations of the x-ray photons, as discussed in Section 2.5.2. Several authors have discussed the propagation of noise through the backprojection algorithm. (See, e.g., [42], [93], [56], and [68]). More references can be found in [92]. Kak and Slaney [93, p. 199] described how the variance in the reconstruction $\sigma_\mu(x_i, y_j)^2$, i.e., the variance of $\tilde{f}(x_i, y_j)$ can be calculated for each point (x_i, y_j) on the reconstruction grid. This calculation is performed for reconstruction according to the algorithm of Ramachandran that was presented above. For a simple estimation of the noise in the reconstruction we will use a simple analytical expression derived by Davis [42].

Davis analytically derived an expression [42, Equations (2),(A22)] for the noise variance σ_μ^2 of a pixel in the center of the reconstruction of a homogeneous cylindrical or a slowly varying object. The calculation is conducted for the reconstruction according to the algorithm of Ramachandran, with the convolution kernel $h(j\tau)$ given in Equation (3.18), i.e., for the equivalent of the ideal ramp filter[10]. Taking the effect of linear interpolation in the backprojection step into account

[10]The influence of filter functions $B(w)$ is described by Kak and Slaney [93]. For our standard reconstruction, the influence of the Butterworth filter can be neglected and Davis formula is a good approximation.

Davis determined the variance as

$$\sigma_\mu^2 = \frac{\pi^2 - 3}{18\tau^2 N_\theta \langle N \rangle} \,. \tag{3.29}$$

Here, τ is the spacing between sampling points, N_θ is the number of projections, and $\langle N \rangle$ is the same average count rate for all pixels. It is assumed that the photon signal obeys Poisson statistics and is uncorrelated, with the same average photon count $\langle N \rangle$ and variance $\langle (\Delta N)^2 \rangle = \langle N \rangle$ for all sampling points. (The assumption of the same count rate for all pixels can be used as a first approximation for our setup). In Appendix C.3, the signal variance for each sample point in the projection is calculated. The result, neglecting the influence of noise in the reference image, is given by Equation (C.44) as

$$\sigma_p^2 = \langle (\Delta p)^2 \rangle = \frac{1}{\langle N \rangle} \,. \tag{3.30}$$

The optimal signal-to-noise ratio p/σ_p in the measurement of the projected attenuation coefficient is achieved for $p \approx 2$ (see derivation in Appendix C.3 or Section 2.5.2).

Hereby, Equation (3.29) can be rewritten as

$$\sigma_\mu^2 = c \, \frac{1}{\tau^2 N_\theta} \, \sigma_p^2 \,, \tag{3.31}$$

where $c = 0.3816$ is a constant.

By introduction of the detector width W, with $W = N_t \tau$, where N_t is the number of sampling points, we obtain

$$\sigma_\mu^2 = \frac{c}{W^2} \, \frac{N_t^2}{N_\theta} \, \sigma_p^2 \tag{3.32}$$

$$= \frac{c}{W^2} \, \frac{N_t^2}{N_\theta \langle N \rangle} \,, \tag{3.33}$$

which demonstrates the dependence of the variance on the sampling parameters N_t, N_θ, and the average photon count $\langle N \rangle$ at each sampling point. The decrease of the variance with increasing detector width W must be related to the typically lower attenuation coefficient μ at increasing sample diameters. This is possible by introduction of the relative variance of the reconstructed attenuation coefficient as

$$R(\mu) = \frac{\sigma_\mu^2}{\mu^2} = \frac{c}{(\mu W)^2} \, \frac{N_t^2}{N_\theta \langle N \rangle} \tag{3.34}$$

The optimal signal-to-noise ratio μ/σ_μ in the center of the reconstruction is again obtained for $p \approx 2$. (Since it is $\mu W \propto p$, the function σ_μ/μ is proportional to the function σ_p/p and consequently has the same minimum).

We shall estimate the relative variance for the reconstruction of a homogeneous cylindrical object, with diameter $D = W$ equal to the detector width. If projections are recorded under optimal condition, i.e., with maximum projected attenuation coefficient $p_{max} = \mu D = \mu W = 2$, the relative

variance at the center of the cylinder in Equation (3.34) becomes

$$R(\mu)\big|_{\mu W=2} = \frac{c}{4}\,\frac{N_t^2}{N_\theta \langle N\rangle}\ . \tag{3.35}$$

Example 1: In a typical SRμCT measurement we have $\langle N_0\rangle = 80\,000$ quanta in the reference image, $N_\theta = 720$ projections, $N_t = 1536$ sampling points in each projection, and optimal attenuation $p = \mu W = 2$. We then can use $\langle N\rangle = \langle N_0\rangle \exp(-p) \approx 8\,000$ as an approximation for the average count rate in each pixel, which gives the variance $\sigma_p \approx 0.011$ in the projection. For these numbers the relative variance in the reconstruction given by Equation (3.35) becomes $R(\mu) \approx 0.039$, the signal-to-noise ratio becomes SNR $= \sqrt{1/R(\mu)} \approx 5.06$, and the standard deviation becomes $\sigma_\mu = \mu\sqrt{R(\mu)} \approx 0.20\,\mu$, with $\mu = \frac{2}{W}$.

3.3.3 Noise form the reference images

The influence of noise in the reference images in SRμCT seems not to have been discussed by other authors before. However, due to the time-dependent structure of the x-ray source in SRμCT the influence of the constantly acquired reference images on the reconstruction cannot be neglected as it is typically done for (stable) x-ray tube sources. Important aspects for the measurement of reference images and their influence on the noise in the reconstruction shall be discussed here.

As can be seen from Equations (3.31) and (C.42) noise in the reference images gives simply an additive contribution to the variance in the reconstructions. The contribution from the radiographic projections to the variance is proportional to $(N_\theta \langle N\rangle)^{-1}$, while the contribution of reference images is proportional to $(N_r\langle N_0\rangle)^{-1}$, where N_θ is the number of projection images and N_r is the number of reference images (compare Section 2.5.2). The contribution of the reference images to the noise in the reconstruction should be considered in recording and processing of images, i.e., the number of images N_θ and N_r should be selected accordingly.

We generally observe a structure in the noisy data that cannot be explained by simple pixel-wise fluctuations in the reconstruction. This noise is especially pronounced for weakly absorbing samples. It is more pronounced at the center of the reconstruction and decreases with increasing distance from the center. With increasing distance from the center also the point-like noise structure changes into small streaks oriented on concentric curves around the reconstruction center. As could be verified by simulation, the observed structures are caused by the **noise in the reference images**. The streak-like structure and the increase to the center could be reproduced in a simulation, where each noisy reference image was used for the calculation of several projection images as in our measurements. The structured noise becomes visible in the reconstructions, when the noise in the reference images makes a relevant contribution to the noise in the projections. Thus, the structured noise caused by the reference images is more pronounced for objects of low absorption.

3.3.4 Binning reduces noise

As to be seen directly from Equation (3.33), the noise σ_μ in the reconstruction depends on the number of sampling points N_t and the average number of recorded quanta $\langle N \rangle$ in a pixel. Sometimes it can, therefore, be desirable to reduce the number of sampling points by binning. This can in practice be done in two ways: using the on-chip binning of the CCD or by binning of the recorded projection data in the computer prior to reconstruction.[11] We shall distinguish between the two binning factors b_t and b_z, where b_t is the binning factor along the t-direction of the projection $p_\theta(t)$ and b_z is the binning factor over the perpendicular direction, i.e., over parallel slices. When both are equal, we write $b = b_t = b_z$. The total (average) number of collected charge quanta given by $\langle N_{tot} \rangle = \langle N \rangle N_\theta N_t N_z$ is changed only in the case of on-chip binning.

1.) The **on-chip binning** in our CCD camera limits the total number of charge quanta in the binned image to the maximum CCD count times the (fixed) CCD gain. Thus, the average count rate $\langle N \rangle$ in the binned image is the same as for the unbinned image. Only the number of sampling points N_t is changed. We can substitute

$$N_t \rightarrow N_t' = N_t / b_t \tag{3.36}$$

in Equation (3.33), with b_t the binning factor along the t-direction of the projection $p_\theta(t)$. There is no influence of b_z. The variance in the reconstruction from the on-chip-binned data is then given by

$$\sigma_\mu'^2 = \frac{1}{b_t^2} \sigma_\mu^2 \, . \tag{3.37}$$

The noise level thus scales with the binning factor as $\sigma_\mu' \propto b_t^{-1}$. The higher the binning factor, the lower is the noise level. The exposure time scales as $t_{acq}' \propto b_t^{-1} b_z^{-1}$ for this type of binning and so does the total number of charge quanta, for which we find $\langle N_{tot}' \rangle \propto b_t^{-1} b_z^{-1}$.

2.) **Binning of the recorded images**, which we perform before calculation of the projection data, can be described by substitution of

$$\begin{array}{rcl} N_t & \rightarrow & N_t' = \frac{N_t}{b_t} \quad \text{and} \\ \langle N \rangle & \rightarrow & \langle N' \rangle = b_t b_z \langle N \rangle \end{array} \tag{3.38}$$

in Equation (3.33). This describes the reduced number of sampling points N_t' in the reconstruction and the simultaneously increased number of collected charge quanta $\langle N' \rangle$ per sampling point. From Equation (3.33) we find

$$\sigma_\mu'^2 = \frac{1}{b_t^3 b_z} \sigma_\mu^2 \, . \tag{3.39}$$

[11] A third variant of binning is of course the binning of the reconstructed slices. One would expect a decrease of the noise variance proportional to b^{-2} for uncorrelated data, when the averaging is performed over b^2 pixels. The values in the reconstructed slices are, however, correlated through the reconstruction process, which must be considered in this case. Comparison of binning before and after reconstruction should be investigated in a future study.

If the binning factor is the same for both detector coordinates, i.e. if $b = b_t = b_z$, then the noise level scales as $\sigma_\mu \propto b^{-2}$. Exposure time and the total number of collected charge quanta are of course unchanged for this type of binning.

It should be noted, that the reduction of noise by the application of binning to the recorded images is probably not optimal, since information is irreversibly lost in this operation. An experimental study that discusses the optimum binning of projections in an SRμCT measurement was presented by Thurner *et al.* [145].

Example 2: The noise σ'_μ in a binned measurement, with binning factor $b = b_t = b_z = 2$ and otherwise the same parameters as in *Example 1* above can be calculated. In *Example 1* the noise variance $\sigma_\mu = 0.2\,\mu$ was found for a typical reconstruction. For the binned measurement we find $\sigma'_\mu = b^{-1}\sigma_\mu = 0.1\,\mu$ for on-chip binning and $\sigma'_\mu = b_t^{-1}b_z^{-1}\sigma_\mu = 0.05\,\mu$ for binning of the recorded data, when it is assumed that the CCD dynamic range is fully utilized.

3.3.5 Geometrical requirements for parallel-beam tomography

The finite source size causes blur in the radiographic images, while the finite source-to-sample distance causes a deviation from the ideal parallel-beam geometry. We can make a simple estimation of the geometrical requirements that must be fulfilled for parallel-beam tomography.

We shall assume that the opening of the radiation cone from the wiggler is wide enough, such that any source point illuminates any point on the sample. This will result in a conservative estimation of the geometrical conditions that have to be met for a parallel-beam tomographic measurement. More blur will be introduced by the source in the horizontal than in the vertical direction due to the larger horizontal source size. Thus, we will formulate the following conditions for the horizontal direction as the limiting factor. The geometry in the horizontal plane is schematically represented in Figure 3.4. The horizontal source size $2\sigma_X$, source-to-sample distance L, and sample diameter D are defined as shown in the figure. We shall assume that the sample-to-detector distance is also given by the distance D.

The **blur induced by the source size** is represented by the spacing of the red lines in 3.4 (at the detector plane) and should be less than the sampling distance τ on the detector. Thus, the condition

$$\frac{\sigma_X}{L} D < \tau \tag{3.40}$$

must be fulfilled. Here, we have approximated the source-to-detector distance by the sample diameter D for all points on the sample. Assuming, that the detector width equals the sample diameter D, we obtain the sampling distance $\tau = D/N_t$, with N_t the number of sampling points. Thus, Equation (3.40) can be rearranged as

$$N_t < \frac{L}{\sigma_X} \,. \tag{3.41}$$

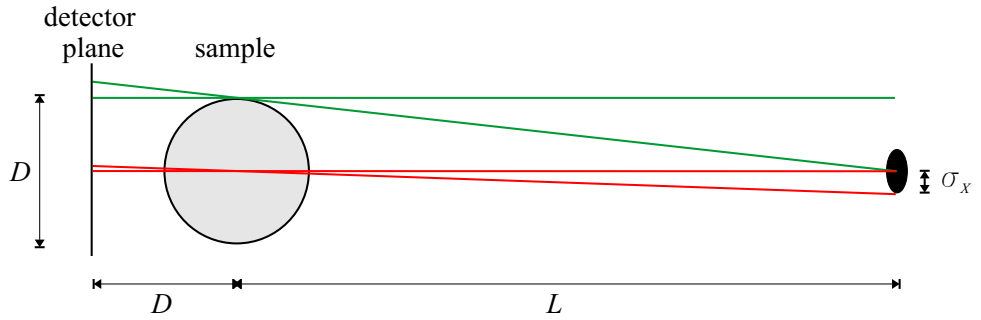

Figure 3.4: Schematic representation of blur induced by source size (red lines) and deviation from the parallel-beam geoemetry (green lines) for the horizontal direction. The scheme shows the source-to-sample distance L, the sample diameter D, and the horizontal source size described by it half diameter σ_X. It is assumed that the sample-to-detector distance is also D. The drawing is not to scale. Typical distances would be $L = 35\,000$ mm and $D = 5$ mm in SRμCT.

Similarly, we can derive a condition for the **deviation from the ideal parallel-beam geometry**, which must be fulfilled for the parallel-beam reconstruction algorithm to be applicable to the recorded projection data. The maximum deviation from the parallel-beam geometry is observed for the outermost sample positions. The projection of the outermost ray that penetrates the sample may not be separated by more than the sampling distance τ from the projection of the ideal parallel-beam projection (illustrated by the spacing of the green lines in 3.4 at the detector plane). This gives the condition

$$\frac{D}{L} D < \tau \,. \tag{3.42}$$

With $\tau = D/N_t$, this can be rearranged to

$$N_t < \frac{L}{D} \,. \tag{3.43}$$

The application of fan- or cone-beam reconstruction algorithms (e.g., the cone-beam reconstruction by Feldkamp *et al.* [57]) must be considered if this condition is not met.

Numerical example: For beamline BW2 (see parameters given in Table 2.1), we have $\sigma_X \approx \sigma_x = 2.22$ mm, and $L = 35\,000$ mm, which gives $L/\sigma_X = 35\,000/2.22 = 15\,766$ (divergence: 0.063 mrad). Thus, for our sampling resolution of $N_t = 1\,536$, the condition for an unblurred image given by Equation (3.41) is easily fulfilled with $N_t = 1\,536 < 15\,766$. The parallel-beam geometry is applicable as long as Equation (3.43) is fulfilled. For $N_t = 1\,536$ sampling points this is the case for samples smaller than $D < 35\,000$ mm$/1\,536 = 22.8$ mm. The beam divergence at the sample position was measured for HASYLAB beamline BW2 with a pinhole (compare Appendix D.7). This verified a beam divergence of less than 0.108 mrad.

3.3.6 Sources for artifacts

Any perceived distortion or other data error caused by the instrument of observation is called an artifact.[12] Recently, an investigation of reconstruction artifacts in SRμCT was presented by Vidal *et al*. [148], who simulated artifacts and compared them with experimental data. Here, it is attempted to give a complete list of the possible artifact sources in SRμCT.

The x-ray source, which must be understood as part of our instrument, gives rise to an always present artifact, which is

- Noise. Noise is introduced by the statistical fluctuations of the x-ray beam as discussed in Section 3.3.2. Readout noise and quantization noise of the CCD are typically negligible.

Leakage of intensity into regions of low intensity (high absorption) can be caused by the following sources. These effects add blur to the incident intensity profile and can result in a non-linear effect in the calculation of the projected attenuation coefficient. This can cause an integral under-estimation of the measured attenuation coefficient in the projections as discussed in Section 2.5.1.

- Beam divergence. The opening angle of the radiation cone and the finite source size can blur the recorded images (compare Section 3.3.5). The source is extended and generates a cone of radiation in each point. It can be described as a four-dimensional function. In order to obtain good projection data, the influence of the source must be the same in all projections. Accordingly, the spread that is introduced in the projection over the distance of the sample diameter D must be small. In our measurements the distance between sample and detector typically is in the order of D and we can neglect the source influence.

- Detector blur (in space and time). The effect of the detector PSF on the recorded projection images and the reconstruction depends on sample geometry and beam profile as discussed in Section 3.2.3. Afterglow of the luminescent screen can cause the blur of intensity in time.

- Scatter. The relevance of Rayleigh and Compton scatter is discussed in Section A.3. For samples of diameter $D < 1\,\mathrm{cm}$ and with the selection of accordingly low x-ray energies, their influence is negligible. If necessary, scatter can be suppressed by the use of x-ray collimators.

- Fluorescence. When atomic fluorescence is excited as secondary radiation inside the sample, it may become visible on the detector much like scattered radiation. The contribution of fluorescence to the signal will mostly be low, due to the isotropic generation of the fluorescent radiation and the typically strong self absorption of the fluorescent radiation.

[12] Definition from `http://en.wikipedia.org/wiki/Artifact`.

- Diffraction phenomena (phase propagation, refraction, total reflection, Bragg reflection). Except for Bragg reflection, these effects are negligible at short sample-to-detector distances. Bragg reflection can occur for samples of crystalline structure, when the Bragg condition is fulfilled. Using an x-ray source with small bandwidth, the probability for Bragg reflection is small and the effect is negligible.

The following are sources of systematic artifacts in the reconstruction:

- Beam hardening. The attenuation coefficient is a strong function of photon energy as described approximately by Equation (A.13). In a polychromatic beam, the low energetic components are more strongly attenuated than the high energetic components, whereby the measurement of the attenuation coefficient becomes non-linear. This effect was described by Brooks and di Chiro [27] and is known as beam hardening. The small bandwidth of the Si(111) reflex causes a negligible variation of the attenuation coefficient as described by Equation (A.15). The contribution of higher harmonics as from the Si(333) reflex can, however, be relevant. It can be suppressed by mirrors that are introduced into the SR beam as low-pass filters.

- Misalignment of projection data. Proper alignment of the rotation axis is required (compare Section D.3). Moreover, the determination of the center of rotation is required and will be discussed in detail in Chapter 5.

- Incomplete data. When the sample leaves the field of view or projections are missing (as in laminography), techniques for the sinogram restoration must be applied before reconstruction.

- Aliasing. The artifacts that are introduced by under-sampling (band-limited data) of the number of projections N_θ, the number of sampling points N_t or by the detectors sampling function are referred to as the aliasing distortions.

- Partial volume effect. The partial volume effect describes the additional blur (averaging) that is caused by the detector sampling function (e.g., form of detector pixels) and the finite reconstruction grid.

- Detector non-linearities. If the same pixel in every projection is recorded incorrectly due to a local non-linearities of the detector, ring-artifacts are created. An example of ring artifacts is shown in the reconstruction of Figure 6.11(d). Ring artifacts are most pronounced at the center of the reconstruction and decrease in intensity with increasing distance from the center. They are typically dominated by non-linearities of the luminescent screen, while the CCD non-linearity is typically negligible.

- Deviation from the parallel-beam geometry. The limit was discussed in Section 3.3.5.

- Sample movements or morphological changes of the sample. Any movement of the sample other than the tomographic rotation will result in inconsistent projection data and reconstruction artifacts. To detect morphological changes, e.g., Du Roscoat *et al.* [130] have calculated the cross-correlation coefficient of equivalent projections that were recorded at different times.

- Source fluctuations. Fluctuations of the SR beam can be caused by the decaying electron (positron) beam intensity, variations of the electron beam position, and heat-load effects on the monochromator crystals. The resulting intensity variation must be small and slow. The decaying beam intensity is compensated as presented in Section 2.5.

- High-energetic hits on the CCD. The hits give rise to single streaks in the reconstructions. They can be corrected by Zinger removal techniques as discussed in Section 2.5.

Beam hardening can cause a similar non-linear effect as the long tails of the point spread function. By measurements with defined absorber plates (not presented) it was verified that beam hardening caused by higher-order harmonic radiation had negligible influence on our measurements. However, if the detector blur is successfully removed (e.g., by deconvolution) then the next limitation for quantitative measurements might be imposed by these high-energetic components.

The same as for beam hardening holds for afterglow in the luminescent material. Afterglow blurs intensity in time, i.e., over projections and can result in a similar non-linear effect. When the exposure times will further reduce with future CCD cameras, the influence of afterglow might become relevant.

Chapter 4

Optical coating of the luminescent screen

4.1 Introduction

The x-ray camera presented in Chapter 2 is based on lens-coupled imaging of a luminescent screen (x-ray phosphor). Part of the luminescent light that is collected by the lens system is reflected or scattered inside the luminescent screen before it leaves the screen. Thus, it does not seem to be emitted at the original place of luminescent light generation (x-ray detection). This is observed as a broadening of the point spread function (blur), which exhibits weak but extended tails, and as the more or less sharp images of crystal defects.

The crystals that are employed as luminescence screens, typically possess polished plan-parallel surfaces, a high refractive index, and are optically clear. A major fraction of luminescent light can, therefore, be trapped between the crystal surfaces by total reflection. This is the case for both luminescent bulk crystals as well as for crystals with only a thin active (luminescent) layer. The trapped light may travel large distances and can be coupled out, when it is scattered at surface defects (e.g., scratches) or crystal impurities that serve as secondary sources. These localized defects that become visible as screen inhomogeneities give rise to ring artifacts in the tomographic reconstruction. Therefore, we want to minimize the fraction of light that is trapped by total reflection, i.e., we want to minimize the reflectivity at the crystal surfaces.

The long tails in the point spread function have been recognized by several authors [36], [66], [70], [96], [129], [142]. Several strategies for their suppression exist. Generally, the reflection properties of optical elements can be tailored by application of absorbing, reflective, or anti-reflective coatings. The application of optical coatings for x-ray detectors has been described in a review article by Gruner [70] and for the field of medical imaging systems in another review article by Rowlands [131]. Koch *et al.* [96] and Cloetens [36] already suggested that an absorbing coating could be used to suppress the long tails appearing in single crystals employed as lumines-

cent screens in microtomography. However, so far only the application of anti-reflection coatings has been reported by Cloetens [36], who applied the coating to both surfaces of doped YAG and LAG crystals. The use of immersion liquids (frequently used in microscopy) between objective and scintillator could also reduce the total internal reflected light, as noted by Koch *et al.* [96]. Structured scintillators can be used to inhibit light propagation in the luminescent material. Structured CsI(Tl) that is deposited by columnar growth or lithographically fabricated phosphor plugs are commercially available. However, the spatial resolution achieved with these screens is in the range of 10 μm only (compare Martin and Koch [102, Fig. 2]).

An optical coating on the screen surface opposite to the imaging detector is called a backing layer and typically is reflective or absorbing. Reflective backing layers result in an increased light output and a reduced spatial resolution of the system, while absorbing backing layers result in a lower light output but also enhance the spatial resolution. In this work an absorbing optical coating of black lacquer paint was applied to the luminescent crystals in order to suppress the long tails in the PSF.

The preparation of crystals is described in Section 4.2.1. The influence of the backing layer on the spatial system response was quantified by edge profile measurements that are presented in Section 4.2.2. Optimal suppression of reflections can be expected, when the refractive indices of luminescent crystal and the backing layer match. Therefore, the refractive index of the lacquer was measured using ellipsometry. The measurement result is presented in Section 4.2.3. From the known refractive indices of crystal and lacquer, the fraction of trapped light is estimated using the Fresnel equations in Section 4.2.4. The influence of the backing layer on the microtomographic measurement of a human femur will be demonstrated in Section 6.2.

4.2 Preparation and characterization of the backing layer

4.2.1 Application of lacquer paint

An absorbing backing was prepared on several $CdWO_4$ crystals of different thickness during this work. Two crystals with thickness of 1.0 mm and 0.08 mm (referred to as CWO1 and CWO2), respectively, were characterized by edge profile measurements before and after application of the backing layer. The results obtained for these two crystals are presented here.

The absorbing backing was applied to the crystal surface that faces the incoming x-ray beam, as shown in Figure 4.1. Black spray lacquer was used to form a thin, optically opaque surface layer on the crystals. The spray lacquer (type: ‘Buntsprühlack seidenmatt’, manufacturer: Eisodur) was applied such that it also covered the edges of the crystals, at which reflections of course should be suppressed too. The attenuation of x-rays caused by this thin lacquer layer can be neglected for SRμCT measurements at energies above 10 keV. At lower energies some x-ray intensity is lost. In

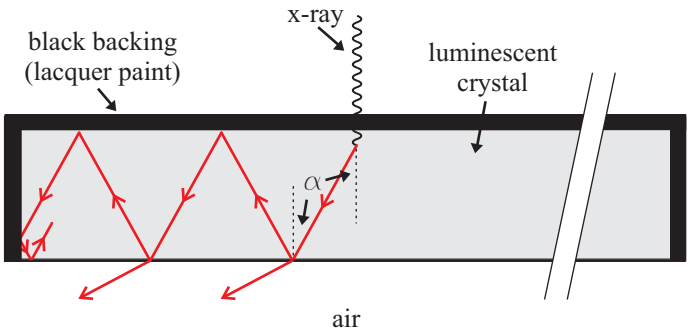

Figure 4.1: Scheme of the luminescent crystal with backing layer. The surface oriented towards the incoming x-ray beam and the crystal edges are covered with black lacquer paint. Internal reflections are suppressed.

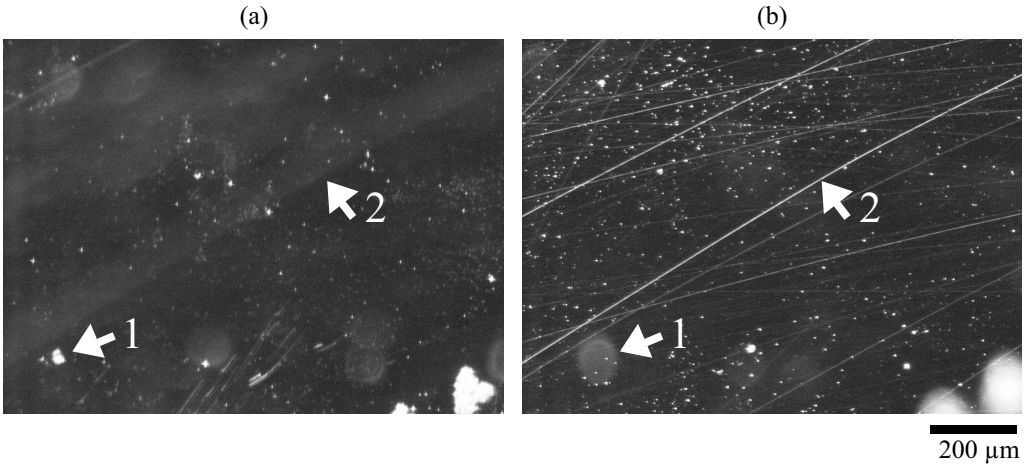

Figure 4.2: Microscope images of a 1 mm thick $CdWO_4$ crystal with many surface defects. Focussed on (a) back surface and (b) front surface. The arrows mark (1) an extended point defect on the backside and (2) a streak on the front side.

any case, the attenuation by the lacquer layer is automatically corrected during the measurement by normalization with reference images.

Light microscope images of the 1.0 mm thick crystal CWO1 taken before application of the backing are shown in Figure 4.2. This crystal displayed a lot of surface defects on both its front and its back surface.[1] Actually, the crystal was selected for the test of the black backing for exactly this reason. The light microscope images give a good indication of the crystal performance in the x-ray camera.[2] Defects on each surface can be identified by focussing the microscope to the crystals back surface [Figure 4.2(a)] and the crystals front surface [Figure 4.2(b)]. Note that our x-ray camera typically is focussed onto a layer close to the back surface. Defects on the back surface will thus give a sharp, disturbing image.

[1] Front/back as seen from the camera or microscope. The back surface carries the black backing.

[2] The image seen with the light microscope will however be different to the image seen with the x-ray camera, although, the x-ray camera is not much different from a microscope. The difference is due to the light source: external light source in the microscope, luminescence light generation inside the crystal in the x-ray camera.

4.2.2 Edge profile measurements

Both crystals CWO1 and CWO2 were characterized by edge profile measurements directly before and after application of the backing layer. The edge profiles were recorded at HASYLAB beamline BW2. The edge profile was realized using a gold plate that was opaque for the incident radiation. The detailed measurement parameters are given in the footnotes of Table 4.1.

Figure 4.3 shows data from the edge-profile measurement for crystal CWO1. Figure 4.3(a) shows the image recorded with the untreated crystal. Figure 4.3(b) shows the equivalent image recorded after application of the backing layer. Both images have been dark image corrected and are plotted in logarithmic scale. The x-ray beam in these measurements was reduced to rectangular shape by the slit system. The central edge in the images corresponds to the gold edge. The images were recorded within about 30 minutes. The observed change of the beam profile during this time was negligible for the evaluation, and the mean CCD count over all pixels in the two (dark image corrected) images was very similar with Mean(N_{ADU}) = 3214.3 and Mean(N_{ADU}) = 3385.65 for the images in Figures 4.3(a) and (b), respectively. Hence, the intensity profile in the tails is directly comparable.

The intensity spreads into the dark regions of the images in both cases. It is directly evident, that the intensity in the tails is higher for the untreated crystal than it is for the crystal with the absorbing backing layer. Figure 4.3(c) shows the measured CCD counts of the same CCD row for the untreated (curve 1) and the treated crystal (curve 2). An intensity reduction of about a factor of two is observed for the treated crystal. Furthermore, a reduction of the signal variation is observed, which can partly be explained by the reduced intensity and the corresponding reduction of photon noise.

The strong inhomogeneities in the profile of Figure 4.3(a) are most likely caused by surface defects on the back surface. Defects on the front surface would not be seen as a sharp image for a crystal of 1 mm thickness (compare the images in Figure 4.2). These inhomogeneities appear much less pronounced after application of the backing in Figure 4.3(b). Light emission from surface defects is obviously strongly suppressed now. Figure 4.3(d) shows a closeup of two weakly visible screen inhomogeneities that correspond to the two peaks in the profile (curve 1) in Figure 4.3(c). It will be shown in Section 6.2 that these two weak spots result in significant ring artifacts in the tomographic reconstruction.

The plots in Figure 4.4(a) show the intensity averaged across a subregion around the central edge profile, i.e., the edge spread function (ESF). The intensity was normalized to the maximum intensity (mean value of the pixels with >95% maximum intensity) in the image for the calculation, and were shifted upon averaging to correct for the edge tilt, as described in Section D.1. In this logarithmic plot, a reduction of the intensity in the tails of the ESF by a factor of about two is observed after application of the backing layer. Note that the observed absolute change of the ESF is only small. However, the relative change and not the absolute change is important for the measurement of projections.

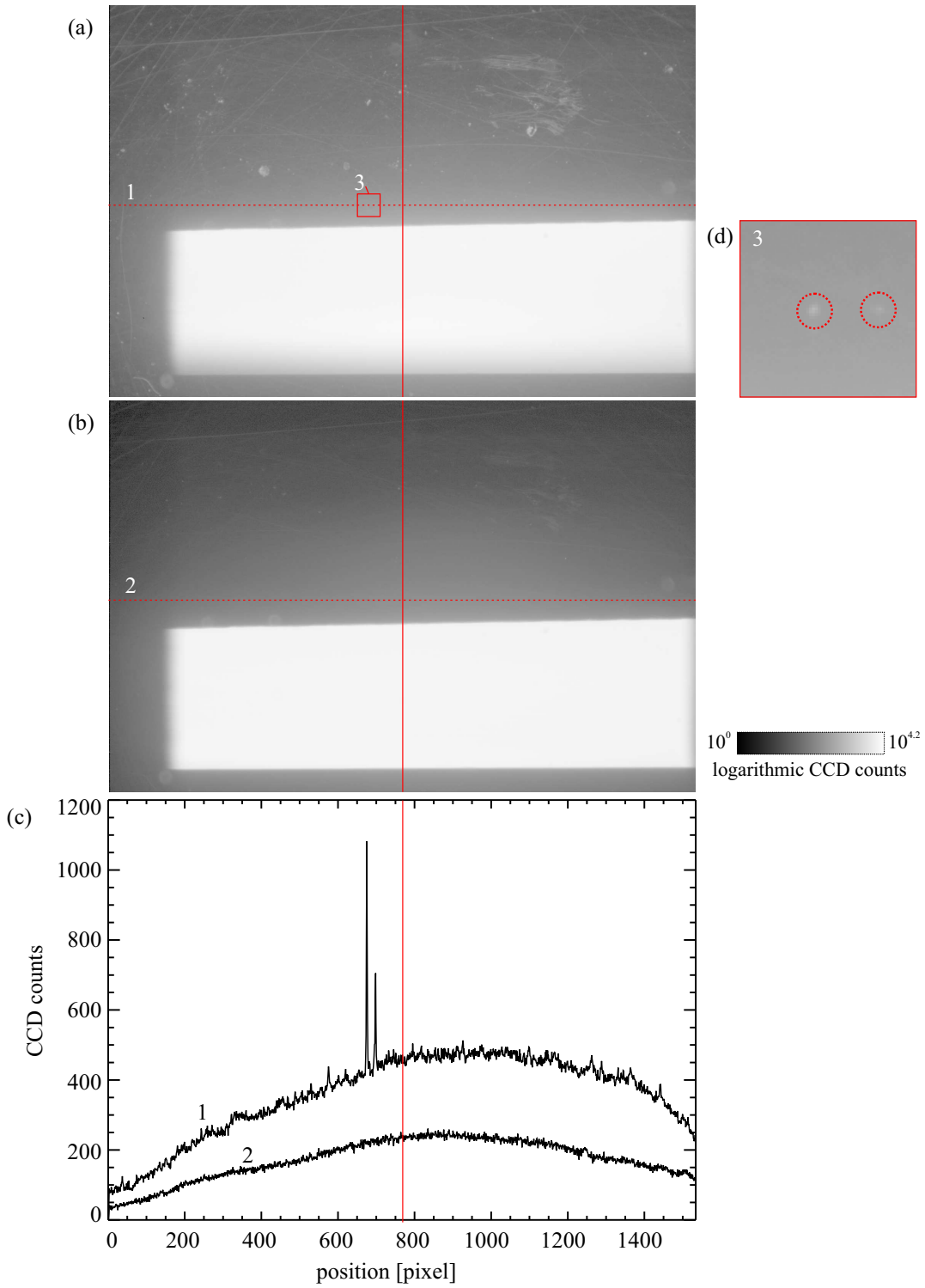

Figure 4.3: Edge profiles recorded with an absorbing gold edge for crystal CWO1 as (a) untreated crystal and (b) after application of the black backing. The images have been dark image corrected and are shown in logarithmic scale. The visible full CCD size corresponds to a field of view of 4.12×2.74 mm. (c) Plot of CCD counts along the dashed lines (1,2) in images (a) and (b). (d) Closeup of the marked region in (a), with two screen defects marked by circles. The two screen defects correspond to the intensity peaks in curve 1 of the plot in (c). The solid, vertical line in (a) to (c) marks the position of the center of rotation in the SRμCT scan presented in Section 6.2.

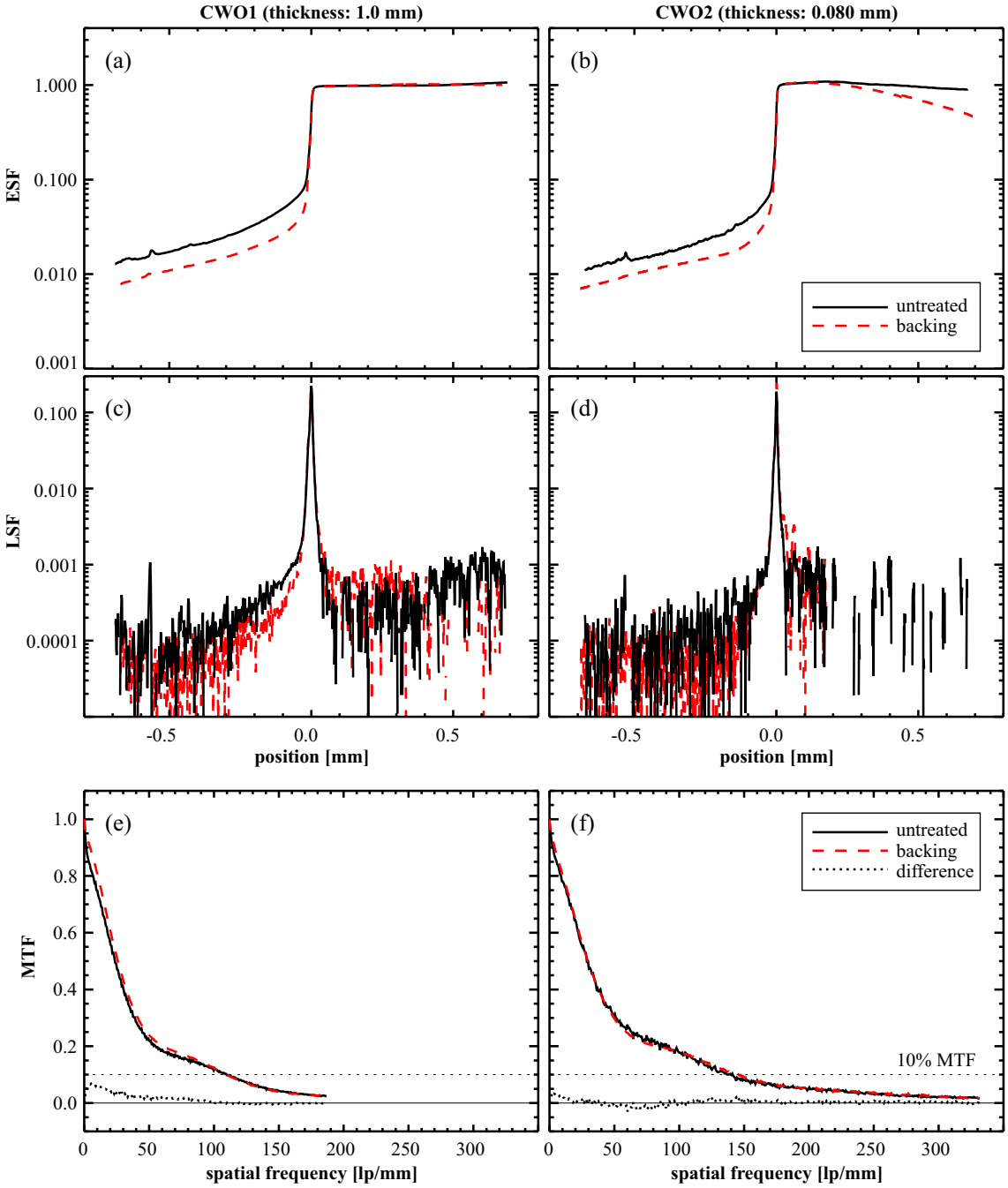

Figure 4.4: ESF, LSF, and MTF determined from the edge profile measurements performed on the two $CdWO_4$ crystals CWO1 and CWO2. Edge profiles were recorded both for the untreated crystal and after application of the backing layer. (a,b) ESF normalized to its maximum as described in the text; the intensity fall off at the right side of the dashed curve for crystal CWO2 is caused by an inhomogeneous beam profile. (c,d) LSF from derivation of the ESF. (e,f) MTF calculated from the symmetrically completed left hand side of the LSF. The difference of the MTF in the untreated case and with black backing is plotted (dotted line) and shows a small increase of the MTF at low frequencies. The MTFs of CWO1 and CWO2 end at the Nyquist frequency, which is different for the two crystals due to difference in the effective pixel size in the measurements.

Table 4.1: Resolution before and after application of the backing layer.

	CWO1[a]		CWO2[b]	
Resolution measure	untreated	backing	untreated	backing
10% MTF [μm]	4.61	4.64	3.66	3.51
FW of 50% int. LSF [μm]	9.99	9.00	7.31	6.35
FW of 90% int. LSF [μm]	168.86	48.72	95.97	41.33

[a]Cryst. th.: 1.0 mm, object. foc. length: 35 mm, f-number: 3.56, magn.: 3.36, x-ray energy: 22 keV
[b]Cryst. th.: 0.08 mm, objective foc. length: 35 mm, f-number: 3.56, magn.: 5.97, x-ray energy: 20 keV

Figure 4.4(c) shows the LSF, which was determined by derivation of the ESF. The same reduction as for the ESF is of course seen for the LSF too. The right hand side of the LSF is very noisy because of the higher photon noise on the bright side of the edge.

The MTF shown in Figure 4.4(e) was calculated from the symmetrically completed left hand side of the LSF as explained in Section D.1. The MTF does not change significantly at high frequencies. Only for low frequencies, the MTF is slightly increased. Again, the change of the MTF is small because the absolute change of the ESF is small.

Table 4.1 gives the spatial resolution that has been determined from the normalized edge profiles using different spatial resolution measures (introduced in Section 2.4.3). The high-frequency-dependent resolution measures corresponding to 10% MTF and the full width (FW) of 50% integrated LSF are only slightly reduced upon application of the backing, while the low frequency sensitive measure of the full width over 90% integrated LSF is drastically decreased. This demonstrates the limited usefulness of a single resolution parameter for the description of the entire system response. The drastic relative change of intensity in the long tails of the PSF is not noticed, if the system is described only by the resolution parameter a_{10}.

For crystal CWO2 very similar effects as for crystal CWO1 were observed. The ESF shown in Figure 4.4(b) displays a similar reduction of intensity in the tails. However, the beam profile in the edge-profile measurement with backing layer was not entirely homogeneous with a maximum of the intensity in the center of the image, which can be recognized as the intensity fall off at the right hand side of the ESF. This probably caused an additional reduction of intensity for the long-range components of the measured ESF.

4.2.3 Refractive index of lacquer paint

The refractive index of the lacquer paint was measured as a function of wavelength using photometric ellipsometry. In ellipsometry, the change in polarization of a light beam upon reflection on a sample is measured. For a detailed description of the method see the book by Azzam [5].

The measurement was carried out at the ‘Institut für Angewandte Physik’, University of Hamburg using a commercially available Sentech SE850 spectrally resolving ellipsometer. A thin film of lacquer paint was prepared for the measurement onto a flat glass substrate. The reflected inten-

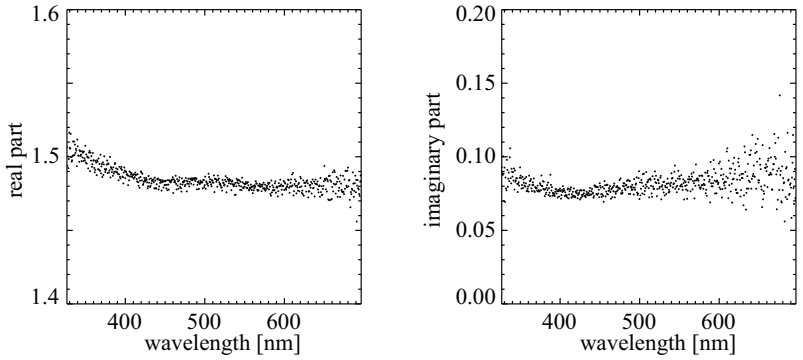

Figure 4.5: Refractive index of the applied lacquer paint. Real part (n) and imaginary part (κ) as function of wavelength were calculated from the photometric ellipsometry measurement.

sity from the lacquer paint was recorded as a function of wavelength at fixed polarizer orientations and fixed reflection angle. A xenon discharge lamp was used as light source and the reflected light was spectrally resolved by a grating spectrometer in combination with a photo diode array. From the measured intensity and assuming a homogeneous, isotropic, and compared with the penetration depth (infinitely) thick sample, the complex refractive index of the lacquer $\tilde{n} = n + j\kappa$ was calculated. Here, the imaginary part κ describes how fast the amplitude of the wave decreases and is called the extinction coefficient. It is directly related to the absorption coefficient given by $4\pi\kappa/\lambda$, where λ is the wavelength of light.

Figure 4.5 shows a plot of the determined refractive index as a function of wavelength. For the central spectral emission wavelength of $CdWO_4$ at 500 nm, the real and the imaginary part of the refractive index are approximately $n = 1.485$ and $\kappa = 0.085$, with only a slight variation with the wavelength over the $CdWO_4$ emission spectrum, which allows us to use these fixed values as an approximation over the full range of the luminescent screen emission spectrum.

4.2.4 Reflectivity and fraction of trapped light

The reflectivity and the transmittance at the crystal surfaces can be calculated from the law of refraction and the Fresnel equations (see Born & Wolf [25, Sect. 1.5]) from the complex refractive indices $\tilde{n}_1$ of the crystal and the complex refractive index $\tilde{n}_2$ of the second medium. Knowing the refractive indices of crystal and lacquer, we can now estimate and compare the fraction of totally reflected light for a crystal with and without absorbing backing.

Figure 4.6(a) shows plots of the reflectivity at the crystal-to-air surface and at the crystal-to-lacquer surface as a function of incident angle. Here, the incident angle is defined as the angle that the direction of incidence makes with the surface normal (see Figure 4.1). The complex refractive indices $\tilde{n}_1 = 2.2$ for the $CdWO_4$ crystal, $\tilde{n}_2 = 1.0$ for air, and $\tilde{n}_2 = 1.485 + j\,0.085$ for the lacquer paint as determined by ellipsometry, were used. The luminescent light was assumed to be unpolarized.[3] The reflectivity at the crystal-to-air surface becomes unity for incident angles of

[3]The assumption of unpolarized light is justified for the emitted luminescent light. However, note that the lumi-

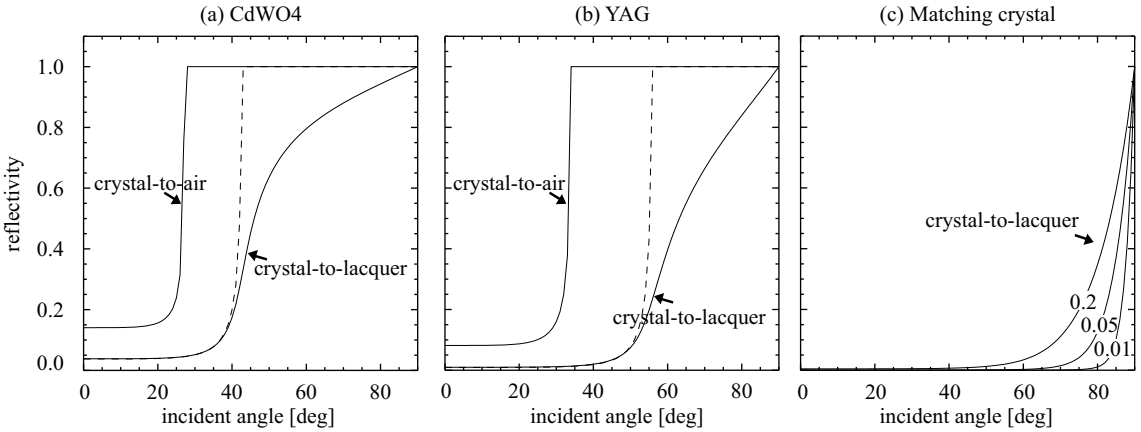

Figure 4.6: Reflectivity of unpolarized light at the internal crystal surface. (a) Calculation for first medium $CdWO_4$ with refractive index $\tilde{n}_1 = 2.2$ and for second media air with $\tilde{n}_2 = 1.0$ and lacquer paint with $\tilde{n}_2 = 1.485 + j\,0.085$. The dashed curve has been calculated neglecting the complex part in the refractive index of the lacquer paint, i.e., for $\tilde{n}_2 = 1.485$. In this case, total reflection appears above a certain angle. (b) Same calculation for first medium YAG with $\tilde{n}_1 = 1.8$. (c) Reflectivity at the crystal-to-lacquer surface of a crystal with assumed refractive index $\tilde{n}_1 = 1.485$ and matching lacquer paint with $\tilde{n}_2 = 1.485 + \kappa$ for assumed imaginary parts $\kappa = 0.01$, 0.05, and 0.2.

$\alpha_{tot} = 27^o$ and above. Here α_{tot} is the angle of total reflection, which is given by

$$\alpha_{tot} = \arcsin \frac{n_2}{n_1} \,, \tag{4.1}$$

in the case, when the refractive indices of both media are real numbers ($\tilde{n}_1 = n_1$ and $\tilde{n}_2 = n_2$), i.e., in the ideal case of zero absorption. All luminescent light emitted under an angle $\alpha > \alpha_{tot}$ is totally reflected at the internal crystal surfaces in this case.

The reflectivity at the crystal-to-lacquer surface [plotted in Figure 4.6(a)] is significantly lower than the reflectivity at the crystal-to-air surface for all incident angles α. This is the desired effect for the suppression of the long tails in the PSF. The lower reflectivity at the crystal-to-lacquer surface is of course due to the closer match of the refractive indices. Since the imaginary part of the refractive index of lacquer paint $\tilde{n}_2$ is not zero, the phenomenon of total reflection has disappeared here. Still the reflectivity is significantly different from zero, especially for high incident angles. When the light travels through the crystal, multiple reflection at the crystal-to-lacquer surface will take place, and more and more light will be absorbed. Thus, the intensity of the propagating light will decrease with increasing distance from its generation. The intensity decay with distance depends on the lateral distance that the light travels in between consecutive reflections, which in turn depends on the crystal thickness.

For an uncoated luminescent crystal, the reflectivity at both plan-parallel surfaces is described by the same crystal-to-air reflectivity curve. Thus, the totally reflected light is trapped inside the crystal. Assuming isotropic generation of luminescent light, the fraction of trapped light intensity

nescent light will be polarized upon reflection at the crystal surface as described by the polarization dependent Fresnel equations.

can be calculated from the total-reflection angle α_{tot} as

$$\epsilon_{trap} = \frac{\text{light emitted with } \alpha > \alpha_{tot}}{\text{total emitted light intensity}} = 1 - 2\,\frac{2\pi\,(1-\cos\alpha_{tot})}{4\pi} = \cos\alpha_{tot}\ . \tag{4.2}$$

For the crystal-to-lacquer surface, which does not show total reflection, the trapped light intensity cannot be calculated in the same way. However, we shall define an effective total reflection angle $\alpha'_{tot} = \arcsin[Re(\tilde{n}_2)/n_1]$, with $Re(\tilde{n}_2) = n_2$ the real part of the refractive index, neglecting its imaginary part. The reflectivity curve that is obtained neglecting the imaginary part of the refractive index is shown for $CdWO_4$ as the dashed curve in Figure 4.6(a) and gives an upper bound for the reflectivity. We then enter α'_{tot} into Equation (4.2) for the calculation of the effective fraction of trapped light ϵ'_{trap}.

For an uncoated $CdWO_4$ crystal it is $\alpha_{tot} = 27^o$ and we find that $\epsilon_{trap} = 89\%$ of the light is trapped inside the crystal. For the same crystal with black backing, we calculate $\alpha'_{tot} = 43^o$ and $\epsilon'_{trap} = 73\%$.

Other luminescent crystals often applied as luminescent screens are Ce-doped Lu_2SiO_5 and Ce-doped $Y_3Al_5O_{12}$ (YAG). Both crystals have refractive indices in the order of 1.8, which is closer to the refractive index of our lacquer paint than the refractive index of $CdWO_4$ discussed so far. Reflectivity curves for a crystal with $\tilde{n}_1 = 1.8$ were calculated and are plotted in Figure 4.6(b). For these crystals, we obtain $\alpha_{tot} = 34^o$ and $\epsilon_{trap} \approx 83\%$ for the uncoated crystal and $\alpha'_{tot} = 56^o$ and $\epsilon'_{trap} = 57\%$ for the crystal coated with lacquer paint. In both cases the trapped light intensity is significantly less than for our present crystal-lacquer combination.

Figure 4.6(c) demonstrates the reduction of reflectivity that would be possible, when the refractive indices of crystal and lacquer would match. Here refractive indices of $\tilde{n}_1 = 1.485$ for the crystal and of $\tilde{n}_2 = 1.485 + j\,\kappa$ for the lacquer paint were assumed. Variation of the extinction coefficient around its true value $\kappa = 0.085$ demonstrates the influence of the extinction coefficient. The lower the extinction coefficient, the lower the reflectivity. The reflectivity is of course much lower than for the equivalent curves of $CdWO_4$ and YAG in Figures 4.6(a) and (b), which demonstrates the high potential of lacquer and crystal with matching refractive indices.

4.3 Results and discussion

For our crystals with high refractive index ($n \approx 2.2$), a major fraction (89%) of the luminescent light is trapped inside the crystal by total reflection, when no coating is applied. Light inside the luminescent crystal can be reflected at the crystal surfaces, or it can be scattered at surface defects (screen inhomogeneities). It was found, that application of the black backing causes a relevant reduction of internal reflectivity and thus reduces the intensity in the long tails of the PSF. This relative reduction of intensity in the long tails is important in order to avoid non-linear effects, when calculating the projection images (compare Section 2.5.1).

Furthermore, the visibility of surface defects that may be present on the crystals is strongly reduced by the backing layer, i.e., scatter or reflection from these defects is significantly reduced. Since surface defects are the cause of screen inhomogeneities with non-linear response, their reduction will directly result in the reduction of ring artifacts in the tomographic reconstruction, as it will be shown in Chapter 6.2.

The visibility of surface defects in the radiographic images differs for the crystal's front and back surface. When the luminescent screen is homogeneously irradiated, defects on the surface that faces the incoming x-ray beam (back surface) are typically observed as an increase of light intensity, while defects on the front surface are observed as a local reduction of the light intensity. These latter defects are visible mostly for thin crystals, for which the front surface is close to the focal plane and, thus, still is in focus. For thick crystals they appear blurry [compare Figure 4.2(a)], which makes them less critical for the tomographic investigation. The backing layer suppresses the visibility of defects on the back surface, to which it is applied, but the blurry defects on the front surface remain. A way of reduction of the front surface defects is given by an increase of the crystal thickness, which brings the front surface out of focus. This approach is however limited by the spherical aberrations (see Appendix B.3) that are introduced by the additional crystal thickness.

The fraction of trapped light is reduced by application of the backing layer. However, the reduction of intensity in the tails must be seen relative to the overall intensity loss caused by the absorbing backing. Fortunately, the intensity (efficiency) loss that can be expected in the images by application of the backing compared with the previously uncoated crystals is small: Without backing, most of the light that is emitted into the opposite direction of the objective's aperture leaves the crystal and is lost for imaging. After application of the backing, this light is absorbed inside the backing layer. Hence, the signal intensity recorded with and without backing layer is similar. Any reduction of intensity in the long tails thus is purely beneficial for our measurements.

Other methods for the reduction of reflectivity might be thought of for the future. Application of an anti-reflective coating ($\lambda/4$ coating) to the crystal's front surface (that faces the objective) seems useful. However, the performance of the anti-reflective coating depends on the light's incidence angle (and wavelength). Thus, the anti-reflective coating is advantageous only for limited values of the numerical aperture. An immersion liquid in the space between crystal and objective could be used to suppress the reflectivity at the crystal-to-air surface and to increase the light collection efficiency of the system (see Appendix C.1) simultaneously. Unfortunately, the use of immersion liquids is difficult for practical reasons. One reason is the typical horizontal orientation of the setup in combination with gravity.

Ellipsometry was applied for the measurement of the refractive index of the backing layer. The refractive indices provided by this method in a simple and fast manner can be used as an input parameter for further system optimization, e.g., employing optical simulation software.[4] Different luminescent screens and backing combinations should now be tested. Higher absorption efficiency

[4]Optical simulation software as, e.g.: TracePro®, OSLO®, or ZEMAX®.

of the backing layer (lower reflectivity) might be achieved by a combination of luminescent crystal and absorbing substance with closely matching refractive indices. Other combinations of luminescent and backing materials should thus be exploited in a future study. It will probably be easier to find a matching coating substance for other luminescent materials than it is for $CdWO_4$ with its high refractive index of $n = 2.2$. For a future comparison of luminescent screens and backing combinations, the use of conventional x-ray tube systems should be considered. Although these systems provide x-rays with a broader energy spectrum than typically used at synchrotron radiation sources, they can provide a large and homogeneous beam profile more easily. Of course, also an optical light source can be used for fast comparison of the optical properties.

Note that entire suppression of long-range blur is not possible for the discussed type of lens-coupled x-ray detector, since it is fundamentally limited by the diffraction pattern of the lens aperture.

However, since the application of an absorbing backing layer presents a simple, cheap, and easy way of system enhancement, all crystals operated in our x-ray camera are being coated with lacquer paint before their first use now. Other methods that make use of the same type of x-ray camera, such as phase-contrast tomography or nano-tomography, can directly profit from the technology of the presented blur-reduced detector.

4.4 Summary

An absorbing backing layer was applied to the luminescent screen of the x-ray camera and characterized by the measurement of edge profiles. Apparently, use of an absorbing backing is reported here for the first time for an SRμCT setup. The application of the backing layer to the $CdWO_4$ luminescent screens resulted in the reduction of the internal light reflections. A reduction in intensity by about a factor of two was observed in the long tails of the edge spread function. Ellipsometry was used to measure the refractive index of the backing material, which in turn allowed to calculate the reflectivity at the crystal-to-lacquer surface and to estimate the trapped light intensity. Besides the reduction of tails, it was found that application of the backing layer is an excellent way for the suppression of screen inhomogeneities (that are the cause of ring artifacts in the tomographic reconstruction).

Chapter 5

Automated determination of the center of rotation

5.1 Introduction

For the tomographic reconstruction of the recorded projections, it is important to know the relative position of the rotation axis and the detector, i.e., the position of the center of rotation, precisely. Otherwise, artifacts arise in the tomographic reconstruction as will be shown below. Owing to the high spatial resolution of microtomography setups, it is difficult to measure the relative position. And even if it has been determined once, the position can be altered, when a new sample is mounted or setup parameters (e.g., camera magnification, luminescent screen, x-ray energy) are changed. It is, however, very inconvenient to spend valuable measurement time remeasuring the center of rotation. The tomographic projections are therefore often recorded without precise knowledge of the center of rotation, which has to be determined from the recorded projection data subsequently.

Mostly two methods are employed for the determination of the center of rotation from the projection data. One method is based on image registration of mirror projections and the other is based on the movement of the center of rotation in the projections. The precision reached by these two methods is limited and often results in unsatisfactory reconstructions. Therefore, it is common practice to calculate test reconstructions and to select the best reconstruction manually. This laborious procedure is unsatisfactory, especially at synchrotron radiation sources, where great numbers of data sets are recorded with short scan times.

In this work a new method for the determination of the center of rotation has been developed. The method has been published by Donath *et al.* [49], [50]. It allows for the automated determination of the center of rotation from the recorded projection data. For demonstration the method is applied to model systems (computer phantoms) and measured SRμCT data. The results are compared with the results obtained from the often used center-of-mass method and image registration based methods. The influence of measurement errors is discussed.

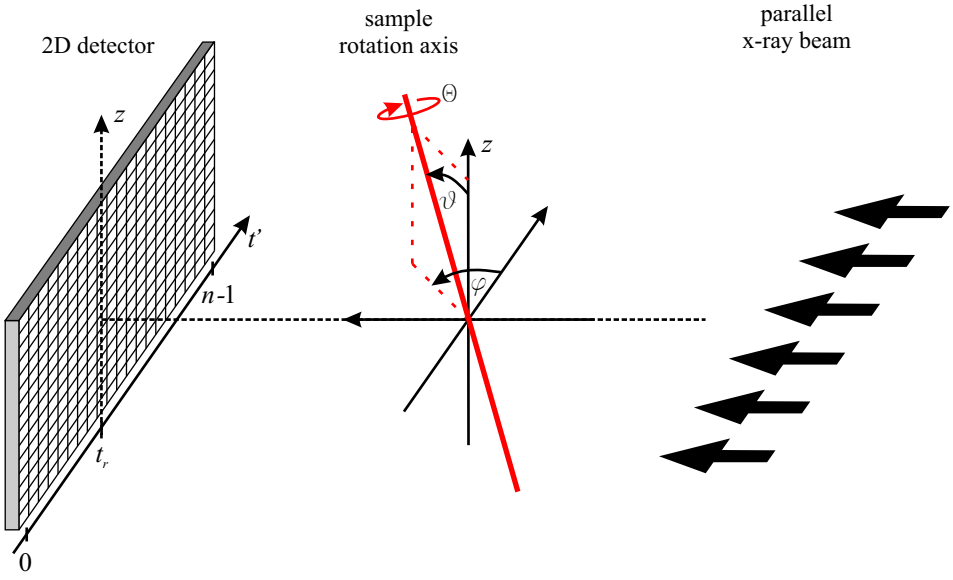

Figure 5.1: Scheme of the microtomography setup at a synchrotron radiation source with the parallel x-ray beam coming from the right. The rotation axis is aligned parallel to the z axis ($\vartheta \approx 0$) prior to the measurement, such that it is perpendicular to the incoming x-ray beam and perpendicular to the detector rows simultaneously. In this situation each detector row records the projection data of one tomographic slice. The position of the aligned rotation axis as it is projected onto the detector (dashed z axis) is uniquely described by the parameter t_r.

Note that the determination of the relative orientation of recorded projections is a problem that occurs in many types of tomography. In high-resolution measurements, this problem naturally exists due to the limited precision of the rotation axis. This is, e.g., the case in electron tomography (see Ziese *et al.* [166]) and in nano-tomography. In medical CT similar difficulties exist. Here patient motion needs to be handled and the active research field of dynamic CT imaging (see, e.g., Bonnet *et al.* [21]) actually aims at reconstructing image sequences of the moving human body as, e.g., heart motion. Compared to these tasks the problem we are confronted with in microtomography is relatively simple. We have to determine a single parameter only, the center of rotation. A wrong center of rotation, however, would result in a systematically wrong alignment of all projection images.

5.1.1 Alignment of the rotation axis

The microtomography setup at a synchrotron radiation source is shown schematically in Figure 5.1. The x-ray beam at a synchrotron radiation source can be assumed to be approximately parallel and thus the simple parallel-beam geometry is approximately realized as discussed in the previous chapter. The projection data are recorded by a two-dimensional x-ray detector. For the projection measurements the rotation axis must be aligned perpendicular to the incident beam direction. At the same time the rotation axis is usually aligned parallel to the detector columns. Then it is $\vartheta \approx 0$ in Figure 5.1 and the rotation axis is parallel to the z axis. After alignment, the angular

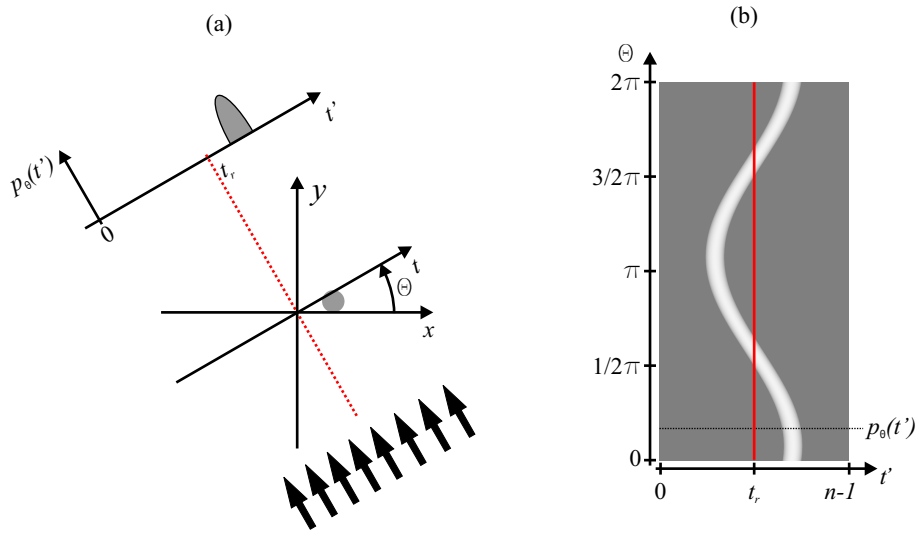

Figure 5.2: (a) Parallel projection of a slice $f(x, y)$ under projection angle θ. (b) The corresponding sinogram consists of all projections. The position of the projected center of rotation t_r corresponds to the vertical line in the sinogram.

orientation of the rotation axis is kept fixed. In this case the position of the projected rotation axis can be uniquely described by the parameter t_r in Figure 5.1. With this alignment the data recorded on a single detector row contain the full information for the reconstruction of the corresponding tomographic slice. The reconstruction of the (three-dimensional) volume data can be split into many reconstructions of parallel slices, which can be calculated using the techniques of (two-dimensional) parallel-beam tomography. Thus, the three-dimensional reconstruction is performed as a stack of two-dimensional reconstructions.

5.1.2 Effect of a wrong center of rotation

The projections in parallel-beam geometry of a two-dimensional function $f(x, y)$ are mathematically described by the Radon transform, which has been defined in Equation (3.3) as

$$p_\theta(t) = \iint f(x, y)\, \delta(x \cos\theta + y \sin\theta - t)\, dx\, dy\ . \tag{5.1}$$

Here $p_\theta(t)$ as a function of θ and t is the sinogram. According to this definition the center of the xy coordinate system is the center of rotation, which is projected by the Radon transform onto the position $t = 0$. The formation of the projection $p_\theta(t)$ is shown schematically in Figure 5.2. The detector coordinate $t' = t + t_r$ is introduced here, which is shifted with respect to t. The parameter t_r describes the position of the projected center of rotation on the detector axis. We will assume the center of rotation t_r to be unknown but fixed in all projections, i.e., independent of the projection angle θ. Then the projected center of rotation corresponds to the vertical line in the sinogram of Figure 5.2.

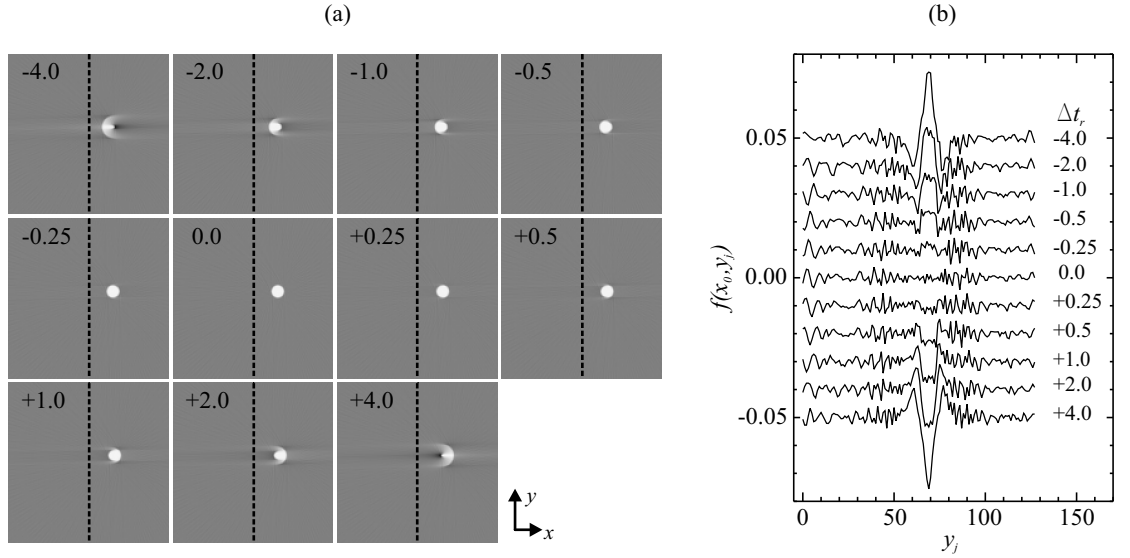

Figure 5.3: (a) Reconstructions from the sinogram data of Figure 5.2. The slices have been calculated on a 128×128 grid using centers of rotation $\tilde{t}_r = t_r + \Delta t_r$ with Δt_r in the range from -4.0 to +4.0. Tuning-fork artifacts become visible for $\Delta t_r \neq 0$. They add a systematic error to the noisy background of the reconstruction. (b) Profiles along the dashed lines in the reconstructions are plotted. The profiles have been shifted for better illustration. For comparison, the value of the ideal slice $f(x, y)$ is 0.2 inside the circle and elsewhere zero. Even offsets $|\Delta t_r|$ of only a fraction of a bin give rise to artifacts.

Figure 5.3 shows reconstructions of the model sinogram in Figure 5.2, which were calculated for different centers of rotation $\tilde{t}_r = t_r + \Delta t_r$. For increasing offsets $|\Delta t_r|$ artifacts appear in the reconstructions. Owing to their characteristic shape, they have been referred to as tuning-fork artifacts by Shepp *et al.* [137]. The profiles in Figure 5.3 show that these artifacts produce a systematic error even for offsets $|\Delta t_r| < 1$, i.e., for offsets of less than one detector bin.[1] (Note: t_r can be any real number and is not limited to points on the sampling grid). Precise knowledge of the t_r parameter is thus a necessity for a high quality reconstruction.

5.1.3 Methods for the determination of the center of rotation

Several methods for the determination of the center of rotation t_r from the projection data exist. In this work a procedure for the scoring of reconstructions is described and compared in its performance with the often used center-of-mass method and the image registration method. These three methods are described in detail below. Another method is based on the detection of the sinusoidal movement prescribed by a fiducial marker as, e.g., used by Lu and Mackie [100]. It is similar to the center-of-mass method and not considered here, since it can only be applied to data sets, which contain a strong marker of a previously known structure.

[1]The quality of reconstructions is sometimes quantified by the definition of a distance measure between the true slice and the reconstructed slices. E.g., Herman [76] uses the sum over the squared difference as distance measure. This is not possible here, since the change of $\tilde{t}_r$ shifts the position of the data, whereby the compared regions would not be identical. In other words: variation of the center of rotation prohibits the definition of a "real" image.

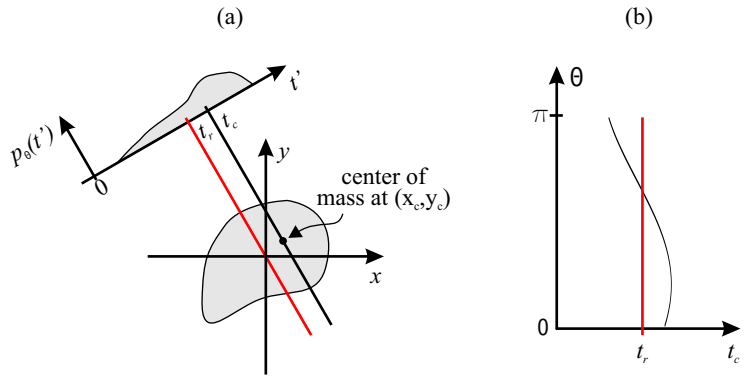

Figure 5.4: (a) The center-of-mass in the two-dimensional slice $f(x,y)$ is projected onto the center-of-mass t_c in the one-dimensional projection $p_\theta(t)$. (b) In the sinogram the center-of-mass t_c as a function of θ describes a sinusoidal movement. For the typical case of a sinogram recorded for projection angles θ over the interval $[0,\pi[$, this results in half a sinusoidal oscillation of the center-of-mass (x_c,y_c).

Center-of-mass method

The center of rotation t_r can be determined from the sinusoidal movement described by the center-of-mass (shown in Figure 5.4) around t_r in the sinogram [4], [77]. The movement of the center-of-mass can be derived directly from the definition of the Radon transform in Equation (5.1) as shown by Azevedo *et al.* [4]. Equivalently, it can be derived from the so called Helgason-Ludwig consistency condition [121], which puts certain constraints on the two lowest-order moments of a Radon transform $p_\theta(t)$ with respect to t.

The center-of-mass of the two-dimensional function $f(x,y)$ is the point (x_c,y_c), with

$$x_c = \frac{\iint f(x,y)\, x\, dx\, dy}{\iint f(x,y)\, dx\, dy} \quad \text{and} \quad y_c = \frac{\iint f(x,y)\, y\, dx\, dy}{\iint f(x,y)\, dx\, dy}\ . \tag{5.2}$$

Similarly, the center-of-mass in the projection is defined for the one-dimensional Radon transform as a function of the projection angle θ as

$$t_c(\theta) = \frac{\int p_\theta(t)\, t\, dt}{\int p_\theta(t)\, dt}\ . \tag{5.3}$$

The Radon transform projects the center-of-mass (x_c,y_c) in $f(x,y)$ onto the center-of-mass $t_c(\theta)$ in the projection according to

$$\begin{aligned} t_c(\theta) &= x_c \cos(\theta) + y_c \sin(\theta) + t_r & (5.4)\\ &= r_c \cos(\theta - \varphi_c) + t_r\ . & (5.5) \end{aligned}$$

In Equation (5.5) the polar coordinate representation (r_c,φ_c) of the two-dimensional center-of-mass (x_c,y_c) has been introduced. The above equations describe the sinusoidal movement of the

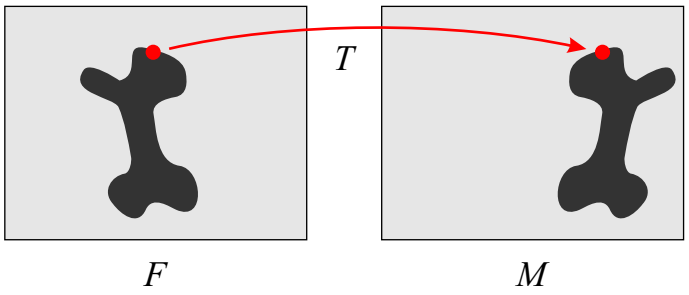

Figure 5.5: Schematic representation of image registration. We search for the spatial transform T that brings the moving image M into alignment with the fixed image F. In our case, F and M are mirror images and the position of the mirror axis must be found.

center-of-mass $t_c(\theta)$ around the position of the center of rotation t_r. They allow for the determination of t_r from the center-of-mass in the recorded projections.

For sinogram data recorded at discrete sampling points θ_i, t_j, we estimate the position of the center-of-mass in the projections by calculating

$$t_c(\theta_i) = \frac{1}{\overline{m}_0} \sum_j p_{\theta_i}(t_j)\ j \tag{5.6}$$

for each projection angle θ_i. Here j is the index of the detector bins and $\overline{m}_0$ [will be defined in Equation (5.14)] is the average mass of all recorded projections, which has to be different from zero. The three free parameters r_c, φ_c, and t_r of Equation (5.5) are found by an iterative non-linear least squares fit to the $t_c(\theta_i)$ values of Equation (5.6).

Image registration method

The image registration method determines the center of rotation by the alignment of projection data recorded at two opposing projection angles θ_1, θ_2, with $\theta_2 = \theta_1 + \pi$. Following from the definition of the Radon transform, the two projections are mirror images of each other, containing redundant information. In a tomography scan, typically projections are recorded at angular positions $\theta \in \{\theta_0, \theta_0 + \delta_\theta, ..., \theta_0 + \pi - \delta_\theta\}$, with equal spacing $\delta_\theta = \pi/N_\theta$, where N_θ is the number of projections. If additionally redundant projections are recorded, these can be used for registration. Since, e.g., the projections $p_0(t)$ and $p_\pi(t)$ are mirror images of each other, there exists a value of $\tilde{t}_r$ for which $p_0(t) = p_\pi(\tilde{t}_r - t)$. Here $\tilde{t}_r$ is the position of the mirror axis, and the two projections are perfectly aligned when $\tilde{t}_r = t_r$.

Aligning two similar images is known as image registration and is a well known tool in image processing [88], [104], [83]. Image registration is schematically represented in Figure 5.5. The basic input of any image registration process are two images: one is defined as the fixed image F and the other as the moving image M. Registration is treated as an optimization problem with the goal of finding the spatial transform T that will bring the moving image into alignment with the fixed image [83]. The main components for image registration are the transform T, the interpo-

lator, which is used to estimate the moving image intensity at non-grid positions, and a metric Q providing a measure of how well the fixed image is matched by the transformed moving image. The value of this metric is optimized by iterating the transform parameters.

In our case the fixed image F and the moving image M are given by the projections $p_0(t')$ and $p_\pi(t'')$, respectively. The projections can either be one-dimensional or two-dimensional, when recorded with a two-dimensional detector. In the latter case the projections become functions $p_\theta(t, z)$ of t and z. The spatial transform T that describes the mirror operation for the mirror axis at the position $\tilde{t}_r$ is simply given by

$$t'' = \tilde{t}_r - t'. \tag{5.7}$$

The estimate of the intensity in the moving image at the position t'' is found by linear interpolation. Data points on the fixed image which correspond to points outside the range of the moving image are set to zero. The cross correlation coefficient [88], also called the normalized correlation metric [83], of two images A, B

$$Q_{NC}(A, B) = -\frac{\sum_i (A_i B_i)}{\left[\left(\sum_i A_i^2\right)\left(\sum_i B_i^2\right)\right]^{\frac{1}{2}}} \tag{5.8}$$

is used as metric, returning values between -1 and $+1$. A minus sign was introduced into the definition, such that for maximum correlation, as in the case of $A = B$, the metric is minimized.

An optimum estimate for the center of rotation is found by minimization of the metric Q_{NC} with respect to $\tilde{t}_r$. The applied minimization procedure is presented in Section 5.3.

Scoring of reconstructions

Scoring of reconstructions is the approach taken in this work. Here the center of rotation is found by comparing reconstructions $\tilde{f}(x_i, y_j)$ calculated for different centers of rotation $\tilde{t}_r$ on a regular reconstruction grid x_i, y_j. The best approximation $\tilde{t}_r$ to the true center of rotation t_r will give the best reconstruction.

The scoring of the reconstructions is often done in a visual inspection step, in which a human scorer simply compares reconstructions, like the ones in Figure 5.3, and selects the reconstruction with, in his opinion, the fewest artifacts. This time-consuming visual inspection can be replaced by the use of image metrics. On the basis of the reconstructions $\tilde{f}$, a scalar metric $Q(\tilde{f})$ is calculated, which reflects the quality of the reconstruction. The best center of rotation is found by optimization of the metric value with respect to $\tilde{t}_r$. An optimization procedure is needed for the automated detection of the center of rotation.

Image metrics have been presented for the correction of motion artifacts in magnetic resonance imaging by Atkinson *et al.* [2] and by McGee *et al.* [103] and recently for the detection of the

center of rotation in microtomography data by Brunetti and de Carlo [28]. These publications studied the performance of several metrics empirically. The applicability of the metrics to the particular problem was not mathematically derived.

In the section below three image metrics are presented, and for two of them a mathematical derivation is presented. The iterative scoring procedure will the subject of Section 5.3.

Other attempts

Several methods for the determination of the center of rotation were developed and tested during this work. Besides the metric-based methods that are presented in the following, two more attempts were made that both are based on methods proposed for sinogram restoration. In the first method, the difference between the sinograms and their reprojected reconstructions was used for optimization. For this purpose a direct reconstruction-reprojection algorithm as proposed by Kim *et al.* [95] was implemented. The second method based on the 2D discrete Fourier transform of the sinogram. The method goes back to Edholm *et al.* [52], who described regions in the Fourier transform that should take values close to zero. It was tried to minimize the contribution to these areas with different weighted measures. Both methods did not successfully provide robust center-of-rotation estimates in all situations. Therefore, only the three reconstruction based metrics that give stable and precise results are presented here.

5.2 Image metrics

Three image metrics for the scoring of reconstructions (see above) have been developed in this work. These simple image metrics are based on the integral of the absolute value Q_{IA}, the integral of the negativity Q_{IN}, and the histogram entropy Q_H (extending the histogram entropy definition used by McGee *et al.* [103]) of a reconstruction $\tilde{f}$. Minimization of any of these metrics with respect to $\tilde{t}_r$ should result in an optimized reconstruction that best approximates the original slice f. For the metrics Q_{IA} and Q_{IN}, it is shown below that they are at minimum for the correct estimate of the center of rotation $\tilde{t}_r = t_r$, as desired. The application of Q_{IA} and Q_{IN} is limited to positive functions, i.e., to cases where $f(x,y) \geq 0$. The entropy-based metric Q_H does not have this restriction and can thus be applied in cases where negative attenuation coefficients are present in $f(x,y)$. (This situation can occur for tomography data of samples recorded in a surrounding medium as, e.g., water). We will present plausibility arguments why the metric Q_H should be at minimum for $\tilde{t}_r = t_r$. A mathematical proof as it is presented for the metrics Q_{IA} and Q_{IN} cannot be given, but Q_H will be shown to perform correctly when applied to model systems and real data in Section 5.4.

5.2.1 Metric Q_{IA}: Integral of absolute value

We define the metric

$$Q_{IA}(\tilde{f}) = \frac{1}{m_0} \iint \left| \tilde{f}(x,y) \right| \, dx\, dy \,, \tag{5.9}$$

with the zero-order moment

$$m_0 = \iint f(x,y)\, dx\, dy = \int p_\theta(t)\, dt \,. \tag{5.10}$$

Here $\tilde{f}$ is the reconstruction calculated for a certain center of rotation $\tilde{t}_r = t_r + \Delta t$ from projections of a positive function f, i.e., a function for which $f(x,y) \geq 0$. The integration is over the full xy plane.

Recognizing that the 0th-order moment of $\tilde{f}$ is given by $\iint \tilde{f}(x,y)\, dx\, dy = \iint f(x,y)\, dx\, dy = m_0$ and with $f(x,y) \geq 0$, it directly follows that

$$\iint |f(x,y)| \, dx\, dy = \left| \iint f(x,y)\, dx\, dy \right| = \left| \iint \tilde{f}(x,y)\, dx\, dy \right| \leq \iint \left| \tilde{f}(x,y) \right| \, dx\, dy \,. \tag{5.11}$$

Division by m_0 gives

$$Q_{IA}(f) \leq Q_{IA}(\tilde{f}) \,. \tag{5.12}$$

The above inequality expresses the fact that the metric Q_{IA} will be at minimum for the reconstruction $\tilde{f} = f$ calculated for the correct center of rotation $\tilde{t}_r = t_r$.

For a reconstruction $\tilde{f}(x_i, y_j)$ performed on a discrete reconstruction grid (x_i, y_j), the metric Q_{IA} in Equation (5.9) is numerically calculated as

$$Q_{IA}(\tilde{f}) = \frac{1}{\overline{m}_0} \sum_{i,j} \left| \tilde{f}(x_i, y_j) \right| \,, \tag{5.13}$$

$$\overline{m}_0 = \mathrm{Mean}_i \left(\sum_j p_{\theta_i}(t_j) \right), \,, \tag{5.14}$$

where $\mathrm{Mean}_i()$ is the mean with respect to the index i and $\overline{m}_0$ is the average mass of all projections in the sinogram.

5.2.2 Metric Q_{IN}: Integral of negativity

We use the definition of negativity as known in digital image processing (see, e.g., Jansson [90]) for the definition of the metric

$$Q_{IN}(\tilde{f}) = -\frac{1}{m_0} \iint u\left[-\tilde{f}(x,y) \right] \, \tilde{f}(x,y) \, dx\, dy \,, \tag{5.15}$$

with

$$u(\alpha) = \begin{cases} 1 & \text{for } \alpha \geq 0 \\ 0 & \text{else} \end{cases} . \tag{5.16}$$

Here m_0 is the total mass given in Equation (5.10) and $u(\alpha)$ is the Heaviside step function.

Again, we assume f to be a positive function with $f(x,y) \geq 0$. Then it is $Q_{IN}(f) = 0$, and therefore

$$Q_{IN}(f) \leq Q_{IN}(\tilde{f}). \tag{5.17}$$

The metric Q_{IN} will take on its global minimum value for the reconstruction $\tilde{f} = f$ calculated for the correct center of rotation $\tilde{t}_r = t_r$.

The numerical calculation of Q_{IN} in Equation (5.15) for a reconstruction $\tilde{f}(x_i, y_j)$ performed on a discrete reconstruction grid (x_i, y_j) is done by the summation

$$Q_{IN}(\tilde{f}) = -\frac{1}{\overline{m}_0} \sum_{i,j} u\left[-\tilde{f}(x_i, y_j)\right] \; \tilde{f}(x_i, y_j) \; , \tag{5.18}$$

wherein $\overline{m}_0$ is the average mass of all projections in the sinogram given in Equation (5.14).

5.2.3 Metric Q_H: Histogram entropy

We can assume that the reconstruction $f(x_i, y_j)$ partly consists of homogeneous regions. This assumption is valid because at least the outer regions of the reconstruction form an area of value zero. Also, the object under investigation typically shows characteristic peaks in the density histogram of $f(x_i, y_j)$. A wrong value of $\tilde{t}_r$ will lead to additional structures and gradients in the reconstruction and smear out the histogram of $f(x_i, y_j)$. We therefore use as a measure of reconstruction quality the histogram entropy of the reconstructed image as it is known in image processing.

The histogram entropy or image entropy, as known in image processing [89], originates from the basics of information theory developed by Shannon [136] and can be applied to the histogram of any image, giving a measure of the amount of information in the image. It is defined for a discrete gray-level image as

$$H_{discrete} = -\sum_{k=1}^{G} p_k \log_2(p_k) \; , \tag{5.19}$$

where the probability histogram p_k gives the fraction of pixels containing the gray value g_k and G is the number of discrete gray-value levels. Continuous gray-value images, as the reconstructions, have to be converted to discrete gray levels before the entropy in Equation (5.19) can be calculated. This conversion to discrete values causes a non-continuous behavior of the entropy.

The non-continuous behavior of the histogram can be removed by application of a kernel density estimator (also known as the Parzen window). The discrete distribution p_k of gray values

is replaced by an estimated probability density function $p(g)$ of a continuous variable of gray values g:

$$p(g) = \frac{1}{hN} \sum_{i=1}^{N} K\left(\frac{g - g_i}{h}\right) , \tag{5.20}$$

with

$$K(u) = \begin{cases} 1 & \text{for } |u| < 1/2 \\ 0 & \text{else} \end{cases} . \tag{5.21}$$

Here g_i are the gray values of individual image pixels $i \in \{1, 2, ..., N\}$ and N is the number of pixels. Thus $p(g)$ is a sum of kernel functions $K(u)$ centered around the gray values g_i of the image. The kernel function used here is a rectangular (box car) function of width h.

We now define the entropy based on the continuous distribution $p(g)$ as

$$H = -\int p(g) \log_2[h\, p(g)]\, dg \tag{5.22}$$

$$= -\sum_{j=1}^{2N-1} p_j \log_2(h\, p_j)\, \Delta g_j . \tag{5.23}$$

The integral could be split into a sum over constant intervals in Equation (5.23) because $p(g)$ is only changing at the points $g_i - 1/2$ or $g_i + 1/2$. Labeling the intervals by the index j, we perform the sum over intervals of length Δg_j with constant $p(g) = p_j$. The number of intervals, including zero length intervals, is $2N - 1$. Note that H has a continuous behavior compared to the histogram entropy definition in Equation (5.19) for discrete bins.

The maximum entropy H_{max} is reached when the contribution of each element is independent of the other. In this case the box car functions are not overlapping, and Equation (5.23) becomes a sum over N equal constant functions of height $p_j = \frac{1}{hN}$ and width $\Delta g_j = h$, resulting in $H_{max} = \log_2(N)$.

We can now define the entropy normalized by H_{max} as our metric

$$Q_H(\tilde{f}) = \frac{H}{H_{max}} , \tag{5.24}$$

which can take values in the range from 0 to 1. The metric Q_H is minimized with respect to $\tilde{t}_r$ to obtain the best reconstruction $\tilde{f}$.

For the numerical calculation of H in Equation (5.23) we set $p_j = \frac{n_j}{hN}$, with n_j as the number of overlapping box car functions that contribute to the j-th interval:

$$H = -\sum_{j=1}^{2N-1} \frac{n_j}{hN} \log_2\left(\frac{n_j}{N}\right) \Delta g_j \tag{5.25}$$

$$= -\frac{1}{hN} \sum_{j=1}^{2N-1} n_j \left[\log_2(n_j) - \log_2(N)\right] \Delta g_j . \tag{5.26}$$

The j-indexed intervals are found by application of a sorting algorithm to the N gray values g_i. Note that the resolution parameter h not only contributes a constant factor but also determines the form of the intervals in the sum. For the calculation of Q_H it is necessary to define a resolution parameter h, which should roughly describe the density resolution of the reconstruction. In practice the density resolution will be strongly noise dependent. Since h is not a critical parameter, we simply chose h as the 1% fraction of an average attenuation coefficient estimate of the sinogram $p_{\theta_i}(t_j)$ as

$$h = 0.01 \frac{1}{N_t} \sum_{i,j} \left| p_{\theta_i}(t_j) \right| , \tag{5.27}$$

where N_t is the number of projection bins t_j.

5.3 Iterative scoring procedure

5.3.1 Reconstruction algorithm

The numerical calculation of the image metrics is based on the reconstructions $\tilde{f}(x_i, y_j)$, which were calculated in the following using the "BKFIL"-type reconstruction algorithm presented in Section 3.2. No frequency filter other than the ideal ramp was applied in the reconstruction.

The application of the image metrics should in principle be independent of the use of any particular reconstruction algorithm. In practice, the image metrics are influenced by the parameters of the reconstruction algorithm, especially by the selection of the reconstruction grid. For the data presented here, the edge length of the quadratic reconstruction grid is chosen such that the full width of the recorded sinogram fits into a centered circle on this grid for all values of $\tilde{t}_r$ that are compared. This requires the adequate continuation of the sinogram data by filling it up with zeros (zero padding) in the t direction to fully cover the reconstruction grid with sinogram data. The center of rotation is placed in the center of the reconstruction grid. The spatial resolution of the reconstruction grid is chosen to be equal to the spatial resolution of the sinogram data.

It should be noted that, for the calculation of the metrics Q_{IA} and Q_{IN}, in principle the integral over an infinite and continuous reconstruction grid has to be performed. In the numerical implementation of the metrics, this integration is calculated on a finite and discrete reconstruction grid. The study of model systems in Section 5.4 will show that this approximation is sufficient.

5.3.2 Noise suppression

The finite reconstruction grid can cause periodic oscillations of the metrics as a function of $\tilde{t}_r$. To suppress this effect, which occurs for noisy data sets, two approaches are taken. The sinograms are averaged over a couple of slices, and they are convoluted with a Gaussian filter function. Averaging is performed over $n_{av} = 20$ adjacent sinograms for the tomography data presented in Section 5.4. Since the position of the center of rotation in the projections is fixed and due to the linearity

of the Radon transform, the reconstruction of the projection average is equal to the average of the individual reconstructions. A significant reduction of the noise level in the reconstruction can thereby be reached. Convoluting the sinograms with a digital Gaussian filter with a sigma value of $\sigma = 1$ and normalized to unity further reduces the noise. The convolution of the projections is performed for each projection angle using a one-dimensional Gaussian filter. Gaussian filtering of the projections is equivalent to the convolution of $f(x, y)$ with a two-dimensional Gaussian function of the same sigma value. The Gauss convoluted projections result in reconstructions of reduced sharpness and reduced noise level. The consistency of the projection data is not influenced by the averaging of sinograms nor by the Gaussian filtering.

The drawback of sinogram averaging and Gaussian filtering is that structures smaller than the number of averaged sinograms n_{av} or the sigma parameter of the convolution σ are suppressed. A gain in performance can be expected as long as n_{av} and σ are small compared with the structure sizes in the reconstruction.

5.3.3 Iterative optimization

The optimum position of the center of rotation is found by minimization of any of the metrics Q_{NC}, Q_{IA}, Q_{IN}, and Q_H with respect to the center of rotation $\tilde{t}_r$ used in the reconstruction. Let $Q(\tilde{t}_r)$ be the metric value, which has been calculated for the center of rotation $\tilde{t}_r$.[2] The absolute minimum of the metric $Q(\tilde{t}_r)$ has to be found. This is complicated by the fact that the metrics $Q(\tilde{t}_r)$ may exhibit local minima in addition to the global minimum that is being searched for. One could calculate $Q(\tilde{t}_r)$ for a wide range of $\tilde{t}_r$ values at high resolution to determine the global minimum. This is, however, computationally expensive and not a practical approach. We therefore make use of an iterative multi-resolution minimum search, which reduces the number of required calculations and stabilizes the convergence towards the optimum value of $\tilde{t}_r$.

A demonstration of the steps of the iterative scoring procedure is presented as Appendix F. The iterative optimization is performed as follows: The sinogram resolution is reduced by reducing the size of the sinogram in the direction of t, keeping its original size in θ. The reduction factor (binning factor) is $b = 2^k$, with $k \geq 1$ as an integer number. In each iteration the minimum of $Q(\tilde{t}_r)$ is found at a resolution of $\delta_t = b$ and used as the center value t_r^0 for the next iteration step. The metric $Q(\tilde{t}_r)$ is being calculated at the five positions $\tilde{t}_r \in \{t_r^0 - 2\delta_t, t_r^0 - \delta_t, t_r^0, t_r^0 + \delta_t, t_r^0 + 2\delta_t\}$. When the resolution $\delta_t = 1$ is reached, the procedure continues reducing the resolution in t_r to $\delta_t = 2^k$, with $k < 1$ an integer value, but keeping the reduction factor $b = 1$, i.e., using the sinogram in its original size.

The multi-resolution approach has several advantages: 1. The global minimum can be found from a reduced number of reconstructions. 2. The risk of converging towards a local minimum,

[2] Note that the metrics Q_{IA}, Q_{IN}, and Q_H are calculated from the reconstructions $\tilde{f}(x_i, y_j)$, while the metric Q_{NC} is calculated from mirror projections using $\tilde{t}_r$ as the position of the mirror axis.

Table 5.1: Definition of the model systems from ellipses[1].

Model system	(x_0, y_0)	A	B	α	μ	g
A: Circle	$(0.4, 0.1)$	0.1	0.1	0.0	10.0	0.0
B: Gradient ellipse	$(0.0, 0.0)$	0.8	0.45	10.0	1.25	0.5
C: Multicircle	300 positions	0.02	0.02	0.0	5.0	0.0
D: Circle plus/minus	$(0.8, 0.0)/(0.3, 0.1)$	0.1	0.1	0.0	10.0/-10.0	0.0

[1]Position (x_0, y_0) and lengthes A, B are given in relative units, the angle α is given in degree.

which is not a global minimum, is reduced. 3. The reduction of the sinograms results in consistent sinograms of highly reduced noise level and thereby stabilizes the procedure. 4. The reconstructions can be performed much faster for the sinograms of reduced size.

5.4 Application and comparison of methods

5.4.1 Application to model systems

The capability of the methods described above for detecting the center of rotation was studied using the projection data of model systems (phantoms) with *a priori* known center of rotation.

The four model systems (defined in Table 5.1) are constructed of ellipses for which the sinogram can be calculated directly as described in Appendix E. The ellipses are fully described by their center point (x_0, y_0), the axis parameters A, B, the rotation angle α, and the attenuation coefficient μ inside the ellipse. In this work the ellipse definition given by Kak and Slaney [93] was extended to allow for a gradient on the ellipse. The calculation of the projection data for the ellipse with gradient is presented as Appendix E. The gradient is specified by the parameter g, such that the attenuation changes linearly from $(1 - g)\mu$ to $(1 + g)\mu$ along the axis described by the axis parameter A. This allows for the creation of model systems containing a continuous range of attenuation coefficients.

The sinograms of the model systems and their optimum reconstructions are shown in Figure 5.6. The sinograms have been calculated for 111 projection bins and 100 angular positions, with the center of rotation located at $t_r = 50$. The center of rotation does not correspond to the center of the projection (here at $t = 55$), which represents a realistic measurement condition. The size of the objects in the sinograms used here is given by multiplying the value in relative units by 50. The attenuation coefficient per pixel in the reconstruction is obtained by dividing the value in Table 5.1 by 50.

The metrics Q_{IA}, Q_{IN}, and Q_H were calculated for the model systems for centers of rotation $\tilde{t}_r$ with resolution of 0.1 bin in the interval $[t_r - 3, t_r + 3]$. The results are plotted in Figure 5.7. All three metrics exhibit a global minimum at the true center of rotation, as it is desired in the case of ideal sinogram data. Applying the iterative optimization described in Section 5.3, we have determined the center of rotation further down to 0.01 bin resolution for the three metrics and for

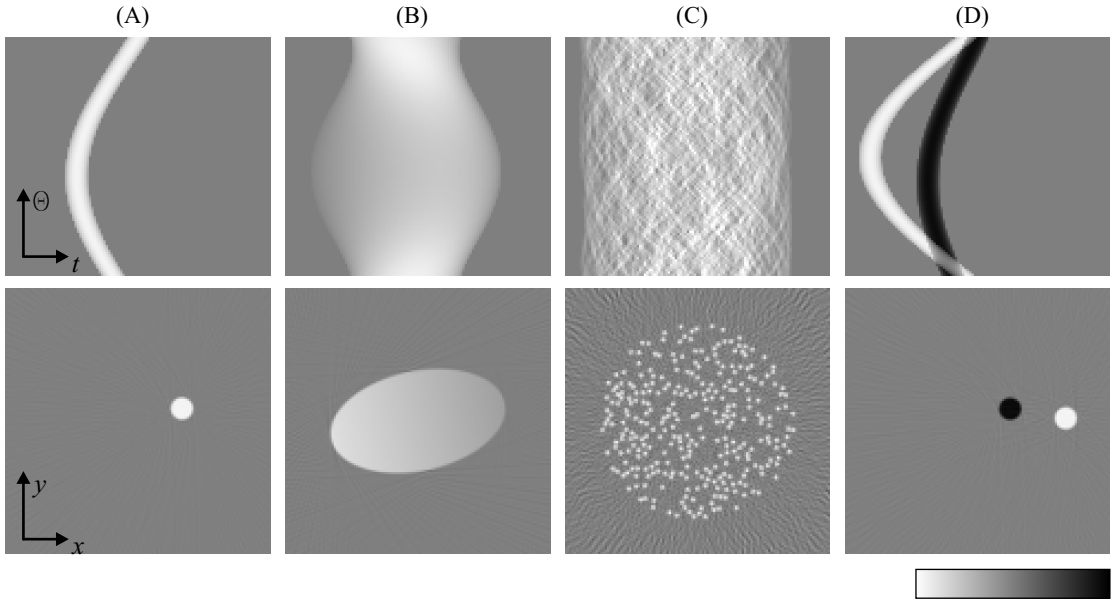

Figure 5.6: Sinograms $p_{\theta_i}(t_j)$ of the four model systems defined in Table 5.1 (*top*) and their reconstructions (*bottom*). Model system: (A) circle, (B) ellipse with gradient, (C) small circles, and (D) two circles of opposite attenuation coefficient. The sinograms have been calculated for 111 projection bins t_j and 100 projection angles θ_i, equally stepped over the interval $[0, \pi[$. The color scale shows the attenuation in the sinogram linearly ranging from -2.2 to +2.2. The reconstructions have been calculated on a 120×120 grid. The color scale in the reconstructions has been adapted to the individual systems. In the sinograms, the center of rotation is located five pixels to the left of the sinogram center. In the reconstructions, the center of rotation corresponds to the center of the reconstruction.

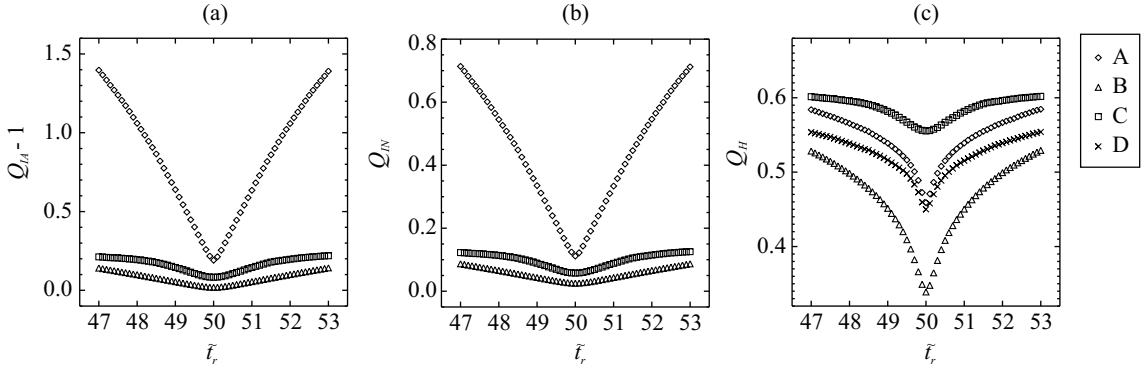

Figure 5.7: Value of the image metrics plotted as a function of the center of rotation $\tilde{t}_r$ for the model systems A, B, C, and D. It is plotted: (a) $Q_{IA} - 1$, (b) Q_{IN}, and (c) Q_H. The calculation was performed at 0.1 bin resolution around the true center of rotation at $t_r = 50.00$. For model system D, which contains negative attenuation values, only the metric Q_H is defined. In all cases a clear minimum is found at the true center of rotation.

Table 5.2: Optimum value of $\tilde{t}_r$ as determined by the different methods for the model systems.[a]

			Image metric[b]		
Model system	Center-of-mass	Registration[b]	H	IN	IA
A	49.90	50.00	50.00	50.00	50.00
B	50.01	50.00	50.00	50.00	50.00
C	49.98	50.00	49.97	50.01	50.00
D[c]	–[d]	50.00	50.01	–	–
A + noise	48.57	50.12	50.05	50.04	50.03
B + noise	49.71	50.23	50.00	50.03	50.01
C + noise	49.76	49.97	49.98	50.01	49.99
D + noise[c]	–	49.95	49.98	–	–
A + gradient	60.95	50.00	50.01	50.01	50.00
B + gradient	52.54	49.92	49.97	49.98	49.98
C + gradient	51.89	50.00	49.98	50.01	50.00
D + gradient[c]	–	50.00	50.00	–	–

[a] The true center of rotation is at $t_r = 50.00$.

[b] Using the iterative optimization procedure down to resolution $\delta_t = 0.01$ bin.

[c] Model system with total mass $m_0 = 0$ and containing negative attenuation values.

[d] –Indicates method is undefined for this model system.

the image registration method. The determined t_r values are shown in the upper part of Table 5.2 together with the values obtained by the center-of-mass method. No results are given for model system D and the methods based on image metrics Q_{IA} and Q_{IN}, since these metrics have been defined for positive functions $f(x,y) > 0$ only. For the ideal sinogram data, all methods return good t_r estimates. The largest deviation from the center of rotation of 0.1 bin is found for the center-of-mass method for system A. Image registration and the presented image-metric-based methods return the result with a maximum deviation of 0.03 bin, which is found for the histogram entropy based metric Q_H.

Recorded tomographic projections contain noise (compare Sections 2.5.2 and 3.3.2). Additionally, modulations can be present on the recorded projections, which are caused by a change of the beam profile during the measurement. The influence of these two measurement errors on the determination of the center of rotation is demonstrated by adding simulated error projections to the ideal projection data:

1. *Noise* of Gaussian distribution with standard deviation of $\sigma_p = 0.1$. For comparsion, the maximum projected attenuation coefficient is $p = 2$ in the sinograms.[3]

[3] The noise level $\sigma_p = 0.1$ of the sinogram with sampling $N_t = 111$ and $N_\theta = 100$ causes the same noise level in the reconstruction as it would be obtained for our standard reconstruction with sampling parameters $N_t = 1536$ and $N_\theta = 720$ for a noise level of $\sigma_p = 0.0175$ [according to Equation (3.33)]. The latter value of σ_p corresponds (without averaging of sinograms) to an average photon count of $\langle N \rangle = 1/\sigma_p^2 \approx 3\,000$ in the projection images, which is lower than in our typical measurements. Thus, the assumed noise level $\sigma_p = 0.1$ for the small sinograms is a realistic value for judging the influence of noise when the metrics are applied to single slices of measured data.

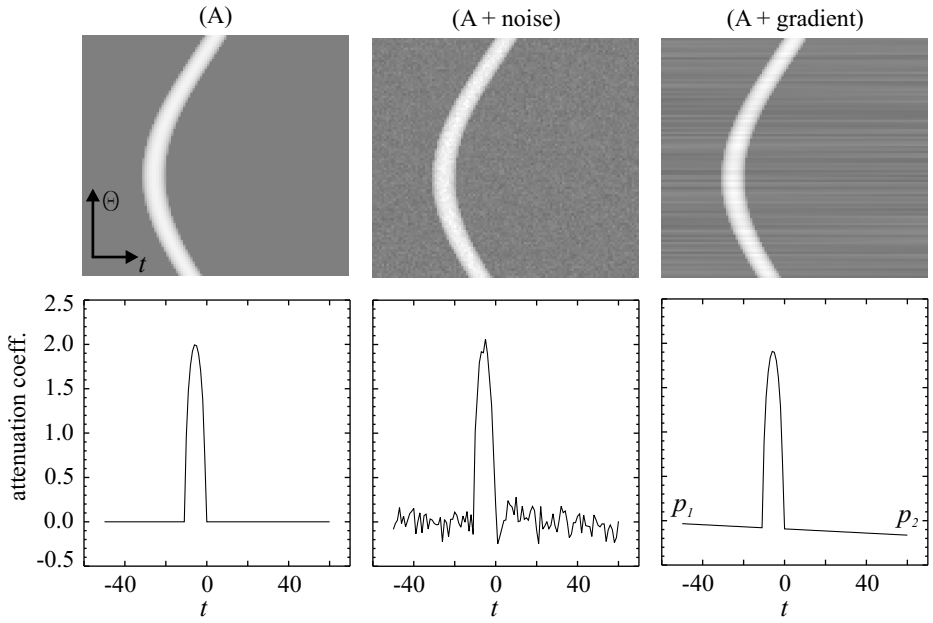

Figure 5.8: Ideal sinogram of sample system A in Figure 5.6 and the same sinogram corrupted by noise and random gradients (*top*). The bottom line of the sinograms is plotted (*bottom*).

2. *Random gradients* for parameters p_1, p_2 randomly chosen for each angular projection between -0.2 and 0.2, varying linearly from p_1 to p_2 over the 111 projection bins (as shown in Figure 5.8).

Figure 5.8 shows the ideal and the corrupted projections of model system A.

The iterative optimization has again been used to determine the center of rotation down to 0.01 bin resolution as before. The results are shown in Table 5.2 together with the values obtained by the other methods.

The t_r estimates become significantly worse for the data with noise. The center-of-mass method returns a t_r estimate that deviates by more than 1.4 bins for system A+noise and by more than 0.2 bin for systems B+noise and C+noise. Image registration shows the largest deviation of 0.23 bin for system B+noise, which contains only little high frequency components in the projections and is, therefore, difficult to align by image registration. The maximum deviation found for the presented image-metric-based methods is 0.05 bin for the projections with noise. Achievable resolution of this order was recently was confirmed recently and published by Donath *et al.* [50].

The projections with random gradients cause drastic deviations of the t_r estimates obtained by the center-of-mass method. This is due to the systematic error introduced by the gradient. Image registration shows a deviation only for projection B. However, it must be expected that the results obtained by image registration strongly depend on the particular form of the random gradients, since the method uses the data of only two projection angles. The presented image metric-based-methods return results of only 0.03 bin deviation at maximum.

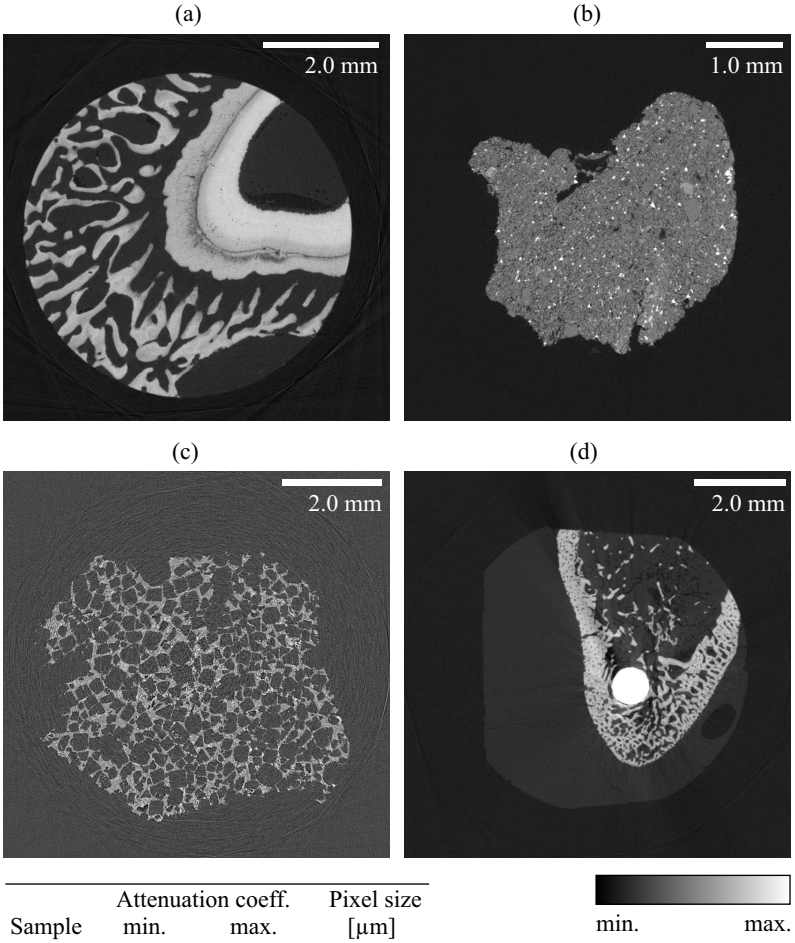

Sample	Attenuation coeff. min.	Attenuation coeff. max.	Pixel size [µm]
a	-0.0003	0.0027	4.255
b	-0.0005	0.0040	3.214
c	-0.0002	0.0005	5.084
d	-0.0005	0.0035	5.491

Figure 5.9: Reconstruction of sinograms recorded at HASYLAB beamlines BW2 and W2 with projection width of 1536 bins at 720 projection angles at HASYLAB beamlines BW2 and W2. (a) Root-bone interface of a monkey tooth (canine) [35], (b) soil aggregate [118], (c) polymer foam [46], (d) bone sample with titanium implant [19]. The samples in (c) and (d) have been recorded under non-optimum conditions, i.e., under low x-ray absorption in (c) and with strong absorption caused by the implant in (d). The minimum and maximum attenuation coefficient per edge length of a pixel and the edge length of a pixel are given in the table.

5.4.2 Application to tomography data

The performance of the different methods is compared here for the sinograms of four representative samples. The data were measured at the synchrotron radiation laboratory HASYLAB at the Deutsches Elektronen-Synchrotron DESY at beamlines W2 and BW2. With the microtomography setup projections of 1536 bins width were recorded at 721 angular positions using the 1536×1024 pixel CCD detector. Reconstructed slices of the data are shown in Figure 5.9.

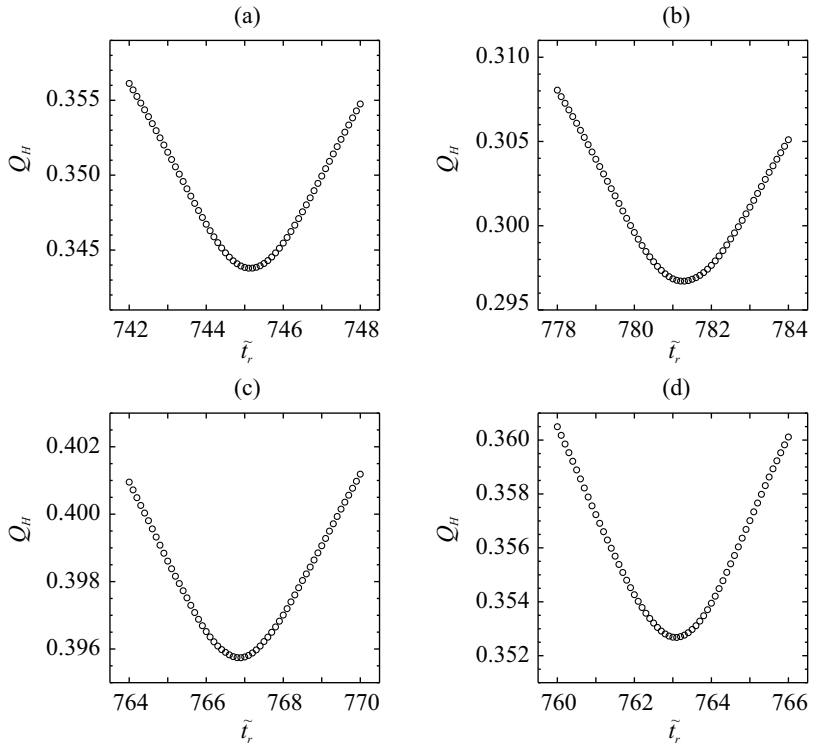

Figure 5.10: Value of the image metric Q_H plotted as a function of the center of rotation $\tilde{t}_r$ at 0.1 bin resolution for the four sample systems (a)–(d) from Figure 5.9. Metrics Q_{IA} and Q_{IN} return qualitatively the same results (not shown).

Samples a and b [Figures 5.9(a) and (b)] could be studied at an optimal absorption coefficient of around or below $p \approx 2$ in the projections (compare Section C.3). Samples c and d [Figures 5.9(c) and (d)] were recorded under non-optimum conditions. Sample c has been recorded with absorption of $p \lesssim 0.2$, and, therefore, displays a high degree of noise. Sample d contains a strongly absorbing titanium implant. Here the projected attenuation coefficient was as high as $p \approx 3.5$ in parts of the projections.

The metrics Q_{IA}, Q_{IN}, and Q_H were calculated as a function of $\tilde{t}_r$ over a range of six bins at a resolution of 0.1 bin around a rough t_r estimate. The result obtained for the three metrics is qualitatively identical and therefore only presented for the metric Q_H in Figure 5.10. Unique minima are found for the metric values of all four samples at individual positions around the center of the projection, which is located at the position $1536/2 = 767.5$.

Table 5.3 lists the t_r estimates found according to the minima in the plots of Figure 5.10 and the results found by image registration and by the center-of-mass method at 0.1 bin resolution. Image registration was performed using the two-dimensional subregions of the projection images recorded at $\theta = 0$ and $\theta = \pi$, which correspond to the n_{av} averaged slices. The result obtained by human scoring is given together with an estimated precision of t_r, in which an improvement of the reconstruction could be noticed. Since no true center of rotation is known for the measured data sets, we compare the automatically determined values with the results obtained by human scoring.

Table 5.3: Optimum value of $\tilde{t}_r$ as determined by the different methods for the sample systems shown in Figure 5.9.

				Image metric[b]		
Sample	Human scorer	Center-of-mass	Registration[a]	H	IN	IA
a	744.9 ± 0.1	747.6	744.3	745.1	745.1	745.1
b	781.2 ± 0.1	780.2	781.2	781.3	781.3	781.3
c	766.9 ± 0.2	764.6	766.7	766.9	766.8	766.9
d	763.2 ± 0.1	765.1	763.1	763.1	763.1	763.1

[a] Using the iterative optimization procedure down to resolution $\delta_t = 0.1$ bin.

[b] According to the minima in the data of Figure 5.10.

The result obtained by the center-of-mass method deviates significantly from the human-scorer result by more than one bin for all samples. The result of image registration agrees well with human scoring for samples b, c, and d but differs by 0.6 bin for sample a. The image metric based methods give results that are correct within the range of the estimated error, except for sample a, where a slightly bigger 0.2 bin deviation is observed.

5.5 Discussion and outlook

By minimization of any of the presented image metrics Q_{IA}, Q_{IN}, and Q_H using the presented iterative minimum search, the position of the center of rotation can be determined from measured sinogram data uniquely and at well below one bin resolution. All projections of the tomographic scan contribute to the reconstruction and influence the image metric values. The scoring of reconstructions is therefore less sensitive to fluctuations in the projections than the image registration method, which has the disadvantage of relying on only two of the recorded projections. Using image registration, a single corrupted image can thus degrade the obtained result drastically. (This could be circumvented by the recording of a larger number of redundant projections, e.g., by the recording of projections over an angular range of 2π, if the additional measurement time is acceptable). The center-of-mass method was shown to be very sensitive to noise and fluctuations. It fails to determine the center of rotation at the required subbin precision when applied to typical measurement data.

The presented metrics Q_{IN} and Q_{IA} can be applied to data of positive attenuation coefficient and return precise t_r estimates. It seems more natural to use the metric Q_{IA}, since it includes all points of the reconstruction grid equally, whereas the metric Q_{IN} only includes information of the negative values of the reconstruction. The metric Q_H was introduced by presenting plausibility arguments. It was shown to return precise t_r estimates as well and is not limited in its application to data of positive attenuation coefficients. For data with positive attenuation coefficient, we suggest use of the metric Q_{IA}.

The image metric Q_{IA} is now routinely applied in our reconstruction process for the determination of the center of rotation. It has been converging at the requested precision (0.05 bin) in all cases, where the sinogram data was consistent, i.e., free of systematic measurement errors. In fact, whenever the algorithm aborted before the final resolution of 0.05 bin was reached, inconsistencies in the recorded projections could be identified. The method does not help to reconstruct these data, but at least gives an indication that the projections are not self-consistent. Inconsistencies can be caused by, e.g., bad reference images, a morphometric change of the sample during the measurement, or a wrong angular position of recorded projections. During the latest measurement period at HASYLAB beamline BW2 (March 2006, beamtime 'desy2006a'), the method was successfully applied for the automated determination of the center of rotation of all 59 recorded scans. In the two cases, where the algorithm aborted before reaching the final iteration step (at 0.05 pixel resolution), inconsistencies in the recorded projection data were found; in one case, sample motion had occurred during the measurement, in another case, the sample had partly left the detector's field of view. In the latter case, a center of reconstruction could be found by use of the histogram based metric Q_H.

The computational costs of the image metrics are of practical importance. The number of operations required for the calculation of metrics Q_{IA} and Q_{IN} directly scales with the number of image pixels in the reconstructed slices. The calculation is thus much faster than the calculation of metric Q_H, which requires a sorting operation. All three metrics are, however, computationally less expensive than the reconstruction process, for which the computational cost was given in Section 3.2.4. The speed of the algorithm is therefore limited by the speed of the reconstruction.

The presented method is readily applicable to any type of tomographic data recorded in parallel-beam geometry. Furthermore, the image metrics should be useful for the detection of the position of the rotation axis for tomography data recorded in fan-beam geometry. In contrast to the simple parallel-beam situation considered in this work, the reconstruction of this data requires more than one input parameter to describe the relative positions of source point, rotation axis, and detector. A multidimensional minimum search could be implemented to return the optimum values of these parameters.

The presented image metrics are, in principle, also applicable to tomography data with image-to-image variations of the center of rotation, i.e., when an individual center of rotation $t_r(\theta)$ must be found for each projection. The number of free parameters is then equal to the number of projections and an iterative optimization scheme as applied by McGee *et al.* [103] can be used to perform the multi-dimensional minimum search in this case.

The visual inspection step in the scoring of test reconstructions can be reliably replaced by the presented iterative procedure. Without the need of visual inspection, the reconstruction process can be fully automated. This accelerates data evaluation and allow researchers to work more efficiently, especially with the new high-throughput microtomography setups.

5.6 Summary

A stable and objective method for the determination of the center of rotation from sinogram data with sub-pixel resolution was developed and implemented. The stability of the method was tested in the presence of noise and gradients in the projections. In order to have a realistic model system (phantom) for the test, the well known ellipse phantom was extended to an ellipse phantom with gradient that has an continuously varying attenuation value. The developed method is readily applicable to any type of tomographic data recorded in parallel-beam geometry and is now routinely applied in our data-processing chain for the determination of the center of rotation with 0.05 pixel resolution. The visual inspection step in the scoring of test reconstructions was replaced by introduction of the presented iterative procedure. Hereby the complete automation of the reconstruction process was achieved.

Chapter 6

Microtomography studies

This chapter presents four selected SRμCT studies carried out during this work. Moreover, these studies are used to demonstrate the improvements made for quantitative SRμCT measurements. The first two examples in Sections 6.1 and 6.2 show the influence of detector blur on the reconstruction and how it can be removed, the example in Section 6.3 discusses the influence of the reconstruction algorithm on the measured attenuation value. The last example in Section 6.4 presents the development of analysis tools for samples (fiberboard) recorded at the spatial resolution limit of the SRμCT apparatus.

6.1 Material flow in friction stir welding

6.1.1 Introduction

The material flow in friction stir welding has been investigated using SRμCT. The results of this study are presented in this section. Furthermore, reconstruction artifacts around strongly

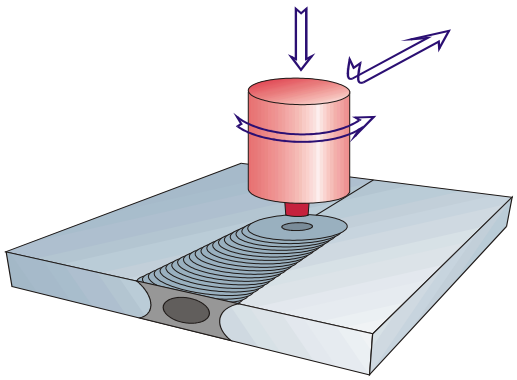

Figure 6.1: Schematic diagram of the friction stir welding process when joining two metal sheets. The two abutting workpieces are joined by the rotating tool that comprises of pin (lower part) and shoulder (upper part). Travel direction, rotation direction, and down force are indicated by arrows.

absorbing sample parts are explained by a simulation that includes the effect of the detector's point spread function. The photon energy for optimal measurements is discussed.

The friction stir welding (FSW) process was developed and patented by The Welding Institute (TWI) of Cambridge, England. See Thomas *et al.* [144]. A schematic diagram of the FSW process is shown in Figure 6.1. The process essentially relies on frictional heating and plastic deformation of the workpieces brought about by the interaction of the workpieces with a non-consumable and rotating tool consisting of a shoulder and a pin. The tool is plunged into and then traversed along the join line between, typically, two abutting workpieces. The frictional heat that is induced by tool rotation and tool travel causes the material in the immediate vicinity of the tool to soften, flow, and mix. At the rear of the pin, the transported material cools and consolidates to form the weld. The shape of the welding tool and its interaction with the base material, i.e., process parameters such as down force, travel and rotational speed, influence the structure and the integrity of the weld. The process is unsymmetric with respect to the two workpieces because of the given directions of travel and rotation. The side of the workpieces having the same rotation and travel direction is termed the advancing side (also: shear side), while the side where travel direction and rotation are opposite is termed the retreating side (also: flow side). Geometric and microstructural differences within the join zone for both sides of a friction stir welded joint are generally observed. In comparison to FSW conventional fusion welding melts the base material during the welding process. This can lead to brittle solidification products and porosity in fusion welds. These effects can be strongly reduced in FSW, since no bulk melting occurs. This is especially advantageous for the welding of highly alloyed aluminum often used in the aerospace industries.

As with fusion welding, there occur changes in the materials microstructure during friction stir welding. In addition there occur volumetric changes due to material transport. These changes determine the quality of the resulting weld. Hence, it is of fundamental importance to not only investigate the materials microstructure using common probes (micro-hardness measurements, strain and stress measurements, and macrographs) but also to understand join zone formation during welding, which depends on local temperatures and forces as well as on the material flow.

The study of material flow in the FSW process is an active field of research. Two different but complementary approaches are generally taken, these being process modeling and experimental flow visualization. For an overview on the activities in FSW modeling, see the publication by Colegrove and Shercliff [37] and the references therein. Experimental studies have examined the material flow in FSW by tracking the flow of embedded tracer materials through sectioning, conventional radiography or x-ray tomography, or by examining the material distribution after welding dissimilar materials. References were reviewed by Fonda *et al.* [62] and Guerra *et al.* [71].

Note that sectioning techniques (as the production of macrographs) are time-consuming and destructive methods that can introduce artifacts and, typically, only provide limited resolution in the sectioning direction. X-ray (attenuation contrast) tomography cannot reveal the mater-

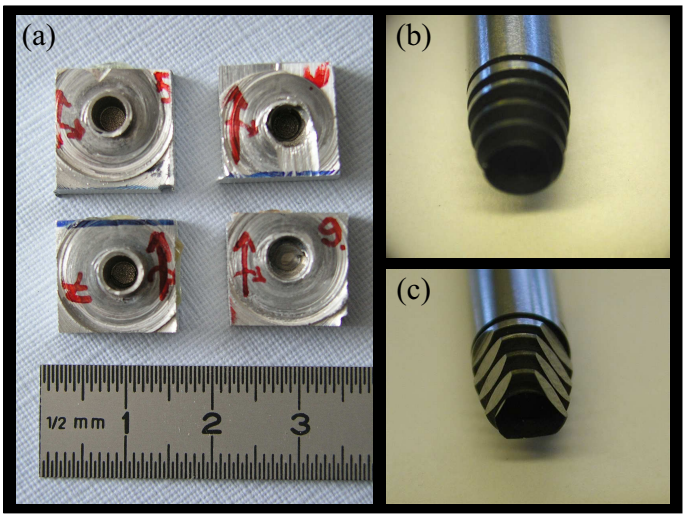

Figure 6.2: (a) Four FSW samples that were produced using the stop-action technique. The pin was partly removed by discharge machining. (b) Joining tool pin of type B (conical threaded). (c) Joining tool pin of type C (conical threaded with three flats). The pin diameter is 5 mm.

ial's microstructure but provides three-dimensional information with high-resolution in a fast and non-destructive manner. This allows to obtain complementary information, when at first microtomography is performed with the FSW sample before the sample is destroyed during, e.g., the preparation of macrographs.

In this study SRμCT was applied for the three-dimensional visualization of material flow in friction stir welding of similar alloys of type 2024-T351. Titanium powder was implanted into aluminum sheets as a contrast-giving marker material prior to welding. The marker distribution during welding (by use of the stop-action technique) and after welding was recorded three-dimensionally using SRμCT and compared with macrographs that were subsequently prepared from the same samples.

The SRμCT study on material flow is part of a larger study investigating the influence of FSW tool geometry and welding parameters on the FSW process. Results of this study, including results from SRμCT, temperature measurements, tensile tests, micro hardness measurements, and the evaluation of macrographs, have already been published by Zettler *et al.* [163], [164], [165], and by Donath *et al.* [47].

6.1.2 Sample preparation

Welding was performed on 4 mm thick sheets of 2024-T351, where each specimen measured 110 × 400 mm (width × length). All welds were produced as butt welds at the GKSS-Forschungszentrum using a Tricept TR 805 robot. A titanium powder measuring 30 – 90 μm in diameter was placed in slots milled into the aluminum sheets. Following a first series of experiments to optimize weld parameters, a second series of 2024-T351 samples was prepared for microtomographic examination. Here, the titanium powder was implanted into the top surface

Table 6.1: Scan parameters for FSW measurements. Here m is the optical magnification, τ is the effective pixel size, a_{10} is the spatial resolution. Unchanged parameters are not repeated.

Beamtime/scanname	Beamline	Energy [keV]	Mode	m	τ [μm]	a_{10} [μm]
desy2003a/gkss03a,b desy2003a/gkss04a,b desy2003a/gkss05a,b desy2003a/gkss06a..d desy2003a/gkss07a..d desy2003a/gkss08a..d desy2003a/gkss09a..e	W2 (old HARWI)	45	180deg	0.98 0.87	9.18 10.34	16.1 18.9
desy2003b/gkss03a..c desy2003b/gkss04a..c desy2003b/gkss05a..c desy2003b/gkss06a..d desy2003b/gkss07a..d desy2003b/gkss08a..d desy2003b/gkss09a..d	W2 (old HARWI)	45 60	180deg	0.87 0.87	10.34 10.34	16.0 19.7
desy2005e/gkss03a..d[b] desy2005e/gkss04a..c[b] – desy2005e/gkss09c	W2 (new HARWI) W2 (new HARWI)	82	360deg	1.357	6.63 13.26[a]	15.77

[a] Recorded with on-chip binning, factor $b = 2$.

[b] Aluminum alloy 6013-T6, data not shown here.

of the workpieces, 1.5 mm away from the join line in the upper half of the workpieces. A small quantity of the marker material was placed into each slot that was, thereafter, closed by insertion of a plug prepared from the same 2024-T351 aluminum alloy. The dimensions of the slots were 10 mm in the direction of welding, 2.5 mm into each workpiece, i.e., transverse to the direction of welding, and about 1.25 mm in height.

Friction stir butt welds were produced from the such prepared sheets with a weld speed of 200 mm/min and rotational speed of 800 rpm using two different welding tools. The welding tools comprised of a concave shoulder (type 1) in conjunction with a welding pin of either type B or C shown in Figures 6.2(b) and (c). The corresponding tool/shoulder combinations will be referred to as tool 1B and tool 1C in the following. Welds produced with and without embedded marker material were compared visually by their macrographs. Only small differences were observed, while the general shape and characteristics of the weld structures were unchanged for all applied tool and weld parameter combinations. Therefore, the use of titanium powder as marker material is believed to have little influence on the welding process.

In the first SRμCT scans samples were investigated after welding had been completed. For the following scans a stop-action technique was employed to halt and capture the welding pin,

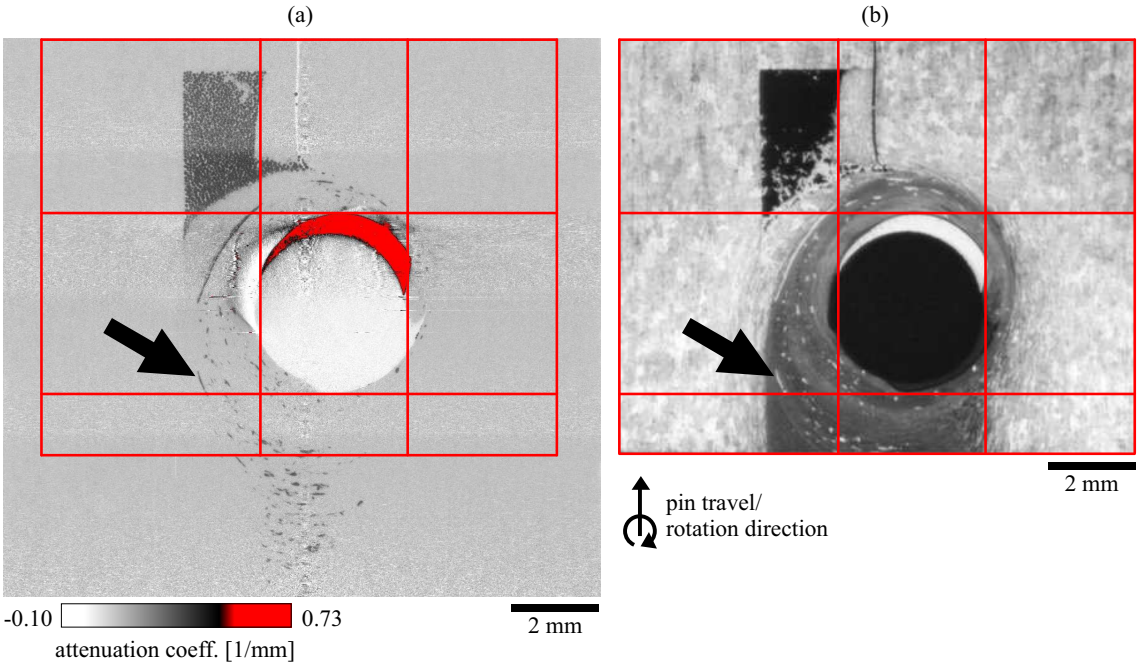

Figure 6.3: (a) Tomographic reconstruction and (b) macrograph showing the same cross section of a FSW sample prepared by the stop-action technique. The same features of titanium marker and pin remains are visible in both images, while microstructure is only visible in the macrograph. The black arrows point towards a corresponding streak of marker material. The grid (red) has been overlayed for better orientation.

while still in contact with the embedded marker material. A small section of the weld of about 10×10 mm that included the welding tool pin was removed from each sample and examined by SRμCT. Four samples are shown in Figure 6.2(a).

6.1.3 Measurement and reconstruction

In total, 14 FSW samples were studied comprising a total of 73 SRμCT scans. Most of the scans were part of stacked measurement with 2, 3, or 4 heights. The 4-height scans resulted in a total reconstructed volume of about $16 \times 16 \times 10$ mm. The full samples measured about $10 \times 10 \times 4$ mm in size and were investigated in an upright position, i.e., with the sample plane parallel to the tomographic axis. Hereby, the maximum extension of the sample and the maximum projected attenuation value were reduced. The here presented measurements were carried out at beamline W2 (old HARWI) described in Section 2.1.2. Table 6.1 gives an overview of the recorded data and the scan parameters.

First scans were recorded at photon energies of 45 keV (after welding, without welding pin) and at the maximum available photon energy of 60 keV (using the stop-action technique, with welding pin). The x-ray energy of 60 keV was not sufficient to penetrate the steel pin. Therefore, tomographic reconstructions could be obtained only from the regions above and below the pin. In order to decrease the projected attenuation value in further examinations, the pin was removed

from the immediate weld zone by spark erosion. Small parts of the pin that could not be removed without the risk of damaging the sample remained inside the sample.

The measurements were recently continued at the redesigned W2 beamline (new HARWI) for the same type of marker-implanted FSW samples of a 6013-T6 aluminum alloy (see Donath *et al.* [48]) at 82 keV photon energy. At this higher energy the reduced absorption of the welding pin allowed for the measurement of samples with the pin remaining inside the sample. The effect of the higher photon energy on the image contrast will be discussed below.

Tomographic reconstruction was performed using the "BKFIL" algorithm of the RECLBL library. All here presented measurements were carried out in 2003. At this time the luminescent screen of the x-ray camera carried no backing layer and the center of rotation was still determined manually. For the later conducted simulations the method for the determination of the center of rotation described in Chapter 5 was applied using the entropy based metric Q_H down to a resolution of 0.05 pixel. The metric Q_H was used here because of the expected inconsistency of the sinogram data due to the strongly absorbing pin fragments (compare below).

6.1.4 Observed redistribution of Ti-marker

The comparison of macrographs with the corresponding tomographic slices (see Figure 6.3) revealed perfect agreement in the visible marker distribution. Thus, it can be concluded that even fine marker particles can generally be detected in the tomographic reconstruction. The material's microstructure is only visible in the macrograph that has been prepared under destruction of the sample after the SRμCT measurement.

An evaluation of the marker flow patterns (cross sections shown in Figure 6.4) revealed that the marker material ahead of the welding pin was ruptured well before the pin threads made contact with it. They also revealed that the titanium powder flowed in the direction of tool rotation (clockwise). It was also evident that much larger clumps of the marker were to be found in the weld nugget produced using tool 1C [Figures 6.4(b) and (d)]. By comparison tool 1B [Figures 6.4(a) and (c)] indicated that the marker was more finely dispersed and distributed throughout both the top and bottom half of the workpieces. Significant differences existed in marker distribution not only between the FSW tools but also between marker flows for each side of a single friction stir weld. The major difference was observed for welds produced using tool 1B. Marker initially embedded on the advancing side of the weld was finely dispersed and deposited at the rear of the tool, again on the advancing side [Figure 6.4(a)]. Marker embedded on the retreating side, however, could be seen to be distributed much more coarsely [Figures 6.4(c)]. Large clumps of the marker material could be seen to form at the rear of the welding tool again on the advancing side of the weld.

It was also observed that the deposition of the marker had been shifted closer towards the original join line interface between the workpieces, while FSW using welding tool 1C. This differed from tool 1B where the majority of the marker material deposited at the rear of the welding

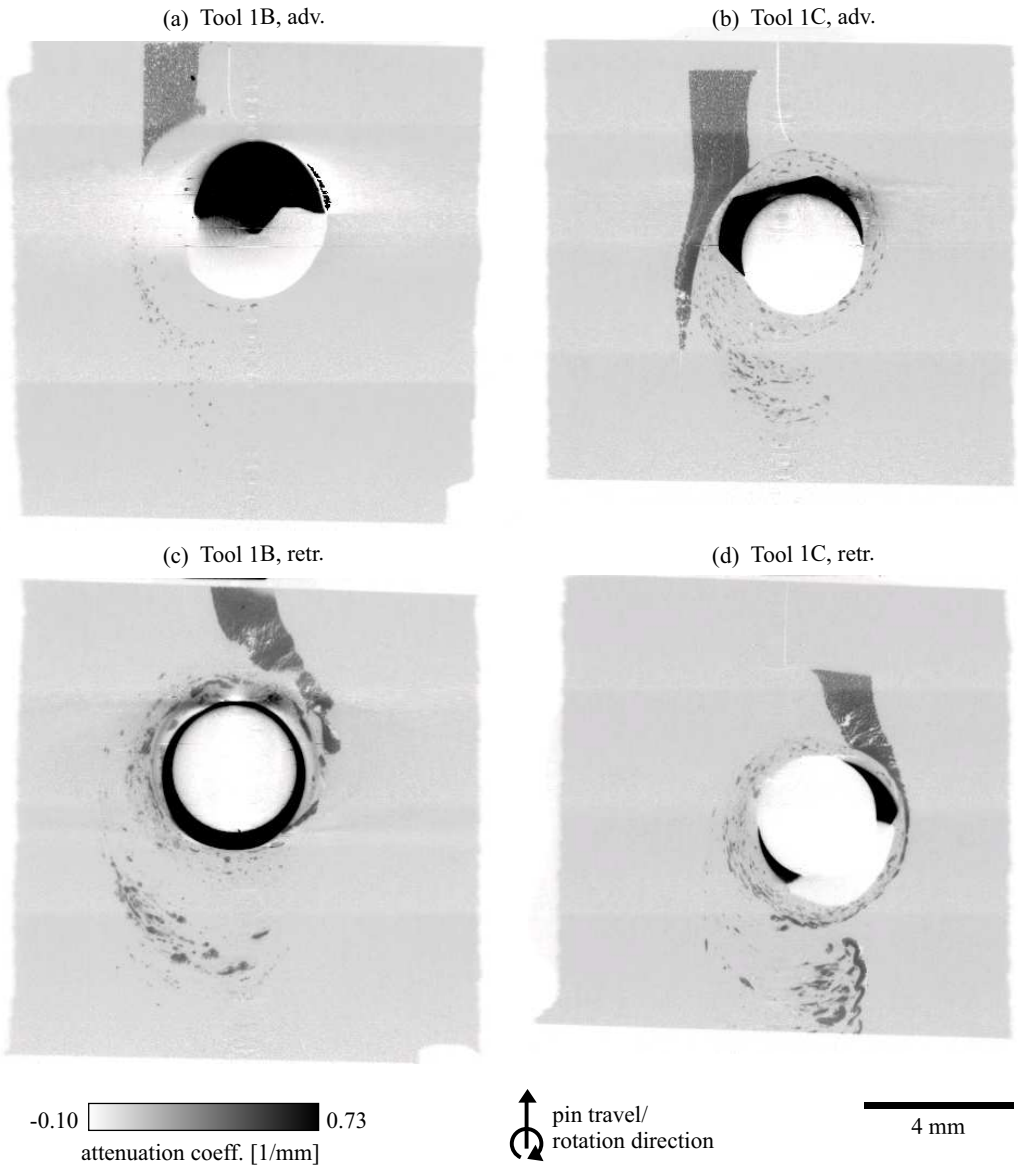

Figure 6.4: Tomographic cross sections from four FSW samples produced using the stop-action technique. The pin of the welding tool was spark eroded prior to examination. The remaining pin fragments (black), titanium powder (dark gray), and aluminum (light gray) are visible. Welding was conducted with titanium powder embedded on the advancing (adv.) and retreating (retr.) side for both tool 1B and tool 1C. The cross sections are oriented parallel to the tomographic rotation axis and were stacked from four scans each. A slight variation in photon energy caused by the bent Laue monochromator results in a slight variation of the attenuation coefficient as a function of height. The large remaining pin fragment in (a) causes artifacts around the pin.

pin could be seen to be biased towards the advancing side of the weld joint. Vertical displacement could be as well revealed from the three-dimensional data sets as can be seen in the volume rendering in Figure 6.5. The volume data set confirmed, what had been suspected from two-dimensional micrographs. Tool 1C produced much less vertical displacement of the marker than tool 1B.

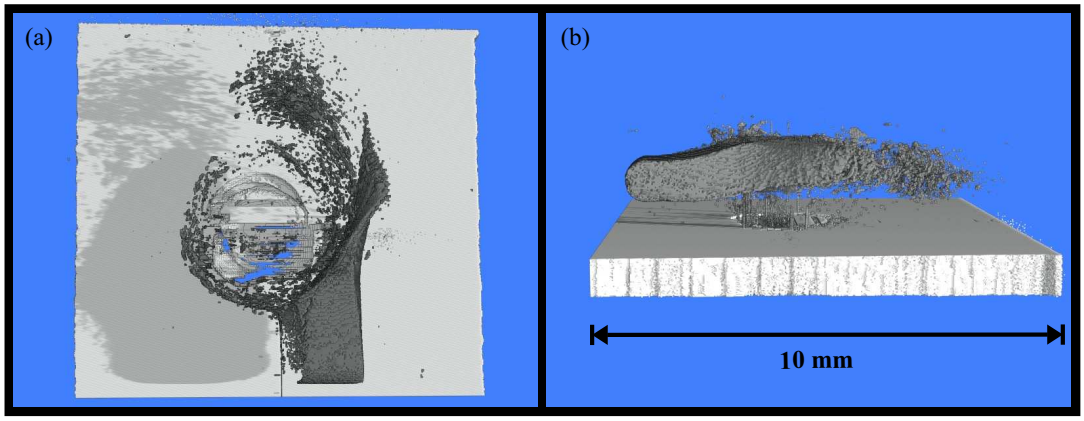

Figure 6.5: 3D rendering of the Ti marker distribution in an FSW sample prepared by the stop-action technique. (a) Top view with pin travel direction from top to bottom of the image and clockwise pin rotation. (b) Side view with pin travel direction from right to left. The upper part of the aluminum sheet (light gray) has been made transparent to allow the view on the redistributed titanium powder (dark gray). Artifacts are observed at the bottom of the weld in the vicinity of pin fragments. [A cross section from the same sample is shown in Figure 6.4(b)].

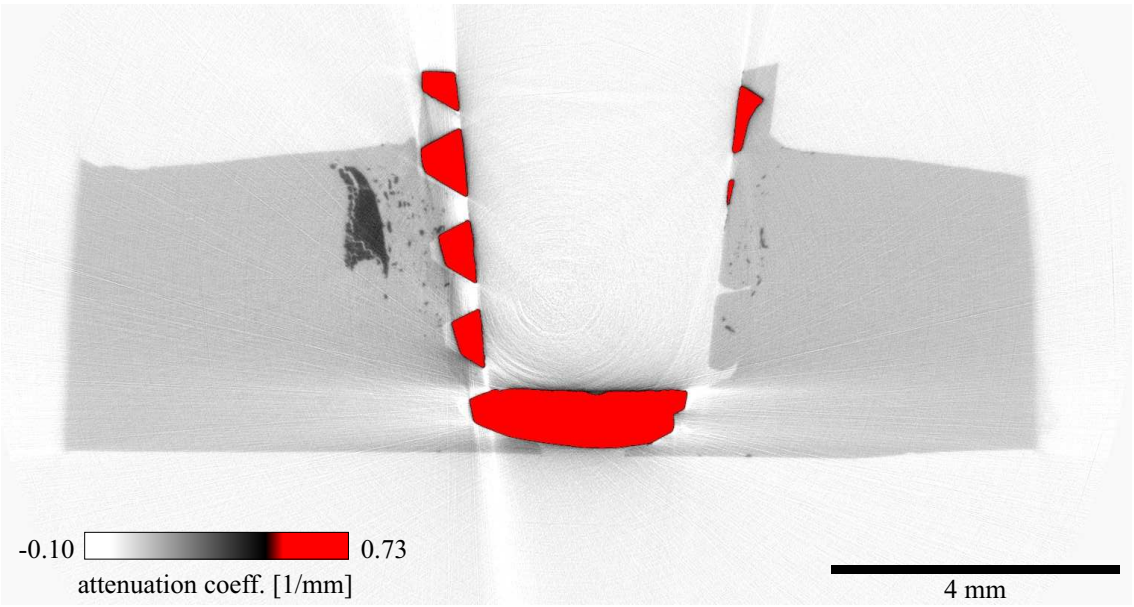

Figure 6.6: Cross section through an FSW sample measured at 60 keV. Aluminum (light gray), marker (dark gray), and remains of the strongly absorbing pin (red) are visible. Strong artifacts along the extension of the pin fragments and a few ring artifacts are observed.

6.1.5 Simulation of artifacts

Figure 6.6 shows a reconstructed slice of a friction stir weld measured at 60 keV that displays artifacts. In close vicinity to the remaining pin fragments, and especially along the directions that contain a lot of pin material, the reconstructed attenuation is shifted to above or below its true value. Ti marker can thus not be identified by simple threshold techniques. It will be shown now, that these artifacts are caused by the high projected attenuation values in combination with the long tails of the detector's point spread function (PSF). To investigate the source of the artifacts, we will compare measured and simulated data.

A typical sinogram of a slice recorded at 60 keV will be the basis for our simulation. In order to speed up the calculations, the sinogram was binned by a factor of $b = 4$ in projection width. For the resulting sinogram shown in Figure 6.7(a), the projection width is $N_t' = 1536/b = 384$ and the number of projections is $N_\theta = 720$. The corresponding reconstruction is shown in Figure 6.8(a) and presents a very similar cross section as Figure 6.6. Here the reconstructed attenuation coefficient displays too low values along the direction of extended pin fragments, which cause a high value of the projected attenuation coefficient p in the sinogram. At the same time the reconstructed attenuation value is increased in the perpendicular directions. In the vicinity of the pin the intensity of the artifacts is comparable with the attenuation of the titanium powder, which inhibits automated segmentation of the titanium powder by threshold selection. Additionally, the reconstruction of Figure 6.8(a) shows ring artifacts. Ring artifacts are typically caused by spatial inhomogeneities of the luminescent screen that was not yet coated with a backing layer in these measurements. They would be strongly suppressed in our new SRμCT setup with optically coated luminescent screens (compare Chapter 4) and we shall not further discuss them here. We rather attempt to describe the effect of detector blur with the following simulation.

From the cross section shown in Figure 6.8(a) a simulated slice was generated that is shown in Figure 6.8(b). The shape of the pin in the simulated slice was based on the real pin and assigned an attenuation value of $0.93\,\mathrm{mm}^{-1}$, while the aluminum was simulated for simplicity as a rectangular block with attenuation coefficient of $0.08\,\mathrm{mm}^{-1}$. From the simulated slice, a sinogram p_{sim} was calculated using the Radon transform procedure of the IDL programming language. The simulated sinogram is shown in Figure 6.7(b). The maximum projected attenuation in the simulated sinogram is $\mathrm{Max}(p_{sim}) = 5.3$, which is far above the desired optimum value of $p \approx 2$ (compare Section 2.5.2). For $p = 5.3$ the dynamic in the recorded images given by $\exp(p) \approx 200$ has to be compared with the detector's dynamic range, which is DR ≈ 6000. Thus, the dynamic range of the detector still is about a factor of 30 higher than the dynamic in the recorded projection data, and is thus not the limiting factor in these measurements. Moreover it was found that the projected attenuation value in the simulated sinogram [Figure 6.7(b)] was locally much higher than in the measured sinogram p_{meas} [Figure 6.7(a)]. In contrast to the simulated sinogram the measured sinogram displayed a much lower maximum projected attenuation of $\mathrm{Max}(p_{meas}) \approx 3.0$. It was suspected that the lower p values in the measured data are the cause of the observed artifacts in

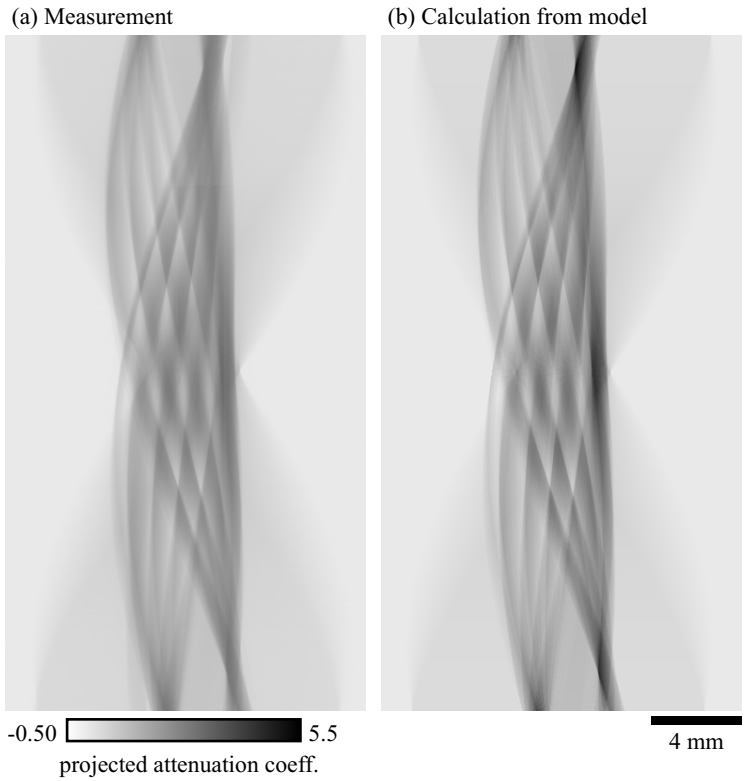

Figure 6.7: Sinogram of a FSW sample recorded at 60 keV photon energy: (a) measured, (b) calculated from the model in Figure 6.8(b). The maximum projected attenuation is ~3.0 in the measured sinogram and ~5.3 in the calculated data. The reconstruction of the measured sinogram is shown in Figure 6.8(a).

the reconstruction and that they can be explained by the detector blur. In order to verify this, the effect of the detector blur was simulated.

From an edge profile measurement that was carried out before the scan, the detector LSF and MTF were determined as described in Section D.1. The determined LSF shown in Figure 6.9 was then manually approximated by the sum of three Gaussian functions, where each Gaussian function is described by its integral value and its sigma parameter. In the following, the sum of the three Gaussians that is used to simulate the detector response will be referred to as LSF_1. Although LSF_1 and the measured LSF do not match perfectly, the approximation by Gaussian functions was used because of the simple relation between the description of Gaussians in real space (slice) and projection space. More importantly, the description by Gaussian functions enables us to study the effect of blur over different length scales easily, i.e., we can systematically change the influence of long range contributions to the LSF by reduction of the integral value or removal (integral value = 0) of the Gaussian functions with large sigma value. The total of all Gaussians must be unity of course.

LSF_1 was then used for the calculation of a blurred sinogram. A second function LSF_2 was defined to demonstrate the effect of long tail suppression. Both functions LSF_1 and LSF_2 are plotted in Figure 6.9 that also contains a table with the function parameters. The blurred sinogram

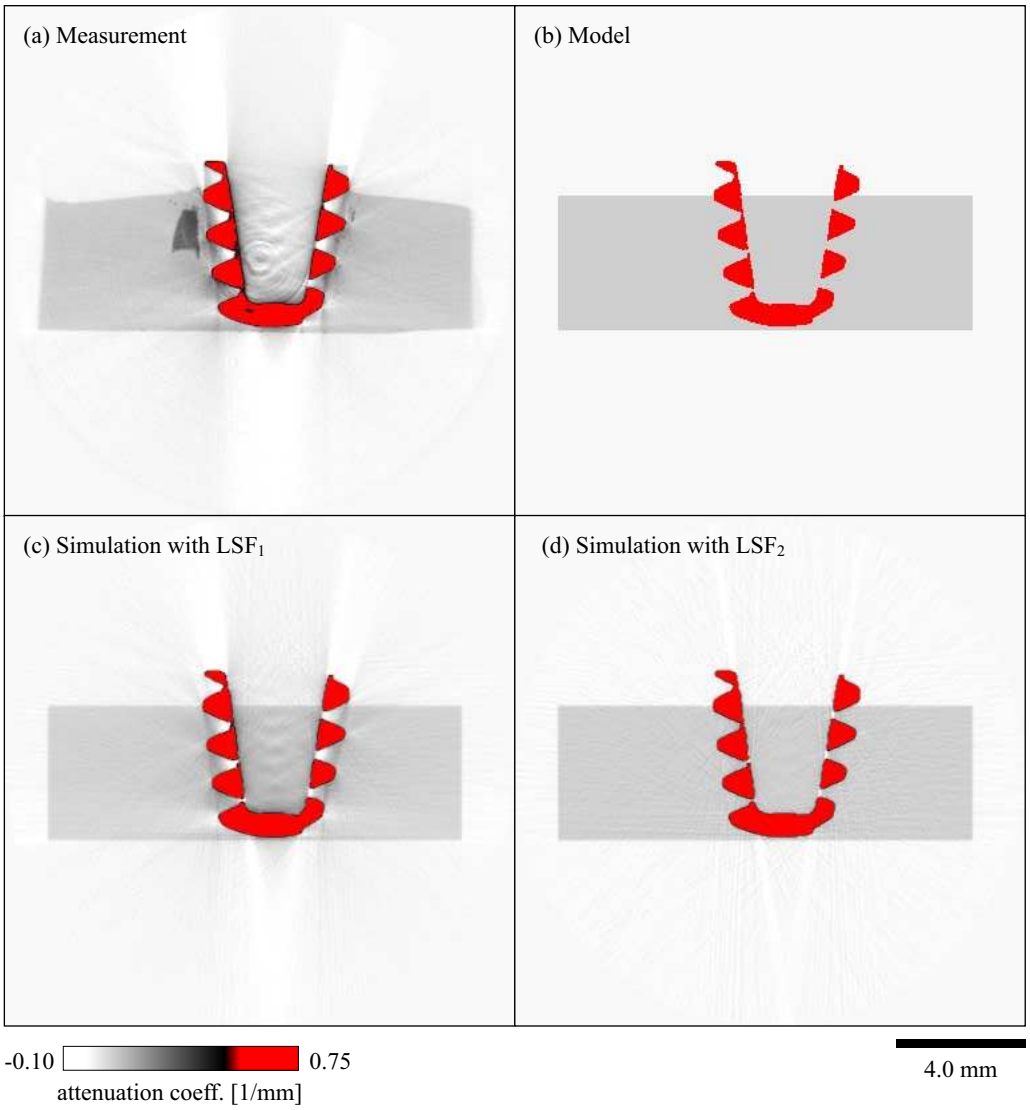

Figure 6.8: Simulation of artifacts in the tomographic reconstruction of an FSW sample. (a) Reconstruction of the measured sinogram shown in Figure 6.7. (b) Model of a tomographic slice for simulation consisting of a pin-like object with attenuation coefficient $0.93\,\mathrm{mm}^{-1}$ and a rectangular, aluminum-like block with attenuation coefficient $0.08\,\mathrm{mm}^{-1}$. (c) Reconstruction of the simulated sinogram blurred with LSF_1 and (d) blurred with LSF_2. All reconstructions were calculated on a 384×384 pixel reconstruction grid using the "RALA"-type reconstruction algorithm. Ring artifacts visible in the original measurement are not part of the simulation.

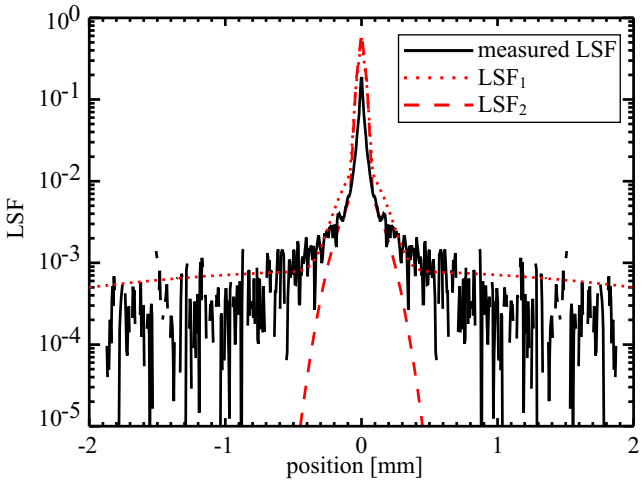

Function	Integral	Sigma [mm]
LSF_1	0.80	0.021
	0.10	0.124
	0.10	2.069
LSF_2	0.95	0.021
	0.05	0.124

Figure 6.9: Plot of the measured LSF and LSF_1, LSF_2 for the simulation of blur. The measured LSF was determined from an edge profile measurement. Line spread functions LSF_1 and LSF_2 are defined as the sum of three and two Gaussian functions respectively. The integral value and the sigma parameter for each Gaussian are given in the table. The width of the smallest Gaussian function in LSF_1 and LSF_2 is approximately equal to the spatial resolution determined from the measured LSF, which is $a_{10} = 19.7\,\mu$m corresponding to the 10% MTF value.

was calculated by convolution of intensity values (assuming a homogeneous reference image) as

$$p_{blur,i} = -\ln[\mathrm{LSF}_i * \exp(-p_{sim})]\,, \tag{6.1}$$

where p_{sim} is the sinogram of the simulated slice, LSF_i is either one of the functions LSF_1 or LSF_2, and the symbol $*$ designates one-dimensional convolution. Convolution of the projection data according to Equation (6.1) was performed for each projection angle. Use of the LSF for the description of blur in the reconstruction implies the assumption that the sample structure is independent of the z direction (compare Section 3.3.1), which is only approximately the case for our sample, and that the beam profile is flat. The simulation may thus differ from the measurement.

Figure 6.8(c) shows the reconstruction obtained for the sinogram blurred with LSF_1. The visible artifacts resemble the artifacts of the real reconstruction in Figure 6.8(a), i.e., the real and the simulated reconstruction are qualitatively identical. Exact quantitative agreement could not be achieved but this was neither expected, due to the above made approximations. However, the comparison of measured and simulated reconstruction confirms that blur introduced by the detector PSF is the most probable cause of the observed artifacts.

The removal of long tails of the PSF has been simulated by the line spread function LSF_2 shown in Figure 6.9. For LSF_2, the broadest component of LSF_1 has been removed and the relative intensities of the remaining components changed to give a sharper LSF. Figure 6.8(d) shows the reconstruction of the simulated sinogram blurred with LSF_2. The reconstruction shows almost no relevant artifacts. Weak streaks are observed here only along edges, i.e., along those directions, for which the projection shows high gradients.

Table 6.2: Attenuation coefficients of iron (Fe), titanium (Ti), and aluminum (Al).

Photon energy E_{ph}	Attenuation coefficient[a] μ [1/mm]		
[keV]	Fe	Ti	Al
45	2.009	0.711	0.118
60	0.925	0.342	0.074
82	0.436	0.175	0.053

[a]Calculated from the tables of Plechaty *et al.* [119].

Convolution with the detector PSF makes a non-linear effect for the measured data (compare Section 2.5.1), which can be seen from the average mass of all projections $\overline{m}_0$ given by Equation (5.14). When compared with the average mass $\overline{m}_{0,sim}$ of the simulated sinogram p_{sim} the convoluted sinograms $p_{blur,1}$ and $p_{blur,2}$ exhibit a value of $\overline{m}_0$ that is 93.3% $\overline{m}_{0,sim}$ and 99.64% $\overline{m}_{0,sim}$ respectively. Thus convolution with LSF_1 makes a strongly non-linear effect, whereas convolution with LSF_2, that does not contain long tails, results in almost no change of $\overline{m}_0$.

6.1.6 Optimal contrast-to-noise ratio

Selection of a higher photon energy reduces the attenuation value and avoids the previously described artifacts but also decreases the contrast in the measurement. The expected contrast-to-noise ratio for measurements at the different applied energies can easily be estimated. The attenuation coefficients of aluminum alloy, titanium marker, and pin is approximately given by the attenuation coefficients of aluminum, titanium, and iron given in Table 6.2 for the applied photon energies. The noise level σ_μ in each pixel of the reconstruction is approximately given by Equations (3.30) and (3.31). For sampling distance $\tau = 10.34\,\mu$m, number of projections $N_\theta = 720$, and average count of $\langle N \rangle = 8.000$ x-ray photons in each pixel, we obtain $\sigma_\mu = 0.025\,\mathrm{mm}^{-1}$ independent of photon energy. The assumption that was made here for the average photon count $\langle N \rangle$, corresponds to the situation of an optimally exposed reference image recorded with our camera and a projected attenuation value of $p \approx 2$ (~10% transmission). We are primarily interested in the contrast between titanium and aluminum that can be described by the contrast-to-noise ratio (CNR) as

$$\mathrm{CNR} = \frac{\mu_{Ti} - \mu_{Al}}{\sigma_\mu}\,, \tag{6.2}$$

with the attenuation coefficients μ_{Ti} and μ_{Al}. At photon energy $E_{ph} = 60\,\mathrm{keV}$ the contrast-to-noise ratio becomes $(0.342 - 0.074)/0.025 = 10.7$, while at 82 keV, the contrast-to-noise ratio becomes $(0.175 - 0.053)/0.025 = 4.88$. Note that we assumed the same projected attenuation value of $p = 2$ (~10% transmission) for both energies, which requires that the pin is almost entirely removed from the sample for the measurement at 60 keV, while it may remain inside the sample for the measurement at 82 keV. In this case, the calculated contrast-to-noise ratio is lower by about a factor of two for the measurement at photon energy 82 keV. Hence, with respect to contrast,

it is desirable to perform the measurement at the lower 62 keV photon energy. However, even at 82 keV a contrast-to-noise ratio of five is obtained. This CNR should be sufficient for visualization of the titanium particles, even when the image of the finest titanium particles (diameter 30 μm) is blurred by the detector point spread function (resolution $a_{10} \approx 20\,\mu$m) in three dimensions. Thus, since measurements at 82 keV photon energy provide sufficient contrast and can be performed with pin remains inside the sample, this higher photon energy is desirable for our measurements. Partial removal of the pin should however still be considered, since it will reduce the noise in the reconstruction.

6.1.7 Summary

The flow and redistribution of a Ti-powder marker material embedded in friction stir welded 2024-T351 alloy has been investigated in relation to variations in tool pin geometry by means of SRμCT and standard metallographic techniques. To the best our knowledge, for the first time a fine-powdered marker material inside friction stir welds has been visualized by SRμCT. From the investigation important insights into the material flow in FSW of similar aluminum alloys could be gained. A comparison of the marker flow and distribution between the two tool types 1B and 1C clearly indicated that differences exist between the marker flows from each side of the workpiece and that marker flow was generally much more homogeneous in nature for the tool of type 1C. Vertical transport of marker material was also found. For the three-dimensional mapping of marker particles SRμCT has proven to be a reliable, non-destructive method that provides higher resolution and requires less time than metallographic sectioning techniques.

A simulation was presented that qualitatively reproduced the artifacts observed in the reconstructions. Hereby, the origin of the artifacts could be explained as the combined effect of a high projected attenuation coefficient caused by remains of the welding pin and the long-range contributions of the detector PSF. As was shown, the reduction of long-range contributions to the PSF or the measurement at higher photon energies avoid these artifacts. The discussion on the contrast-to-noise ratio showed that an increase of the photon energy to 82 keV is favorable for this type of FSW sample. This was confirmed by first measurements at GKSS-operated beamline W2 (new HARWI), which can provide this energy, and which is available for measurements since this year.

The SRμCT study on the material flow in FSW is being continued at beamline W2 (new HARWI) for the further investigation of the influence of the welding tool and the welding parameters on the welding process. Furthermore, investigations were recently started for two similar joining techniques that are being developed at the GKSS-Research Center: ‘friction riveting’ and ‘hybrid friction diffusion bonding’ (HFDB). The first measurement of a friction rivet was recently presented by Beckmann *et al.* [17].

6.2 Density of cortical bone

6.2.1 Introduction

The contrast obtained between bone and soft tissue makes x-rays an ideal probe for biomedical research. Bone mass measurements (or bone mineral density measurements), which are typically based on conventional x-ray radiography or CT data, are mostly applied for the diagnosis of osteoporosis and for research on this common disease. However, quantitative CT measurements are also important to relate bone density values to mechanical properties (stiffness and strength), in case one wants to build finite element models with the correct input for the material properties.

Assuming a certain mass attenuation coefficient (μ/ρ) for bone, the measured x-ray attenuation coefficients μ can be directly converted into a value for the bone density ρ. For a deeper discussion, see the description of the radiographic determination of mineral content by Elliott *et al.* [54]. The high degree of monochromaticity in x-ray beams available at synchrotron radiation sources enables the precise determination of the attenuation coefficient and, thus, the precise determination of the bone density in SRμCT as was, e.g., presented by Nuzzo *et al.* [117]. However, blur introduced by the detector limits this capability. The influence of detector blur is discussed here for the example of a cortical bone measurement. The suppression of blur by application of the backing layer (presented in Chapter 4) and by deconvolution of the detector PSF is demonstrated. Furthermore, the reduction of ring artifacts after application of the backing layer is shown.

The cortical bone sample that is used for demonstration here was examined as part of a larger study on the remodeling of bone that had been started in 2002. This study aims at the quantitative evaluation of the remodeling process in osteoporotic cortical bone (human bone) with focus on examination of the bone structural unit, the osteon, and more specifically its mineralization level. For the investigation SRμCT measurements were performed on 8 samples from the femur of a male donor and 4 samples from the femur of a female donor. The osteonal mineralization patterns in the cortical bone samples (as shown in the rendering of Figure 6.10) were studied and compared with images obtained by scanning acoustic microscopy (SAM) that can be related to the elastic constant (Young's modulus) of the bone.[1] The results of this study have been published by Dalstra *et al.* [41] and in the master thesis of Karaj [94].

6.2.2 Measurement and reconstruction

The presented data from the cortical bone of an osteoporotic, female donor were recorded in 2004. In total, four matchstick-like samples ($2.5 \times 2.5 \times 40$ mm) were prepared from the proximal end of the right femur of the donor from the medial, anterior, lateral, and posterior position. The sample shown here is the posterior sample. All scans were performed at beamline BW2 at 22 keV photon energy. The scan parameters are given in Table 6.3. The maximum projected attenuation

[1] The relation between the acoustic impedance and the elastic constant is given in Karaj [94, Eq. (33)].

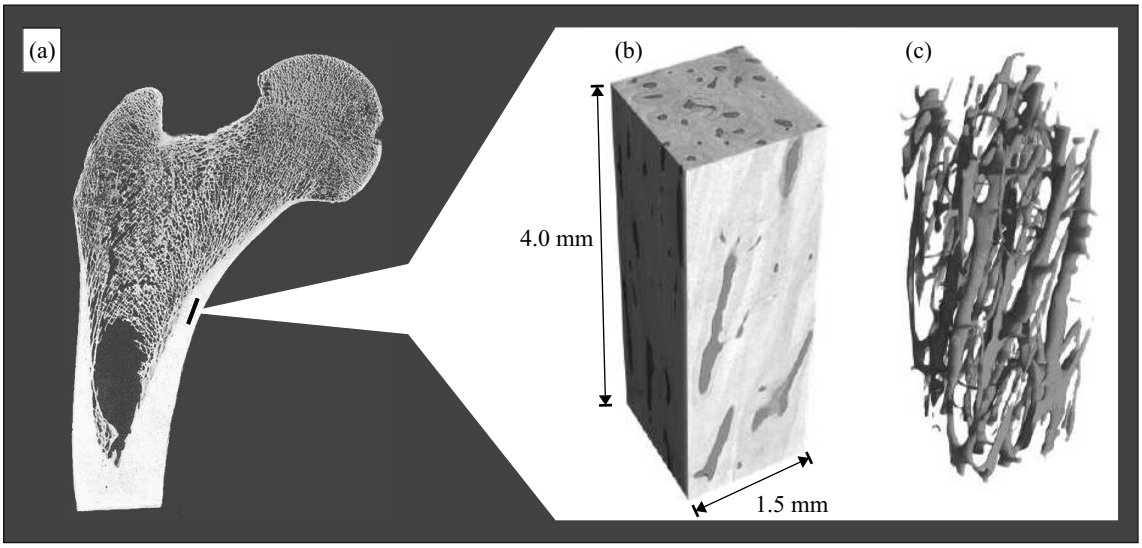

Figure 6.10: (a) Longitudinal section of upper human femur from H. Gray, 'Anatomy of the Human Body', 1918. The mark shows the approximate location of cortical-bone extraction for the medial sample. (b) Tomographic reconstruction of the sample volume and (c) rendering of the Haversian canal system.

coefficient was $p \approx 2$ as required for a measurement with optimum signal-to-noise ratio (compare Section 3.3.2). Projections were recorded with the x-ray aperture slightly smaller than the field of view such that the intensity was close to zero in the outer areas of the field of view. Binning was applied to the recorded images with binning factor $b = 2$ to decrease the noise level in the reconstructions (compare Section 3.3.4). The resulting binned projections had a width of $N_t = 768$ pixels. The 55 outer-most pixels on each side of the projections were set to zero after binning and before reconstruction. This was necessary because of the low intensity in the outer areas of the field of view, which would result in undefined values of the projected attenuation coefficient otherwise. Reconstruction was performed using the "RALA"-type reconstruction algorithm that was implemented under IDL (see Section 3.2) and produces reconstructions free of DC-shift. The center of rotation was determined for each scan from the sinogram data with precision of 0.05 pixel, using the method presented in Chapter 5. The calculation of the MTF from an edge profile measurement was performed before the scan as described in Appendix D.1.

A stacked scan (scans: gkss08a–f in Table 6.3) of the sample at six different positions was performed. The luminescent screen was then removed from the apparatus for application of the black backing. The sample was not translated during this procedure. The luminescent screen was remounted, the camera was focussed and the 'new' MTF was recorded. Only about 30 minutes later, the previous scan was repeated at the same sample position (scan: gkss08g), with the luminescent screen now covered with lacquer paint under otherwise unchanged conditions. The specific luminescent screen was referred to as screen CWO1 in Chapter 4, where the recorded edge profiles were shown in Figure 4.3. They showed the reduction of the intensity in the long tails of the PSF and a reduction of the visibility of screen inhomogeneities.

Table 6.3: Scan parameters for bone measurements. Here m is the optical magnification, τ is the effective pixel size, a_{10} is the spatial resolution. Unchanged parameters are not repeated.

Beamtime/scanname	Beamline	Energy [keV]	Mode	m	τ [μm]	a_{10} [μm]
desy2004b/gkss08a..f [a]	BW2	22	180deg	3.36	2.68	4.61
desy2004b/gkss08g[a,b]						4.64

[a] Reconstructed with binning of recorded images ($b = 2$). Effective pixel size in reconstructions is 2τ.

[b] Repetition of scan gkss08f after application of the backing layer.

6.2.3 Deconvolution of projection data

Deconvolution of the spatial detector response (removal of blur) was tested for the evaluation of the data set recorded with absorbing backing (scan: gkss08g). The direct deconvolution approach presented in Section 2.5.3 was applied, which requires that the entire beam profile must be recorded within the field of view of the x-ray detector, i.e., the intensity should be zero outside the field of view of the detector. This was experimentally realized by closing the x-ray aperture to a little less than the extension of the field of view. Hereby, a slight reduction of the usable detector size was caused that was irrelevant for the examination of the sample in this case. The one-dimensional MTF(w) shown in Figure 4.4(e) describes the spatial system response and was used for deconvolution.

The direct deconvolution was implemented using IDL routines. The deconvolution of images i_{mn} with $M \times N$ pixels were calculated using the fast Fourier transform (FFT) routine. The resulting FFT(i_{mn}) is a complex image in frequency space of size $M \times N$. The measured MTF was assuming rotational symmetry interpolated to the frequencies that correspond to the positions of the elements in FFT(i_{mn}). The deconvoluted images were calculated by division in frequency space [compare Equation (2.62)] and inverse fast Fourier transform (FFT^{-1}) as

$$o_{mn} = \mathrm{FFT}^{-1}\left\{\frac{\mathrm{FFT}(i_{mn})}{\mathrm{Interpolate2D[MTF}(w)]}\right\} . \tag{6.3}$$

The deconvolution procedure was applied to the dark image corrected projection images ($i - \bar{d}$) and to the averaged reference images ($r - \bar{d}$) before calculation of the projection images according to Equation (2.45) [or more precisely Equation (D.4)]. The cyclic behavior of the DFT/FFT was not accounted for in the deconvolution (possible using zero padding) and might produce cross talk from one to the other side of the image upon deconvolution. However, the effect of cross talk is assumed to be negligible here, since the intensity falls off to almost zero at the edges of the images. In principle, the photoresponse of each pixel must be corrected prior to deconvolution, which can be achieved by normalization with a CCD flat-field image recorded with homogeneous illumination of the CCD. Because of the very small photoresponse non-uniformity of the CCD in the x-ray camera of ~1%, this correction could be omitted here.

6.2.4 Expected attenuation value

The mass attenuation coefficient $(\mu/\rho)_{bone}$ of bone at a certain photon energy can be calculated according to Equations (A.6) and (A.7) if its elemental composition is known. This was done using the elemental composition of cortical bone given in the ICRU-44 report[2] [84]. Using the elemental attenuation coefficients from the tables of Plechaty *et al.* [119], the total mass attenuation coefficient at 22 keV photon energy was calculated as $(\mu/\rho) = 2.99\,\mathrm{cm}^2/\mathrm{g}$. This value agrees perfectly with the mass attenuation coefficients tabulated by NIST.[3]

As mentioned above, the mass attenuation coefficient (μ/ρ) can be used to convert the measured x-ray attenuation coefficient μ into the bone density ρ. We will not convert our data, since the determined mass attenuation coefficient relies on unjustified assumptions on the elemental composition of the bone. However, we can calculate the attenuation coefficient that we can expect from the description of cortical bone in the ICRU-44 report for comparison with our data. At 22 keV, we obtain for the attenuation coefficient $\mu = \rho_{bone}\,(\mu/\rho)_{bone} = 0.57\,\mathrm{mm}^{-1}$, where an average bone density of $\rho_{bone} = 1.920\,\mathrm{g/cm}^3$ (given in the ICRU-44 report) has been assumed.

6.2.5 Results

Figure 6.11 shows a comparison of cross sections from the cortical bone sample that were recorded first with the untreated luminescent crystal, after application of the black layer, and after additional deconvolution of the PSF from the projection data. Figures 6.11(a) – (c) show the reconstructed cross sections. Actually, the reconstructions in the figure were reduced from the original reconstruction size (700×700 pixels) to about the size of the sample (540×540 pixels). All cross sections were recorded on the same central row of the CCD detector. The position of this line was marked in the measured edge profiles shown in Figures 4.3(a) and (b) of Chapter 4.

A closeup of the reconstructions is shown in Figures 6.11(d) – (f). Several ring artifacts are visible in the reconstruction of Figure 6.11(d). The two strong ring artifacts on the right half of the image can be directly attributed to the two (weakly visible) screen inhomogeneities that were shown in the closeup of Figure 4.3(d). The other less pronounced ring artifacts could not be related to any features in the edge profiles of Figure 4.3(a), which are probably too weak to be visible. The equivalent reconstructions obtained after application of the backing layer [closeups in Figures 6.11(e) and (f)] display no ring artifacts. The position of the luminescent screen may have been changed slightly upon remounting after application of the backing layer. Since the sample

[2] Data of the ICRU-44 report can be found online at a website of the National Institute of Standards and Technology (NIST): `http://physics.nist.gov/PhysRefData/XrayMassCoef/cover.html`. Table 2 gives the composition of cortical bone and other human tissues. Table 4 gives the mass attenuation coefficients for a number of photon energies. The elemental weight fractions for cortical bone are given as: H (0.034), C (0.155), N (0.042), O (0.435), Na (0.001), Mg (0.002), P (0.103), S (0.003), Ca (0.225).

[3] (See also the previous footnote). The closest tabulated value is given for photon energy $E_{ph} = 20\,\mathrm{keV}$ as $(\mu/\rho) = 4.001\,\mathrm{cm}^2/\mathrm{g}$. This agrees perfectly with our value $(\mu/\rho) = 2.99\,\mathrm{cm}^2/\mathrm{g}$ for $E_{ph} = 22\,\mathrm{keV}$ that was calculated here using the tables of Plechaty. The two values were compared by the relation $\mu \propto E_{ph}^{-3}$ given by Equation (A.13).

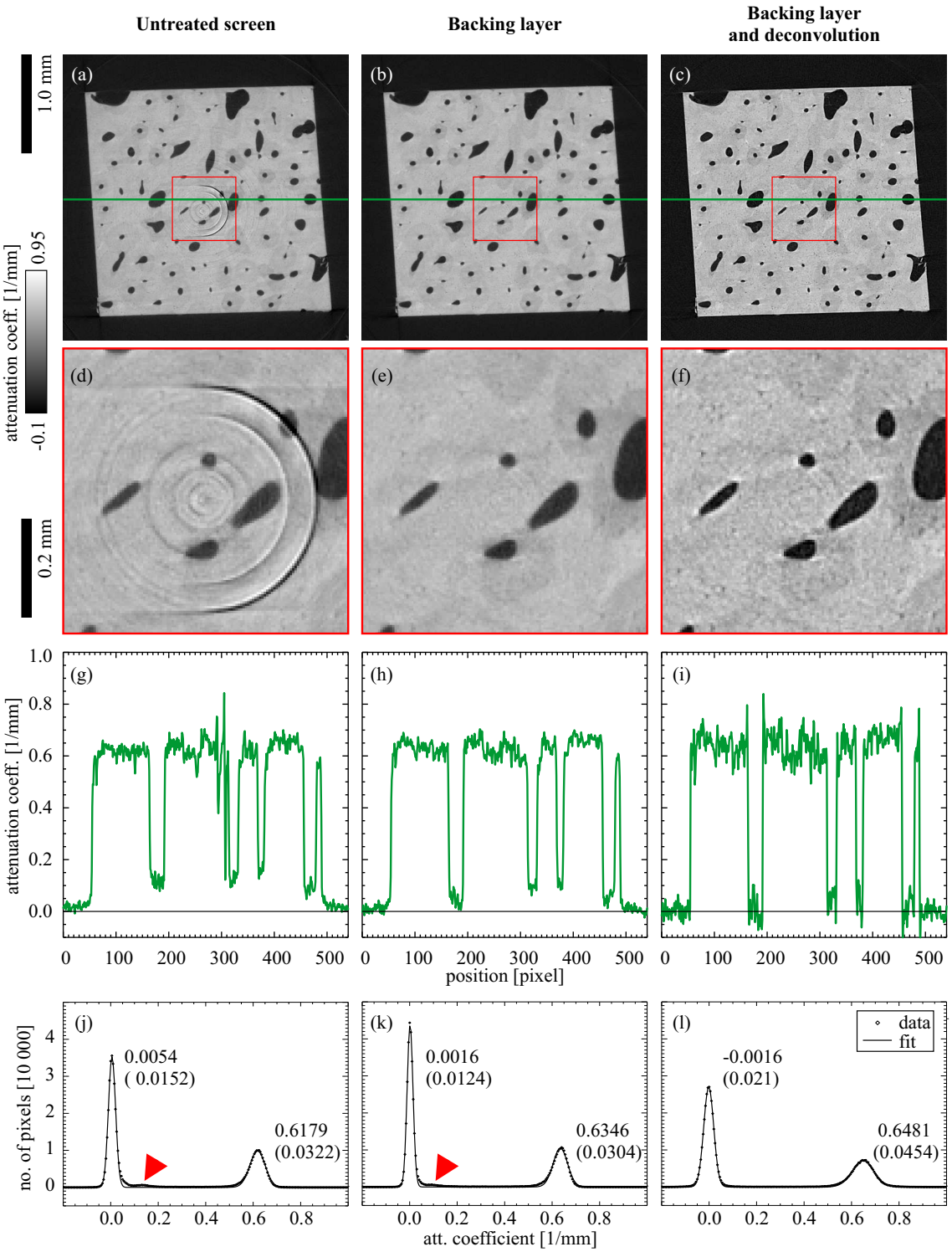

Figure 6.11: Comparison of SRμCT cross sections from a cortical bone sample that were recorded (a) with the untreated luminescent crystal, (b) after application of the black layer, and (c) with additional deconvolution of the PSF from the projection data. The size of the cross sections is 540×540 pixels. (d) – (f) Closeup from the red rectangle. (g) – (i) Attenuation profile along the green line. (j) – (l) Histogram over the entire reconstructed slice (700×700 pixels) together with the best fit of a function consisting of two Gaussians. For each Gaussian, its center and its sigma parameter (in brackets) is given. The red arrow in the histogram points to the peak caused by the observed non-zero attenuation in the Haversian canals. The peak is less pronounced with the backing layer and vanishes for the deconvoluted reconstruction.

remained fixed, all reconstructions show the same slice of the sample, but light generation may have taken place at a slightly different positions of the luminescent screen in the measurements carried out with and without backing layer. To ensure that this was not the cause for the vanishing of the ring artifacts, the adjacent slices were checked. Strong ring artifacts as from the two screen inhomogeneities under consideration could not be found in any other slice below or above the slice shown in Figure 6.11(c), and the significant reduction of ring artifacts could be verified for all slices.

From the closeups of the reconstructions in Figures 6.11(d) – (f) it is observed that the reconstruction becomes clearer after application of the backing layer and even clearer after the additional convolution of the data, i.e., blur is reduced. Edges appear pronounced in the deconvoluted data of Figure 6.11(f), which is visible as a small bright ring of 1 – 2 pixels extension around the Haversian canals. This effect appears like an overcompensation of the PSF by deconvolution.

The plots in Figures 6.11(g) – (i) show line profiles of the attenuation coefficient through the reconstructions in Figures 6.11(a) – (c). The attenuation coefficient in the presented reconstruction varies between $\sim 0.6\,\mathrm{mm}^{-1}$ for the darkest values inside the osteons (newly formed bone, low level of mineralization) and $\sim 0.7\,\mathrm{mm}^{-1}$ for the brightest values in the bone structure (high level of mineralization). These values were estimated from line profiles through the slice in Figure 6.11(b) after application of additional 4-fold binning to the slice, which provided averaged values. A relevant deviation from the expected attenuation coefficient is found in the small void spaces of the Haversian canals. The attenuation coefficient in the canals should be zero in an unblurred measurement but is clearly above zero for the case of the untreated crystal in 6.11(g).

Figures 6.11(j) – (l) show histograms of the attenuation coefficient that were calculated over from the reconstructed slices. Note that the histograms were calculated over the entire reconstruction (700×700 pixels) and include more pixels that contain air than are visible in the reduced cross sections of Figures 6.11(a) – (c). Position and width of the peaks in the histogram were quantified by fitting the sum of two Gaussian functions to each histogram. Center position and sigma parameter of the Gaussians for the air peak and the bone peak are given in the histograms. Stronger mineralized (old) osteons show a higher attenuation than the newly formed ones. However, it is impossible to resolve the bone peak into two peaks that would correspond to the contribution from newly formed and old osteons as might be expected. This is due to the continuous distribution of the attenuation coefficient within the osteons and the variation between osteons. A reduction of the peak widths is observed after application of the backing layer. As derived from the parameters in Figures 6.11(j) and (k) the reduction is about ~20% for the air peak and ~6% for the bone peak. This reduction can be explained by the suppression of weak ring artifacts. After deconvolution, which causes an amplification of high-frequency components (including noise), the peak width increases again by about 50%.

Intensity in the Haversian canals that was observed in the measurements appears in the corresponding histogram in Figure 6.11(j) as a small fraction of voxels with attenuation coefficient

significantly above zero and centered at about $0.12\,\mathrm{mm}^{-1}$ [marked by the red arrow in Figure 6.11(j)]. After application of the backing layer, the attenuation observed in the Haversian canals is reduced as it is visible in the line profile of Figure 6.11(h) and the corresponding histogram in 6.11(k). For the deconvoluted data set, the attenuation in the line profile of Figure 6.11(i) drops to zero in the Haversian canals as ideally expected and the peak in the corresponding histogram in 6.11(l) disappears.

6.2.6 Discussion

The significant reduction of ring artifacts after application of the absorbing backing is explained by the suppression of screen inhomogeneities that is caused by the backing layer (compare Chapter 4). Not only the clearly visible ring artifacts have disappeared after application of the backing layer, but also a reduction of the peak widths in the histogram is observed. This indicates the suppression of many weak (non-visible) ring artifacts, which cause a similar broadening of the peak widths as noise.

The attenuation coefficient was determined as $\mu = 0.6346\,\mathrm{mm}^{-1}$ from the position of the bone peak in 6.11(k). This value is about 10% above the theoretically expected value $\mu = 0.57\ \mathrm{mm}^{-1}$ that was derived for the elemental composition of cortical bone above. However, we can resolve bone and Haversian canals in our measurements. Thus, the theoretical bone density assumed in the calculation is too low, since it is an average over the bone tissue and the Haversian canals. The bone material (bulk) has a higher density and consequently a higher attenuation coefficient that will be very close to the measured value. Differences may of course also arise due to variation of the elemental bone composition and/or density.

The position of the bone peak indicates the improvement in the absolute measure of the attenuation coefficient. Blur on the reconstructions produces voxels that take an attenuation coefficient between the true zero attenuation of air and the attenuation coefficient of bone (partial volume effect). This is most pronounced for the space in the Haversian canals. The intensity that appears blurred into the Haversian canals is lost for the surrounding. Thus, the bone peak is shifted towards lower values compared with the true attenuation coefficient. Upon application of the black backing, the bone peak shifts back up (from 0.6179 to $0.6346\,\mathrm{mm}^{-1}$) by 2.7%, and after deconvolution (to $0.6481\,\mathrm{mm}^{-1}$) by another 2.1%. The combined effect of backing and deconvolution thus causes an increase of the measured bone density by 4.8%. The zeroth-order moment of the reconstructions was determined and increases by 0.6% and 0.5% at the same time. This can be explained as a non-linear effect caused by detector blur, whereby the zeroth-order moment decreases (compare Section 2.5.1). The change of the zeroth-order moment is significantly smaller than the peak shift, which indicates that blur predominantly makes a linear effect here.

The intensity in the Haversian canals becomes zero (as ideally expected) after application of the black backing and additional deconvolution. This indicates that a precise measurement of absolute attenuation coefficient with simultaneously high spatial resolution is achieved in this case.

As described above, the PSF seems to have been overcompensated by the deconvolution. This effect can occur, when the MTF used for deconvolution does not describe the PSF on the short length scale correctly. Since short-range contributions to the PSF are difficult to measure, this is not very surprising. Compare also the discussion on measurement of the MTF in Appendix D.1. Hence, the simple direct (Fourier) deconvolution approach applied here is not optimal for the restoration of high-frequency components in the reconstruction, while it is very efficient in the suppression of long-range blur. It would of course be better to record unblurred projections than to perform a deconvolution operation on the recorded images, since deconvolution always requires assumptions on the detector response and degrades the image quality to some extend. The suppression of blur by the backing layer is thus the right approach. But since we cannot suppress blur in this type of detector entirely, the additional use of a proper deconvolution method is advised.

Deconvolution, or more generally, image processing of the radiographic images prior to reconstruction (image pre-processing) should thus be exploited beyond the direct deconvolution approach. The development of image pre-processing steps that achieve deconvolution of predominantly the long and middle range PSF with minimal amplification of high-frequency components (and noise) seems feasible and should be investigated. The application of optimal digital filters that make use of the approximately known PSF and the noise characteristics (as, e.g., the Wiener filter) should be systematically investigated and further developed in a future work.

Other ongoing studies such as the morphological characterization of bone around dental implants [35], titanium implants [18], [19], or the in-vitro/in-vivo corrosion measurement of magnesium implants [60], [160] will directly profit from the enhanced performance of the SRμCT setup.

6.2.7 Summary

The apparently first SRμCT scan was presented here, in which the luminescent screen of the x-ray camera carried a black backing as optical coating. The effect of the absorbing backing on the reconstruction was investigated using as an example the measurement of cortical bone. Furthermore, the influence of deconvolution of the MTF (PSF) from the recorded projections prior to reconstruction was studied. It was found that ring artifacts in the reconstruction are drastically reduced after application of the absorbing backing. Blur was partly removed after application of the backing and finally removed by the deconvolution operation. The combined removal of blur caused a 4.8% increase of the average attenuation coefficient of bone, as was determined from the shift of the bone-peak position in the histogram and resulted in an accurate reconstruction of the attenuation coefficient of bone. This is essential for the precise determination of the bone mineral density that can be further used, e.g., for the study of osteoporosis or as input parameter for finite element models that allow for the simulation of the mechanical bone properties.

6.3 Porosity of hydroxyapatite scaffolds

6.3.1 Introduction

Hydroxyapatite is a calcium phosphate with promising properties as building material for bone grafts that are needed in medical surgery for the substitution of large bone defects. Rapid prototyping techniques such as 3D printing in principle allow for the preparation of patient-specific scaffolds based on medical CT or MRI[4] data. The design of the scaffolds has to fulfill different criteria to ensure cell viability and function. These include nanoporosity to allow diffusion of molecules for nutrition and signaling, micropores to ensure cell migration and capillary formation as well as macropores for arteries and veins [58]. Consequently, the analysis of the scaffold porosity is important for the optimization of the manufacturing process and the implant design. The quantification of the porosity using other techniques such as Hg-porosimetry and electron microscopy is problematic and does not yield a satisfying description. In this study, SRμCT was used to provide information on the structural properties of interest.

Goal of the SRμCT study was the morphological characterization of the volume structure on three different length scales: macroscopic (down to ~0.1 mm), microscopic (down to ~5 μm), and nanoscopic (below ~1 μm). SRμCT allows for the morphological characterization in the macroscopic and microscopic regime. Methods from 3D image analysis as, e.g., the euclidean distance transform (compare, e.g., Müller *et al.* [106]) can be applied for this purpose. Results of this study, especially on the characterization of scaffolds on the microscopic scale, were presented by Irsen *et al.* [86].

Structures on the nanoscopic scale cannot be spatially resolved by SRμCT. However, the porosity at this scale can be determined from the reconstructed attenuation coefficient, when attenuation coefficient and density of the bulk material are known. Thus, the characterization on the nanoscopic scale requires the precise reconstruction of the attenuation coefficient. Any influence of the reconstruction algorithm on the reconstructed attenuation value will thus directly influence the measured porosity and must be avoided.

The reconstruction algorithm itself can influence the reconstructed attenuation coefficient. A comparison of the precision that can be achieved with the two different algorithms discussed in Section 3.2.2 is presented here. Reconstructions of hydroxyapatite scaffolds that were studied by SRμCT will be used for demonstration. In fact it was during this study, that the slight deviation caused by the applied reconstruction algorithm was recognized.

[4] magnetic resonance imaging (MRI)

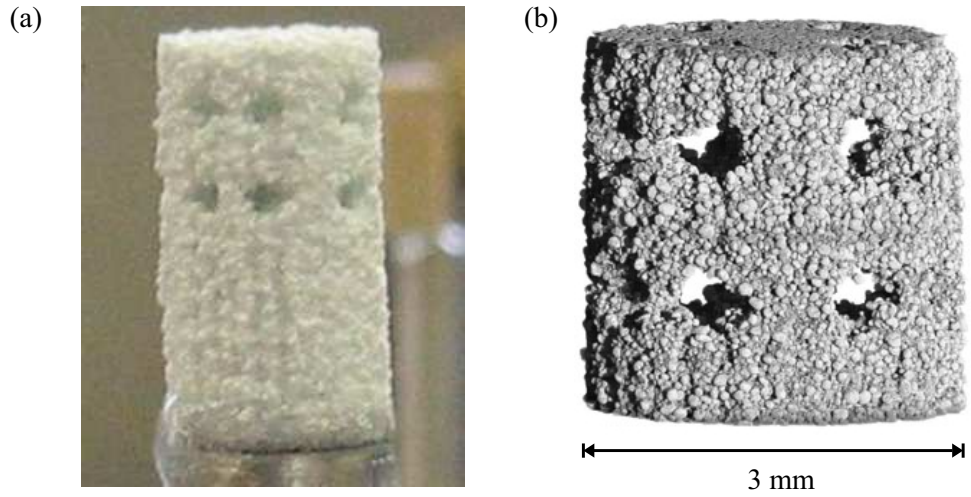

Figure 6.12: (a) Photograph of a 3D-printed scaffold and (b) 3D rendering of the SRμCT data of the same sample.

6.3.2 Sample preparation

The examined hydroxyapatite scaffolds were prepared at the Caesar Research Center.[5] An experimental 3D-printing setup (Bio-3DP) was used for the fabrication of all scaffolds. A detailed description of the 3D-printing facilities used for this study was presented by Seitz *et al.* [135]. Figure 6.12(a) shows a photo of a sample after printing. The corresponding volume rendering from the recorded and reconstructed tomographic data is shown in Figure 6.12(b).

Hydroxyapatite granules for 3D printing were prepared by spray drying of water based hydroxyapatite slurries (solid content of 55 weight percent). Various organic additives were added to the hydroxyapatite suspensions for adjustment of slurry as well as granule properties.

The 3D printing was performed with an ink-jet like printer in a layer-by-layer process that comprises of three repeating steps: In the first step a layer of powder (hydroxyapatite granulate) is spread on the building platform. Thereafter, a 2D layer of binder solution is printed onto this powderbed, which glues the granules in the wetted regions together. Finally, the building platform is lowered corresponding to the layer thickness and the process is repeated for the following layer, which is prepared on top of the previous one. All investigated samples were printed with an pitch size of 250 μm in the slices and a slice thickness of 200 μm. The mean droplet diameter was in the range of 200 μm.

The final 3D-printed scaffold (green body) was removed and freed from unglued powder using a slight airstream. To enhance the mechanical stability of the 3D-printed scaffolds, the green bodies are normally sintered. Upon transformation from the green body to the final sintered body, the material develops the desired mechanical properties. The density of the material and its strength are increased. The details of the production process were described in [86].

[5] Samples were prepared by Stephan Irsen, Caesar Research Center, Ludwig-Erhard-Allee 2, 53175 Bonn.

6.3.3 Measurement and reconstruction

Table 6.4: Scan parameters for hydroxyapatite measurements. Here m is the optical magnification, τ is the effective pixel size, a_{10} is the spatial resolution. Unchanged parameters are not repeated.

Beamtime/ scanname	Sample	Beam- line	Energy [keV]	Mode	m	τ [μm]	a_{10} [μm]
desy2005a/eth01a	sintered	BW2	24.0	180deg	2.11	4.27	6.36
desy2005a/eth02a	green body						
desy2005a/eth03a	infiltrated gr. body						
desy2005b/eth10a	compr. gr. body	BW2	24.0	180deg	2.139	4.21	7.04
desy2005b/eth11a	compr., sintered						

Scaffolds were examined in different production states. Table 6.4 gives an overview of the measured samples and the scan parameters. All measurements were carried out at HASYLAB beamline BW2 at the highest available photon energy of 24 keV within two different measurement periods (beamtimes) in 2005. The same luminescent screen with backing layer was used in both beamtimes. The scans were performed in '180deg' mode with $N_t = 720$ recorded projections in each scan.

One slice of each data set was reconstructed for this comparison using both the "RALA"-type reconstruction and the "BKFIL"-type reconstruction algorithms (IDL implementation) presented in Chapter 3. The center of rotation required for reconstruction was determined for each slice using the method presented in Chapter 5 with precision of 0.05 pixel using metric Q_{IA}.

6.3.4 Comparison of "RALA"- and "BKFIL"-type reconstruction

The difference in the "RALA"-type reconstruction according to Ramachandran and Lakshminarayanan [128] and the "BKFIL"-type reconstruction algorithm according to Budinger and Gullberg [30] was explained in Section 3.2.2. As discussed, a shift towards negative attenuation values is expected for the "BKFIL"-type reconstruction. Thus, the reconstructions were compared in order to investigate this shift and to detect possible further differences.

Two homogeneous samples (compressed raw material as green body and after sintering) and a structured 3D-printed sample (as green body) were selected for the comparison here. Figure 6.13 shows the reconstructions from the three data sets that were calculated by "RALA"-type reconstructions. The equivalent reconstructions calculated with the "BKFIL"-type reconstruction appear visually identical and are therefore not shown. Histograms over the reconstructed slices were calculated for both types of reconstruction and are again shown only for the "RALA"-type reconstruction next to the corresponding reconstructions. The histograms for the "BKFIL"-type reconstructions (not shown) appear identical except for a slight shift. The position and width of the peaks corresponding to air (surrounding) and the material itself were determined. For this

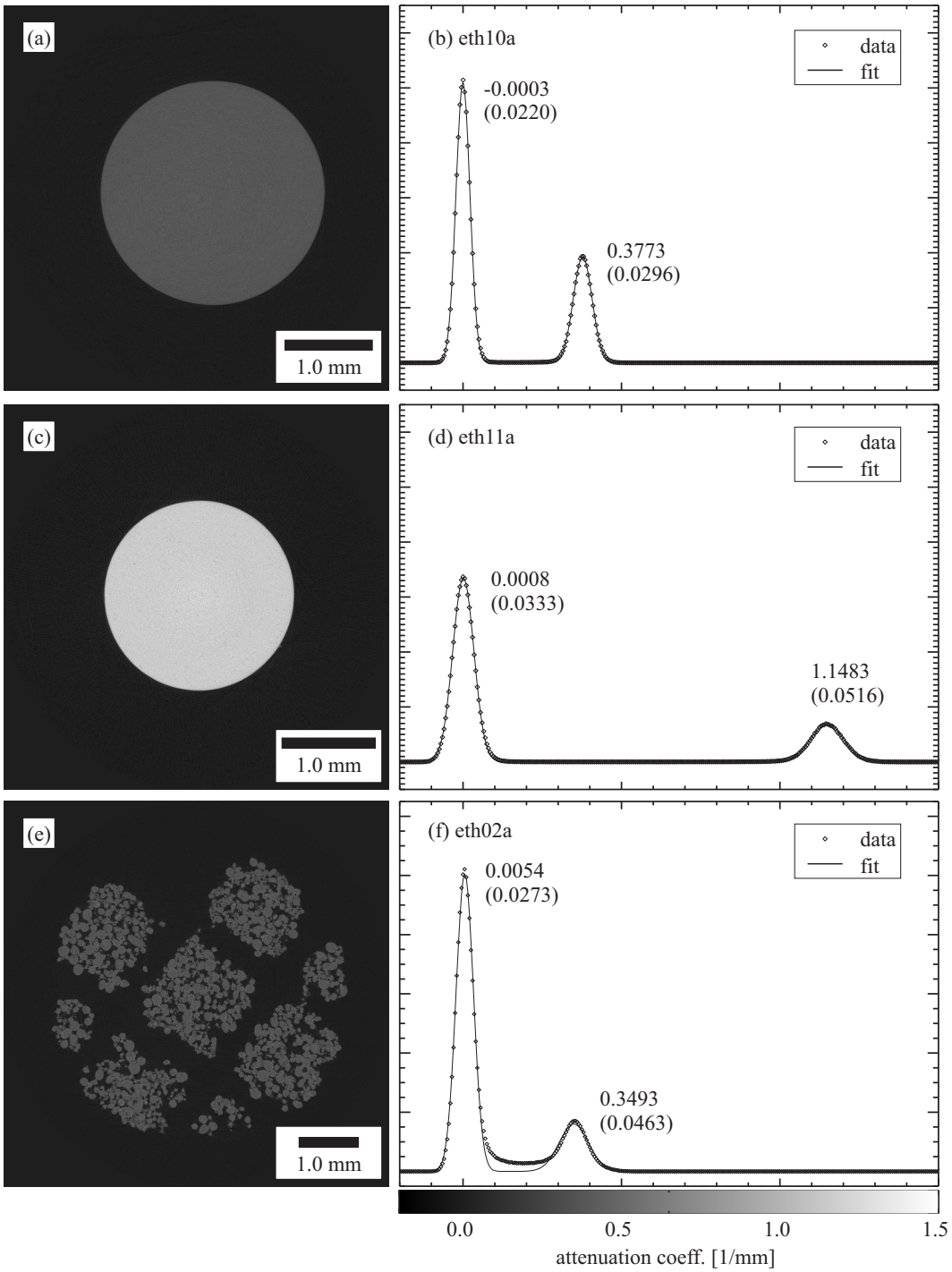

Figure 6.13: Tomographic reconstructions of hydroxyapatite granules in different production states: (a) Compressed green body, (c) compressed and sintered body, and (e) 3D-printed green body. All reconstructions were calculated using the "RALA"-type reconstruction algorithm. (b), (d), and (f) show the corresponding histograms recorded for each slice together with the best fit of a function that is the sum of two Gaussians. Position and sigma parameter for each Gaussian are printed next to the corresponding peaks (sigma parameter in brackets). The scale of the histogram ordinate is given in arbitrary units and was enlarged for the histogram of the 3D-printed green body.

purpose a least-squares fit to the histogram was made using a fit function consisting of the sum of two Gaussian functions. The position and width (sigma parameter) of each Gaussian are given in the histograms.

The average difference, i.e., the shift of the attenuation value between the two different reconstructions was calculated as

$$\overline{\Delta f} = \overline{f_B - f_R}\,, \tag{6.4}$$

where f_B is the reconstruction obtained from "BKFIL"-type, f_R is the reconstruction obtained from the "RALA"-type reconstruction, and the overline indicates the average over the (circular) reconstructed area. Since the reconstruction is a linear calculation, the shift $\overline{\Delta f}$ depends on the zeroth-order moment (total mass) of the reconstruction. For comparison of the shift for the different slices, we thus needed to compare the relative shift $\overline{\Delta f}/\overline{f}$. Here, $\overline{f}$ is the average density in the reconstructions calculated as

$$\overline{f} = \frac{\overline{(f_B + f_R)}}{2}\,. \tag{6.5}$$

The determined absolute shift $\overline{\Delta f}$ and the relative shift $\overline{\Delta f}/\overline{f}$ are given for each slice in Table 6.5. It was found that for all reconstructed slices, the reconstructions by the "BKFIL" algorithm were shifted to negative attenuation values. The observed relative shift between the two types of reconstruction varies between −1.47% and −3.30%. This variation can be explained by the variation of the projection (sinogram) width with different number of sampling points N_t (given in Table 6.5) for the different sinograms as was discussed in Section 3.2.2. For identical values of N_t, as for scans eth02a and eth03a, the same relative shift is observed. The reconstructions were compared for further differences. The difference image of the reconstructions $f_B - f_R - \overline{f}$ (corrected for the shift) showed structure with intensity far below the noise level of the reconstructions. Thus, no other relevant difference than the uniform DC-shift was found.

For the data sets shown in Figure 6.13, additionally to the average value, the position of the histogram peaks was compared for both types of reconstruction. As expected for pure DC-shift the difference in the peak positions between the two algorithms agreed perfectly with the size of the DC-shift $\overline{\Delta f}$ for all three samples.

So far, we compared the reconstructions obtained with both types of algorithm relative to each other. The position and width of the histogram peaks were then used to check the absolute precision of each algorithm. For the homogeneous and cylindrical samples shown in Figures 6.13(a) and (c), the attenuation coefficient in the slice is constant over large areas that correspond to either hydroxyapatite or air. Hence, a very accurate position of the peaks (negligible influence of the partial volume effect and blur) in the histogram can be expected. Note that the attenuation coefficient of air should be exactly zero in these measurement because we measure the attenuation coefficient relative to air. Therefore, we can use the position of the air peak μ_B^{air} for the "BKFIL"-type reconstruction and μ_R^{air} for the "RALA"-type reconstruction of these measurements (given in Table 6.5) directly as a measure for the absolute offset Δf_{abs}.

Table 6.5: Shift from "RALA"-type to "BKFIL"-type reconstruction.

Beamtime/scanname	N_t	$\overline{\Delta f}$ [1/mm]	$\overline{\Delta f}/\overline{f}$ [%]	μ_B^{air} [1/mm]	μ_R^{air} [1/mm]
desy2005a/eth01a	1136	-0.00771	-3.30	-[a]	-
desy2005a/eth02a	1536	-0.00126	-1.47	0.004140	0.00540
desy2005a/eth03a	1536	-0.00136	-1.47	-	-
desy2005b/eth10a	968	-0.00353	-2.75	-0.00386	-0.00032
desy2005b/eth11a	936	-0.00665	-2.38	-0.00583	0.00085

[a]- Not determined.

The air peak of sample eth11a in the "RALA"-type reconstruction showed the highest deviation from zero of $\mu_R^{air} = -0.00583\,\mathrm{mm}^{-1}$. To get a better understanding of the relative error in the measurement, this deviation must be compared with the attenuation coefficient of the material μ^{mat} that is to be examined. Since the attenuation coefficient of the material is in the order of $\mu^{mat} \approx 1\,\mathrm{mm}^{-1}$ in this case, we find a relative deviation $\Delta f_{abs}/\mu^{mat}$, which is in the order of 0.5% for the "BKFIL"-type reconstruction and below 0.1% for the "RALA"-type reconstruction for both measurements eth10a and eth11a. The simple conclusion from this is that the "RALA"-type implementation of the filtered backprojection algorithm should be preferred.

The noise level (error) in the reconstructed attenuation values is closely related to the sigma parameter of the histogram peaks. The sigma parameter of the peaks in the measurement of homogeneous objects (measurements eth10a, eth11a) gives a direct measure for the noise level. We estimated a noise level of about $\sigma_\mu = 0.03\,\mathrm{mm}^{-1}$ from the width of the air peaks in Figures 6.13(b) and (d). This value is almost a factor of ten higher than the shift caused by the "BKFIL"-type reconstruction. Note that this does not make the DC-shift negligible: The sigma parameter describes the variation of the attenuation coefficient in an individual pixel, i.e., it can be reduced by averaging over many pixels, while the DC-shift will not be reduced by averaging. The DC-shift shifts the peak positions in the histogram, while additional noise 'only' increases the peak widths.

It was observed that the noise level (width of the fitted Gaussian) for the material peak is higher than for the air peak in all three histograms of Figure 6.13. This can be related to the lower average photon count that is recorded in the projection of the central region of the sample (due to the sample thickness), when compared with the outer regions, where almost no attenuation is observed. The lower photon count results in the higher noise level in the projection (compare Section 2.5.2).

6.3.5 Results and discussion

The reconstructions/histograms of Figure 6.13 calculated with the "RALA"-type were used for the calculation of average porosities. The compressed material in the sintered sample in Figure 6.13(d) has an attenuation value of $\mu = 1.1483\,\mathrm{mm}^{-1}$, which is given by the material-peak position

in the histogram. This value can be directly compared with the attenuation value expected for stoichiometric hydroxyapatite [$Ca_{10}(PO_4)_6(OH)_2$] at 24 keV photon energy and of density ρ_{HA} = 3.156 g/cm^3, which is μ = 1.199 mm^{-1}. Here, the data of Plechaty *et al.* [119] were used for the calculation of the attenuation coefficient. The somewhat lower value measured for the attenuation coefficient must be due to a slightly lower density of the compressed body as compared with the assumed bulk density. The density was calculated relative to the bulk density as ρ = 95.7%ρ_{HA}, i.e., a porosity of about 4.3% was found.

The nanoscale porosity of the granular material can be derived from the comparison of the materials attenuation coefficient in the measurements eth02a (green body) and eth10a (green body, compressed). Thus, the densities of the materials in Figures 6.13(a) and (e) were compared relative to each other. However, the air peak of the 3D-printed, fine-structured sample in Figure 6.13(e) is significantly shifted from zero towards higher attenuation values, while the material peak that must be compared to the peak of the base material in Figure 6.13(a) shifts towards lower values. This indicates that part of the pixels are influenced by the partial volume effect and by detector blur (compare Section 3.3.6). This causes pixels (voxels), especially those close to a material-air surface, to take on attenuation coefficients in the range between the attenuation coefficient of air and that of the bulk material. The direct comparison of histogram peaks will thus be influenced by this effect. A histogram free of blur artifacts should be obtainable after deconvolution of the PSF (compare Section 2.5.3). However, this approach relies on the precise measurement of the PSF (compare Section D.1 and the previous Section 6.2) in the short distance range (several pixels) and increases the noise level in the data. Another way towards a histogram that is free of blur and of partial volume effects, might be given by the exclusion of surface voxels from the histogram using an appropriate mask. So far, we obtained the ratio of densities directly from the ratio of peak positions. The porosity of the granular material was determined by comparison of the material peak position as 7.4% (ratio of attenuation coefficients 92.6%).

6.3.6 Summary

The difference between two implementations of the filtered backprojection algorithm was discussed using the example of a study on hydroxyapatite scaffolds. The DC-shift caused by the "BKFIL"-type reconstruction algorithm was shown to cause an effect in the order of 0.5% relative to the attenuation value that was to be measured. It was shown that this DC-shift in the reconstruction is avoided by use of the "RALA"-type reconstruction algorithm. For the "RALA"-type reconstruction, a relative shift of less than 0.1% was verified, as was deduced from the position of the air peak in the histograms that were obtained for homogeneous material. The selection of the appropriate reconstruction algorithm thus enabled the measurement of a precise attenuation coefficient for hydroxyapatite.

Hydroxyapatite scaffolds were examined in several production states and their nanoscopic porosity was determined. The presented results complement the results obtained on the macro-

and microscopic scale previously. They give valuable insights into the nanoporosity that can be used as feedback for the optimization of the manufacturing process.

6.4 Microstructure of fiberboard

6.4.1 Introduction

Medium and high density fiberboard (MDF/HDF) are common wood composite products that are widely used in the furniture industry and for laminate flooring. About 33 Mio. m^3 of MDF [as the typical MDFs shown in Figure 6.14(a)] were commercially produced in the year 2004 alone. Fiberboard is made of a wood furnish material consisting of single wood fibers and fiber bundles. During production the wood furnish is treated with adhesive and consolidated under temperatures in the range from 180 to 220 ^{o}C to panels of different densities ranging from 300 to 800 kg/m^3 for MDF and from 800 to about 1000 kg/m^3 for HDF. Examination of the fiberboard microstructure is important for modeling and understanding of the relation between the microstructural features and the macroscopic behavior of the end product and, clearly, can have a strong economical impact.

Macroscopic properties of fiberboard such as the mechanical strength, thermal conductivity, and the water vapor transmission are largely determined by the fiberboard's three-dimensional microstructure. The microstructure of the composite and the effect of the compression process on the individual fibers is usually studied by scanning electron or light microscopy. However, both methods suffer from surface artifacts that can easily be created during sample preparation and are limited to the examination of two-dimensional surfaces. Simulations of the macroscopic fiberboard behavior have so far been based on assumptions about the microstructure or have used random generated structures as an input for the simulation (see Faessel *et al.* [55], Wang and Shaler [155], and the PhD thesis by Wang [154]). A simplified description of the fiberboard microstructure from measured data has so far not been available as input for these simulations.

In this study, the microstructure of MDF of four different densities was recorded three-dimensionally using SRμCT. The measurements were carried out with x-ray attenuation contrast at 12 keV photon energy at beamline BW2 of HASYLAB/DESY. Goal of the study was the extraction of material parameters that can be used as input for simulations or for statistical analysis. Additionally, the visualization of the spatial distribution of adhesive on the fibers was attempted. For this purpose marker substances were added to the adhesive prior to fiberboard production. A segmentation procedure was developed for this purpose that makes use of 3D image processing methods. The study was performed in collaboration with the 'Zentrum Holzwirtschaft' and the 'Fachbereich Informatik' of the University of Hamburg. The procedure for the segmentation of fiber parameters from the SRμCT data and first results of the statistical analysis were published by Walther *et al.* [152].

The small structure size of the fiberboard, which is in the order of the spatial resolution of the camera, made the segmentation of wood fibers challenging. A systematic oscillating structure (artifact) that was observed close to the around 2 – 5 μm thick cell walls will be discussed here.

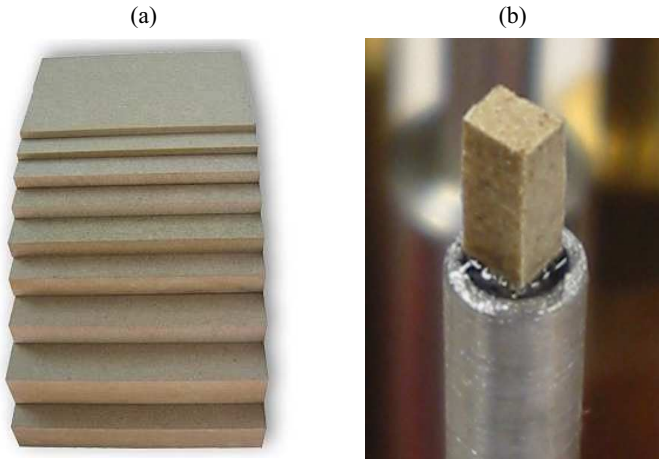

Figure 6.14: (a) Industrially produced medium density fiberboards. (b) A laboratory sample measuring $2 \times 2 \times 5$ mm glued to the sample holder.

6.4.2 Literature review

Fiberboard and paper both are cellulosic structures with similar properties. A few studies on the three-dimensional microstructure of both materials have been presented in recent years.

Among the first Groom *et al.* [69] derived quantitative information from SRμCT data of fiberboard. They applied absorption contrast microtomography for the examination of a single MDF sample measuring $1.3 \times 1.1 \times 0.4$ mm at the X2B beamline of the National Synchrotron Radiation Light Source (NSLS) using 8.5 keV radiation. They discussed the effect of fiber properties (physical, mechanical), fiber-to-fiber stress transfer, and fiber orientation onto the fiberboard's macroscopic properties. The authors determined parameters of individual fibers as the secant (straight line connecting the fiber ends) length and curl (ratio of secant length and segment length) from the volume data by manual image interpretation. Faessel *et al.* [55] investigated the structure of fiberboard by means of SRμCT and derived a pore size distribution from the data. They presented a simulation of the thermal conductivity, which they based on a simulated three-dimensional random model for the description of fiberboard rather than on the measured SRμCT data. Their thermal conductivity model is based on the distribution of fiber lengths, the fiber density (porosity), the average orientations of the fibers, and the tortuosity of fibers.

Sintorn *et al.* [138] obtained the three-dimensional representation of a single paper sample from a series of in total 73 SEM images of microtome sections. The resolution within the sections (pixel size: 0.7 μm) is, thus, about seven times higher than in the direction of the surface normal, where the distance between consecutive sections is 5 μm. The sample was embedded in epoxy. Image processing was used in this publication for the labeling of individual pores.

An SRμCT study on the microstructure of paper was presented by Antoine *et al.* [1] and was also described in the PhD thesis of Weitkamp [157]. The authors made use of near-field coherent imaging with a partially coherent x-ray beam of 20 keV photons at the ID22 beamline of the

European synchrotron radiation facility (ESRF). They claim that higher spatial resolution can be obtained in near-field coherent imaging when compared to absorption contrast mode. However, they present no measure of resolution. Using image processing methods, they obtained a binary representation of air space and fibers. Holmstad [78] and Holmstad *et al.* [79] compared SRμCT in phase contrast mode with conventional μCT and presented a number of image processing tools for the investigation of paper.

Du Roscoat *et al.* [130] presented another SRμCT study of paper performed at the ID19 beamline of the ESRF. The photon energy of this study is not reported. Absorption contrast seems to have been dominating, although the authors describe that phase contrast can be recognized in the reconstruction as a fringe pattern at edges.

6.4.3 Sample preparation

Fiberboards were produced in a laboratory hot-press at the 'Zentrum Holzwirtschaft' at the University of Hamburg with densities of 300, 500, 800, and 1 000 kg/m^3 (i.e. 1 000 kg/m^3 = 1 g/cm^3) and a thickness of 5 mm. Furthermore, another two series of boards with the same density settings were produced. For these, the adhesive was stained with either iodine or barium sulfate ($BaSO_4$) as marker for visualization. Another set of boards contained a combination of 50% wood fibers and 50% sisal or hemp fibers.

Samples of 2×2 mm size were cut out from the 5 mm thick fiberboards, thus resulting in a sample volume of about $2 \times 2 \times 5$ mm [see Figure 6.14(b)]. The fiberboards were manually cut using razor blades, which produced almost artifact free surfaces. The density profile of the fiberboard along its surface normal is symmetric with respect to the center of the fiberboard. Thus, only one half of the 5 mm long samples had to be investigated for the qualitative description of the entire fiberboard profile.

6.4.4 Measurement and reconstruction

Following preliminary studies in 2004, the total of 15 samples was scanned within two days in January 2005 at beamline BW2 of HASYLAB. The photon energy was 12.0 keV and the optical magnification factor $m = 3.94$ resulted in a sampling interval (effective pixel size) of $\tau = 2.28\,\mu$m. The spatial resolution corresponding to 10%-MTF value was determined as $a_{10} = 3.9\,\mu$m from the projection of a gold edge as described in Section D.1. In '180deg' mode, $N_\theta = 720$ projections were recorded using the full field of view of the camera, which measured 1536×1024 pixels or correspondingly 3.51×2.34 mm. The scan parameters are summarized in Table 6.6. Two scans were recorded per sample at different distances from the sample surface and combined into one stacked data set (compare Section D.2). By combination of the data, a little bit more than half the sample thickness was covered and, thus, all relevant information about the otherwise symmetrical fiberboards obtained. The center of rotation was determined for each scan from the sinogram

Table 6.6: Scan parameters for MDF measurements. Here m is the optical magnification, τ is the effective pixel size, a_{10} is the spatial resolution.

Beamtime/scanname	Beamline	Energy [keV]	Mode	MTF	m	τ [μm]	a_{10} [μm]
desy2005a/holz01a,b desy2005a/holz02a,b desy2005a/holz03a,b ... desy2005a/holz15a,b	BW2	12.0	180deg	mtf00120	3.94	2.28	3.90

data using the method presented in Chapter 5 with precision of 0.05 pixel and using metric Q_{IA}. Reconstruction of the data was performed using the "BKFIL"-type algorithm on a 1536×1536 reconstruction grid. The DC-shift (compare Section 3.2.2) caused by this algorithm is not of relevance for the performed three-dimensional segmentation of the data described below.

Cellulosic samples can be sensitive to humidity and temperature. Du Roscoat *et al.* [130] observed swelling of paper samples in their measurements. No swelling was observed for the studied samples here and, probably, the swelling is much less critical for fiberboard than it is for paper. Nevertheless, care was taken, to bring the samples to the laboratory place of examination in reasonable time before the measurement and to maintain constant climate conditions at the place of examination before and during the measurement.

Figure 6.15 shows the cross section of a typical sample that was prepared with orientation parallel to the rotation axis. The cross section of most of the wood fibers is visible in this view, since the preferred fiber orientation is parallel to the fiberboard surface, i.e., perpendicular to the rotation axis.

6.4.5 Spatial resolution and noise

The structure size of wood fibers is close to the spatial resolution limit of the x-ray camera. The outer fiber diameter is in the range of 10 – 20 μm and the fiber wall thickness is in the range of 2 – 5 μm. Thus, the typical fiber wall thickness corresponds to the extension of just about two pixels ($\sim 2\tau$), where $\tau = 2.28\,\mu$m is the effective pixel size of the detector and the voxel size in the reconstructed volume. The spatial resolution of the camera was determined from an edge profile measurement as $a_{10} = 3.90 \approx 1.71\,\tau$.

Figure 6.16 shows a magnified subregion of an unstained MDF sample with density 500 kg/m^3. The cross section of several cells is clearly visible. However, the attenuation coefficient systematically deviates from zero at some places outside the fiber material and displays a structure that cannot be explained simply as noise or blur. Negative values are found for the attenuation coefficient in short distance (2 – 3 pixels) from the center of the fiber walls, while at larger distance (5 – 6 pixels) a slight increase of the attenuation coefficient to clearly above zero is observed. This

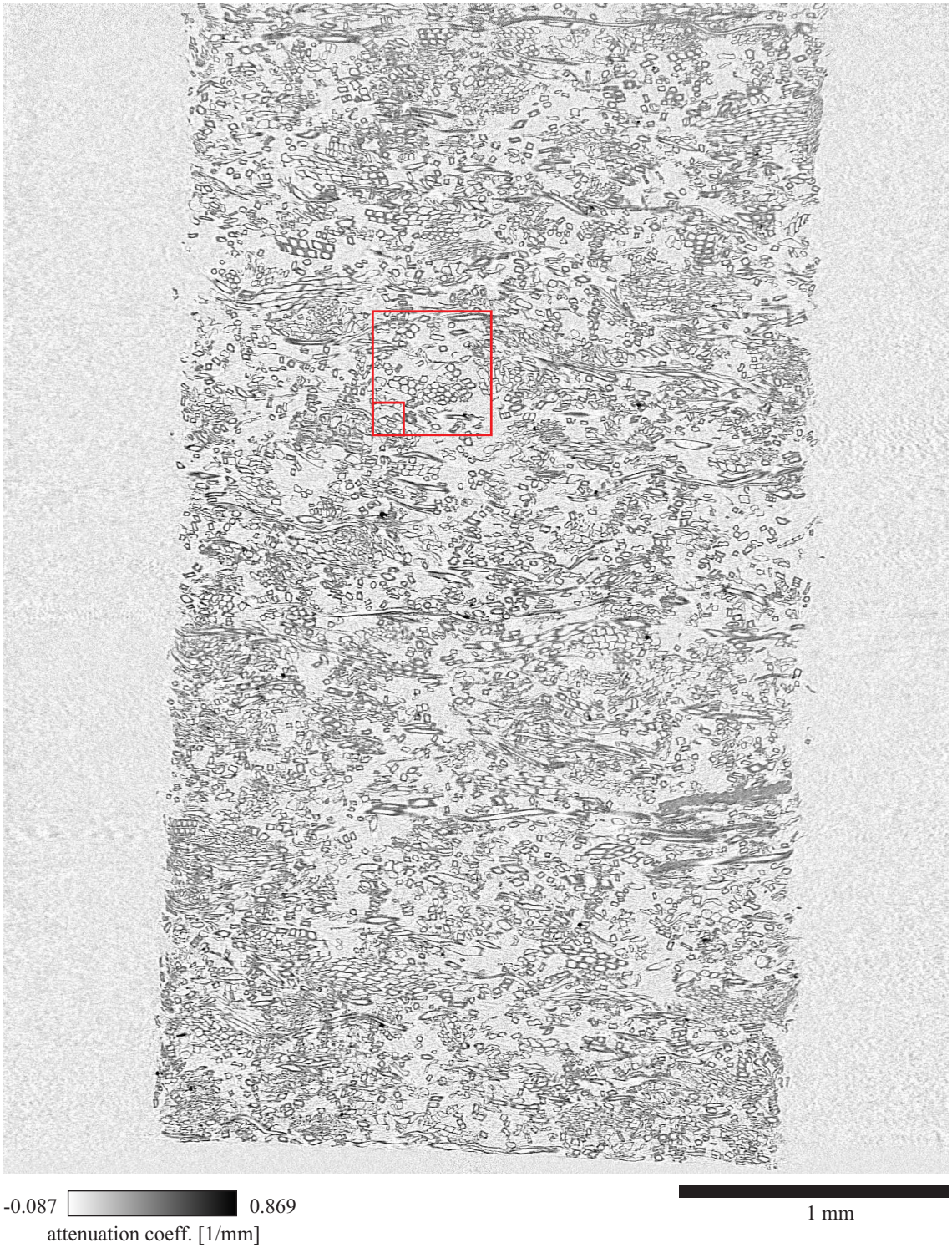

Figure 6.15: Cross section of an MDF sample with density 500 kg/m^3. The orientation of the slice is parallel to the rotation axis and has been produced from a combination of two μCT scans at different sample positions. The size of the image is 1536×1901 pixel, the first value corresponding to the CCD width. The pixel edge length is $\tau = 2.3\,\mu$m.

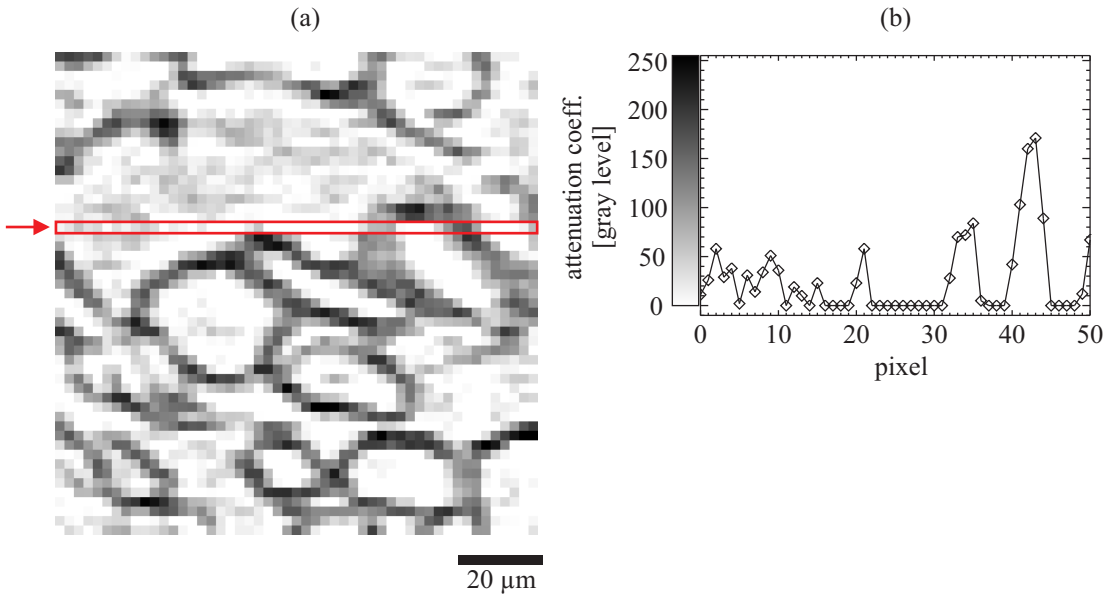

Figure 6.16: (a) Magnified subregion of the unstained 500 kg/m^3 sample from the smaller box in Figure 6.15. The size of the image is 50×50 pixels. (b) Plot of the attenuation in units of image gray levels (0 – 255) along the row marked in the subregion. Zero attenuation corresponds to a value of ~23. The noise structure on the left and the fiber walls on the right are in a similar range of values. Close to the fibers, the attenuation coefficient systematically takes values below zero attenuation.

effect appears like the so-called ringing effect that can be caused by the naturally band-limited reconstruction process. The band limit causes oscillations similar to the Frauenhofer diffraction pattern of a circular aperture in the reconstruction as it was discussed in Section 3.3.1. Presumably, the negative attenuation coefficient close to the fiber walls corresponds to the first minimum of the diffraction pattern, and the positive attenuation coefficient next to this minimum corresponds to its first maximum. The effect was simulated by reconstruction of a model system that simulates the fiber structures. For this purpose a 2D model system was constructed of two concentrical circles (ellipses with equal axis parameters, see Appendix E) of opposite sign. The projection was calculated and blurred by a Gaussian function with width corresponding to the measured resolution parameter. Reconstruction of the sinogram reproduced the negative attenuation values between the cell walls qualitatively, while the positive attenuation value in larger distance could not be reproduced. It is believed that the effect can be fully reproduced, when the real point spread function of the detector would be used for the simulation. The PSF is however difficult to determine, especially on the short length scale of a few pixels that is of interest here (compare Section D.1). Note that the PSF itself is band limited by the aperture of the lens system and may contribute to the ringing structure, although a Frauenhofer diffraction pattern could not be seen on a PSF that was reconstructed from the edge profile measurement (compare Section 2.4.1).

The noise level in the reconstructions can be estimated from the peak widths in the histogram. The histogram of the attenuation coefficient in the reconstruction of the unstained 500 kg/m^3 sample is shown in Figure 6.17. The peak at $\mu = 0\,\mathrm{mm}^{-1}$ corresponds to air and strongly overlaps the

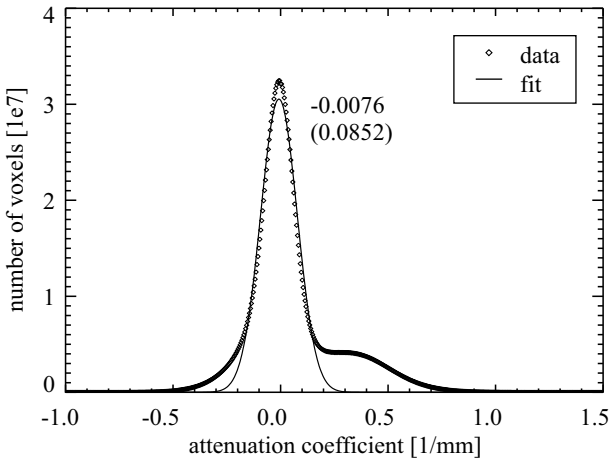

Figure 6.17: Histogram of the unstained 500 kg/m^3 sample (over the entire volume of one of two scans). A Gaussian function (solid line) has been fitted to the data. The center position and sigma parameter (in brackets) are given.

peak corresponding to the fiber material, which for pure cellulose $C_6H_{10}O_5$ of density 1.5 g/cm^3 and at 12 keV photon energy would be expected at $\mu = 0.333\,\mathrm{mm}^{-1}$ (calculated according to the data of Plechaty *et al.* [119]). The fit of a function consisting of two Gaussian functions for the description of air-peak and material-peak (cellulose material) to the measured histogram was not successful. Without fixation of the fit parameters, the material peak did not converge into the expected position. Therefore, a single Gaussian function was fitted to the histogram for the determination of the air-peak width only. The fitted curve is plotted in Figure 6.17. The determined sigma parameter of the peak is $0.085\,\mathrm{mm}^{-1}$, which is reasonable for the selected scan parameters.[6]

Noise and ringing cause artificial structures in the reconstruction that locally can have similar appearance as the cell wall material. These structures, which extend over several voxels, impose a problem for fiber segmentation. The differentiation between these artificial structures and the real eventually very thin cell walls is difficult. It was therefore necessary to employ a more sophisticated method than the simple threshold technique for the segmentation of fibers and, in any case, for the desired segmentation of individual fibers.

6.4.6 Fiber segmentation

A procedure for the segmentation of individual fibers from the recorded volume data sets was developed together with the 'Fachbereich Informatik' of the University of Hamburg based on the VIGRA[7] library. This collaboration, initiated during this work, enabled application and adaptation of state-of-the-art algorithms for the given segmentation problem.

[6] By inverse application of the formula for the calculation of the noise level in the reconstruction [Equation (3.31)] and with $N_\theta = 720$, we can obtain the corresponding average photon count in each pixel. The calculation gives $\langle N \rangle = 14\,058$ in this case, which is in the order of photon counts that are usually acquired in each pixel of the projection.

[7] VIGRA - Vision with Generic Algorithms. The software package is developed at the 'Arbeitsbereich Kognitive System, Fachbereich Informatik, Universität Hamburg'. Authors: Ullrich Köthe and Hans Meine. Software and documentation are online available at `http://kogs-www.informatik.uni-hamburg.de/~koethe/vigra/` [visited July, 1st 2006].

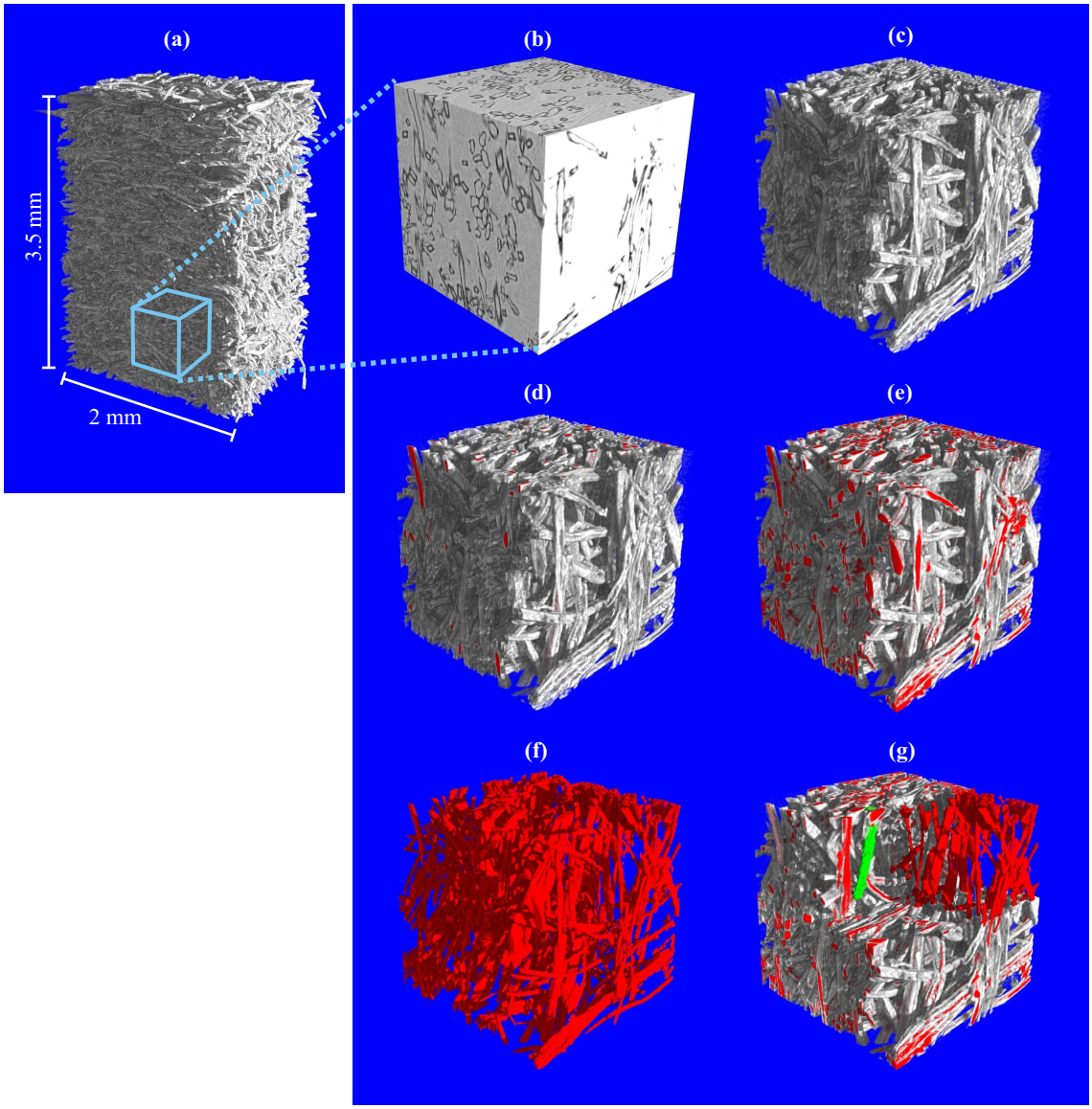

Figure 6.18: Demonstration of the fiber segmentation for the 300 kg/m^3 MDF sample. (a) Selection of a $256 \times 256 \times 256$ voxel sub-volume, which corresponds to $0.58 \times 0.58 \times 0.58$ mm^3. (b) – (g) Segmentation steps (see text). Segmented fiber cavities (red) and a single segmented fiber (green) are shown.

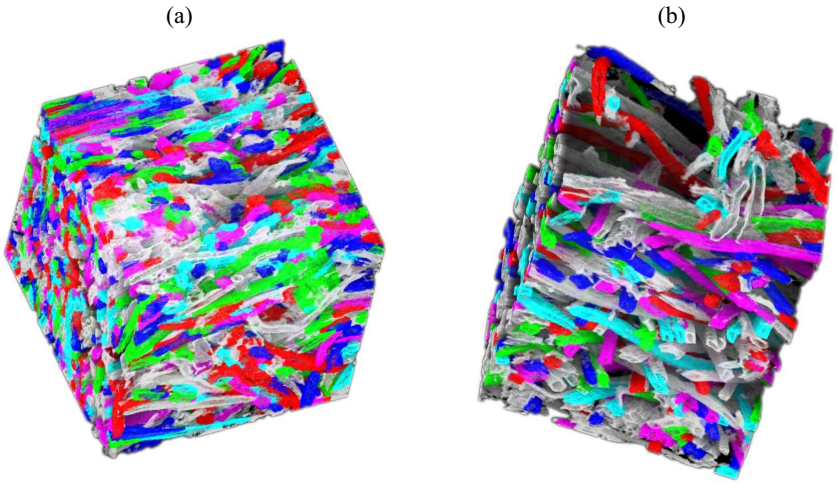

Figure 6.19: A subvolume of $256 \times 256 \times 256$ voxels with individually segmented fibers. The individual fibers were assigned eight alternating colors. (a) 500 kg/m^3 and (b) 300 kg/m^3 sample.

For the demonstration of the segmentation procedure a subregion of the unstained 300 kg/m^3 sample was selected as shown in Figure 6.18(a). Figures 6.18(b) – (g) show the different steps of the segmentation procedure. Figure 6.18(b) shows a rendering of the sub-volume without any segmentation. In Figure 6.18(c) the region of low attenuation coefficient has been made transparent. The data set was then segmented into air, fibers, and cavities within the fibers. First the outside air was marked using seeded region growing, then the remaining voxels were separated into fibers and cavities through thresholding and subsequent seeded region growing. Figure 6.18(d) shows the marked cavities that have no contact to the outer air. Finally, the cavities with contact to outer air were separated in Figure 6.18(e) through a series of morphological operations (erosion and dilation). Figure 6.18(f) shows all cavities detected in the fibers. Individual fibers [shown in Figure 6.18(g)] were then segmented using dilation on individual cavities and using the segmented image as a mask. The output of the segmentation process are three-dimensional data sets containing either labeled fibers or labeled fiber lumina, in which voxels that belong to the same fiber/lumen are indexed by the same number. Figure 6.19 shows the labeled fibers in a $256 \times 256 \times 256$ sub-volume of the unstained 300 and 500 kg/m^3 MDF sample. A more detailed description of the segmentation and labeling procedure can be found in the publication by Walther *et al.* [152].

6.4.7 Results and discussion

Cross sections with orientation parallel to the rotation axis [as the one shown in Figure 6.15] were prepared for all samples. A closeup from the equivalent position within each sample and of all other studied samples is shown in Figure 6.20. The iodine marker is soluble in water and to be seen in the reconstructions as a homogeneously distributed increase of the attenuation coefficient of fiber material that varies locally. The barium sulfate marker is practically insoluble in water and seen as tiny clumps of highly-absorbing marker, which are attached to the fiber material. Even in the unstained samples, a small number of highly absorbing particles was found. They were not

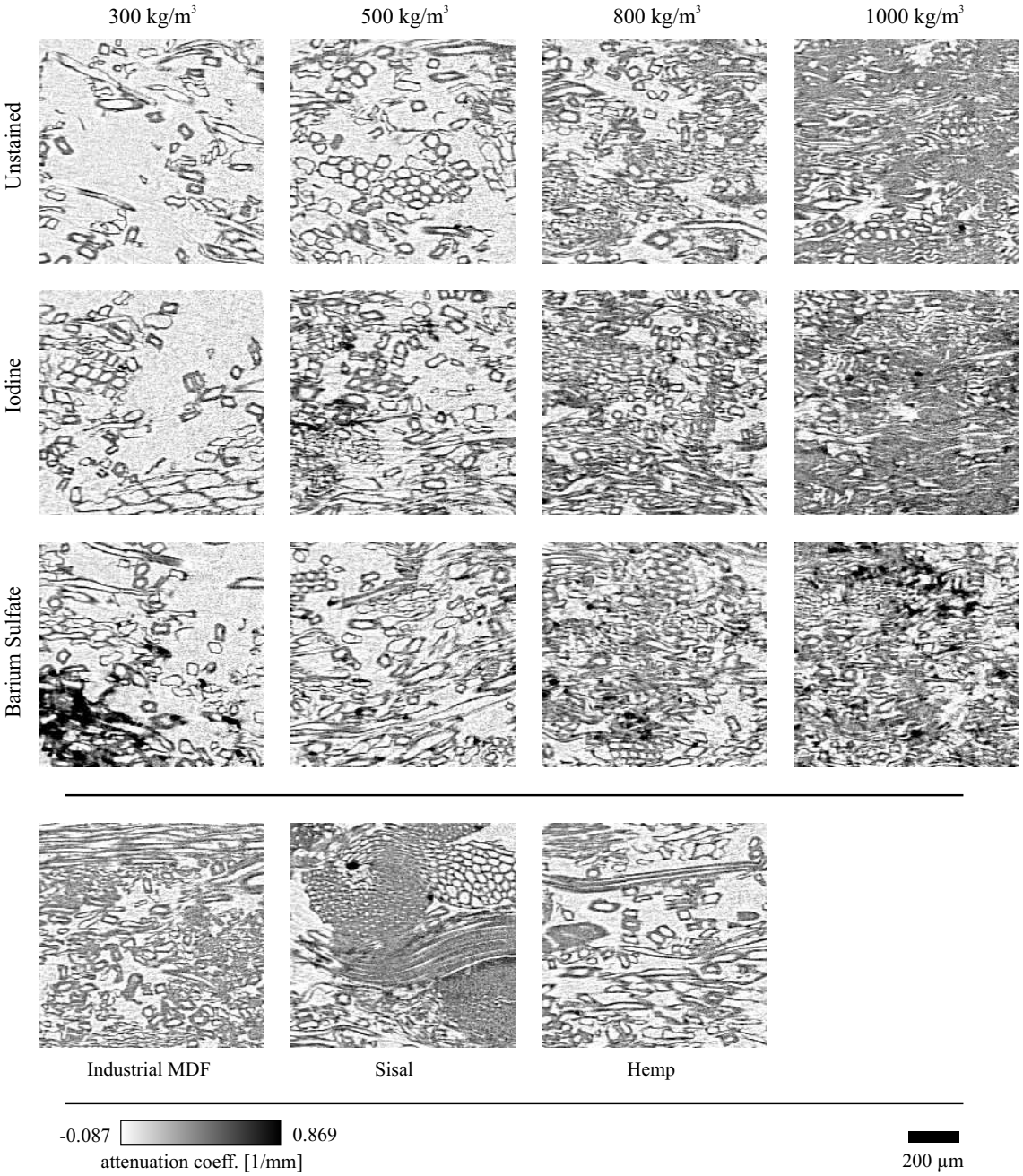

Figure 6.20: Overview of all MDF samples, showing a 200×200 pixels cross section from each sample. The cross section of the unstained $500\,\mathrm{kg\,m^{-3}}$ sample corresponds to the larger box in Figure 6.15. An equivalent subregion has been selected for all samples.

observed in the industrial sample. Most probably the particles are metallic grit from the laboratory production machines.

The distribution of the water-soluble iodine marker was recognized in the reconstructions by an increase of the average attenuation coefficient of the fibers. Because of natural variations of the wood fiber material and the limited resolution, the attenuation coefficient could not be related to the iodine or adhesive concentration, though. It is unclear, whether further statistical evaluation of the marker distribution could give valuable information. The barium sulfate marker that becomes visible in the reconstruction as highly-absorbing particles was found to be non-uniformly distributed. The data did thus not allow for a characterization of the marker distribution.

The segmented and labeled data sets obtained from the segmentation procedure enabled further analysis of the data sets and of individual fibers. Parameters were determined from several sub-volumes ($512 \times 512 \times 256$ voxels) with varying distance from the sample surface for each data set. In total 57 sub-volumes were analyzed. For each labeled fiber in the sub-volume were determined:

- volume of cell wall,
- volume of lumen,
- surface area (inner/outer),
- orientation,
- contact area with other fibers.

Fiber bundles that were labeled as a object could be detected by analysis of these parameters. As further parameters of the entire sub-volume were determined:

- inter-cellular volume,
- inner-cellular volume,
- total cell wall volume,
- number of fibers.

The volume of fibers and of their lumen is calculated by counting voxels within the segmented images. The surface area of the fibers is calculated by counting the contact surfaces between fiber and air. The orientation of the fibers is obtained by performing principal component analysis (PCA) on the segmented cavities or fibers. During PCA analysis the eigenvectors of a three-dimensional covariance matrix are calculated. The largest eigenvector can be directly related to the main orientation of a fiber. The contact area between individual fibers (fiber-to-fiber bonding) is retrieved from the labeled fiber walls by neighborhood operations. The results for each analyzed sub-volume are in detail presented in the PhD thesis of Walther [153].

The availability of individual fiber labeling opens further possibilities for evaluation. Parameters as the secant length and curl that were derived manually by Groom *et al.* [69] can now easily be determined from the segmented data. Distance transform or granulometry can be applied to the labeled fiber lumina and provide information on the lumen collapse induced during fiberboard production. Also dynamic studies with fiber tracking become possible. The change of individual fiber parameters as position, length, volume, curl, or orientation could now be followed for fiberboards, e.g., during wetting or under mechanical load. Algorithms similar to those developed by Nielsen *et al.* [115] for the tracking of marker particles (in this case in a metal matrix) by their characteristic parameters can be implemented.

6.4.8 Summary

SRμCT was successfully applied for the three-dimensional visualization and characterization of the fiberboard microstructure for several fiberboards with densities between 300 and 1 000 kg/m^3. The microstructure with a structure size close to the resolution limit of the tomography setup could be resolved. An oscillating structure that was observed around the fibers was qualitatively explained as a result of the band limit in the reconstruction. A robust segmentation procedure was developed that allows for the segmentation of individual fibers (labeling of fibers) even in the presence of noise and oscillating structures. Parameters of individual fibers as surface area/volume, position, length, volume, orientation, or contact area were obtained from the labeled data sets. These parameters were used for the statistical characterization of the fiberboard structure and, furthermore, can be used as input for modeling and optimization of the macroscopic fiberboard properties. This will give a much better foundation for the applied models than the so far used random generated input or the limited data obtained from sectioning techniques.

Chapter 7

Summary and outlook

SRμCT was applied in this work for the three-dimensional characterization of specimens with spatial resolution in the micrometer range. Further developments were made on the existing SRμCT setup, especially on the x-ray camera and the reconstruction chain. These developments enhance the capabilities of SRμCT and allow to make even better use of the special advantages of synchrotron radiation (no beam hardening) for quantitative measurements. Examples of studies conducted in the fields of material and medical science were presented.

Quantitative measurements rely on artifact-free reconstructions. Therefore, possible artifact sources in SRμCT were summarized. The influence of noise in the recorded reference images was derived. Especially long-range blur in the x-ray camera was intensively discussed, since it causes blur and may even cause non-linear artifacts in the tomographic reconstructions. Blur-free x-ray cameras (e.g., lens-less detectors) that would achieve the same spatial resolution of $\sim 1\,\mu$m are not available today. However, the suppression of blur in the lens-coupled x-ray camera could be successfully demonstrated.

In order to physically suppress blur an absorbing coating (black backing) was applied to the luminescent screen of the x-ray camera. Apparently, this was done for an SRμCT setup for the first time. The characterization of the camera showed that long-range blur and, additionally, the visibility of screen defects were strongly suppressed after application of the absorbing backing. Consequently, and as was shown experimentally, blur and ring artifacts in the reconstruction could be drastically reduced. Other methods that make use of the same type of x-ray camera, e.g., phase-contrast tomography or nano-tomography, should directly profit from the technology of the presented blur-reduced detector.

The center of rotation in the projection data must be precisely known for the tomographic reconstruction, but the determination of the center of rotation had been a pending problem for a long time. No precise and objective method for this purpose had been available. In this work a robust method for the determination of the center of rotation was developed that achieves sub-pixel precision. It was implemented into the reconstruction chain, whereby automation of the

entire reconstruction chain was achieved. In combination with the automation of camera focussing and magnification measurement that were introduced in this work, the reliability, speed, and user-friendliness of measurement and reconstruction were thus significantly increased. Moreover, the objectivity in the obtained data is ensured.

A study on the material flow during friction stir welding of aluminum alloys was performed and revealed important insights into the influence of the welding tool on the welding process. Artifacts were observed in these measurements around strongly absorbing objects. The combination of high contrast and long-range blur in the detector was identified as the source of these artifacts by a simulation. This simulation furthermore showed that the removal of blur would eliminate these artifacts.

The removal of blur by application of the backing layer and additionally by deconvolution of the radiographic images was successfully demonstrated for the measurement of cortical bone. Blur was partly removed by the black backing and finally removed by the deconvolution operation performed on the recorded radiographic projections. The combined removal of blur resulted in an accurate reconstruction of the attenuation coefficient of bone. This is essential for the precise determination of the bone mineral density that can be further used, e.g., for the study of osteoporosis or as input parameter for finite element models that allow for the simulation of the mechanical bone properties.

The porosity of hydroxyapatite scaffolds intended for use as implant material was measured at the nanoscopic scale. The influence on the measurement caused by the partial volume effect and by the reconstruction algorithm itself was discussed here. A significant shift of the reconstructed attenuation value was observed that was caused by the applied filtered backprojection algorithm. It was shown that using a different implementation of the reconstruction according to Ramachandran and Lakshimarayanan avoids the shift and achieves a precise absolute value for the attenuation coefficient. This allows insights into the nanoporosity of the scaffolds that can be used as feedback for the optimization of the manufacturing process.

The microstructure of fiberboard was examined and characterized using 3D image processing methods. An oscillating structure observed around the cell walls was qualitatively explained as a direct consequence of the band limit of the system, and could therefore not be removed. A procedure for the segmentation and labeling of fibers could, however, be developed, based on 3D image processing methods. Several characteristic parameters for each individual wood fiber in the fiberboard could hereby be quantitatively determined and can further be used for the statistical description, modeling, and the optimization of fiberboards.

In this work a number of important steps have been taken to improve the SRμCT method for quantitative measurements, towards full automation, and by the development of new data analysis tools. For the future these developments should allow to address an even larger number of scientific questions in traditional and new scientific fields using SRμCT.

Appendix A

The interaction of x-rays with matter

A short summary of the fundamental interaction processes of x-rays with matter is presented here. A more elaborate summary with focus on radiological imaging can be found in the book by Barrett and Swindell [8, Appendix C].

A.1 Wavelength and energy relation

The relation between wavelength λ and photon energy E for photons in vacuum is given by de Broglie's wavelength of a particle with rest mass zero as

$$\lambda = \frac{hc}{E}\,, \tag{A.1}$$

where c is the speed of light and h is Planck's constant. The following numerical expression of the equation above is helpful in every day use:

$$\lambda[\text{nm}] \approx \frac{1239.8}{E[\text{eV}]}\,. \tag{A.2}$$

A.2 Attenuation coefficient

A pencil beam of monochromatic photons in a homogeneous medium is attenuated according to Beer's law:

$$\Phi(d) = \Phi_0 \exp(-\mu d)\,, \tag{A.3}$$

where Φ_0 is the incident photon flux (photons/s/unit area), $\Phi(d)$ is the flux after traveling distance d, and μ is the **linear attenuation coefficient** or simply **attenuation coefficient** of the medium.

The attenuation coefficient is given in units of mm^{-1} in this work. In conventional CT the relative attenuation coefficient is also quantified according to the Hounsfield scale.[1]

In microtomography the beam travels along a medium with varying attenuation coefficient $\mu(s')$ along the traveling direction. In this case, the photon flux is given by:

$$\Phi(s) = \Phi_0 \exp\left[-\int_0^s \mu(s')\,ds'\right] . \tag{A.4}$$

The derivation of this equation is simple. It can be found in the book of Barrett and Swindell [8]. The integral in the exponential function describes the projected attenuation

$$p = \int_0^s \mu(s')\,ds' . \tag{A.5}$$

For a homogeneous object of thickness d and with linear attenuation coefficient μ_0 this gives again $\mu_0 d$ as the simple form of Beer's law above.

The **mass attenuation coefficient** (μ/ρ) is defined by the ratio of the linear attenuation coefficient μ and density ρ. It is useful for calculating the mass of material required to attenuate a primary beam by a prescribed amount, i.e.,

$$\frac{\Phi}{\Phi_0} = \exp[-(\mu/\rho)s_m], \tag{A.6}$$

where $s_m = \rho s$ is the mass of attenuator per unit area of beam. Here ρ is the density of the attenuator and s is its thickness. The formula can also be used to calculate the materials density from the measured attenuation coefficient, when the attenuation coefficient $(\mu/\rho)_{subst}$ of the substance is known.

Chemical binding energies are so small compared to x-ray energies of interest that chemical compounds may be treated as mixtures. The **mass attenuation coefficient of a mixture** that consists of I components, each with mass attenuation coefficient $(\mu/\rho)_i$, $i = 1, ..., I$ is given by

$$\left(\frac{\mu}{\rho}\right)_{subst} = \sum_{i=1}^{I} \left(\frac{\mu}{\rho}\right)_i W_i, \tag{A.7}$$

where W_i is the fraction by weight of the i-th component. The linear attenuation coefficient is obtained by multiplying both sides of the equation by the density of the mixture.

[1]The linear Hounsfield scale in Hounsfield units (HU) is defined by the signal of distilled water (0 HU) and air (-1000 HU). The Hounsfield units of common substances in medical CT are: air (-1000 HU), fat (-120 HU), water (0 HU), Muscle (+40 HU), bone (+1000 HU). The definition of a relative scale in conventional CT is helpful because of the strong dependence of the attenuation coefficient on the photon energy and the varying photon spectrum used in different setups.

A.3 Competing processes

In the energy range 10 keV to 100 MeV, there are three principle ways in which the incident beam becomes attenuated. They are photoelectric absorption, Compton scatter, and pair production. They are usually described by their cross sections σ_{PE}, $Z\sigma_C$,[2] and σ_{PP}, with the atomic number Z. Here it is assumed that all electrons are free electrons and partake equally in Compton collisions. For heavy elements and low x-ray energies this is not generally true. The total atomic cross section is defined as

$$\sigma_{tot} = \sigma_{PE} + Z\sigma_C + \sigma_{PP} \,. \tag{A.8}$$

The atomic cross section is related to the attenuation coefficient by $\mu_{tot} = \sigma_{tot} n$, where n is the volume density in atoms per cubic centimeter. It is $\rho = n\, m_{at}$, where m_{at} is the atomic mass.

The total attenuation coefficient is given by

$$\mu_{tot} = \mu_{PE} + \mu_C + \mu_{PP} \,. \tag{A.9}$$

The total atomic cross section is related to the mass attenuation coefficient by

$$(\mu/\rho)_{tot} = \frac{\sigma_{tot}}{m_{at}} \tag{A.10}$$

and equivalently for the individual components. Typically, (μ/ρ) is given in units of $\mathrm{cm^2\,g^{-1}}$, σ is given in units of barn,[3] and the atomic mass is given in atomic mass units u.[4] The following numerical expression relates the two quantities:

$$(\mu/\rho)\,[\mathrm{cm^2\,g^{-1}}] = 0.602\,\frac{\sigma\,[\mathrm{barn}]}{m_{at}[\mathrm{u}]} \,. \tag{A.11}$$

Figure A.1 shows the components to the atomic cross section of carbon (Z=6) and lead (Z=82) in units of barn.

Commonly, attenuation is understood as the sum of two effects, namely, photoelectric absorption and scatter. Pair production does not occur below 1 MeV photon energy. Depending on the experimental details of the μCT apparatus used, scatter can increase or decrease image contrast. Fortunately, in most μCT examinations the contribution by scatter is small compared with that by photoelectric absorption. Therefore, the term 'attenuation' can often be substituted by 'absorption', a procedure frequently followed in the μCT related literature. However, a rigorous treatment of image contrast has to take into account the effect of scatter [10].

From an imaging standpoint there is an important distinction between absorption and scattering. A scattered photon has lost all, or almost all, of its 'memory' regarding its initial direction of

[2] σ_C is given per electron and not per atom
[3] $1\,\mathrm{barn} = 10^{-24}\,\mathrm{cm^2}$
[4] $1\,\mathrm{u} = 1.661 \times 10^{-24}\,\mathrm{g}$

travel. It no longer appears to emanate from the small focal spot and, therefore, cannot be expected to cast a sharp shadow image on the detector. Instead, the scattered radiation forms a broad, diffuse distribution on the detector, severely impairing the contrast of the image formed by unscattered radiation. Photoelectric absorption presents no such problem. The photon completely disappears, giving up all of its energy to an electron, and is therefore not detected at all. If, however, we succeed in making our detector insensitive to scattered photons, either by geometric or electronic means, then the distinction between absorption and scattering disappears [8]. Scattered radiation is often rejected by the use of collimators. Compton scattered radiation is shifted in energy with respect to the incident radiation, which also enables energy discrimination of this type of scatter, when energy resolving detectors are applied.

The relevance of Compton scatter can be related to the sample diameter, as shall be shown here. In the tomographic examination of small samples below a diameter of about $D = 1\,\mathrm{cm}$ we can generally assume that photoelectric absorption is the dominating process. This can be derived as follows.

We discuss the relevance of scatter for the measurement of cylindrical homogeneous objects of diameter D for the two materials carbon (C) and lead (Pb). The following derivation for these materials can be seen as a limiting case for most material mixtures, with density and atomic numbers in between the values of carbon and lead. Generally, we investigate samples at a photon energy, at which the projected attenuation coefficient is $p \leq 2$ (compare Section 3.3.2). From this condition we find for the mass attenuation coefficient $(\mu/\rho) \leq 2/(\rho D)$. For carbon with density $\rho = 1\,\mathrm{g\,cm^{-3}}$ this gives $(\mu/\rho)_{opt} \leq 1\,\mathrm{cm^2 g^{-1}}$. From Figure A.1(a) it can be seen that this value corresponds to a photon energy $E_{ph} \lesssim 10\,\mathrm{keV}$. In this regime photoelectric absorption dominates. Similarly, for lead of density $\rho = 11.36\,\mathrm{g\,cm^{-3}}$ we find $(\mu/\rho) \leq 0.176\,\mathrm{cm^2 g^{-1}}$, which is reached for photon energies $E_{ph} \lesssim 400\,\mathrm{keV}$ as can be seen from Figure A.1(b). Again, photoelectric absorption dominates in this regime. For smaller objects, with $D \leq 1\,\mathrm{cm}$ or objects of lower density the photoelectric effect becomes even more dominant. Thus, for our measurement of small objects, the attenuation coefficient is dominated by the photoelectric absorption coefficient and we assume that we can perform our measurements without collimator in front of the x-ray camera. Moreover, we can identify the attenuation coefficient with the absorption coefficient in this regime.

A.4 Dependence on energy and atomic number

Experimentally it is found that the linear attenuation coefficient for photoelectric absorption μ_{PE} is given by

$$\mu_{PE} \approx k \frac{\rho}{m_{at}} \frac{Z^m}{E^n}\,, \tag{A.12}$$

where k is a constant that depends on the atomic shell involved, ρ is the density, m_{at} the atomic mass, E is the photon energy, and Z the atomic number of the material. The quotient (ρ/m_{at}) gives the density of atoms. The parameters m and n are slowly varying functions of Z and E.

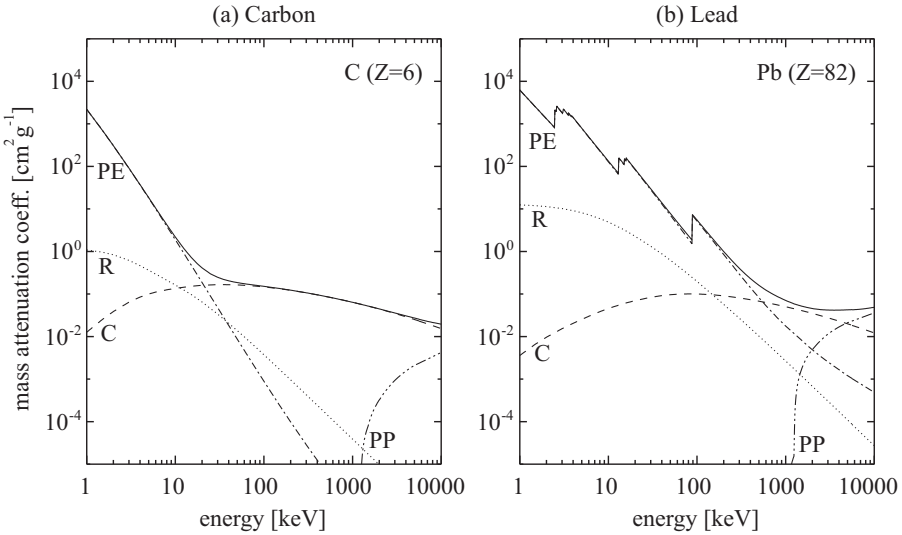

Figure A.1: Mass attenuation coefficient for (a) carbon (atomic number Z=6) and (b) lead (Z=82) as a function of photon energy. The dominating components are the photoelectric effect 'PE', Compton scatter 'C', and pair production 'PP', which starts above 1 022 keV. Rayleigh scattering 'R' is a coherent effect that is normally negligible in tomography. Note that the mass attenuation coefficient and not the cross section is plotted here. The attenuation for carbon and lead is obtained by multiplication of the plotted values with the material's density. Data compiled from the tables of Plechaty *et al.* [119].

A general rule of thumb, which works well in the range form 10 to 100 keV, is

$$\mu_{PE} \approx k \frac{\rho}{m_{at}} \frac{Z^4}{E^3} \ . \tag{A.13}$$

A relative variation of the photon energy by $\delta E/E$ results in a variation of the attenuation coefficient $\delta\mu_{PE}/\mu_{PE}$. The relation between the variations can be approximated by Taylor expansion of Equation (A.13). Expansion of the energy dependence according to

$$(1+x)^{-3} = 1 - 3x + ... \tag{A.14}$$

gives the relation

$$\Delta\mu/\mu \approx -3\delta E/E \ . \tag{A.15}$$

This relation is a good approximation in the limit of small $\delta E/E \ll 1$.

Appendix B

Spatial resolution limits of the x-ray camera

The spatial resolution of the system is determined by diffraction, out of focus light generation, and the aberration due to the refractive index of the luminescent screen. In the following, simple approximations are presented that allow to estimate the relevance of the individual effects.

Numerical calculations of MTFs based on a geometrical model and under variation of screen thickness, x-ray attenuation length, and the numerical aperture were already presented by Busch [31]. He concluded that the luminescent screen thickness is without influence, when it is significantly larger than the attenuation length and when light generation takes place over the entire screen thickness [31, pp. 68–69].

The objective's optical transfer function (OTF) or MTF as a function of the defect of focus (out-of-focus distance δz) can be calculated from the pupil function of the system. The classic paper on the MTF for the combination of diffraction and focus error is by Hopkins [80][1] and gives an analytical expression for the OTF as a function of δz. Koch *et al.* [96] and Cloetens [36] presented formulas based on Hopkins [80] formula.

B.1 Diffraction limit

The diffraction limit of microscopes is typically derived from the Fraunhofer diffraction pattern of a circular aperture. The intensity profile from a circular aperture is given in [25, Chapter 8.5, Equation (14)].

The resolution limit of a microscope is typically defined by the distance of the central maximum and the first minimum of the diffraction pattern. The diffractive resolution limit for a micro-

[1]The paper by Hopkins [80] has been reprinted in [6]. A more recent discussion on formulas describing the defect of focus in microscopic imaging was presented by Ellenberger [53].

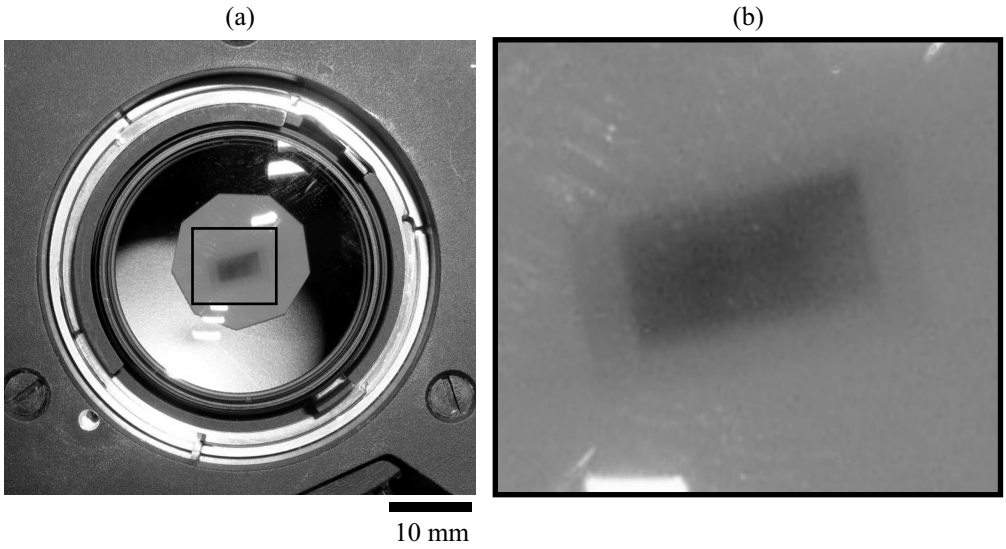

Figure B.1: (a) Haze on the lens system. (b) Magnification of the central lens region. The rectangular beam profile is imprinted in the lens.

scope with circular aperture under incoherent illumination is given by Born and Wolf [25, Chapter 8.6, Equation (32)] as

$$\text{resolvable distance} \sim 0.61\frac{\lambda}{A} \,. \tag{B.1}$$

The resolvable distance is small (high resolution), when the wavelength λ is small and the numerical aperture A is big. The aperture of our system typically is $A = 0.1$ (compare Table 2.3). This results for the emission wavelength of $\lambda = 500\,\text{nm}$ of the luminescent screen in a resolvable distance of $\sim 3\,\mu\text{m}$.

High-energetic x-rays that penetrate the luminescent screen and enter the lens system are known to create **haze on the objective**. Figure B.1 shows the imprint that the incident beam created on the 35 mm objective of our system. Haze degrades the resolution properties of the camera. Thus, the observed diffraction pattern may deviate significantly from the ideal one. Also for non-inline geometries (using mirrors or reflective objectives) haze remains a problem for the first optical component.

B.2 Depth of field

From the numerical aperture one can estimate the depth of field of the lens. It should be larger than the light emitting layer in the luminescent screen, which for this setup with a bulk crystal is approximately given by the attenuation length of the x-rays in the screen.

Depth of field is determined by the distance from the nearest object plane in focus to that of the farthest plane also simultaneously in focus. At high numerical apertures of the microscope, depth of field is determined primarily by wave optics, while at lower numerical apertures the geometrical

optical circle of confusion dominates the phenomenon. Using a variety of different criteria for determining when the image becomes unacceptably sharp, several authors have proposed different formulas to describe the depth of field in a microscope. The total depth of field is given by the sum of the wave and geometrical optical depths of fields as[2]

$$d_{tot} = \frac{\lambda n}{A^2} + \frac{n}{m A} e \,, \tag{B.2}$$

where d_{tot} represents the depth of field, λ is the wavelength of the luminescent radiation, $n \approx 1$ is the refractive index of the medium between screen and objective, and A is the numerical aperture. The variable e is the smallest distance that can be resolved by a detector that is placed in the image plane, whose lateral magnification is m.

B.3 Spherical aberrations

The applied objectives are not corrected for spherical aberrations that are caused by the finite thickness of the luminescent crystals. Some commercial microscope objectives are designed to compensate the effect of cover glasses (refractive index $n_{glass} \approx 1.5$). But even these do not correct for the high refractive index n_{ls} of the transparent luminescent crystals that are used in microtomography as, e.g., $n_{ls} \approx 2.3$ for $CdWO_4$. Cloetens [36, Eq.3.73] presented a simple condition for the maximum crystal thickness, for which spherical aberrations are negligible compared with the defect of focus. If this condition is solved for the crystal thickness, it reads

$$t \leq \frac{2\, n_{ls}^2\, d}{A^2\, (n_{ls}^2 - 1)} \,. \tag{B.3}$$

Here t is the thickness of the luminescent screen, n_{ls} is refractive index of the luminescent screen, A is the numerical aperture, and homogeneous light emission over a layer of thickness d is assumed.

Koch *et al.* derived a tolerance condition [96, Eq.(6)] for the maximum crystal thickness. It is based on a tolerance condition for spherical aberrations (maximum deviation of the wavefront of less than 0.94 wavelength) from Born and Wolf [25]. This condition, again solved for t, requires the thickness t of luminescent layer and substrate to be

$$t \leq 3.76\, \frac{\lambda}{A^4} \frac{n_{ls}^3}{n_{ls}^2 - 1} \,, \tag{B.4}$$

where n_{ls} is the refractive index of the luminescent screen, λ is the wavelength of the luminescent light, and A is the numerical aperture.

[2] From `http://www.microscopyu.com/articles/formulas/formulasfielddepth.html`, 9.1.2006, 'Basic Concepts and Formulas in Microscopy: Depth of Field and Depth of Focus'.

B.4 Energy spread in the luminescent screen

The absorbed x-rays give rise to secondary processes as, e.g., the emission of characteristic x-rays or Auger electrons. Thus, the generation of luminescent light will take place not only at the primary interaction side. This spread of energy will contribute to the point spread function of the x-ray camera. The spread of energy deposited in the scintillator was studied by Koch *et al.* [96]. They determined the radial absorbed dose distributions using Monte Carlo simulations. For 100 μm thick YAG:Ce crystals they found that the dose decreases rapidly within a few hundred nanometer and does not limit the high-spatial-frequency response of the detector. They point out that the tails of the radial energy distribution may have a deteriorating effect on the middle and low-frequency parts of the MTF. However, for 30 keV x-rays, their plots show a decrease to below 10^{-4} of the central maximum within 4 μm radial distance. This spread is negligible and can be neglected for our system.

Appendix C

Calculations

C.1 Light collection efficiency of the lens system

Only part of the luminescent light generated in our x-ray camera enters the aperture of the lens. The accepted fraction of light as a function of magnification and aperture size (m and k) can be calculated from geometrical considerations. The calculation was already presented in the PhD thesis of Busch [31]. His result was correct, except for a missing factor of two [compare Busch's Equation (6.18) with Equation (C.4) below]. We shall repeat the calculation here. Moreover, we will also express the collection efficiency in terms of the numerical aperture (A).

Confusion with the definition of opening angles of light cones, obviously, let to the missing factor of two in Busch's result. To avoid any confusion, the half opening angles of light cones will be explicitly expressed as $\alpha/2$ and $\beta/2$ in the following, as shown in Figure C.1. Note that this definition of angular variables differs from the typical representation of the Fresnel equations and also from the use in the rest of this work. However, the resulting formulas will be independent of the angular variables.

The reflectivity at the inside crystal surface, which is described by the Fresnel equations, is not included in the calculation. The generation of luminescent light inside the crystal is assumed to take place on the optical axis of the imaging system and to have an isotropic angular distribution.

The fraction of luminescent light ϵ_{coll} emitted into a cone with half opening angle $\beta/2$ and solid angle $\Omega_{cone} = 2\pi\,[1 - \cos(\beta/2)]$ is simply given by the ratio of the solid angle Ω_{cone} and the full solid angle, which is 4π. Thus we have

$$\epsilon_{coll} = \frac{\Omega_{cone}}{4\pi} = \frac{1 - \cos\frac{\beta}{2}}{2} = \sin^2\frac{\beta}{4}\,. \tag{C.1}$$

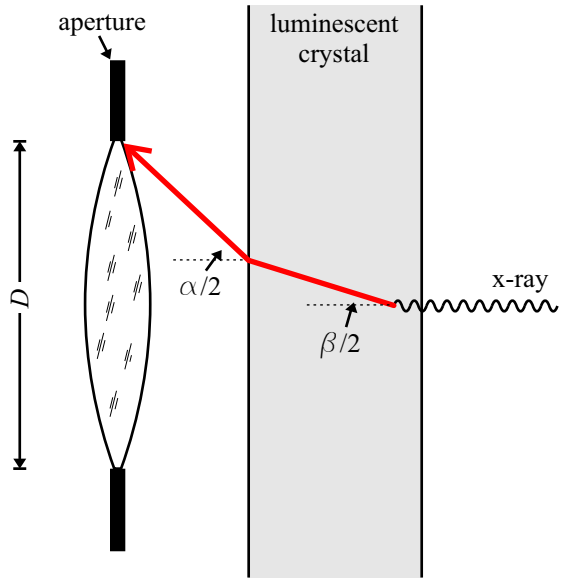

Figure C.1: Scheme of the light path in the x-ray camera. The distance between aperture and screen is not drawn to scale.

The half opening angle $\alpha/2$, which is accepted by the optical system is on the other hand given by

$$\frac{\alpha}{2} = \arctan\left(\frac{D/2}{a}\right) = \arctan\left(\frac{D\,m}{2f(m+1)}\right) = \arctan\left(\frac{m}{2k(m+1)}\right) . \tag{C.2}$$

Here f is the focal length, D the diameter of the entrance pupil, a the object distance, m is the optical magnification factor[1], k is the f-number of the objective given by $k = f/D$, and we have used the relation $a = f(1 + m^{-1})$.

The relation between α and β is given by the law of refraction

$$n_{ls} \sin\frac{\beta}{2} = \sin\frac{\alpha}{2} , \tag{C.3}$$

with n_{ls} the refractive index of the luminescent screen. Using this relation, the above equations can be combined into an expression for the fraction of radiation accepted by the aperture as a function of f-number (k), magnification m, and refractive index n_{ls} of the luminescent screen:

$$\epsilon_{coll} = \sin^2\left(\frac{1}{2}\arcsin\left\{\frac{1}{n_{ls}}\sin\left[\arctan\left(\frac{m}{2k(m+1)}\right)\right]\right\}\right) . \tag{C.4}$$

For $x \ll 1$ the trigonometric functions can be approximated as $\sin(x) \approx \arcsin(x) \approx \arctan(x) \approx x$.

[1] We define the magnification factor m as a positive quantity here. A different convention, e.g., used by Schröder [132], defines the magnification as a negative quantity, which logically describes the inversion of the image upon lens imaging.

For small apertures, i.e., large f-numbers k, the above equation thus can be reduced to

$$\epsilon_{coll} \approx \left(\frac{1}{4n_{ls}} \frac{m}{k(m+1)} \right)^2 . \tag{C.5}$$

The collection efficiency can also be expressed as a function of the numerical aperture $A = n \sin(\alpha/2)$, where n is the refractive index in the space between object and lens. Our setup has an air-filled gap with refractive index $n \approx 1$. The numerical aperture A is typically used to characterize microscopes, while for photographic equipment mostly magnification m and f-number k are given. In the case of $n = 1$, numerical aperture A and f-number k are related by

$$\arcsin(A) = \arctan\left(\frac{1}{2k} \frac{m}{(m+1)} \right) , \tag{C.6}$$

through the magnification factor m.

Equation (C.4) can be rewritten as a function of numerical aperture and becomes

$$\epsilon_{coll} = \sin^2\left(\frac{1}{2} \arcsin\left\{ \frac{A}{n_{ls}} \right\} \right) \tag{C.7}$$

and can for small apertures be approximated by

$$\epsilon_{coll} \approx \left(\frac{A}{2n_{ls}} \right)^2 . \tag{C.8}$$

Equations (C.4) and (C.7) give the collection efficiency. For small apertures with accordingly small values for the arguments $m/[k(m+1)]$ or A/n_{ls}, the approximations in Equations (C.5) and (C.8) can be used.

C.2 Detective quantum efficiency of a cascaded system

The DQE of the x-ray camera system can be calculated by looking at it as a cascade of statistical processes, also called cascaded event sequence [63] or Markov-chain. In the publication by Bonse and Busch [23] and more detailed in Busch's PhD thesis [31] the calculation of the DQE for x-ray cameras employing powder or luminescent screens was presented. Their derivation of the DQE makes use of the Burgess variance theorem, which is presented below. The variance theorem can be expressed in an elegant form as a function of relative variances. This notation shall be introduced and used for the derivation of the DQE of the x-ray camera here. The obtained result is of course the same as the result of Bonse and Busch. Finally, the variance of the CCD signal will be given and the importance of the statistical distribution of luminescence photons is discussed.

Burgess variance theorem

The Burgess variance theorem (Sect. 6.5, p.425 of Frieden [63]) allows to calculate the DQE of a cascaded event sequence as a function of the variance introduced by the individual stages and the variance of the input signal. A proof of the variance theorem was given by Mandel [101] in his work on 'Image fluctuations in cascaded amplifiers'.

The Burgess variance theorem: If for the i-th stage of a cascaded system on the average $\overline{\eta_i}$ quanta are generated per incident quantum, then the average number of quanta after the i-th stage will be

$$\overline{N_i} = \overline{\eta_i}\,\overline{N_{i-1}}\ , \tag{C.9}$$

where $\overline{N_{i-1}}$ is the average number of quanta of the preceding $(i-1)$-th stage and the mean variance after the i-th stage is

$$\overline{\Delta N_i^2} = \overline{\eta_i^2}\,\overline{(\Delta N_{i-1})^2} + \overline{N_{i-1}}\,\overline{(\Delta\eta_i)^2}\ . \tag{C.10}$$

Here, the parameters $\overline{\eta_i}$ and its variance $\overline{(\Delta\eta_i)^2}$ describe the statistical process involved in the i-th stage. The recursion formulas in equations (C.9) and (C.10) make up the variance theorem. From Equation (C.9) directly follows the average number of quanta at the m-th stage, which simply is given by multiplication as

$$\overline{N_m} = \overline{\eta_m}\cdot\ldots\cdot\overline{\eta_1}\overline{N_0}\ , \tag{C.11}$$

with $\overline{N_0}$ the average number of quanta incident to the 1st stage. This equation describes the obvious fact, that the quantum efficiency (QE $= N_m/N_0$) of the cascaded system is given by the product of the quantum efficiencies of the individual stages. [The corresponding equation for our x-ray camera is Equation (2.12).]

The parameters $\overline{\eta_i}$ and $\overline{(\Delta\eta_i)^2}$ depend on the statistical process. Amplification processes are often described by Poisson statistics. Selection processes are described by Binomial statistics. For

a Poisson process, it is $\overline{\eta_i}$ the number of quanta generated on average and the variance is

$$\overline{(\Delta\eta_i)^2} = \overline{\eta_i} \quad \text{Poisson} . \tag{C.12}$$

For a selection process, which simply decides wether or not a quantum is detected and produces a quantum in the next stage, Binomial statistics is applied. Here, it is $\overline{\eta_i} \leq 1$ the fixed probability of generation of a quantum and the variance is

$$\overline{(\Delta\eta_i)^2} = \overline{\eta_i}\,(1 - \overline{\eta_i}) \quad \text{Binomial} . \tag{C.13}$$

The variance theorem can be brought into an elegant form, when the variance is replaced by the relative variance. We introduce the relative variance $R(x)$ of a random variable x as

$$R(x) = \frac{\overline{(\Delta x)^2}}{\overline{x}^2} . \tag{C.14}$$

Using Equations (C.9) and (C.10), we obtain for the relative variance at the i-th stage as

$$R(N_i) = R(N_{i-1}) + \frac{1}{\overline{N_{i-1}}}\, R(\overline{\eta_i}) , \tag{C.15}$$

which together with Equation (C.9) is an alternative representation of the variance theorem. The variances for Binomial and Poisson processes given by Equations (C.12) and (C.13) then have the corresponding relative variances

$$R(\eta_i) = \frac{1}{\overline{\eta_i}} \quad \text{Poisson} \tag{C.16}$$

and

$$R(\eta_i) = \frac{(1 - \overline{\eta_i})}{\overline{\eta_i}} \quad \text{Binomial} . \tag{C.17}$$

The relative variance of the number of quanta at the m-th stage can now be found by recursive application of Equation (C.15), which results in:

$$R(N_m) = R(N_0) + \frac{1}{\overline{N_0}}\, R(\eta_1) + \frac{1}{\overline{\eta_1}\,\overline{N_0}}\, R(\eta_2) + \ldots + \frac{1}{\overline{\eta_{m-1}} \cdot \ldots \cdot \overline{\eta_1}\,\overline{N_0}}\, R(\eta_m) . \tag{C.18}$$

In the special case, when the input N_0 is a Poisson distributed signal, it is $R(N_0) = 1/\overline{N_0}$ and the relative variance becomes

$$R(N_m) = \frac{1}{\overline{N_0}} \left[1 + R(\eta_1) + \frac{1}{\overline{\eta_1}}\, R(\eta_2) + \ldots + \frac{1}{\overline{\eta_{m-1}} \cdot \ldots \cdot \overline{\eta_1}}\, R(\eta_m) \right] . \tag{C.19}$$

Table C.1: Statistical description of the incident radiation and the statistical processes 1 to 3.

Stage	Description	Distribution	Average	Relative variance
–	Incident x-ray quanta	Poisson	$\overline{N_0}$	$R(N_0) = 1/\overline{N_0}$
1	Probability of x-ray absorption	Binomial	$\overline{\eta_1}$	$R(\eta_1) = (1-\overline{\eta_1})/\overline{\eta_1}$
2	luminescence photons per x-ray	Poisson	$\overline{\eta_2}$	$R(\eta_2) = 1/\overline{\eta_2}$
3	Probability of lum. photon detection	Binomial	$\overline{\eta_3}$	$R(\eta_3) = (1-\overline{\eta_3})/\overline{\eta_3}$

Detective quantum efficiency of the x-ray camera

We will now employ the Burgess variance theorem for the calculation of the relative variance at the x-ray camera output. From this we will derive the detective quantum efficiency (DQE) of the system.

The statistical processes of the system are given for the x-ray camera by the elements (ϵ's and ν_{lum}) of Table 2.2. All efficiencies (ϵ's) correspond to selection processes and are governed by Binomial statistics. The process of photon generation, with on the average ν_{lum} generated photons per absorbed x-ray, is an amplification process that is generally assumed to obey Poisson statistics. The average number of generated quanta of a stage $\overline{\eta_i}$ is assigned the corresponding ϵ or ν_{lum} value. The associated relative variances $R(\eta_i)$ of the processes are given according to Equations (C.16) for Poisson processes and (C.17) for Binomial processes.

For the calculation, we define three processes in the x-ray camera: The absorption process in the x-ray screen is the first stage of our system, with $\overline{\eta_1} = \epsilon_{abs}$ and relative variance $R(\eta_1) = (1-\overline{\eta_1})/\overline{\eta_1}$. The generation of luminescence photons is the second stage, with $\overline{\eta_2} = \nu_{lum}$ and $R(\eta_2) = 1/\overline{\eta_2}$. The order of the following stages (e.g., those described by the 'light collection efficiency' and 'transmission efficiency') is somehow arbitrary. In fact, the calculation turns out to be independent of the order of these selection processes. When calculating the relative variance according to (C.19), the result is simply a function of the product of all the selection process efficiencies. The third stage of our system is thus described by the total probability for the detection of a luminescence photon in the CCD, given by $\overline{\eta_3} = \epsilon_{ccd}\,\epsilon_{t,cov}\,\epsilon_{t,ls}\,\epsilon_{t,obj}\,\epsilon_{coll}$, and with the relative variance $R(\eta_3) = (1-\overline{\eta_3})/\overline{\eta_3}$. We shall further assume in the following that the number of quanta N_0 incident to the first stage is Poisson distributed,[2] with relative variance $R(N_0) = 1/\overline{N_0}$. An overview of the statistical processes is given in Table C.1.

The relative variance at the output of the third stage is obtained by entering the relative variances $R(\eta_1)$, $R(\eta_2)$, and $R(\eta_3)$ into Equation (C.19), which gives

$$R(N_3) = \frac{1}{\overline{N_0}}\,\frac{1+\dfrac{1}{\overline{\eta_2}\,\overline{\eta_3}}}{\overline{\eta_1}}\,. \tag{C.20}$$

[2] This assumption is generally made and implies that the photon noise in the x-ray beam is uncorrelated. This has been discussed by Busch [31] in more detail.

The DQE has been defined in Equation (2.9) as ratio of signal-to-noise ratios as DQE = $(\mathrm{SNR}^2_{out}/\mathrm{SNR}^2_{in})$. The signal-to-noise ratio is by its definition closely related to the relative variance. Expressed for the i-th stage, we have

$$\mathrm{SNR}_i^2 = \frac{1}{R(N_i)} \,. \tag{C.21}$$

We can thus determine the detective quantum efficiency of the cascaded system from the ratio of the relative variance of the last m-th stage, given by Equation (C.19), and the variance $R(N_0) = 1/\overline{N_0}$ of the Poisson distributed input as

$$\mathrm{DQE} = \frac{\mathrm{SNR}_m^2}{\mathrm{SNR}_0^2} = \frac{R(N_0)}{R(N_m)} = \left[1 + R(\eta_1) + \frac{1}{\overline{\eta_1}} R(\eta_2) + \ldots + \frac{1}{\overline{\eta_{m-1}} \cdot \ldots \cdot \overline{\eta_1}} R(\eta_m)\right]^{-1} \,. \tag{C.22}$$

Entering the relative variances $R(\eta_1)$, $R(\eta_2)$, and $R(\eta_3)$ into Equation (C.22) gives the DQE of the signal output at the third stage as

$$\mathrm{DQE} = \frac{\overline{\eta_1}}{1 + \dfrac{1}{\overline{\eta_2}\,\overline{\eta_3}}} \,. \tag{C.23}$$

This result depends on only two quantities. Introducing the variable $\gamma = \overline{\eta_3}\,\overline{\eta_2}$ and using the identity $\epsilon_{abs} = \overline{\eta_1}$, the DQE can be rewritten as

$$\mathrm{DQE} = \frac{\epsilon_{abs}}{1 + \gamma^{-1}} \,. \tag{C.24}$$

The obtained DQE is directly proportional to the absorption efficiency ϵ_{abs} and depending on the quantity γ, which describes the number of detected luminescence photons per absorbed x-ray. This is further discussed in Section 2.3.

The DQE in Equation (C.24) describes the relative degradation of the SNR from the 0th to the 3rd stage of the system, i.e., from the signal of incident x-ray photons to the signal of charge carriers in the CCD. So far, we have not looked at the digitization of the charge carrier signal that takes place during CCD readout, and which will introduce electronic readout noise. In the following section, we derive the variance and the SNR from the DQE in Equation (C.24) and introduce readout noise into these expressions.

Variance SNR in the CCD output signal

Of practical interest for tomography is the variance in the recorded CCD images. Thus, we shall present the variance as a function of the signal in digital units of the recorded images rather than as a function of the input intensity. This enables the estimation of the noise level in the recorded images, which are used as input for the reconstruction. (Of course, the noise level can

also be experimentally determined from the variance in two or more identical measurements). We will also introduce the CCD gain g and the CCD readout noise n_{el}, which are given for our CCD in Appendix G.

Substituting $\overline{N_0} = (\overline{\eta_3}\,\overline{\eta_2}\,\overline{\eta_1})^{-1}\,\overline{N_3}$ into the expression for relative variance in the output of the third stage, given as Equation (C.20), we obtain

$$R(N_3) = \frac{1}{\overline{N_3}}\,(1 + \overline{\eta_2}\,\overline{\eta_3})\ . \tag{C.25}$$

The variance of the output signal is thus given by

$$\overline{\Delta N_3^2} = R(N_3)\,\overline{N_3}^2 = \overline{N_3}\,(1 + \overline{\eta_3}\,\overline{\eta_2})\ . \tag{C.26}$$

The signal N_3 gives the number of charge quanta (electrons) created in a CCD pixel. The CCD readout noise can be described as an additive term to this variance. With the readout noise n_{el} in units of electrons, we obtain

$$\overline{(\Delta N_3)^2} = \overline{N_3}\,(1 + \overline{\eta_3}\,\overline{\eta_2}) + n_{el}^2\ . \tag{C.27}$$

This quantity models the noise behavior at the CCD output. The influence of quantization noise (limited resolution of the CCD output due to digitization) is typically smaller than the readout noise and is neglected here.[3]

From now on, we will write $\overline{N}$ in place of $\overline{N_3}$ for the measured signal in units of charge quanta (electrons). With $\overline{N} = \overline{N_3}$ and by introduction of the quantity $\gamma = \overline{\eta_3}\,\overline{\eta_2}$ in the above equation, the variance of the electronic signal at the CCD output can be rewritten as

$$\overline{(\Delta N)^2} = \overline{N}\,(1 + \gamma) + n_{el}^2\ . \tag{C.28}$$

The corresponding signal-to-noise ratio is given by

$$\mathrm{SNR} = \frac{\overline{N}}{\sqrt{\overline{(\Delta N)^2}}} = \frac{\overline{N}}{\sqrt{\overline{N}\,(1 + \gamma) + n_{el}^2}}\ . \tag{C.29}$$

These expressions for the variance and the SNR are given in units of charge quanta. They must be related to the digital output of the CCD, which is given in units of the analog-to-digital converter unit (ADU). The average output signal $\overline{N_{ADU}}$ of the CCD in units of ADU is assumed to scale linearly with $\overline{N}$ as

$$\overline{N_{ADU}} = g^{-1}\,\overline{N}\ , \tag{C.30}$$

where g is the CCD gain factor. The noise at the output scales also with g. Hence, the variance at

[3] For our system the readout noise of 15 electrons corresponds to 3 analog-to-digital convert units (ADU).

the CCD output in units of ADU is given by

$$\overline{(\Delta N_{ADU})^2} = g^{-2}\,\overline{(\Delta N)^2}\,, \tag{C.31}$$

where $\overline{(\Delta N)^2}$ is the variance from Equation (C.28). Thus, the signal-to-noise ratio for the CCD output signal N_{ADU} in units of ADU is still given by the SNR in Equation (C.29).

Statistical distribution of the luminescence process

In the above derivation the luminescence process, i.e., the generation of the η_2 luminescence photons with average $\overline{\eta_2} = \nu_{lum}$, was assumed to obey Poisson statistics. This assumption is a strong simplification.

The absorption of an x-ray quantum is a complex process. The probability distribution of η_2 will depend on how the x-ray energy is split into different channels (processes). If the only channel was the generation of luminescence photons of energy E_{lum}, then a fixed number E_0/E_{lum} of luminescence photons would be generated for each absorbed x-ray photon of energy E_0. Such a process can obviously not be described by Poisson statistics.

Fortunately, the statistical distribution of the amplification process has little influence on the derived result as pointed in the original work by Mandel [101]. He expressed the variance of the luminescence process as

$$\overline{(\Delta\eta_2)^2} = k\,\overline{\eta_2}\,, \tag{C.32}$$

where k describes the deviation of the observed variance from the variance of a Poisson distribution signal with the same expectation value.[4] Mandel showed [101, Eqs.(7,8)] that the factor k can be neglected, when the amplification is a large number, $\overline{\eta_2} \gg 1$. This is a direct consequence from application of the variance theorem. The variance of the following stage is then determined by the variance of the previous stage. In the luminescence process in our camera it is $\overline{\eta_2} = \nu_{lum} \approx 272$ photons. Hence, we can neglect the deviation from a Poisson processes in application of the variance theorem.

The probability distribution of the luminescence process is of great interest in energy resolving detectors, where the x-ray energy is to be determined from the number of generated photons. (See for example the discussion of energy resolution in scintillator materials by Moses [105] and Swank [140]).

[4] The factor k was first introduced by Fano to describe the variance of the number of ions produced when stopping electrons and is called the Fano factor.

C.3 Noise in the projection images

In microtomography, the projected attenuation coefficient p is determined from measurements of an attenuated signal N and the reference signal N_0 according to $p = -\ln(N/N_0)$, where the signals N, N_0 can be described as random variables. We will determine the expectation value of the measured projected attenuation $\langle p \rangle$ and its variance $\langle (\Delta p)^2 \rangle$, with $\Delta p = p - \langle p \rangle$. In the following, the variance will be written without braces as $\langle \Delta p^2 \rangle = \langle (\Delta p)^2 \rangle$. In the derivation, we will later assume that the number of quanta measured in the attenuated beam N and in the reference beam N_0 obey Poisson statistics. The quantities N, N_0 correspond to the number of charge quanta detected in the CCD and are related to the CCD count by the CCD gain factor. The exact calculation would have to be based on the transformation of the probability distributions (integral transformation described by the 'Transformationssatz'[5]). For the calculation here, simply a Taylor series expansion of the logarithm as, e.g., shown by Hawkins [72][6] is used as an approximation.

Taylor series expansion of logarithm

The attenuation p in each image pixel is calculated from the random variables N, N_0 as

$$p = -\ln \frac{N}{N_0} = -\ln N + \ln N_0 \ . \tag{C.33}$$

Here, the logarithm splits into a sum.[7]

We write for N (and equivalently for N_0)

$$N = \langle N \rangle + \Delta N \ , \tag{C.34}$$

with the average $\langle N \rangle$ and the deviation ΔN whose average is $\langle \Delta N \rangle = 0$. Using this together with the Taylor expansion for $\ln(1 + x) = x - \frac{1}{2}x^2 + \frac{1}{3}x^3 - \frac{1}{4}x^4 + \ldots$, we can derive

$$\ln N = \ln \langle N \rangle + \frac{\Delta N}{\langle N \rangle} - \frac{1}{2}\left(\frac{\Delta N}{\langle N \rangle}\right)^2 + \ldots \tag{C.35}$$

and its average

$$\langle \ln N \rangle = \ln \langle N \rangle - \frac{1}{2}\frac{\langle \Delta N^2 \rangle}{\langle N \rangle^2} + \ldots \ . \tag{C.36}$$

Equivalently $\langle \ln N_0 \rangle$ is derived. We obtain for the average measured attenuation coefficient

$$\langle p \rangle = -\langle \ln N \rangle + \langle \ln N_0 \rangle = -\ln \frac{\langle N \rangle}{\langle N_0 \rangle} + \frac{\langle \Delta N^2 \rangle}{2\langle N \rangle^2} - \frac{\langle \Delta N_0^2 \rangle}{2\langle N_0 \rangle^2} + \ldots \ . \tag{C.37}$$

[5] See `http://de.wikipedia.org/wiki/Transformationssatz`

[6] Hawkins refers in large parts to Barret and Swindell [8].

[7] Because the expression splits up into a sum and since the noise in N and the noise in N_0 are uncorrelated, the two terms can in principle be studied independently of each other.

Assuming Poisson distributed signals with variances $\langle \Delta N^2 \rangle = N$ and $\langle \Delta N_0^2 \rangle = N_0$, the above expression simplifies to

$$\langle p \rangle = -\ln \frac{\langle N \rangle}{\langle N_0 \rangle} + \frac{1}{2\langle N \rangle} - \frac{1}{2\langle N_0 \rangle} + \dots \tag{C.38}$$

$$= \hat{p} + \frac{1}{2\langle N_0 \rangle} \left(e^{\hat{p}} - 1 \right) + \dots \ , \tag{C.39}$$

where in the second line the true attenuation coefficient $\hat{p}$ in form of the relation $\langle N \rangle = \langle N_0 \rangle \exp(-\hat{p})$ was introduced. The Taylor series expansion converges rapidly for $\langle N \rangle \gg 1$ and $\langle N_0 \rangle \gg 1$.

For the variance $\langle \Delta p^2 \rangle = \langle (p - \langle p \rangle)^2 \rangle$ of the measured attenuation, we find

$$\langle \Delta p^2 \rangle = \frac{\langle \Delta N^2 \rangle}{\langle N \rangle^2} + \frac{\langle \Delta N_0^2 \rangle}{\langle N_0 \rangle^2} + \dots \ , \tag{C.40}$$

where we have neglected higher order terms. We would have obtained the same result by error propagation.[8]

In the case of Poisson distributed signals N, N_0, the above equation simplifies to

$$\langle \Delta p^2 \rangle = \frac{1}{\langle N \rangle} + \frac{1}{\langle N_0 \rangle} + \dots \tag{C.41}$$

$$= \frac{1}{\langle N_0 \rangle} \left(e^{\hat{p}} + 1 \right) + \dots \ . \tag{C.42}$$

The two elements of the sum in Equation (C.41) describe the noise caused by the projection image i and the reference image r. The square root of the variance is the noise of the signal p

$$\sigma_p = \sqrt{\langle \Delta p^2 \rangle} \approx \frac{1}{\langle N_0 \rangle^{1/2}} \left(e^{\hat{p}} + 1 \right)^{1/2} \ , \tag{C.43}$$

which is plotted as a function of $\hat{p}$ and independent of the count rate in Figure C.2(a).

In the case of a well known reference signal, with variance $\langle \Delta N_0^2 \rangle \approx 0$, the variance simplifies to the expression[9]

$$\langle \Delta p^2 \rangle = \frac{1}{\langle N \rangle} + \dots \ . \tag{C.44}$$

The average measured $\langle p \rangle$ in Equation (C.39) and its variance $\langle \Delta p^2 \rangle$ in Equation (C.42) are valid approximations in the limit $\langle N \rangle \gg 1$ and $\langle N_0 \rangle \gg 1$.

[8] Assuming uncorrelated random variables N, N_0, error propagation gives:
$\langle \Delta p^2 \rangle = \langle \Delta N^2 \rangle (\partial p / \partial N)^2 + \langle \Delta N_0^2 \rangle (\partial p / \partial N_0)^2$.

[9] For x-ray tubes systems, the reference N_0 is well known and is typically treated as a constant with variance zero.

Shift of attenuation value

We can now compare the average of the measured attenuation $\langle p \rangle$ with the real attenuation coefficient $\hat{p}$. From Equation (C.39), we find the difference

$$\langle p \rangle - \hat{p} \approx \frac{1}{2\langle N_0 \rangle} \left(e^{\hat{p}} - 1 \right) . \tag{C.45}$$

This describes a shift of the measured attenuation towards higher values. This was expected because the logarithm is not a linear function.

In the limit of large numbers $\langle N_0 \rangle \to \infty$, the difference converges towards zero and $\langle p \rangle$ converges towards the real attenuation coefficient $\hat{p}$. At the same time, the variance $\langle \Delta p^2 \rangle$ vanishes.

It should be noted that repetition of the measurement (averaging of attenuation coefficients) will not generally reduce the observed shift in the data. The shift is present in the average of measurements! Only the increase of the average number of measured quanta in a single measurement will thus reduce the shift. This can be achieved by adding (or averaging) individual measurement values of N and N_0, before the logarithm is calculated. Fortunately, the shift is very small and not of relevance for our measurements, as can be easily shown in an example.

Example: Assuming a measurement with a very low count rate, with only $\langle N_0 \rangle = 5000$ charge quanta in the CCD (equivalent to 1000 ADU for our CCD gain of $g = 5$) and a rather high attenuation coefficient of $\hat{p} = 3$ and accordingly $\langle N \rangle = 5\,000 \exp(-3) \approx 249$. Even in this extreme case, the difference is only $\langle p \rangle - \hat{p} \approx 8.2{\times}10^{-4}$ and can be neglected. Only for an extremely low average number of counts $\langle N \rangle$ the shift will be of importance. Note that Equation (C.39) neglects the higher-order terms of the Taylor expansion and is valid only for $\langle N \rangle$, $\langle N_0 \rangle \gg 1$. It will, therefore, not give a quantitatively correct result at low average number of counts.

Optimum signal-to-noise ratio

From the variance in Equation (C.42), the relative variance of p directly follows as

$$R(p) = \frac{\langle \Delta p^2 \rangle}{\hat{p}^2} \approx \frac{1}{\langle N_0 \rangle} \frac{e^{\hat{p}} + 1}{\hat{p}^2} . \tag{C.46}$$

The relative noise is just the square root of this function, which is

$$\frac{\sigma_p}{\hat{p}} \approx \frac{1}{\langle N_0 \rangle^{1/2}} \left(\frac{e^{\hat{p}} + 1}{\hat{p}^2} \right)^{1/2} . \tag{C.47}$$

It corresponds to the inverse signal-to-noise ratio (SNR). The relative noise is plotted as a function of $\hat{p}$ and independent of count rate in Figure C.2(b). Relative noise and relative variance obey a minimum at $\hat{p} \approx 2.218$, which correspond to about 11% transmission. Thus, this is the attenuation value that can be measured with the best signal-to-noise ratio.

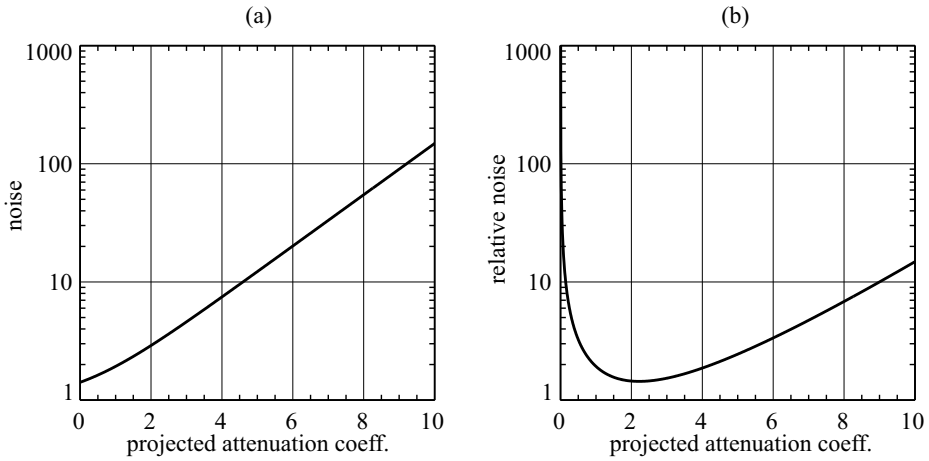

Figure C.2: (a) Noise and (b) relative noise of the measured projected attenuation coefficient p, plotted as a function of the projected attenuation coefficient $\hat{p}$. The functions are plotted independent of count rate $\langle N \rangle$: noise as $\sigma_p \langle N_0 \rangle^{1/2}$, with σ_p from Equation (C.43) and relative noise as $(\sigma_p/\hat{p}) \langle N_0 \rangle^{1/2}$, with the relative noise $(\sigma_p/\hat{p})$ in Equation (C.47).

So far we have assumed that the reference signal N_0 is determined from a single measurement. In the case of a well known reference signal ($N_0^{-1} \to 0$) the variance of p is given by Equation (C.44), and Equation (C.46) becomes

$$R(p) = \frac{\langle \Delta p^2 \rangle}{\hat{p}^2} \approx \frac{1}{\langle N_0 \rangle} \frac{e^{\hat{p}}}{\hat{p}^2} \,. \tag{C.48}$$

The minimum of this function is at $\hat{p} = 2$, whereby we obtain the condition $\mu D = 2$ given by Grodzins [68] for optimal tomographic measurements of an object of thickness D.

To find the optimal value for p and thus the optimal photon energy for the measurement it was implicitly assumed above, that the number of incident x-ray quanta $\langle N_0 \rangle$ is fixed and identical at all photon energies. In reality, the photon spectrum will be given and one might rather be interested in optimization of the required measurement time or in minimization of the radiation dose.

In practice, we try to select a photon energy that results in the optimum attenuation value of $p \approx 2$ at maximum. The exposure time is then selected such that the CCD almost reaches its maximum value in the reference image. The average number of incident quanta $\langle N_0 \rangle$ is then given by the maximum CCD capacity for charge quanta in a pixel.

Appendix D

Measurement procedure

D.1 Characterization of the spatial system response (MTF/PSF)

The spatial system response of our system is characterized using the method for calculation of the MTF from an edge trace (edge profile) that was presented by Jones [91]. For the measurement of the spatial system response, we assume that the system is linear shift invariant (LSI) and radially symmetric. In this case the MTF can be determined by

1. measurement of the edge spread function ESF(t),
2. calculation of the line spread function LSF(t) by derivation of the ESF(t), as given by Equation (2.39), and
3. calculation of the MTF(w) by Fourier transform of the LSF(t), as given by Equation (2.41).

This was theoretically derived in Section 2.4.1 and Section 2.4.2. We shall now describe the practical realization of these three steps for the determination of the MTF in detail. The determination of the point spread function (PSF) is not described explicitly. However, the reconstruction (see previous section) of the PSF from the LSF that is obtained in step 2 is straightforward.

1.) An edge profile of the incoming radiation is realized by an edge device that is opaque for the incident x-rays. A gold plate or a block of Densomed are available at the microtomography setup as edge devices. The edge is positioned close to the luminescent screen, to avoid effects from the beam divergence or from x-ray scatter. Three sub-frame images are recorded in an approximately symmetric region around the edge: a CCD image of the edge profile i_E, a reference image (beam without edge) r, and a dark image d. A normalized edge profile is calculated from the recorded images as

$$\text{normalized edge image} = \frac{i_E - d}{r - d} \ . \tag{D.1}$$

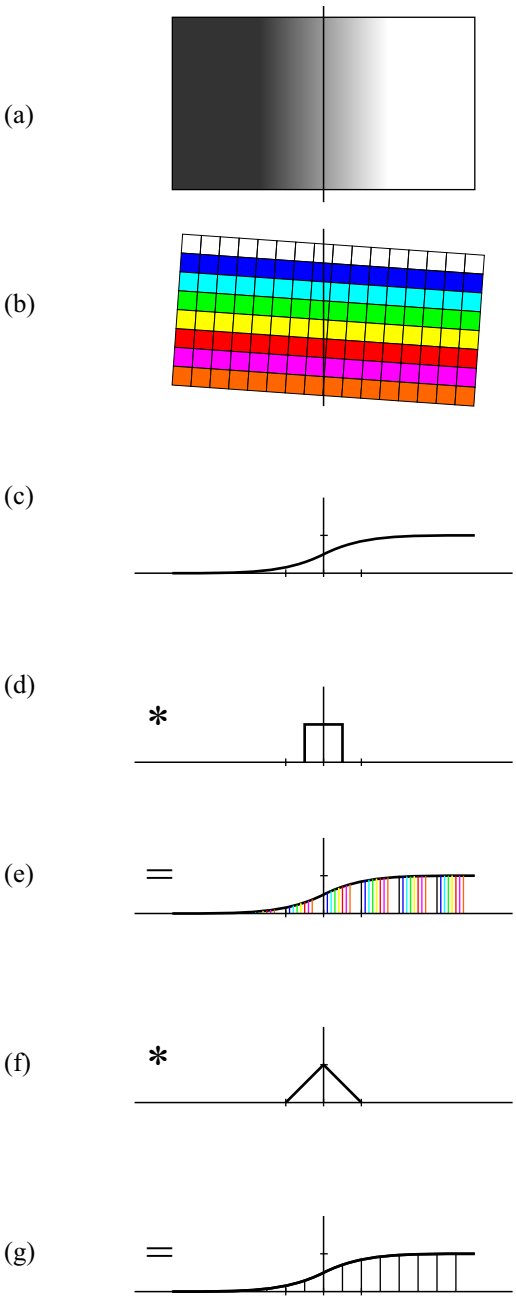

Figure D.1: Calculation of the one-dimensional edge spread function (ESF) from an (a) edge profile using a (b) tilted detector grid. (c) – (d) Calculation steps as explained in the text.

The reference image should ideally be a flat image with constant intensity and infinite extension (infinite field of view). In reality the recorded images and the impinging x-ray beam are limited in size. This fact hinders the measurement of long-range contributions (tails) present in the PSF and ESF.

In the measurement, the edge is oriented almost horizontally but with a slight tilt with respect to the CCD rows. The slight tilt of the edge profile results in a sampling interval better (smaller) than the 9 μm pitch of the CCD pixels. The calculation of a one-dimensional representation of the edge profile from the measured data is schematically shown in Figure D.1. Figures D.1(a) and (b) represent the two-dimensional edge profile and the tilted two-dimensional detector. The vertical line represents the true position of the edge. The small effect of the edge tilt on the square shape of the pixels is neglected in the calculation. Figure D.1(c) shows the one-dimensional representation of the edge profile that is to be determined. The sampling function of the detector (see below) is a rectangular function shown in Figure D.1(d). Its width corresponds to the pixel edge length. Thus the measured signal is the convolution of the edge profile with this rectangular function. The sampling points are given at a resolution that is given by the tilt. Figure D.1(e) schematically shows how the position of the sampling points is related to the edge position. Here the sampling points have been coded with the color of the detector rows, according to Figure D.1(b). For the further evaluation of the data new software has been implemented in this work. The alignment of the data requires the knowledge of the edge position in each detector row. It is determined by linear interpolation of the position, at which the normalized intensity raises to above 0.5 with sub-pixel resolution. From the recorded data and the edge position, the intensity of the edge profile at any distance from the edge can now be determined by linear-interpolation for each row. A new sampling grid of 0.5 pixel resolution and with a grid point on the edge position is defined, as shown in Figure D.1(g). The edge profile of each detector row is now linearly interpolated to values on the new sampling grid, and the contribution of the individual rows is added up. It is possible to describe the linear interpolation as convolution with the triangular function shown in D.1(f).[1]

2.) The LSF is the derivative of the ESF. It is calculated from the difference of every two neighboring ESF values, which is the reason why the resulting LSF has one sampling point less than the ESF. The number of sampling points of the LSF is thus even and the sampling point resolution (0.5 bin) is maintained. The LSF obtained in this way will not be fully symmetric, which is mainly a consequence of noise in the recorded images. However, for a radially symmetric system that we assume, the LSF must be symmetric too. To force radial symmetry of the resulting PSF/MTF we have to symmetrize the data now.

Other authors simply calculated the Fourier transform from the non-symmetric LSF. They then used the real part or the absolute of the result as the MTF. This approach gives an MTF that describes a radially symmetric system with a PSF that is a real function as required, but it

[1] Other sampling grids and interpolation schemes can be realized. Grids with higher sampling density than 0.5 pixel are possible, but they won't have a strong influence on the result. Using, e.g., nearest neighbor interpolation (that can be described by the convolution with a rectangular function) instead of linear interpolation will give a different result.

does not make optimal use of the given data. The software implemented in this work calculates a symmetric ESF in real space. This is done by replacement of the data on one side of the LSF with data from the other side.[2] Here the LSF from the dark side of the beam profile is used to replace the LSF on the bright side. This approach profits from the fact that the noise level on the dark side of the recorded edge profiles is lower, which is a direct consequence of photon noise. The lower noise level can directly be seen, e.g., in the LSFs of Figures 4.4(c) and (d). The implemented symmetrization results in an LSF with less noise. Additionally, the influence of beam profile fluctuations is minimized, since these influence the edge profile less strongly on the dark side than on the bright side.

3.) The MTF is calculated from the symmetrized LSF using the fast Fourier transform (FFT). The absolute of the result is calculated in order to convert all values to real numbers and gives our MTF. The MTF is purposely not (!) normalized to $\mathrm{MTF}(0,0) = 1$ as reported in other publications. Normalization was already achieved by calculation of the normalized edge profile in Equation (D.1) and is not required. For long tails in the PSF we, in fact, expect $\mathrm{MTF}(0,0) < 1$, and the deviation of the MTF from unity indicates how much of the intensity spreads to the region outside the field of view. By normalization to $\mathrm{MTF}(0,0) = 1$ the MTF would be overestimated.

Influence of sampling function and interpolation

The influence of the sampling function and the interpolation step in the above calculation of the LSF can be described as convolution operations. One of these convolution operations is due to the so called 'detector sampling function', while the other is due to the calculation itself. The two convolution operations can be described by multiple convolution with a rectangular function as is shown in the following.

The active area of a CCD pixel defines the sampling function. For the CCD we shall neglect the gap between adjacent pixels and assume that the response of the pixel is constant over the pixel area. The sampling function of such a pixel is given by the product of a normalized rectangular (box car) function along the horizontal and the vertical direction. We shall reduce our discussion to the one-dimensional case, which is sufficient for the description of the edge profile. Then the rectangular function is defined as

$$s_{rect}(x) = \begin{cases} 1/d, & |x| \leq d/2 = const \\ 0, & \text{else} \end{cases} , \tag{D.2}$$

where d is the edge length of a detector pixel. The effect on the measured signal is described by the convolution of the signal and this sampling function. Equivalently in Fourier space, the sampling function contributes to the MTF of the system by the multiplication with the Fourier transform of

[2] Alternatively, the software also performs symmetrization by calculation of the average of the LSF and the reversed LSF. This actually corresponds to taking the real part of the Fourier transform as described before and provides no additional advantage.

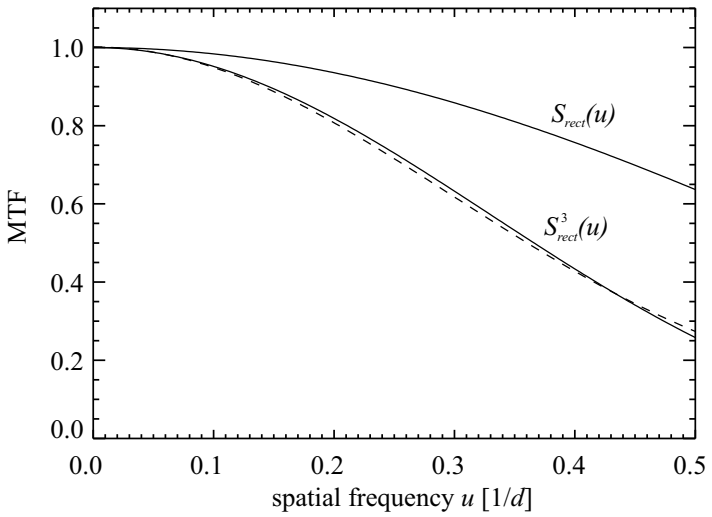

Figure D.2: The calculated MTF of a perfect and tilted edge (dashed line) in comparison with the expected MTF(u)=$S^3_{rect}(u)$. The Fourier transform of a single normalized rectangular function $S_{rect}(u)$ is also shown.

$s_{rect}(x)$, which is

$$S_{rect}(u) = \frac{\sin(\pi d u)}{\pi d u} \ . \tag{D.3}$$

This function is plotted in Figure D.2 and results in a reduction of the determined MTF values at high frequencies. At the Nyquist frequency $u = 1/(2d)$, the function $S_{rect}(u)$ has dropped to the value $2/\pi$. A properly measured MTF cannot take values above this function, i.e., it will be MTF(u) < $S_{rect}(u)$ for all frequencies.[3]

The interpolation step in the calculation of the MTF can be described by the convolution with the triangular function that is shown in Figure D.1(f). This triangular function can be described as convolution of the rectangular function with itself as $s_{rect}(x) * s_{rect}(x)$ or equivalently in frequency space as the multiplication with $S^2_{rect}(u)$. The combined effect of the detector sampling function and the MTF calculation gives the maximum achievable MTF of $S^3_{rect}(u)$. This curve is plotted in Figure D.2.

The MTF calculation was tested with simulated data of a perfect and tilted edge. The simulated edge image was calculated for 400 detector rows of 1000 pixel length and a centered edge with tilt 0.025, i.e., the edge running over $400 \times 0.025 = 10$ pixel. The value of 0 or 1 was assigned to the corresponding sides of the edge. The pixel that is intersected by the edge was assigned the fractional value that corresponds to the position of the edge on the pixel. The calculated MTF for this test object is shown as the dashed curve in Figure D.2. There is a slight difference between this simulated MTF of the perfect edge and the expected $S^3_{rect}(u)$. The difference is probably caused by the selection of the new sampling points. Apart from that, the theoretically expected curve is well described by this simulated MTF.

[3]The measured MTF(u) may take values above $S_{rect}(u)$, when the edge is not tilted in the measurement.

Remarks on deconvolution using the MTF/PSF

It was shown above how the calculation of the MTF degrades the resulting MTF values. For the correct calculation of the MTF (or PSF) corrections must be applied. In fact the correction is important, when the PSF or the MTF are to be used for deconvolution. For the reconstruction of the two-dimensional MTF or PSF, not only the effect from the calculation must be corrected. It must further be corrected for the detector's sampling function. The sampling function, generally, is not a radially symmetric function and, typically, is a rectangular function for CCDs. The MTFs presented in this work have not been corrected and, hence, under-estimate the MTF of the system.

It should be kept in mind, which further simplifications are made when using linear systems theory for the description of the x-ray camera by a PSF. The assumption of a linear and space invariant system might be incorrect. Thus, the space-dependent variation of the PSF must be carefully investigated. Especially, long-range components of the detector PSF might vary as a function of position. Recently, measurements of pinhole images have been recorded with our setup that will enable direct comparison of the point-spread function at different detector positions.

Both the long and the short range contributions to the PSF are difficult to measure: The short range contributions are influenced by any additional blur in the system (imperfections of the edge profile, scatter), while the long-range contributions are difficult to measure with a non-homogeneous beam profile. A good measurement of the PSF and thus a major improvement by deconvolution seems to be achievable in the range of approximately 5 to 100 pixels PSF radius.

D.2 Tomographic acquisition schemes

Different acquisition schemes can be used in a tomographic scan that shall be referred to as 'scan modes' in the following. During this work a variable 'scanmode' was introduced into the reconstruction software. It can take the values '180deg' or '360deg'. The processing software was adapted such that it automatically performs the appropriate operations for either mode.

The '180deg' mode is used for the typically performed tomography scan, in which projection images are recorded over a range of 180^o. The center of rotation lies approximately in the middle of the reconstruction [see Figure D.3(a)], whereby the sample diameter is limited to the field of view of the detector. Examination of samples larger than the field of view of the detector (or larger than the x-ray beam) is basically possible. The sample must then be scanned (sampled). Projection images are recorded at each position and combined into the entire projection image.

Scanning the sample along the rotation axis (z-direction) is easily possible with the built-in motor of the rotation stage. This results in additional independent projections that can be stacked after reconstruction [Figure D.3(c)]. Horizontal scanning (perpendicular to z-direction) is more

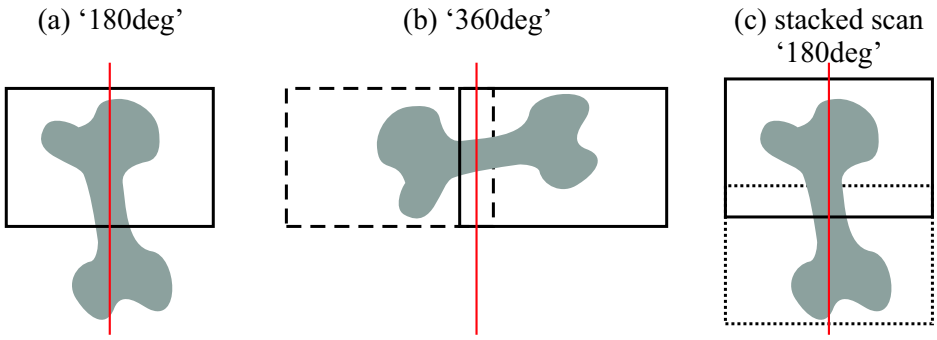

Figure D.3: Implemented acquisition schemes for the tomographic scan. (a) '180deg' scan mode with the center of rotation (red solid line) in the center of the field of view (black box). (b) '360deg' scan mode with the center of rotation at the side of the field of view. The mirror projection (indicated as dashed box) is used for combination of the entire projection image. (c) In a stacked scan the sample is translated parallel to the rotation axis.

troublesome, since a precise horizontal shift of the rotation axis or a very good alignment procedure (registration) for the images is required. However, we can easily increase the field of view to almost double width, when the scan is performed over 360^o.

In the '360deg' mode the center of rotation is set to one side of the field of view rather than to its center [Figure D.3(b)]. Tomographic projections are recorded over a range of 360^o, whereby almost one half of the sample is outside the field of view. Two projection images recorded at 180^odisplaced projection angles are subsequently combined into the full projection image, with almost the double width of the field of view. The center of rotation is positioned such that mirror images have about 10% overlap. The number of sampling points N_t in each mirror projection (typically $N_t = 1536$) is thereby increased to almost $2N_t$ in the combined projections. Thus even samples with a diameter of almost double the width of the field of view can be investigated. For the larger number of sampling points the time required for reconstruction is also prolonged (see Section 3.2.4), and the noise in the reconstruction increases (see Section 3.3.2). Therefore, it is often made use of binning (on-chip binning or binning of recorded images) in the '360deg' mode.

In the standard setting, projections are recorded in steps of $\Delta\theta = 0.25^o$. Thus, the number of recorded projections is $N_\theta = 720$ in both the '180deg' and '360deg' scan mode. In '360deg' scan mode, actually $2N_t = 1440$ projection images are combined into half the number of projections. Typically $N_d = 4$ dark images (optical shutter of the CCD closed) are measured before each scan. One or several reference images are usually measured after every eight projections, as well as before and after the scan.

The scan duration is determined by the CCD exposure time t_{exp}, the CCD readout time, time for sample moves (rotation, in/out translation for the measurement of reference images). For a typical exposure time of $t_{exp} = 1$ s, a scan in the 180^o-mode takes about 2 hours for full-frame CCD readout without on-chip binning and $N_\theta = 720$ projections. During the scans the exposure time is automatically adjusted to compensate for the exponentially decaying beam intensity. Hereby optimal use of the dynamic range of the x-ray camera is made.

D.3 Setting up the apparatus for a tomographic scan

Before a tomographic scan is started, the apparatus is aligned and the x-ray camera settings are adjusted. During this work several enhancements were made to the microtomography apparatus and its control software that simplify (automate) the setup procedure. After the description of the procedure details the setup sequence is summarized in form of a list at the end of this section.

Magnification selection and automated focussing

The magnification factor is determined by the distance between CCD and luminescent screen and by the focal length of the lens system. Before a tomographic scan the position of CCD-camera and lens system are set approximately to those positions that give the desired optical magnification factor. Finally, focusing is performed by fine-tuning of the lens position.

An automated focussing procedure was implemented in this work that iterates the lens position until a sharp image is obtained. The procedure makes use of the MTF measurements that were described in Section D.1. Maximization of the integral over the determined MTF curve is performed.[4] The MTF is calculated at each iteration step and stored. When the final iteration step (depending on final resolution setting) is reached, the objective returns to the best lens position and the final resolution value a_{10} (corresponding to an MTF value of 10%, compare Section 2.4.3) is determined in units of the effective pixel size τ. All images recorded for the MTF calculation are deleted, except for those recorded for the final focussing position.

Conversion to the absolute resolution is possible only after determination of the optical magnification factor m that also determines the effective pixel size $\tau = \tau_{CCD}/m$. A procedure for the automated determination of the optical magnification factor was implemented in this work that can be run directly after the auto-focussing procedure has finished. Here the same edge that is used for auto-focussing is translated by a known distance Δz along the z-direction. Projection images are recorded before and after translation of the edge. From the distance of the edge position in units of pixels, together with the known absolute distance, the effective pixel size τ and the optical magnification factor m are calculated. The measurement is carried out two times. First, an approximate value is found with only a small translation of the edge, which ensures that the edge (typically in the center after MTF measurement) does not leave the field of view. In the second measurement, the edge can already be quite well positioned. A translation over ~90% of the vertical direction of the field of view is performed. From the known translation distance, again τ and m are calculated. A precision of ~1 pixel is reached by this method. The precision in m and τ depends on the size of the field of view and is typically better than 1%.

The magnification value determined by this method is now used in our reconstruction chain for the alignment of stacked data sets from the known z-translation of the sample.

[4] Other measures as the gradient in the images would probably be more appropriate. More ideas can be found in the literature on auto-focussing techniques.

Alignment of x-ray beam, CCD camera and rotation axis

As described in Section 5.1.1 (with help of Figure 5.1), the rotation axis must be oriented perpendicular to the incident x-ray beam, when the reconstruction is to be calculated as a stack of two-dimensional reconstructions. Additionally, it should be oriented perpendicular to the CCD rows. Thereby each row of the CCD acquires the data needed for the reconstruction of one tomographic slice, and resolution losses by rotation of the CCD images (requires interpolation) can be avoided. The required alignment of the rotation axis is performed at the start of each measurement period or after relevant system changes have been made.

The rotation axis (z-direction) is aligned perpendicular to the incident beam direction by rotation of the entire apparatus (including rotation platform and camera). The deviation from the perpendicular orientation is measured from radiographic projections. A test device of diameter $d = 240\,mm$ is mounted on the sample holder and two mirror projections at $\theta = 0^o$ and 180^o are recorded. From the vertical offset of the same feature in both images, the orientation is corrected until the offset is in the range of one pixel. The apparatus is set to the highest optical magnification $m = 6$ for this measurement. Here the effective pixel size is $\tau = 1.5\,\mu$m and an angular precision of $\Delta\vartheta \approx \tau/d \approx 6.25 \times 10^{-6}$ rad is reached. We can assume that the sample has a maximum diameter that is equal to the width of the CCD with $N_t = 1536$ pixels. Thus, the projecting rays, when they pass through the sample, travel a distance along the z-direction that is $\Delta z = \Delta\vartheta\, N_t \approx 0.01$ pixel at maximum. Hence we can apply two-dimensional reconstruction techniques. The orientation of the aligned apparatus is regularly checked by the reading of an electronic water level that was implemented at the apparatus during this work. Hereby, the accurate position of the axis is monitored and an influence of mechanical moves (apparatus height, lens system, or CCD camera) can be detected.

The rotation axis is aligned parallel to the detector columns by rotation of the CCD. Two mirror projections of a gold mesh are used to measure the tilt of the CCD with respect to the rotation axis. From the vertical displacement δz in units of pixels of a corresponding feature in both mirror projections, the tilt is calculated. For a measurement at the side of the projections of width $N_t = 1536$, the tilt is given by $\varphi = \delta z/N_t$. By this manual procedure a precision of one pixel and $\Delta\varphi \approx 1/N_t \approx 6.5 \times 10^{-4}$ is reached. Higher precision is reached using an image registration procedure that was developed and implemented during this work. The procedure uses the entire projection images of the grid recorded at $0^o$and $180^o$and calculates the optimum tilt of the projections. Simultaneously the position of the rotation axis is determined as a by-product. The procedure converges at a precision that is significantly better than the manually reached precision. Its precision has not been validated yet.

Setup sequence

1. The photon energy is selected with the monochromator. The aim is to achieve the optimum projected attenuation coefficient of $p \lesssim 2$. (Compare Section 3.3.2).

2. The magnification factor is set and automated focussing is performed (see above). The resolution parameter a_{10} and the magnification m are determined from projection images of a gold edge.

3. The objectives aperture is set to achieve a good compromise between the flux of luminescence photons and resolution.

4. [The required alignment of the rotation axis is performed (see above). First, the rotation axis is aligned perpendicular to the incident beam direction by tilt of the entire apparatus. Secondly, the rotation axis is aligned parallel to the detector columns by rotation of the CCD.][5]

5. The position of the center of rotation (rotation axis) is set depending on the scan mode (see above): to the center of the field of view in '180deg' mode, and to the side of the field of view in '360deg' mode.

6. The x-ray aperture is closed to about the size of the field of view for suppression of stray radiation. When deconvolution of the images is planned, the aperture should be closed to slightly below the field of view.

7. The sample is mounted and positioned in the center of the rotation axis with the xy-positioning stage.

8. The sampling parameters are selected: number of projections N_θ, on-chip binning factors b_t, b_z, CCD sub-frame size $N_t \times N_z$. Equation (3.31) can be used to estimate the noise level in the reconstructions and for selection of the optimal number of projections N_θ. The sampling condition $N_\theta \gtrsim (\pi/2)\, N_t$ should be met. Usually, the resolution is $a_{10} > \tau$, which allows to relax the condition by replacing N_t with $(\tau/a_{10})\, N_t$ (compare Section 3.2.3).

D.4 Recording projection images

In the tomographic scan radiographic images of the sample i, reference images of the beam profile r, and dark images with no illumination d are recorded. The attenuation image p is calcu-

[5] Only performed at the start of each measurement period or after relevant system changes have been made.

lated as

$$\begin{aligned} p &= -\ln \frac{(i-\overline{d})/t_i}{(r-\overline{d})/t_r} \\ &= -\ln \frac{i-\overline{d}}{r-\overline{d}} + \ln \frac{t_i}{t_r} , \end{aligned} \tag{D.4}$$

where $\overline{d}$ is an average dark image that will be described in the next section. The expression in the denominator of the first line of Equation (D.4) is in fact an interpolated reference image that will be calculated below. The images i and r are corrected for the CCD dark image by substraction of $\overline{d}$ and normalized to their exposure times t_i and t_r. The normalization to the exposure times is necessary, since the exposure time is constantly adjusted during the measurement. The exponentially decaying intensity of the synchrotron radiation is thereby compensated. As to be seen from the second line of Equation (D.4), different exposure times t_r and t_i would cause a constant offset in p without normalization.[6]

The dark-image-corrected reference image $(r-\overline{d})/t_r$ in Equation (D.4) is actually a linear interpolation of two corrected reference images recorded before and after the radiographic projection i. Hereby, the effect of a varying beam profile is minimized. We introduce the recording times T_{r_1} and T_{r_2} of the reference images r_1 and r_2, and the recording time T_i of the radiographic projection i. The corrected reference image is then calculated as

$$(r-\overline{d})/t_r = \frac{T_{r_2}-T_i}{T_{r_2}-T_{r_1}}(r_1-\overline{d})/t_{r_1} + \frac{T_i-T_{r_1}}{T_{r_2}-T_{r_1}}(r_2-\overline{d})/t_{r_2} . \tag{D.5}$$

Noise in the images can eventually cause the term $(i-\overline{d})/(r-\overline{d})$ in Equation (D.4) to become negative. In this case, the logarithm would be undefined. The corresponding pixels of the absorption image are replaced by an average of the values calculated for neighboring pixels of the same line. Since this happens only rarely and statistically distributed over the CCD area, it does not affect the tomographic reconstruction considerably.

The calculated absorption images are finally resorted in increasing order of projection angle; the so formed sinograms are stored. The implemented image processing software allows for binning of the recorded images before calculating the absorption images. This generally improves the signal-to-noise ratio in the data at the cost of a reduction in spatial resolution, which is further discussed in Section 3.3.4. In the case of binning, the image correction can be calculated after binning of the raw data.

[6] It might be assumed that a constant offset is not relevant for the tomographic reconstruction. The filtered backprojection theoretically filters out the zero frequency component. However, the constant background would impose a problem for reconstruction, during which the sinograms are zero-padded. Moreover, there is an influence of the zero-frequency component to the “RALA”-type reconstruction. (Compare Chapter 3).

D.5 Calibration and correction of CCD images

This section briefly describes the correction applied to the raw CCD images. General details concerning the calibration of CCD images can be found, e.g., in the publications by Barna *et al.* [7], Gruner *et al.* [70], and a software manual by Diffraction Ltd. [43].

Each CCD chip has a different bias level (zero point), dark current (sensitivity to temperature), and sensitivity to light. These effects don't just vary from camera to camera; they vary from pixel to pixel in the same camera. Each of these effects corrupts the intensity represented in every pixel of the image in a specific way [43]. The bias level adds a constant value to the readout of each pixel, independent of exposure time. A bias frame (no illumination, exposure time: ~0 sec.) can be used for correction. Dark current accumulates during the exposure at a different rate within each pixel. The dark frame (no illumination, finite exposure time) therefore depends on the exposure time. The dark current of our camera with Peltier cooling is very low, with 0.1 – 0.2 electrons/pixel/sec at -10^{o}C. Individual pixels that show an increased amount of dark current are called hot pixels. With only a few hot pixels in our camera and otherwise negligible dark current, dark frame or bias frame can be used equivalently for correction, since the influence of the exposure time can be neglected. We therefore correct the reference and projection images by substraction of an average dark image. The average dark image is calculated from several CCD dark images that are recorded before each tomographic scan. The Zinger removal procedure described below is used for averaging. Besides the average it provides a value for the variance of each pixel. For our camera the mean variance of a single pixel in an average of $N_d = 4$ dark images is below 2.0 ADU of the CCD, which agrees well with the specified CCD readout noise of 3.0 ADU (corresponding to $n_{el} = 15$ electrons).

So called Zingers are another source of error in the recorded images. Zingers are unwanted, localized random events in an image that are caused by cosmic rays, decay of radioactive isotopes present in the material of the detector itself, or, at synchrotron sources, hard stray radiation from sources other than the direct beam [7]. The identification of Zingers and their correction is known as dezingering, which is also referred to as 'cosmic ray removal/rejection' in astronomy or 'outlier detection' in so called 'robust statistics'. During this work a simple procedure was implemented that rejects the contribution of pixels with outlying values, when calculating the average of several otherwise identical images. A more sophisticated algorithm for Zinger removal is implemented in the XVISTA package.[7] The simple Zinger removal used here is applied for the calculation of the averaged dark image only. Because of the short exposure times in our tomographic scans, Zingers are observed only very occasionally in the radiographic images and make a negligible contribution to the reconstruction.

[7] The PICCRS routine of XVISTA optimally combines frames with outlier rejection. It was originally written for the statistical removal of cosmic rays from Hubble space telescope data. XVISTA is a software package for astronomical image processing, largely written in FORTRAN 77 and available online at `http://ganymede.nmsu.edu/holtz/xvista/` [visited June, 10th 2006].

Each pixel in the CCD camera has a slightly different sensitivity to light. Typical CCD sensors have a pixel-to-pixel variation of the light sensitivity that is in the order of 1% [43]. The photoresponse non-uniformity of our camera is 1% (see Appendix G). Moreover, imperfections in the optical system (e.g., vignetting, which describes a decrease of intensity towards the edges of the image) may result in a spatial variance of the camera sensitivity. Fortunately, we are not interested in absolute measurements, but rather in the ratio of reference images and radiographic projection in Equation (D.4). Therefore, pixel-to-pixel variations will be automatically corrected upon calculation of the intensity ratios for each pixel.

The linearity within each CCD pixel as a function of incident intensity is of much more importance for the calculation of correct intensity ratios. It is specified as the photoresponse non-linearity, which for our CCD is 1%. This is the maximum deviation of the pixel response to a straight line fit. Thus the intensity ratio is also known with about 1% precision or better.

D.6 Image-processing chain and reconstruction

The recorded CCD images are stored in 16-bit integer representation (CCD output has 14-bit resolution) and are processed for the determination of the projected attenuation p as described above. Binning of the recorded images can be applied for the reduction of noise as described in Section 3.3.4. The finally calculated projections are stored in 32-bit floating point representation.

The entire projection data is a three-dimensional array $p = p_{\theta_i}(t_j, z_h)$ that contains a value for each pixel position (t_j, z_h) and projection angle θ_i. The calculated projections are given as an image for each projection angle θ_i. Using an IDL-routine, the projections are resorted into sinograms, i.e., two-dimensional files for each slice z_h that can be independently reconstructed (because of the parallel-beam geometry). For projection data recorded in '360deg' mode, the sinograms are combined into a complete sinogram with projections over a range of only 180^o. New projections are combined from mirror projections by linear interpolation. The width of the new projections is $N_t' \lesssim 2N_t$.

The center of rotation in the sinogram data is determined from the average of 20 sinograms (from the center of the scan) using the method for the determination of the center of rotation developed during this thesis and presented in Chapter 5. The obtained optimum center of rotation (t_r) is used as input parameter for the reconstruction, which now starts automatically.

The standard reconstruction is performed with the filtered backprojection algorithm "BKFIL" of the RECLBL library described in Chapter 3. The butterworth filter "BUTER" with the parameters "ORDERX" = 0.5 and "FREQX" = 10.0 is applied to the discrete Fourier transform of the projections. The routine 'BIN' is used for backprojection and performs linear interpolation of the inverse Fourier transformed data onto the reconstruction grid. The rotation axis lies in the center of the reconstruction grid, which is of the size N_t^2, where N_t is the number of pixels in a projection image row (number of sampling points). The reconstructed slices contain values corresponding to

the attenuation per sampling distance τ in the (binned) projections. Division by τ gives the attenuation coefficient. Reconstruction of the sinograms is performed on an extendable computer cluster. An average speed of one tomographic slice in 7 seconds for a 1536×1536 pixel reconstruction grid is achieved with parallel computation at the moment. A full scan with $N_z = 1024$ slices, thus, is reconstructed within two hours.

The reconstructed slices are stored as 32-bit floating point values. The size of a reconstructed data set for a full field scan is 9 GByte. This number is reduced by a factor of four by conversion of the reconstructed slices to 8-bit images in the uncompressed tiff file format. A range of attenuation values between μ_{min} and μ_{max} is selected and rescaled to values between 0 and 255. Values below μ_{min} are assigned the values 0 and values above μ_{max} are assigned the value 255. The selection of a gray value range is also known as windowing. The parameters μ_{min}, μ_{max} have to be selected by the user (typically after analysis of the histogram) over all slices and are stored in a log-file together with the reconstructed data.

Another IDL procedure is used to create volume data sets from the tiff images. The tiff images of several scans that were performed at different heights (z-position of the sample) can be stacked into one data set. The known translation distance between the scans and the known sampling distance τ (pixel size divided by magnification) enables the alignment of the data. The new stack is created by interpolation of the single stacks along the z-axis. Stacks of up to eight scans have already been created in this way. The reduction to a certain xyz range as well as additional binning is possible upon stack generation. The stacks can be loaded into the software package VGStudio[8] for volume visualization (rendering) of the data.

D.7 Verification of negligible beam divergence

The angular distribution of the x-ray beam, its divergence, determines the amount of geometrical blur that is introduced in the imaging step. A pinhole measurement was carried out in this work to measure the beam divergence at beamline BW2.

The characteristic distribution of the radiation intensity (from the wiggler) at the sample position is a function of position and angle. The resulting distribution depends on the size and divergence of the electron distribution in the ring, the characteristic of the radiation cone (depending on electron energy and wiggler parameters), and the source to sample distance L. The effective horizontal source size σ_X and the effective vertical source size σ_Z of the wiggler can be calculated as described, e.g., in the PhD thesis of Busch [31].

However, these calculated values do not incorporate the influence of the optical components in the beamline. In particular the influence of the (bent) monochromator crystals or the beamline windows is neglected. Therefore the beam divergence was measured in this work at BW2 at a photon energy of 24 keV. For this purpose, a pinhole was placed in a known distance in front of the

[8] VGStudio, supplier: Volume Graphics GmbH, `http://www.volumegraphics.com/`.

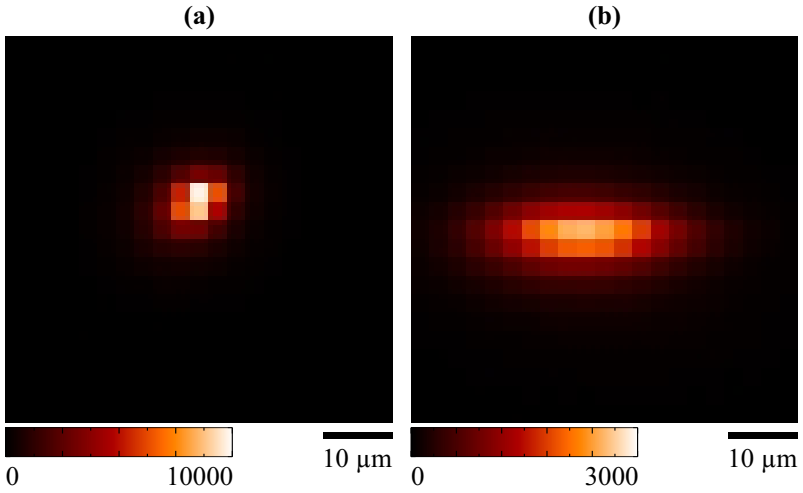

Figure D.4: Pinhole images recorded with the x-ray camera at beamline BW2 for pinhole-detector distances (a) 10 mm and (b) 100 mm. The photon energy was 24 keV. The images are averages of ten images and were corrected by the average of ten dark images. A subregion of 30×30 pixels from the images is shown.

x-ray camera into the center of the x-ray beam. The transmitted radiation was then observed with the x-ray camera. From the extension of the projected pinhole in the image, both, the horizontal and vertical beam divergence, were estimated. This gave an indication of the amount of blur that can be expected in the tomography measurements. Furthermore, the pinhole measurements were compared with the result of the MTF measurement.

The applied pinhole is a hole of 5 μm diameter that was lithographically prepared into a 100 μm thick gold foil with an aspect ratio of 1:20. This allowed to image the source, since the pinhole and the detector form a pinhole camera. Collimation effects can be neglected, since the beam divergence is much less than the limit imposed by the aspect ratio. The foil with the pinhole was mounted onto the sample holder with parallel orientation to the holder. Hereby vertical orientation was achieved. Then the sample holder was rotated until maximum intensity was transmitted by the pinhole, whereby the pinhole was perfectly aligned with the x-ray beam. The measurement was carried out at beamline BW2, at a photon energy of $E_{ph} = 24.0$ keV, optical magnification $m = 3.347$ (corresponding to an effective pixel size of $\tau = 2.69\,\mu$m), and using a $CdWO_4$ luminescent screen of 300 μm thickness with absorbing backing.

Figures D.4(a) and (b) show pinhole images that were recorded in 10 mm and 100 mm distance behind the pinhole. The images were dark image corrected. The observed intensity distribution is only a few pixels in diameter. The spread of intensity was determined from the square root of the second order moment of the images. The calculation was performed according to

$$\text{Spread}^2 = \sum_{\text{Pixels}} \left(\text{Distance to center-of-mass}^2 \, \frac{\text{Intensity in pixel}}{\text{Total intensity}} \right) . \tag{D.6}$$

The spread values obtained from the images according to this calculation are given in Table D.1. For increasing camera distance an increase of spread is observed predominantly for the

Table D.1: Spread of intensity in the pinhole images of Figure D.4(a) and (b).

Image	Pinhole-to-camera distance [mm]	Spread (H × V) [μm]
(a)	10	6.578×6.444
(b)	100	10.754×6.859

horizontal direction, i.e., in the plane of the storage ring. An upper limit of the beam divergence can be estimated from the maximum spread in 10 mm distance as

$$\text{Maximum beam divergence} = \frac{\text{Spread}}{\text{Pinhole-to-camera distance}} \,. \tag{D.7}$$

This gives a maximum beam divergence of 0.108 mrad. In a tomographic measurement the sample-detector distance is in the order of $2W$, where W is the detector width. Thus, the beam divergence causes a spread of the recorded image by $0.108 \times 10^{-3}\, W$. This can be compared with the sampling distance given by $\tau = W/N_t \approx 0.651 \times 10^{-3}\, W$ for the number of sampling points $N_t = 1536$. The beam divergence can, thus, be neglected. At any magnification of the x-ray camera, the added blur will also be much less than the width of the detector resolution.

The detector resolution was determined with an edge profile measurement (see Chapter 2). From a horizontally oriented (slightly tilted with respect to the detector grid) gold edge in short distance to the x-ray camera (~2 mm) the resolution parameter a_{10}, corresponding to 10% MTF, was determined as $a_{10} = 4.779\,\mu$m. Assuming a Gaussian intensity profile and approximating the pinhole as an aperture with Gaussian profile with spread of $5\,\mu$m, we can calculate the expected spread. The convolution of the two (assumed) Gaussians is given by $(4.779^2 + 5^2)^{-1/2} = 6.917\mu$m, which agrees well with the observed spread at 10 mm distance.

Appendix E

Model systems (computer phantoms)

Model systems (often called ‘computer phantoms’) are used to study the performance of CT reconstructions. A model system is the mathematical description of an ideal tomographic slice $f(x,y)$, from which projections $p_\theta(t)$ can be calculated. Note that the term ‘phantom’ can also refer to the real objects that are used for the test of CT setups.

Model systems are typically built from a combination of simple geometrical objects, for which the projections can be analytically calculated. The projections of the whole phantom are simply the sum of the projections of the individual objects. This follows directly from the linearity of the Radon transform. Generators for projection data are, e.g., included in the 2D reconstruction software of the RECLBL library and in the SNARK05[1] programming system. In the latter software the following elemental objects are implemented for the model system: triangles, rectangles, ellipses, circles, segments of a circle, and sectors of a circle. All of these are objects of homogeneous (attenuation) value.

Projections $p_\theta(t)$ of the elemental objects can be calculated analytically, which is important for the creation of exact projection data. Calculation of the projection data from only a finite representation $f(x_i,y_i)$ of $f(x,y)$ of the tomographic slice could introduce systematic error, with oscillations of one projection bin period. This would be critical for the study at subbin resolution, presented in Chapter 5. Using the analytical expressions given below, projection data can be calculated exactly and for any given combination of projection angle θ and position t.

The calculation of projections has been implemented in this work for two elemental objects: the well known ellipse, and an ellipse with gradient. Sinograms and reconstructions that were calculated as an example for both objects are shown in Figure E.1. The ellipse with gradient apparently has not been reported in the literature before. In contrast to the simple ellipse the ellipse with gradient shows a continuous variation of the attenuation value along one axis. It was developed in this work for the test of the entropy-based metric presented in Chapter 5, for which the normal objects with continuous attenuation coefficient are too ’simple’.

[1] The SNARK05 manual [32] is available online at `http://www.snark05.com/`. [visited May, 25th 2006]

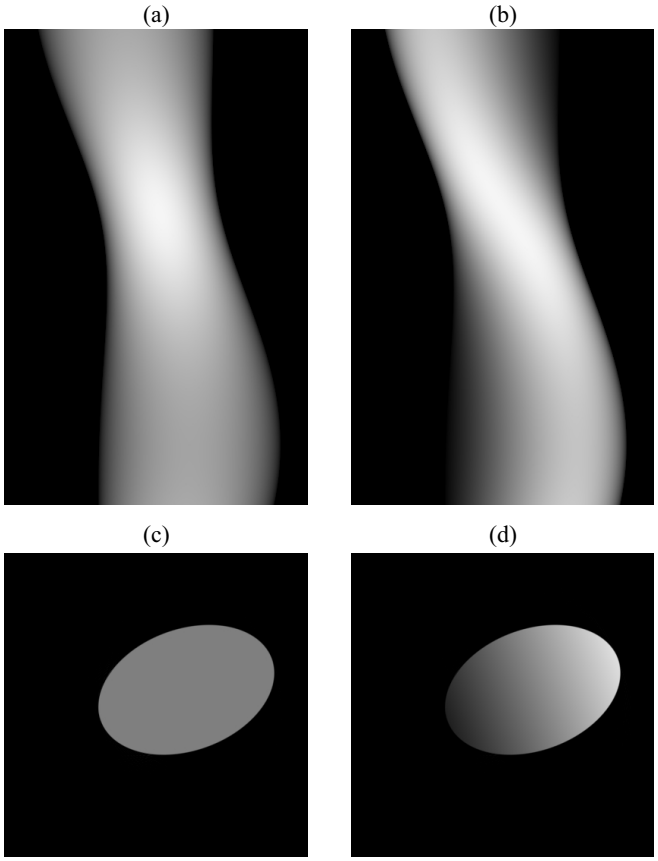

Figure E.1: (a) Projection data for an ellipse with center point $(x_0, y_0) = (0.2, 0.1)$, axis lengthes $A = 0.6$, $B = 0.4$, tilt angle $\alpha = 20^o$, and attenuation $\rho = 2.0$, calculated at $N_t = 400$ positions and for $N_\theta = 627$ projection angles. (b) Projection data of the same ellipse but with gradient $g = 0.75$. (c),(d) Reconstructions of the projection data calculated on a 400×400 pixel reconstruction grid.

E.1 Ellipse

The calculation of the projections of an ellipse is, e.g., described by Kak and Slaney [93]. We first present the result for a centered, and not tilted ellipse and afterwards generalize the result for an ellipse of arbitrary position and orientation.

The centered ellipse $f(x, y)$ [shown in Figure E.2(b)] is defined as

$$f(x,y) = \begin{cases} \rho & \text{for } \frac{x^2}{A^2} + \frac{y^2}{B^2} \leq 1 \\ 0 & \text{else} \end{cases} . \tag{E.1}$$

This ellipse is symmetric around the coordinate center and has axes of length A and B that are parallel to the x and y-axis respectively. The projection of the ellipse under an angle of θ is given as

$$p_\theta(t) = \begin{cases} \frac{2\rho AB}{a^2(\theta)} \sqrt{a^2(\theta) - t^2} & \text{for } \frac{x^2}{A^2} + \frac{y^2}{B^2} \leq 1 \\ 0 & \text{else} \end{cases} , \tag{E.2}$$

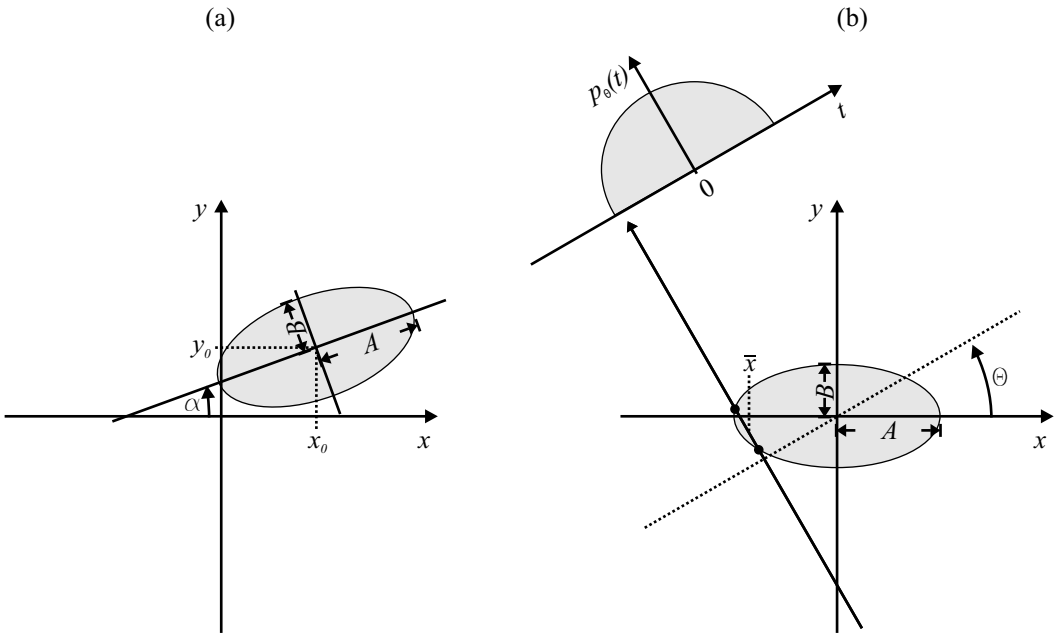

Figure E.2: (a) The geometrical parameters used for the description of an ellipse are the center point (x_0, y_0), the half length of the axes A and B, and the tilt angle α. (b) The formation of the projection under projection angle θ for a centered and non-tilted ellipse is shown. The midpoint of the intersection of line integral and ellipse, projected onto the x-axis, determines the position $\bar{x}$.

with

$$a^2(\theta) = A^2 \cos^2\theta + B^2 \sin^2\theta \; . \tag{E.3}$$

The projection of any arbitrary ellipse [Figure E.2(a)] with center at (x_0, y_0) and tilted by an angle of α can be given in terms of the projections of the centered and not tilted ellipse as

$$p'_\theta(t) = p_{\theta-\alpha}[t - s\cos(\gamma - \theta)] \; , \tag{E.4}$$

with $s = \sqrt{x_0^2 + y_0^2}$ and $\gamma = \arctan(y_0/x_0)$.

E.2 Ellipse with gradient

Similarly to the definition of $f(x,y)$ above, a centered and non-rotated ellipse with a gradient can be defined as

$$f_g(x,y) = \begin{cases} \rho\left(1 + \frac{x}{A}g\right) & \text{for } \frac{x^2}{A^2} + \frac{y^2}{B^2} \le 1 \\ 0 & \text{else} \end{cases} \; , \tag{E.5}$$

where the gradient is determined by the factor g. The value of $f(x,y)$ changes along the x-axis over the range of the ellipse from $\rho(1-g)$ to $\rho(1+g)$.

The projections $p_{g,\theta}(t)$ of f_g can be derived using the projections $p_\theta(t)$ given above. In the line integrals, which have to be evaluated to obtain $p_{g,\theta}(t)$, the value of $f_g(x,y)$ changes linearly over

the region of the ellipse. Therefore, the average of the integral over the range of the ellipse is equal to the value of f_g at the center of the intersections that the line integral makes with the ellipse. The projections are thus given by

$$p_{g,\theta}(t) = p_\theta(t)\left(1 + \frac{\overline{x}}{A}g\right) , \tag{E.6}$$

where $\overline{x}$ in Figure E.2(b) is the midpoint between the intersections projected onto the x-axis (direction of the gradient).

The point $\overline{x}$ is found by solving $x\cos\theta + y\cos\theta = t$ for y and substituting the result into the ellipse equation. The resulting quadratic equation is

$$x^2 - \frac{2A^2 t\cos\theta}{A^2\cos^2\theta + B^2\sin^2\theta}x + \frac{A^2\left(t^2 - B^2\sin^2\theta\right)}{A^2\cos^2\theta + B^2\sin^2\theta} = 0 . \tag{E.7}$$

It can easily be solved with the well known solution of a quadratic equation of the form $x^2+px+q = 0$, which is $x_{1,2} = -p/2 \pm \sqrt{p^2/4 - q}$. Here x_1 and x_2 are the x-values at the intersection points. Only the midpoint $\overline{x}$ of x_1 and x_2 is of interest. It is given by

$$\overline{x}(\theta, t) = \frac{x_1 + x_2}{2} = -\frac{p}{2} = \frac{A^2 t\cos\theta}{A^2\cos^2\theta + B^2\sin^2\theta} , \tag{E.8}$$

which corresponds to the first fraction in Equation (E.7).

This result can be generalized for the projections of any arbitrary ellipse with center at (x_0, y_0) and tilted by an angle of α as done before for the normal ellipse, now substituting the projections $p_{g,\theta}(t)$ into Equation (E.4). For $g = 0$ the ellipse has no gradient and corresponds to the basic ellipse described above.

Appendix F

Demonstration of the iterative scoring procedure

The method for the determination of the center of rotation presented in Chapter 5 is based on the iterative minimization procedure with multi-resolution approach described in Section 5.3. For demonstration of the iterative optimization, the method using metric Q_{IA} was applied to the multicircle model system of Figure 5.6(c). The five reconstructions calculated in each iteration step are shown in Figure F.1. The metric values of each of these sets of reconstructions have been calculated and are plotted in Figure F.2. The reconstruction that corresponds to the minimum value of $Q_{IA}(\tilde{t}_r)$ in the plots has been marked by an asterisk in Figure F.1 at each resolution.

During iteration the resolution of the reconstruction is increased until resolution $\delta t_r = 1$ is reached. Reconstructions in Figures F.1(A) – (D) have been reconstructed from the sinogram binned with binning factor $b = \delta_t$, the others without binning ($b = 1$). All reconstructions are shown in the same length scale. The size of the reconstruction grids varies due to the adapted zero padding as described in Section 5.3 .

At low resolution the artifacts caused by the wrong center of rotation are clearly visible. At increasing resolution visual detection of differences in the reconstructions becomes almost impossible at least without adjustment of the windowing parameters, i.e., the image scaling. However, even at resolution $\delta_t = 0.05$ bin, the plots of the metric in Figure F.2(J) still exhibit a clear minimum.

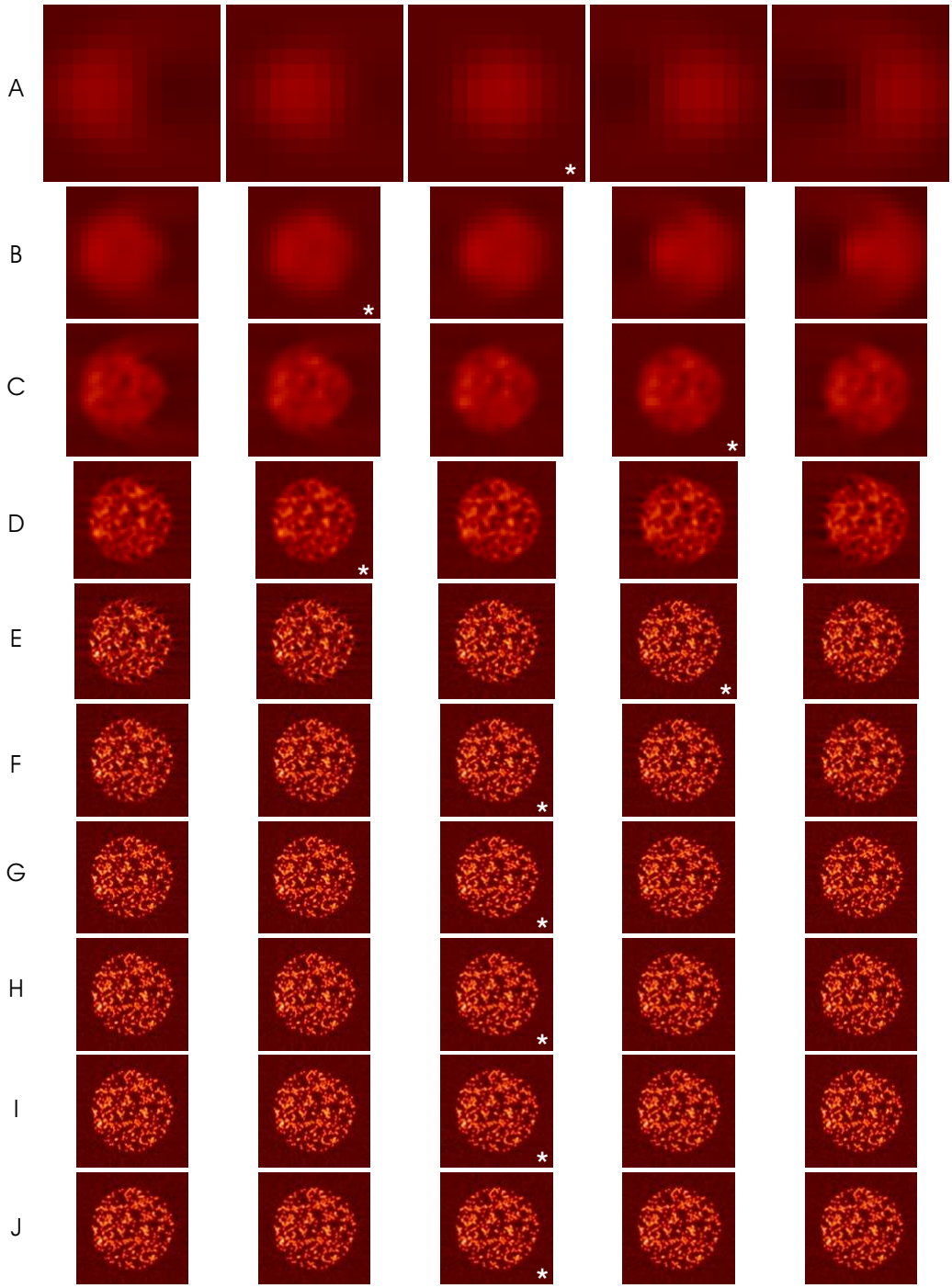

Figure F.1: The iterative scoring procedure for the determination of the center of rotation is illustrated for the multicircle model system from Figure 5.6. Reconstructions were calculated during the iteration with resolution δ_t: (A) 16.0, (B) 8.0, (C) 4.0, (D) 2.0, (E) 1.0, (F) 0.5, (G) 0.25, (H) 0.125, (I) 0.06125, and (J) 0.05 pixel. The reconstruction with minimum metric value Q_{IA} corresponding to the plots in Figure F.2 is marked with an asterisk.

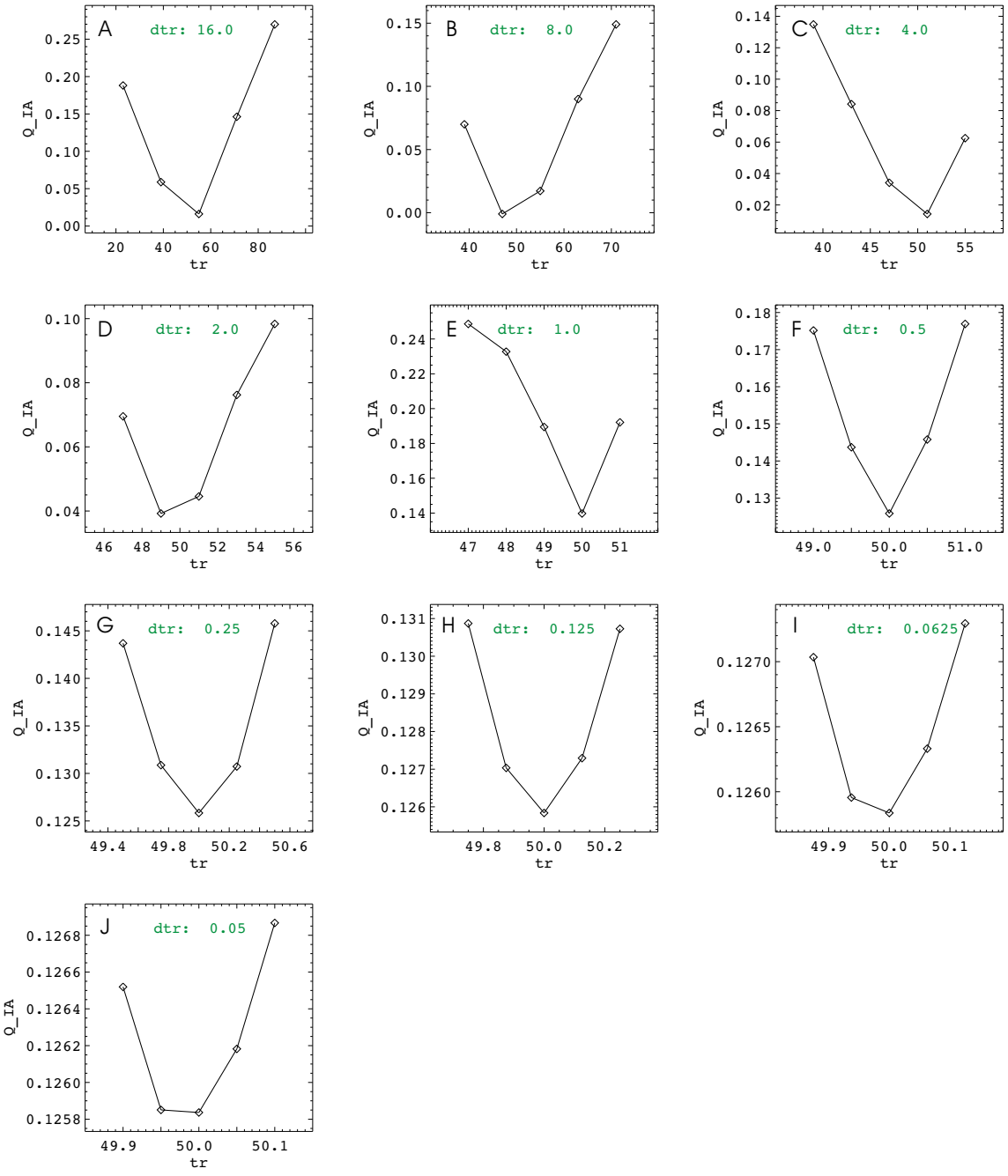

Figure F.2: Plots of the metric value Q_{IA} calculated during the iterative optimization for the reconstructions shown in Figure F.1. The different resolutions δ_t are given as the parameter 'dtr' in the plots. At all resolutions a unique minimum is found. Notice the increase of abscissa and ordinate resolution towards smaller δt_r, this is from (A) to (J).

Appendix G

X-ray camera component characteristics

Entrance window	Black Kapton® foil (thickness 25 μm), double layer with total thickness 50 μm
Luminescent screens	
Material	Cadmium tungstate ($CdWO_4$) single crystals
Coating	Absorbing backing formed by a layer of black lacquer paint on the screen´s back surface; complex refractive index of coating at 500 nm: $1.485 + j\,0.085$ (see Section 4.2.3)
Thickness	80 μm – 1000 μm
Refractive index n_{ls}	2.2 – 2.3
Scavenging gas (optional)	Helium or other, applied through crystal holder
Conversion efficiency	$\epsilon_{conv} \approx$ 3.4% or 13.6/[keV], according to Equation (2.16)
Central emission wavelength	500 nm (see Figure 2.6)
Decay time[b]	5 μs
Afterglow[b]	< 0.1% (after 3 ms), < 0.02% (after 100 ms)
Lens systems	Objectives (photographic lenses) operated in retrofocus position are used. The focal length (in mm) and the minimum f-number are given.
50 mm system:	
Model, supplier	Nikkor, 50 mm f/1.2, Nikon Inc.
Magnification range	0.7 – 4.1
Transmission	(95.8 %)[a] at 500 nm

35 mm system:	
Model, supplier	Nikkor, 35 mm f/1.4, Nikon Inc.
Magnification range	1.4 – 6.0
Transmission[a]	(93.2 %) at 500 nm
CCD camera	
Model, supplier	KX2, Apogee Instruments Inc.
Digitization	14 bits at 1.3 MHz
System gain g	5 electrons/ADU
Pixel binning	1×1 to 8×64, on chip
Frame sizes	Full frame, subframe
Exposure time	0.03 sec to 17 min
Optical shutter	Melles-Griot, 35 mm iris
Cooling	Peltier and water cooling (operated at -15 ^{o}C)
Readout time	1.2 sec (full frame, no binning)
Image data size	3.2 MB (full frame, no binning)
CCD chip	
Model, supplier	KAF-1600, Eastman Kodak Company
Technology	Front side illuminated, transparent gate, full frame CCD
Resolution (H×V)	1536×1024 pixels
Pixel size	$9 \times 9\,\mu$m^2
Sensitive area	14.0×9.3 mm^2
Saturation charge[b] N_{sat}	1×10^5 electrons
Photoresponse non-linearity[c]	Nom. 1%, max. 2%
Photoresponse non-uniformity[d]	Nom. 1%, max. 3%
Dark current	0.1 - 0.2 electrons / pixel / sec (at -10 ^{o}C)
Readout noise n_{el}	15 electrons rms
Readout bias	~550 ADU
Dynamic range (N_{sat}/n_{el})	6310:1 (equal to 76 dB or 12.7 bits)
Charge transfer efficiency:	~0.99998
Quantum efficiency	12% at 450 nm, 35% at 550 nm, 35% at 650 nm, (see Figure 2.6)

[a] Technical design value. From correspondence with Nikon GmbH, Nikon Professional Service (NPS), Nov./Dec. 2005.

[b] Data from van Eijk [146].

[c] Worst case deviation from straight line fit, between 1% and 90% of saturation voltage.

[d] One Sigma deviation of a 128×128 sample when CCD illuminated uniformly.

References

[1] C. Antoine, P. Nygård, Ø. W. Gregersen, R. Holmstad, T. Weitkamp, C. Rau. 3D images of paper obtained by phase-contrast X-ray microtomography: image quality and binarisation. *Nucl. Instrum. Methods Phys. Res. A*, 490:392–402, 2002.

[2] D. Atkinson, D. L. G. Hill, P. N. R. Stoyle, P. E. Summers, S. Clare, R. Bowtell, S. F. Keevil. Automatic compensation of motion artifacts in MRI. *Magnetic Resonance in Medicine*, 41:163–170, 1999.

[3] A. Authier. *Dynamical Theory of X-ray Diffraction*. Oxford Univ. Press, reprint with corrections edition, 2005.

[4] S. G. Azevedo, D. J. Schneberk, J. P. Fitch, H. E. Martz. Calculation of the rotational centers in computed tomography sinograms. *IEEE Trans. Nucl. Sci.*, 37(4):1525–1540, 1990.

[5] R. M. A. Azzam and N. M. Bashara. *Ellipsometry and Polarized Light*. Elsevier Science B.V., 4th edition, 1999.

[6] L. Baker, editor. *Selected papers on optical transfer function – foundation and theory*, volume MS 59 of *Milestone Series*. SPIE Opt. Eng. Press, 1992.

[7] S. L. Barna, M. W. Tate, S. M. Gruner, and E. F. Eikenberry. Calibration procedures for charge-coupled device x-ray detectors. *Rev. Sci. Instrum.*, 70(7):2927–2934, 1999.

[8] H. H. Barrett and W. Swindell. *Radiological Imaging*, volume 1. Academic Press, 1981.

[9] A. Becker, I. Sötje, C. Paulmann, F. Beckmann, T. Donath, R. Boese, O. Prymak, H. Tiemann, and M. Epple. Calcium sulfate hemihydrate is the inorganic mineral in statoliths of scyphozoan medusae (cnidaria). *Dalton Trans.*, 8:1545–1550, 2005.

[10] F. Beckmann, U. Bonse, F. Busch, and O. Günnewig. X-Ray Microtomography (μCT) Using Phase Contrast for the Investigation of Organic Matter. *J. Comput. Assist. Tomogr.*, 21:539–553, 1997.

[11] F. Beckmann. *Entwicklung, Aufbau und Anwendung eines Verfahrens der Phasenkontrast-Mikrotomographie mit Röntgen-Synchrotronstrahlung*. PhD thesis, Universität Dortmund, 1998.

[12] F. Beckmann, T. Lippmann, U. Bonse. High-energy microtomography using synchrotron radiation. In U. Bonse, editor, *Proc. SPIE Vol. 4142*, pages 225–230, 2000.

[13] F. Beckmann, T. Donath, T. Lippman, A. Schreyer, and H. Clemens. Synchrotron-radiation based microtomography of new materials for lightweight construction. In *DGZfP-Proceedings BB 84-CD*, pages 299–204, 2003.

[14] F. Beckmann, T. Lippmann, J. Metge, T. Dose, T. Donath, M. Tischer, K. D. Liss, and A. Schreyer. HARWI-II, the new high-energy beamline for materials science at HASYLAB/DESY. In *AIP Conf. Proc. 705: SRI 03 San Francisco, California*, pages 392–395, 2004.

[15] F. Beckmann, T. Donath, T. Dose, T. Lippmann, R. V. Martins, J. Metge, and A. Schreyer. Microtomography using synchrotron radiation at DESY: current status and future developments. In U. Bonse, editor, *Proc. SPIE Vol. 5535*, pages 1–10, 2004.

[16] F. Beckmann, J. Vollbrandt, T. Donath, H. W. Schmitz, A. Schreyer. Neutron and synchrotron radiation tomography: New tools for materials science at the GKSS-research center. *Nucl. Instrum. Methods Phys. Res. A*, 542(1–3):279–282, 2005.

[17] F. Beckmann, T. Donath, J. Fischer, T. Dose, T. Lippmann, L. Lottermoser, R. V. Martins, and A. Schreyer. New developments for synchrotron-radiation-based microtomography at DESY. In U. Bonse, editor, *Proc. SPIE Vol. 6318*, page 631810, 2006.

[18] R. Bernhardt, D. Scharnweber, B. Müller, P. Thurner, H. Schliephake, P. Wyss, F. Beckmann, J. Goebbels, and H. Worch. Comparison of microfocus- and synchrotron X-ray tomography for the analysis of osteointegration around Ti6Al4V implants. *Eur Cell Mater*, 30(7):42–51, 2004.

[19] R. Bernhardt, J. van den Dolder, S. Bierbaum, R. Beutner, D. Scharnweber, J. Jansen, F. Beckmann, H. Worch. Osteoconductive modifications of Ti-implants in a goat defect model: characterization of bone growth with SRμCT and histology. *Biomaterials*, 26(16):3009–3019, 2005.

[20] G. Blasse and B. C. Grabmaier. *Luminescent Materials*. Springer-Verlag, 1994.

[21] S. Bonnet, A. Koenig, S. Roux, P. Hugonnard, R. Guillemaud, and P. Grangeat. Dynamic x-ray computed tomography. *Proc. IEEE*, 91(10):1574–1587, 2003.

[22] U. Bonse, Q. Johnson, M. Nichols, R. Nusshardt, S. Krasnicki and J. Kinney. High resolution tomography with chemical specificity. *Nucl. Instr. and Meth. in Phys. Res. A*, 246(1–3):644–648, 1986.

[23] U. Bonse and F. Busch. X-ray computed microtomography (μCT) using synchrotron radiation (SR). *Prog. Biophys. Mol. Biol.*, 65(1–2):133–169, 1996.

[24] U. Bonse, F. Beckmann, M. Bartscher, T. Biermann, F. Busch, O. Günnewig. Phase-contrast x-ray tomography using synchrotron radiation. In U. Bonse, editor, *Proc. SPIE Vol. 3149*, pages 108–119, 1997.

[25] M. Born and E. Wolf. *Principles of optics*. Cambridge Univ. Press, 7th edition, 1999.

[26] R. Bracewell. *The Fourier Transform and Its Applications*. McGraw-Hill, 2nd edition, 1978.

[27] R. A. Brooks and G. di Chiro. Beam hardening in x-ray reconstructive tomography. *Phys. Med. Biol.*, 21(3):390–398, 1976.

[28] A. Brunetti and F. de Carlo. A robust procedure for determination of center of rotation in tomography. In U. Bonse, editor, *Proc. SPIE Vol. 5535*, pages 652–659, 2004.

[29] O. Brunke, S. Odenbach, T. Donath, and F. Beckmann. Al-Foam Microtomography. HASYLAB annual report, 2002.

[30] T. F. Budinger and G. T. Gullberg. Three-Dimensional Reconstruction in Nuclear Medical Emission Imaging. *IEEE Trans. Nucl. Sci.*, NS-21(3):2–20, 1974.

[31] F. Busch. *Auflösungsvermögen einer Mikrotomographie-Kamera für Röntgen-Synchrotronstrahlung*. PhD thesis, Univ. Dortmund, 1994.

[32] B. Carvalho, W. Chen, J. Dubowy, G. T. Herman, M. Kalinowski, H. Y. Liao, L. Rodek, L. Ruskó, S. W. Rowland, and E. Vardi-Gonen. *SNARK05: A programming system for the reconstruction of 2D images from 1D projections*, Dec. 2005.

[33] P. M. Cattaneo, M. Dalstra, F. Beckmann, T. Donath, and B. Melsen. High-resolution micro-tomography of orthodontically loaded dental implants. HASYLAB annual report, 2002.

[34] P. M. Cattaneo, M. Dalstra, F. Beckmann, T. Donath, and B. Melsen. Comparison of Conventional and Synchrotron-Based Microtomography of Bone around Dental Implants. HASYLAB annual report, 2003.

[35] P. M. Cattaneo, M. Dalstra, F. Beckmann, T. Donath, B. Melsen. Comparison of conventional and synchrotron radiation based microtomography of bone around dental implants. In U. Bonse, editor, *Proc. SPIE Vol. 5535*, pages 757–764, 2004.

[36] P. Cloetens. *Contribution to phase contrast imaging, reconstruction and tomography with hard synchrotron radiation: principles, implementation and applications*. PhD thesis, VUB (Faculteit Toegepaste Wetenschappen, Vakgroep Natuurkunde en Fotonica), 1999.

[37] P. A. Colegrove and H. R. Shercliff. 3-Dimensional CFD modelling of flow round a threaded friction stir welding tool profile. *Journal of Materials Processing Technology*, 169(2):320–327, 2005.

[38] H.-A. Crostack, J. Nellesen, F. Beckmann, W. Czayka, and C. Müller. Tensile test rig for in-situ x-ray microtomography at beamline BW2. HASYLAB annual report, 2000.

[39] H.-A. Crostack, J. Nellesen, G. Fischer, F. Beckmann, T. Donath, and J. Fischer. High Energy μCT at HARWI-II and SEM of a Cobalt / Diamond Composite. HASYLAB annual report, 2005.

[40] J. C. Dainty and R. Shaw. *Image Science*. Academic Press, second printing edition, 1976.

[41] M. Dalstra, E. Karaj, F. Beckmann, T. Andersen, P. M. Cattaneo. Osteonal mineralization patterns in cortical bone studied by synchrotron radiation-based computed microtomography and scanning acoustic microscopy. In U. Bonse, editor, *Proc. SPIE Vol. 5535*, pages 143–151, 2004.

[42] G. R. Davis. The effect of linear interpolation of the filtered projections on image noise in X-ray computed tomography. *J. X-Ray Sci. Technol.*, 4:191–199, 1994.

[43] Diffraction Limited, Ottawa, Ontario, Canada. *MaxIm DL – CCD imaging software*. Version 4.

[44] M. Di Michiel, J. M. Merino, D. Fernandez-Carreiras, T. Buslaps, and V. Honkimäki, P. Falus, T. Martins, and O. Svensson. Fast microtomography using high energy synchrotron radiation. *Rev. Sci. Instrum.*, 76(4), 2005.

[45] T. Donath, F. Beckmann, A. Schreyer, and H. Clemens. X-ray absorption contrast μCT of porous core Ti-6Al-4V metal foam. HASYLAB annual report, 2002.

[46] T. Donath, F. Beckmann, R. G. J. C. Heijkants, O. Brunke, and A. Schreyer. Characterization of polyurethane scaffolds using synchrotron radiation computed microtomography. In U. Bonse, editor, *Proc. SPIE Vol. 5535*, pages 775–782, 2004.

[47] T. Donath, F. Beckmann, R. Zettler, J. dos Santos, D. Lohwasser, T. Lippman, H. Clemens, and A. Schreyer. Investigation of material flow in friction stir welding using computed microtomography. In *AIP Conf. Proc. 705: SRI 03 San Francisco, California*, pages 1312–1315, 2004.

[48] T. Donath, R. Zettler, F. Beckmann, J. Fischer, J. F. dos Santos, D. Lohwasser, and A. Schreyer. Investigation of material flow in friction stir welds using high energy synchrotron radiation at HARWI II. HASYLAB annual report, 2005.

[49] T. Donath, F. Beckmann, and A. Schreyer. Automated determination of the center of rotation in tomography data. *J. Opt. Soc. Am. A*, 23(5):1048–1057, 2006.

[50] T. Donath, F. Beckmann, and A. Schreyer. Image metrics for the automated alignment of microtomography data. In U. Bonse, editor, *Proc. SPIE Vol. 6318*, page 631818, 2006.

[51] W. Drube, H. Schulte-Schrepping, H.-G. Schmidt, R. Treusch, and G. Materlik. Design and performance of the high-flux/high-brightness x-ray wiggler beamline BW2 at HASYLAB. *Rev. Sci. Instrum.*, 66:1668–1670, 1995.

[52] P. R. Edholm, R. M. Lewitt, and B. Lindholm. Novel Properties of the Fourier Decomposition of the Sinogram. In *Proc. SPIE Vol. 671*, pages 8–18, 1986.

[53] S. L. Ellenberger. *Influence of defocus on measurements in microscope images*. PhD thesis, Technische Universiteit Delft, 2000.

[54] J. C. Elliott, F. S. L. Wong, P. Anderson, G. R. Davis, and S. E. P. Dowker. Determination of mineral concentration in dental enamel from x-ray attenuation measurements. *Connective Tissue Research*, 38(1–4):61–72, 1998.

[55] M. Faessel, C. Delisée, F. Bos, and P. Castéra. 3D Modelling of random cellulosic fibrous networks based on X-ray tomography and image analysis. *Composites Science and Technology*, 65:1931–1940, 2005.

[56] K. Faulkner and B. M. Moores. Noise and contrast detection in computed tomography images. *Phys. Med. Biol.*, 29(4):329–339, 1984.

[57] L. A. Feldkamp, L. C. Davis, and J. W. Kress. Practical cone-beam algorithm. *J. Opt. Soc. Am. A*, 1(6):612–619, 1984.

[58] F. Fierz, B. Leukers, Ö. Degistirici, S. Irsen, F. Beckmann, and B. Müller. Design and characterization of 3D-printed hydroxyapatite scaffolds using synchrotron-radiation-based micro computed tomography. *European Cells and Materials*, 11(2):22, 2006.

[59] J. Fischer, J. Nellesen, H.-A. Crostack, T. Donath, F. Beckmann, and F. Witte. Determination of in-vivo corrosion rates of degradable implants by SR-microtomography. HASYLAB annual report, 2004.

[60] J. Fischer, T. Donath, F. Beckmann, and F. Witte. Direct corrosion measurement of Mg-alloys by SRμCT. HASYLAB annual report, 2005.

[61] B. P. Flannery, H. W. Deckman, W. G. Roberge, K. L. D'Amico. Three-Dimensional X-Ray Microtomography. *Science*, 237(4821):1439–1444, 1987.

[62] R. W. Fonda, J. F. Bingert, K. J. Colligan. Development of grain structure during friction stir welding. *Scripta Materialia*, 51:243–248, 2004.

[63] B. R. Frieden. *Probability, Statistical Optics and Data Testing*. Springer-Verlag, 2nd edition, 1991.

[64] G. E. Giakoumakis. Matching factors for various light-source-photodetector combinations. *Appl. Phys. A*, 52(1):7–9, 1991.

[65] G. H. Glover, R. L. Eisner. Theoretical resolution of computed tomography systems. *J. Comput. Assist. Tomogr.*, 3(1):85–91, 1979.

[66] H. Graafsma and R. Y. de Vries. Deconvolution of the two-dimensional point-spread function of area detectors using the maximum-entropy algorithm. *J. Appl. Cryst.*, 32:683–691, 1999.

[67] W. Graeff, L. Bittner, W. Brefeld, U. Hahn, G. Heintze, J. Heuer, J. Kouptsidis, J. Pflüger, M. Schwartz, E. W. Weiner, and T. Wroblewski. HARWI–A hard x-ray wiggler beam at DORIS. *Rev. Sci. Instrum.*, 60(7):1457–1459, 1989.

[68] L. Grodzins. Optimum energies for x-ray transmission tomography of small samples. *Nucl. Instrum. Methods*, 206:541–545, 1983.

[69] L. H. Groom, L. Mott, S. Shaler. Relationship between Fiber Furnish and the Structural Performance of MDF. In Michael P. Wolcott, editor, *33rd International Particleboard/Composite Materials Symposioum Proceedings*, 1999.

[70] S. M. Gruner and M. W. Tate, E. F. Eikenberry. Charge-coupled device area x-ray detectors. *Rev. Sci. Instrum.*, 73(8):2815–2842, 2002.

[71] M. Guerra, C. Schmidt, J. C. McClure, L. E. Murr, A. C. Nunes. Flow patterns during friction stir welding. *Mat. Charact.*, 49:95–101, 2003.

[72] W. G. Hawkins. *Mathematics of Computed Tomography*. PhD thesis, The University of Arizona, 1983.

[73] R. G. J. C. Heijkants, F. Beckmann, T. Donath, R. V. van Calck, T. G. van Tienen, N. Ramrattan, P. Buma, J. H. de Groot, A. J. Pennings, R. P. H. Veth, and A. J. Schouten. Micro CT of polyurethane scaffolds for meniscus replacement. HASYLAB annual report, 2003.

[74] R. G. J. C. Heijkants. *Polyurethane scaffolds as meniscus reconstruction materials*. PhD thesis, Univ. of Groningen, The Netherlands, 2004.

[75] S. Helgason. *The Radon Transform*, volume 5 of *Progress in Mathematics*. Birkhäuser, Boston Basel Stuttgart, 1980.

[76] G. T. Herman. *Image Reconstruction from Projections*. Academic Press, New York, 1980.

[77] J. P. Hogan, R. A. Gonsalves, and A. S. Krieger. Micro computed tomography: removal of translational stage backlash. *IEEE Trans. Nucl. Sci.*, 40(4):1238–1241, 1993.

[78] R. Holmstad. *Methods for paper structure characterisation by means of image analysis*. Phd thesis, Norwegian University of Science and Technology, 2004.

[79] R. Holmstad, O. Gregersen, U. Aaltosalmi, M. Kataja, A. Koponen, A. Goel, S. Ramaswamy. Comparison of 3D structural characteristics of high and low resolution X-ray microtomographic images of paper. *Nordic Pulp and Paper Research Journal*, 20(3):283–288, 2005.

[80] H. H. Hopkins. The frequency response of a defocused optical system. *Proc. Roy. Soc. A*, 23(1):91–103, 1955.

[81] G. N. Hounsfield. Computerized transverse axial scanning (tomography): Part I. Description of system. *British Journal of Radiology*, 46:1016–1022, 1973.

[82] R. H. Huesman, G. T. Gullberg, W. L. Greenberg, and T. F. Budinger. *RECLBL Library users manual: Donner algorithms for reconstruction tomography*. Lawrence Berkeley Laboratory, University of California, 1977.

[83] L. Ibáñez, W. Schroeder, L. Ng, J. Cates, and the Insight Software Consortium. *The ITK Software Guide 1.4*. Kitware Inc., 2003.

[84] ICRU – International Commission on Radiation Units and Measurements. Tissue substitutes in radiation dosimetry and measurement. Report 44, 1989.

[85] G. Illing, J. Heuer, B. Reime, M. Lohmann, R. H. Menk, L. Schildwächter, W.-R. Dix, and W. Graeff. Double beam bent Laue monochromator for coronary angiography. *Rev. Sci. Instrum.*, 66(2):1379–1381, Feb. 1995.

[86] S. H. Irsen, B. Leukers, B. Bruckschen, C. Tille, H. Seitz, F. Beckmann, and B. Müller. Image-based analysis of the internal microstructure of bone replacement scaffolds fabricated by 3D printing. In U. Bonse, editor, *Proc. SPIE Vol. 6318*, page 631809, 2006.

[87] J. D. Jackson. *Classical electrodynamics*. John Wiley & Sons, Inc., 3rd edition, 1999.

[88] B. Jähne. *Digital image processing*. Springer, 5th revised and extended edition, 2002.

[89] A. K. Jain. *Fundamentals of digital image processing*. Prentice Hall, 1st edition, 1988.

[90] P. A. Jansson. *Deconvolution: With Applications in Spectroscopy*. Academic Press, 1984.

[91] R. A. Jones. An automated technique for deriving MTF's from edge traces. *Photographic Science and Engineering*, 11:102–106, 1967.

[92] M. Kachelrieß and W. A. Kalender. Presampling, algorithm factors, and noise: Considerations for CT in particular and for medical imaging in general. *Med. Phys.*, 32(5):1321–1334, 2005.

[93] A. C. Kak and M. Slaney. *Principles of Computerized Tomographic Imaging*. IEEE Press, 1988.

[94] E. Karaj. Osteonal mineralization of the cortical bone studied with the scanning acoustic microscopy and micro computed tomography. Master thesis, University of Siegen, 2004.

[95] J. H. Kim, K. Y. Kwak, and S. B. Park. Iterative reconstruction-reprojection in projection space. *Proc. IEEE*, 73:1140–1141, 1985.

[96] A. Koch, C. Raven, P. Spanne, and A. Snigirev. X-ray imaging with submicrometer resolution employing transparent luminescent screens. *J. Opt. Soc. Am. A*, 15(7):1940–1951, 1998.

[97] M. Kuehbacher, J. Fischer, B. Gruenewald, T. Donath, D. Behne, A. Kyriakopoulos, and F. Beckmann. Honeybee in 3D – Neuroimaging with μ-Tomography. HASYLAB annual report, 2005.

[98] O. Lame, D. Bellet, M. Di Michiel, D. Bouvard. In situ microtomography investigation of metal powder compacts during sintering. *Nucl. Instr. and Meth. in Phys. Res. B*, 200:287–294, 2003.

[99] M. Lohmann, W.-R. Dix, J. Metge, and B. Reime. Instrumentation for diffraction enhanced imaging experiments at HASYLAB. In *AIP Conf. Proc. 705: SRI 03 San Francisco, California*, page 392, 2004.

[100] W. Lu and T. R. Mackie. Tomographic motion detection and correction directly in sinogram space. *Phys. Med. Biol.*, 47:1267–1284, 2002.

[101] L. Mandel. Image fluctuations in cascade intensifiers. *Br. J. Appl. Phys.*, 10:233–234, 1959.

[102] T. Martin and A. Koch. Recent developments in X-ray imaging with micrometer spatial resolution. *Journal of Synchrotron Radiation*, 13(2):180–194, Mar 2006.

[103] K. P. McGee, A. Manduca, J. P. Felmlee, S. J. Riederer, and R. L. Ehman. Image metric-based correction (autocorrection) of motion effects: Analysis of image metrics. *J. Magn. Reson. Imag.*, 11(2):174–181, 2000.

[104] J. Modersitzki. *Numerical Methods for Image Registration*. Numerical Mathematics and Scientific Computation. Oxford University Press, 2004.

[105] W. W. Moses. Current trends in scintillator detectors and materials. *Nucl. Instrum. Methods Phys. Res. A*, 487:123–128, 2002.

[106] B. Müller, F. Beckmann, M. Huserand, F. Maspero, G Székely, K. Ruffieux, P. Thurner, and E. Wintermantel. Non-destructive three-dimensional evaluation of a polymer sponge by micro-tomography using synchrotron radiation. *Biomolecular Engineering*, 19:73–78, August 2002.

[107] L. Nagornaya, G. Onyshchenko, E. Pirogov, N. Starzhinskiy, I. Tupitsyna, V. Ryzhikov, Yu. Galich, Yu. Vostretsov, S. Galkin, and E. Voronkin. Production of the high-quality $CdWO_4$ single crystals for application in CT and radiometric monitoring. *Nucl. Instrum. Methods Phys. Res. A*, 537:163–167, 2005.

[108] F. Natterer. *The Mathematics of Computerized Tomography*, volume 32 of *Classics in Applied Mathematics*. Soc. for Industrial & Applied Math., 2001.

[109] F. Natterer and E. L. Ritman. Past and Future Directions in X-Ray Computed Tomography (CT). *International Journal of Imaging Systems and Technology*, 12:175–187, 2002.

[110] M. Nickel, E. Bullinger, H. M. Reiswig, T. Donath, and F. Beckmann. Functional Micromorphology of Sponges (Porifera). HASYLAB annual report, 2004.

[111] M. Nickel, J. U. Hammel, T. Donath, and F. Beckmann. Quantitative morphometrics and contraction analysis of the marine sponge *Tethya wilhelma* using synchrotron radiation based x-ray microtomography and in vivo x-ray imaging. HASYLAB annual report, 2005.

[112] M. Nickel, T. Donath, M. Schweikert, F. Beckmann. Functional morphology of Tethya species (Porifera): 1. Quantitative 3D-analysis of Tethya wilhelma by synchrotron radiation based X-ray microtomography. *Zoomorphology*, 125(4):209–223, 2006.

[113] M. Nickel, E. Bullinger, F. Beckmann. Functional morphology of Tethya species (Porifera): 2. Three-dimensional morphometrics on spicules and skeleton superstructures of T. minuta. *Zoomorphology*, 125(4):225–239, 2006.

[114] M. Nickel, T. Donath, J. U. Hammel, J. Fischer, F. Beckmann. Functional morphology of Tethya species (Porifera): 3. In vivo x-ray micro-imaging of skeletal superstructure dynamics during contraction in T. wilhelma. *J. Struct. Biol.*, 2006. In preparation.

[115] S. F. Nielsen, H. F. Poulsen, F. Beckmann, C. Thorning, and J. A. Wert. Measurements of plastic displacement gradient components in three dimensions using marker particles and synchrotron x-ray absorption microtomography. *Acta Mater.*, 51:2407–2415, 2003.

[116] R. Nußhardt. *Elementspezifische und hoch ortsauflösende Mikrotomographie mit Synchrotronstrahlung*. Phd thesis, Universität Dortmund, 1990.

[117] S. Nuzzo, F. Peyrin, P. Cloetens, J. Baruchel, G. Boivin. Quantification of the degree of mineralization of bone in three dimensions using synchrotron radiation microtomography. *Med. Phys.*, 29(11):2672–2681, 2002.

[118] S. Peth, F. Beckmann, T. Donath, J. Fischer, A. J. M. Smucker, and R. Horn. Pore space analysis of soil aggregates investigated by microtomography using synchrotron radiation. HASYLAB annual report, 2005.

[119] E. F. Plechaty, D. E. Cullen, and R. J. Howerton. Tables and graphs of photon-interaction cross sections from 0.1 keV to 100 MeV derived from the LLL evaluated-nuclear-data library. Report UCRL-50400, vol. 6, rev. 3, Lawrence Livermore National Laboratory, 1981.

[120] W. H. Press, B. P. Flannery, S. A. Teukolsky, and W. T. Vetterling. *Numerical Recipes in C*. Cambridge Univ. Press, 2nd edition, 1992.

[121] J. L. Prince and A. S. Willsky. Hierarchical reconstruction using geometry and sinogram restoration. *IEEE Transactions on Image Processing*, 2(3):401–416, 1993.

[122] O. Prymak, C. Schiller, H. Tiemann, I. Soetje, J. Marxen, T. Donath, F. Beckmann, M. Epple. Mikrotomographie an Biomaterialien. HASYLAB annual report, 2005.

[123] O. Prymak, D. Bogdanski, M. Köller, S. A. Esenwein, G. Muhr, F. Beckmann, T. Donath, M. Assad, M. Epple. Morphological characterization and in vitro biocompatibility of a porous nickel-titanium alloy. *Biomaterials*, 26(29):5801–5807, 2005.

[124] O. Prymak, H. Tiemann, I. Sötje, J. C. Marxen, A. Klocke, B. Kahl-Nieke, F. Beckmann, T. Donath, M. Epple. Application of synchrotron-radiation-based computer microtomography (SRlCT) to selected biominerals: embryonic snails, statoliths of medusae, and human teeth. *J. Biol. Inorg. Chem.*, 10(6):688–695, 2005.

[125] R. C. Puetter, T. R. Gosnell, and Amos Yahil. Digital image reconstruction: Deblurring and denoising. *Annual Review of Astronomy & Astrophysics*, 43(1):139–194, 2005.

[126] M. Rabbani and R. Shaw. Detective quantum efficiency of imaging systems with amplifying and scattering mechanisms. *J. Opt. Soc. Am. A*, 4(5), 1987.

[127] J. Radon. Über die Bestimmung von Funktionen durch ihre Integralwerte längs gewisser Mannigfaltigkeiten. *Ber. Ver. Sächs. Akad. Wiss. Leipzig, Math-Phys. Kl.*, 69:262–277, April 1917. In German. An english translation can be found in S. R. Deans: *The Radon Transform and Some of Its Applications*, Appendix A.

[128] G. N. Ramachandran and A. V. Lakshminarayanan. Three-dimensional Reconstruction from Radiographs and Electron Micrographs: Application of Convolutions instead of Fourier Transforms. *Proc. Natl. Acad. Sci. U.S.A.*, 68:2236–2240, 1971.

[129] C. Raven. *Microimaging and Tomography with High Energy Coherent Synchrotron X-Rays*. Phd thesis, R.-W. Technische Hochschule Aachen, 1998.

[130] S. Rolland du Roscoat and J.-F. Bloch and X. Thibault. Synchrotron radiation microtomography applied to investigation of paper. *J. Phys. D*, 38:A78–A84, 2005.

[131] J. A. Rowlands. The physics of computed radiography. *Phys. Med. Biol.*, 47:R123–R166, 2002.

[132] G. Schröder and H. Treiber. *Technische Optik: Grundlagen und Anwendungen*. Vogel Buchverlag, 9., erw. Aufl. edition, 2002.

[133] C. G. Schroer, J. Meyer, M. Kuhlmann, B. Benner, T. F. Günzler, B. Lengeler, C. Rau, T. Weitkamp, A. Snigirev, and I. Snigireva. Nanotomography based on hard x-ray microscopy with refractive lenses. *Appl. Phys. Lett.*, 81(8):1527–1529, 2002.

[134] H. Schulte-Schrepping, J. Heuer, and B. Hukelmann. Adaptive indirectly cooled monochromator crystals at HASYLAB. *J. Synchrotron Rad.*, 5:682–684, 1998.

[135] H. Seitz, W. Rieder, S. Irsen, B. Leukers, C. Tille. Three-dimensional printing of porous ceramic scaffolds for bone tissue engineering. *J. Biomed. Mater. Res. B*, 74(2):782–788, 2005.

[136] C. E. Shannon. A mathematical theory of communication. *The Bell System Technical Journal*, 27:379–423, 623–656, 1948.

[137] L. A. Shepp, S. K. Hilal, and R. A. Schulz. Tuning fork artifact in computerized tomography. *Computer Graphics and Image Processing*, 10(3):246–255, July 1979.

[138] I.-M. Sintorn, M. Axelsson, S. Svensson, and G. Borgefors. Segmentation of individual pores in 3D images of paper. *Nordic Pulp and Paper Res. J.*, 20(3):346–349, 2005.

[139] M. Stampanoni, G. Borchert, R. Abela, P. Rüegsegger. Nanotomography based on double asymmetrical Bragg diffraction. *Appl. Phys. Lett.*, 82(17):2922–2924, 2003.

[140] R. K. Swank. Absorption and noise in x-ray phosphors. *J. Appl. Phys.*, 44(9):4199–4203, 1973.

[141] D. Tadic, F. Beckmann, T. Donath, and M. Epple. Untersuchungen an unterschiedlichen Knochenersatzmaterialien mittels Synchrotron μ-Computertomographie. HASYLAB annual report, 2003.

[142] M. W. Tate, D. Chamberlain, S. M. Gruner. Area x-ray detector based on a lens-coupled charge-coupled device. *Rev. Sci. Instrum.*, 76, 2005.

[143] G. Taton, T. Rok, E. Rokita, Z. Tabor, M. Karwala-Szytula, F. Beckmann, T. Donath, and J. Fischer. 3D Bone Architecture in Osteoporosis. HASYLAB annual report, 2005.

[144] W. M. Thomas, E.D. Nicholas, J.C. Needham, M. G. Church, P. Templesmith, C. J. Dawes. International Patent Application No. PCT/GB92/02203 and GB Patent Application No. 9125978.9, 1991.

[145] P. Thurner, F. Beckmann, and B. Müller. An optimization procedure for spatial and density resolution in hard x-ray micro-computed tomography. *Nucl. Instrum. Methods Phys. Res. B*, 225:599–603, 2004.

[146] C. W. E. van Eijk. Inorganic scintillators in medical imaging detectors. *Nucl. Instrum. Methods Phys. Res. A*, 509:17–25, 2003.

[147] R. Verker, P. K. Pranzas, F. Beckmann, T. Donath, A. Schreyer, N. Eliaz, and E. Grossman. Characterisation of the Effect of Simulated Space Debris on Polymers Using X-ray Microtomography. HASYLAB annual report, 2004.

[148] F. P. Vidal, J. M. Létang, G. Peix, and P. Cloetens. Investigation of artefact sources in synchrotron microtomography via virtual x-ray imaging. *Nucl. Instrum. Methods Phys. Res. B*, 234(3):333–348, 2005.

[149] T. Vugrin, F. Beckmann, T. Donath, J. Fischer, A. Schreyer. Investigation of Root Flaws in Friction Stir Welds. HASYLAB annual report, 2005.

[150] T. Walther, H. Thömen, T. Donath, F. Beckmann. Microstructure of Medium Density Fiberboard (MDF). HASYLAB annual report, 2004.

[151] T. Walther, T. Donath, K. Terzic, H. Meine, H. Thömen, and F. Beckmann. Microstructural Investigations on Natural Fiber Composites and Medium Density Fiberboard (MDF). HASYLAB annual report, 2005.

[152] T. Walther, K. Terzic, T. Donath, H. Meine, F. Beckmann, and H. Thoemen. Microstructural analysis of lignocellulosic fiber networks. In U. Bonse, editor, *Proc. SPIE Vol. 6318*, page 631812, 2006.

[153] T. Walther. *Methoden zur qualitativen und quantitativen Analyse der Mikrostruktur von Naturfaserwerkstoffen*. Dissertation, University of Hamburg, Hamburg, Germany, Department of Wood Science, Mechanical Wood Technology, 2006.

[154] H. Wang. *Creating Virtual Wood Particulate Composites*. Phd thesis, University of Maine, Orono, Maine, USA, 2000.

[155] H. Wang and S. M. Shaler. Computer-simulated three-dimensional microstructure of wood fibre composite materials. *Journal of Pulp and Paper Science*, 24(10):314–319, 1998.

[156] D. Weiß, G. Schneider, S. Vogt, P. Guttmann, B. Niemann, D. Rudolph, G. Schmahl. Tomographic imaging of biological specimens with the cryo transmission x-ray microscope. *Nucl. Instr. and Meth. in Phys. Res. A*, 467-468:13081311, 2001.

[157] T. Weitkamp. *Imaging and Tomography with High Resolution Using Coherent Hard Synchrotron Radiation*. PhD thesis, Universität Hamburg, 2002.

[158] K. Wille. *Physik der Teilchenbeschleuniger und Synchrotronstrahlungsquellen; Eine Einführung*. Teubner Verlag, 2002.

[159] F. Witte, J. Fischer, J. Nellesen, H.-A. Crostack, T. Donath, and F. Beckmann. In-vivo corrosion rates of magnesium alloys determined by synchrotron-radiation based microtomography (SRμCT). HASYLAB annual report, 2005.

[160] F. Witte, J. Fischer, J. Nellesen, H.-A. Crostack, V. Kaese, A. Pisch, F. Beckmann, and H. Windhagen. In vitro and in vivo corrosion measurements of magnesium alloys. *Biomaterials*, 27(7):1013–1018, 2006.

[161] R. Zettler, T. Donath, F. Beckmann, J. dos Santos, D. Lohwasser, T. Lippmann, and A. Schreyer. Investigation of Material Flow in Friction Stir Welds of Aluminium Alloys using Micro CT. HASYLAB annual report, 2003.

[162] R. Zettler, J. F. dos Santos, T. Donath, F. Beckmann, T. Lippmann, D. Lohwasser, and A. Schreyer. Validation of Marker Material Flow in 4 mm Thick Friction Stir Welded Al 2024-T351 as reported by Computed Microtomography using Standard Metallographic Techniques. HASYLAB annual report, 2004.

[163] R. Zettler, S. Lomolino, J. F. dos Santos, T. Donath, F. Beckmann, T. Lippman, D. Lohwasser. A study on material flow in FSW of AA 2024-T351 and AA 6056-T4 alloys. In Philip Threadgill, editor, *5th International FSW Symposium - Metz, France 14-16 September*, 2004.

[164] R. Zettler, S. Lomolino, J. F. dos Santos, T. Donath, F. Beckmann, T. Lippman, D. Lohwasser. Effect of tool geometry and process parameters on material flow in FSW of an AA 2024-T351 alloy. *'Welding in the World' Journal of the International Institute of Welding*, 49(3/4):41–46, 2005.

[165] R. Zettler, T. Donath, J. F. dos Santos, F. Beckmann, and D. Lohwasser. Validation of marker material flow in 4 mm thick friction stir welded Al 2024-T351 alloy through computer microtomographic and dedicated metallographic techniques. *Advanced Engineering Materials*, 8(6):487–490, 2006.

[166] U. Ziese, A. H. Janssen, J.-L. Murk, W. J. C. Geerts, T. van der Krift, A. J. Verkleij, and A. J. Koster. Automated high-throughput electron tomography by pre-calibration of image shifts. *Journal of Microscopy*, 205:187–200, 2002.

Acknowledgments

This thesis is based upon research carried out at the outstation of the GKSS-Research Center Geesthacht that is located at the Hamburger Synchrotronstrahlungslabor HASYLAB at the Deutsches Elektronen-Synchrotron DESY. Many persons contributed in very different ways to make this work successful.

First of all I want to thank my supervisor Prof. Dr. Andreas Schreyer for giving me the possibility to work in his group, for his advice, and the excellent working conditions he provided.

Dr. Felix Beckmann was the mentor of this work and the one who introduced me to microtomography. Thank you Felix, for the many fruitful discussions on tomography and, not to forget, for enriching my life with memorable concerts and barbecues.

Jens Fischer has been an important member of our tomography team. Thank you Jens, for the enjoyable time we spent together at the beamline and in the office and, of course, for regularly fixing my bike.

The tomographic studies that are presented in this work were made possible by the help of many microtomography users and collaborators. Rudolf Zettler and Dr. Jorge dos Santos were the driving force behind the friction stir welding pin. Dr. Michel Dalstra, Paolo Cattaneo, and Evis Karaj prepared and carried out the examination of the cortical bones. Stephan Irsen prepared the porous scaffolds and, fortunately, Dr. Bert Müller had a very close and critical look at the data that we produced. Thomas Walther prepared the fiberboards and Kasim Terzic and Hans Meine from the group of Dr. Ulrich Köthe made a large contribution to the characterization of those little wood fibers with their 3D algorithms. Furthermore, data that I used for demonstration were recorded within the projects of Prof. Dr. R. Horn and S. Peth, R. Bernhardt and D. Scharnweber, and R. G. J. C. Heijkants. Danny Chan carried out the refractive index measurements and Jens Nellesen cross-checked the reconstruction algorithms. Thanks to you all for your contribution!

I am grateful to all colleagues of HASYLAB and GKSS, who helped to keep the microtomography setup and the beamlines running, for their often invisible work. Dr. Horst Schulte-Schrepping, Dr. Wolfgang Drube, and Bernd Reime set up the beamlines. Dr. Lars Lottermoser and Dr. Joachim Metge managed all those Gigabytes of disk space and Teraflops of computing power that were needed. Thomas Dose was always there, when technical problems occurred as those with the air condition.

Thanks to my room mates Bernd Hasse and Oliver Brunke for freezing and sweating with me in our office and making it a lively and enjoyable working place.

Special thanks to Julia Herzen and my mother Bettina Donath for proof-reading this thesis.

Most of all I want to thank my Family and Doctor Moni for their support, patience, and for being there at any time, when needed.